Interaction Notes
Note 423

October 1981

Synthesis of SEM-Derived Equivalent Circuits For Electromagnetic Energy Collecting Structures

Krzysztof A. Michalski
L. Wilson Pearson

Department of Electrical Engineering
University of Mississippi
University MS 38677

FOREWORD

This Document was prepared by the Department of Electrical Engineering of the University of Mississippi as the Final Technical Report on Subtask 03-06 of Contract F29601-78-C-0082. Mission Research Corporation is the prime contractor. This work was begun at the University of Kentucky and the activity and associated contract moved to the University of Mississippi when the authors changed affiliation.

ABSTRACT

A systematic approach is developed for the synthesis of physically realizable equivalent circuits for antennas and scatterers with definable ports from their SEM (Singularity Expansion Method) description. The necessary SEM information includes the complex natural resonances (or "poles") of the structure and the associated modal currents ("natural modes") and normalization coefficients. From the poles and natural modes one can compute the coupling coefficients, which weight the given singularity's contribution to the response for a given incident field.

The synthesis is performed as a superposition of circuit modules associated with conjugate pairs of poles. This approach leads to simple circuits for which explicit expressions for the element values in terms of the SEM parameters can be given. The entire equivalent network can be divided into two parts — an immittance part describing the driving-point properties of the structure, and a source part describing its energy-collecting properties. The immittance part is intrinsic to the structure and is independent of the incident field. The source part, however, depends on the direction of arrival of the impinging plane wave and is driven by an automatic voltage source with the waveform corresponding to the time history of incident field.

The developed equivalent circuit synthesis procedures are tested on a thin-wire loop and dipole antennas and on a spherical antenna. Results are presented showing good agreement between the SEM equivalent circuits' responses and responses obtained by other means.

TABLE OF CONTENTS

LIST OF FIGURES

9

10

11

LIST OF TABLES

12

13

Table   Page

CHAPTER 1

INTRODUCTION

1.1 Statement of the Problem

Equivalent circuits containing frequency dependent elements, or circuits valid only in narrow bands of frequencies, have been used for years by the electromagnetics community to model the terminal behavior and receiving properties of radiating and scattering structures. In contrast, this work is concerned with the synthesis of broad-band equivalent circuits with frequency and time invariant elements, for electromagnetic energy collecting structures with definable ports.

Our goal can be perhaps best explained with the help of Figure 1.1. In Figure 1.1(a) is shown an energy collecting structure (a cylindrical dipole in this case) excited by a plane wave having some time history $f(t)$, and loaded at its terminals by a general impedance Z_{ℓ}, which is permitted to be nonlinear and/or time-varying. Our task is to proceed from the known mathematical description of the structure and a given specification of the spatial character of the impinging field, to synthesize an equivalent active network (Figure 1.1(b)) consisting of a finite number of lumped, linear circuit elements, whose behavior at the terminals is a good approximation to that of the original object for any loading conditions. The network should be driven by an autonomic voltage source with a waveform $f(t)$ and, with the source shorted, it should replicate the driving-point immittance of the structure with no external incident field present. This equivalent network should also be applicable in the time-harmonic mode of operation.

The question which naturally arises is, "Why would one want to construct an equivalent circuit for an electromagnetic/radiating

15
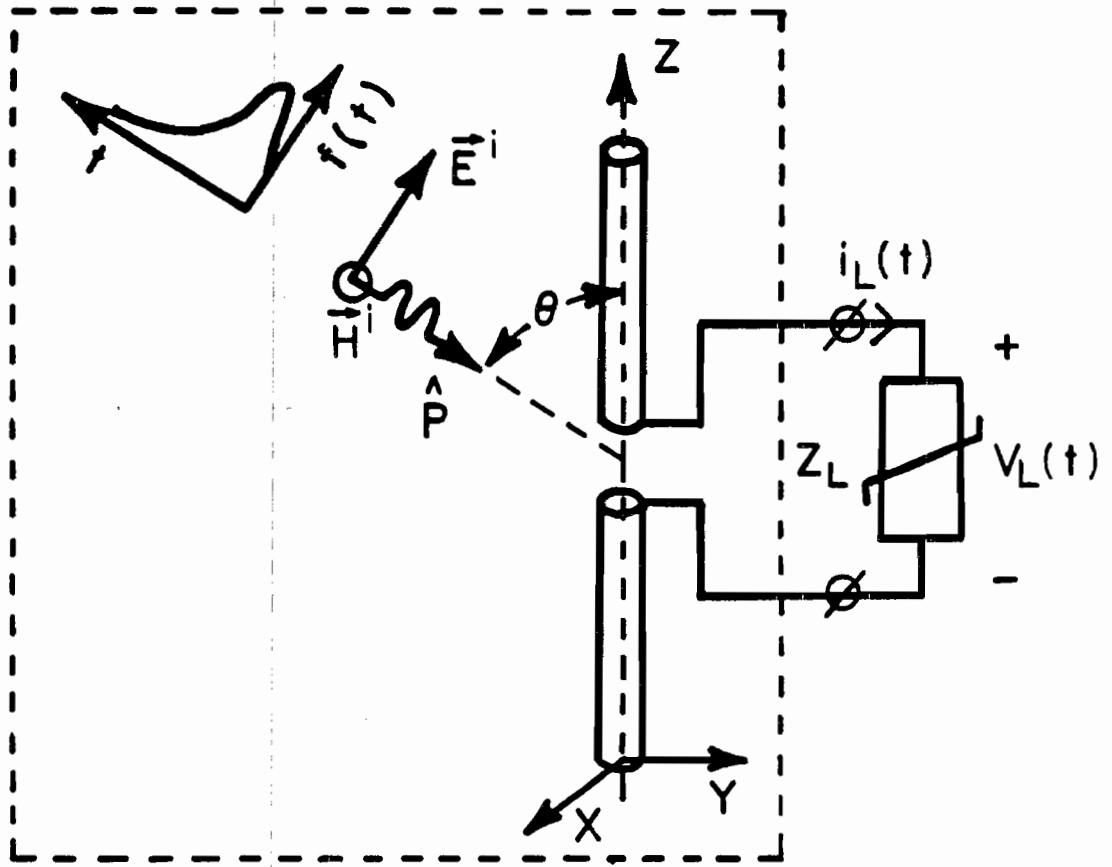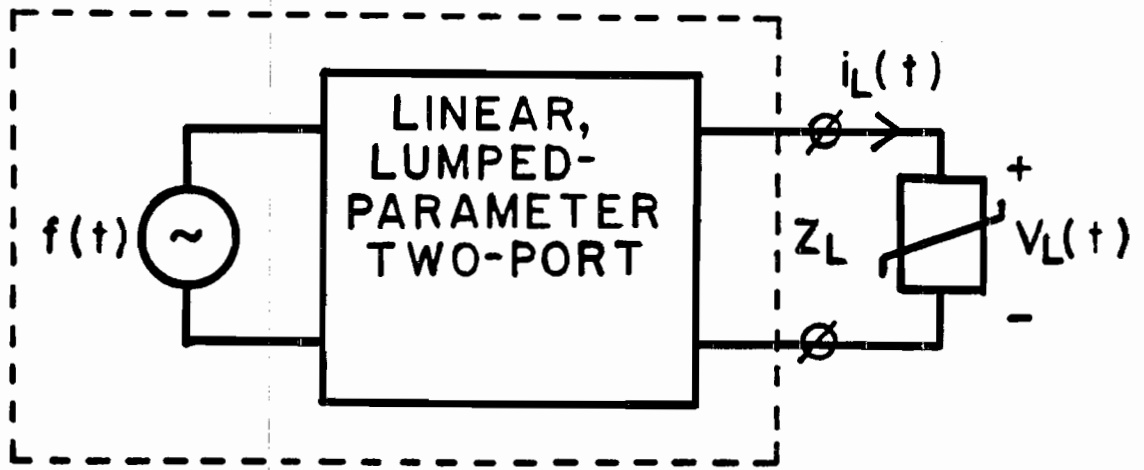
Figure 1.1 Illustration of the synthesis problem. (a) Energy-collecting structure excited by a plane wave with a time history f(t) and headed at a prot by a load Z_ℓ; (b) its equivalent circuit representation.

problem?" *Baum* [1976a] in his work introducing the singularity expansion based equivalent circuit synthesis states that these circuits, under certain circumstances, could be helpful in providing some or all of the following:

1. physical insight

2. computational convenience

3. capability of using established circuit transformation techniques

4. capability to combine the electromagnetic analysis with physical circuit elements, transmission lines, etc., which are constructed as part of an antenna or scatterer

5. capability of using existing computerized circuit analysis programs.

In a more recent paper *Baum and Singaraju* [1980] add to this list two new areas of application:

6. physical construction of equivalent circuits for use in special types of electromagnetic pulse (EMP) simulators

7. radar target detection and camouflage techniques.

The desired features of the equivalent networks depend, of course, on the area of application. In general, they should be simple, easy to construct, and accurate in the frequency band of interest. It is desirable that the networks be physically realizable, *i.e.*, they should not contain any negative or complex-valued elements. It is self-evident that this requirement is essential if the equivalent circuit is to be physically constructed. This feature is not essential, but it is potentially helpful in other applications, because negative-valued elements are difficult to interpret physically and they can cause numerical problems in some circuit analysis codes. A potential application of the hardware-realized circuits is in the high-voltage environment of transient pulse simulation. This environment precludes the use of any controlled

17

sources, gyrators, and ideal or perfect transformers, because these elements can only be realized by active devices which usually do not tolerate high voltages and currents. It is also desirable that the angle of incidence and other parameters of the incident field enter the circuit in the simplest possible way. For example, we would prefer that a change in the angle of incidence θ in Figure 1.1(a) would change perhaps some element or source values but not the topology of the circuit. Furthermore, neither the topology nor the element values should depend on the time history $f(t)$. It would be also convenient for the autonomic source to be connected to only one pair of terminals in implementation.

Perhaps the most convenient and powerful mathematical description of an electromagnetic energy collecting structure for purposes of equivalent circuit synthesis is the Singularity Expansion Method (SEM) introduced by *Baum* [1971] (see also [*Baum*, 1976b] and [*Baum*, 1976c]. SEM is a generalization of well-known techniques of linear circuit theory in which the singularities of a transfer function are used to determine the transient response by the Heaviside expansion theorem. In electromagnetic theory, the singularities are found by first applying a two-sided Laplace transform to Maxwell's equations and then constructing an integral equation for the scattered field. Complex singularities $\{s_n\}$ appear as poles of the inverse of this equation and these are the frequencies for which non-trivial solutions of the corresponding homogeneous integral equation exist. These non-trivial solutions are termed the natural modes of the structure. From these modes and the integral operator the so-called normalization coefficients can be found. Poles, natural modes and normalization coefficients constitute the fundamental SEM parameters. If the poles and the associated modal

18

distributions are known, one can compute the coupling coefficients which weight a given singularity's contribution to the response for a given incident field. From these quantities and the normalization coefficients the residues associated with the poles can be evaluated. Since a distributed-parameter system has an infinite order of complexity, it can only be described by an infinite series of terms associated with poles and other singularities (see Section 2.4). In practice, however, for band-limited excitations, the response of such system is dominated by a limited number of resonances, so that the series can be truncated without introducing appreciable error.

Following this introduction, the main objective of this work can be stated as follows: To develop simple and reasonably accurate procedures for the synthesis of finite, lumped-parameter, physically realizable circuits for electromagnetic energy collecting structures from their SEM description. These procedures should be practically tested on some representive canonical structures, their responses for broadband excitations should be computed and compared with available data or with responses obtained by other means.

1.2 Brief Literature Survey

One of the early attempts to extend circuit theory concepts to distributed-parameter system was made by *Schelkunoff* [1944], who applied the *Foster* [1924] expansion theorem to immittances of lossless structures with an infinite number of degrees of freedom. He observed that this infinite series representation was slowly convergent or did not converge at all. He then used a Mittag-Leffler theorem from the theory of functions of a complex variable to convert it into a more rapidly convergent form (he in effect introduced what we call in Chapter

19

2 the modified pole modules). Subsequently, Schelkunoff modified this

series to allow for slight dissipation. He did not present any equivalent

circuits for this case.

In a later work, *Schelkunoff and Friis* [1952] discussed the

representation of driving-point immittances of antennas in terms of

their poles and zeros. They conjecture there that the impedance of

any physical circuit may be expressed as a ratio of two products of

linear factors exhibiting the natural oscillation constants of the

circuit with its terminals at first floating and then short-circuited.

For a distributed-parameter system the number of factors is infinite

and the convergence of this product form is governed by the Weierstrass

theorem from the theory of functions of a complex variable. Then they

state that the static capacitance (inductnace) of a dipole (loop) antenna,

together with its natural oscillation constants, determines the antenna

impedance at all frequencies. They do not present any equivalent

circuits for antennas, except for parallel and series resonant circuits

valid in the vicinity of the antenna resonance.

An explicit expression for the driving-point admittance can be

written only for a few structures, such as the spherical or spheroidal

antenna with circumferential slot. This expression is in a form of an

infinite series of terms associated with the eigenfunctions of the

problem. For the spherical antenna [*Stratton and Chu*, 1941] the nth

term involves a ratio of a spherical Hankel function of order n and its

derivative. As shown by *Chu* [1948], this ratio can be expanded in a

finite continued fraction with positive real coefficients, which can

be physically realized by an LC ladder network terminated into a single

resistance. A complete equivalent circuit consists of a parallel connection

of an infinite number of such "eigennetworks". Unfortunately, this representation is not practical because it converges very slowly. *Schelkunoff* [1952] and, more recently, *Franceschetti* [1976] (see also [*Bucci and Franceschetti,* 1974]) observed that each of the eigennetworks contributes to the static capacitance C of the antenna. They were able to sum explicitly the infinite series for C. The subtraction of this series term-by-term from the series for the admittance resulted in a more rapidly convergent series. Franceschetti constructed an equivalent circuit representation for this modified series by introducing gyrators (with frequency-dependent gyration resistance) to each eigennetwork. Neither Schelkunoff nor Franceschetti discussed the source problem.

An important development for the equivalent circuit synthesis for energy collecting structures was the introduction in 1971 of the Singularity Expansion Method [*Baum,* 1971]. *Barnes* [1973] constructed perhaps the first SEM driving-point equivalent circuit for a thin dipole antenna. He used the approximate poles and residues derived analytically by *Lee and Leung* [1972]. In his circuit each pole pair was represented by a series RLC module. *Hess* [1975] has used SEM analysis to develop a transfer function model for determining EMP coupling to a dipole antenna. He used the SEM data obtained numerically by *Tesche* [1973]. He did not, however, synthesize any equivalent circuits so no loading effects could be analyzed by this method.

Perhaps a more systematic approach to SEM equivalent circuit synthesis was propsoed by *Baum* [1976a] (some of this material appeared recently in [*Baum,* 1978]). In this work he introduced the formalism and terminology which stimulated and influenced most of the subsequent

research in this area, including the present effort. In his paper, however, Baum developed only formal equivalent circuits without addressing the issues of their practical realizability. In a latter work *Baum and Singaraju* [1980] utilized a sinusoidal natural-mode approximation and an analysis similar to that presented by *Marin* [1974], to derive driving-point admittance equivalent circuits for a thin-wire dipole antenna. They did not, however, present any active equivalent circuits for an illuminated dipole.

Schaubert [1979] constructed lumped-parameter equivalent circuits for a center-driven dipole and a Yagi antenna using experimentally derived SEM description. He used Prony's algorithm [*Van Blaricum and Mittra,* 1975] (a technique for parametrization in terms of complex exponentials) to extract SEM data from the antenna terminal voltage waveform due to a step-like excitation and used these data to construct the driving-point impedance function in the form of a ratio of two polynomials in s. He then used Brune's [*Brune,* 1931] synthesis method to derive equivalent circuits. As usual in Brune's method, perfect transformers were employed. Schaubert did not consider the source problem but limited his concern to the determination of the driving-point impedance part of the equivalent circuit.

The first extensive study of the physical realizability of passive equivalent circuits for thin-wire dipole and loop antennas was performed by *Streable and Pearson* [1981]. They utilized the Bott-Duffin [*Bott and Duffin,* 1949] synthesis method to realize input admittances using different grouping of pole terms and used the resistive padding technique [*Guillemin,* 1977] for an approximate synthesis of pole-pair circuits. In a companion paper, *Pearson and Wilton* [1981] proved

that the eigenadmittances (reciprocal eigenvalues) of a structure are positive real (PR) [*Brune*, 1931] functions of frequency s and speculated on the PRness of the admittances associated with individual current eigenmode contributions to total current. They also briefly discussed the source synthesis issue, but they did not present any actual active circuits.

Another approach to equivalent circuit synthesis has been to compute the driving-point or transfer function of the structure on the imaginary axis in the s-plane and then to use a curve fitting technique to develop the corresponding rational function in s, which can be subsequently submitted to some standard synthesis procedure [*Weber and Toulios*, 1974; *Sharpe and Roussi*, 1979]. This technique was used by *Sharpe and Roussi* [1979] to obtain a ladder network representation for the input admittance of a biconical antenna [*Tai*, 1981]. This method, however, does not offer the advantages of the SEM appraoch, as discussed above.

Recently *Tesche and Giri* [1981] presented some active SEM equivalent circuits for a dipole antenna. Their networks, however, are intended for computational purposes only and contain negative-valued elements.

The foregoing discussion can be summarized with the observation that, to date and to the best of the author's knowledge, no active, physically realizable equivalent circuits valid over significant frequency band-widths have been synthesized and analyzed for electro-magnetic energy collecting structures.

1.3 Scope of the Present Work

The outline of this work is as follows. In Chapter 2 the SEM formalism is defined and the SEM expansion for the current density on a scattering object is developed. This representation is derived formally via the eigenfunction expansion. It is based on some evidences for which a rigorous proof has not been furnished, to date. Some questions concerning the formal development fo the SEM exapnsion are elaborated upon in Appendix A. The convergence properties of the two SEM coupling coefficient forms (termed class 1 and class 2), as a function of the time origin location, are investigated. Then the most convenient choice of the time origin location for the purposes of SEM equivalent circuit synthesis is determined. Also, the dominant-pole approximation is discussed and numerical evidence is presented showing that it can be successfully used, at least in the case of highly-resonant structures.

In Chapter 3 is presented a formal development of SEM equivalent circuits for energy-collecting structures. Both the short-circuit and the open-circuit boundary value problems are discussed. With some exceptions, the material of this chapter is a recasting of the results obtained previously by *Baum* [1976a], in a notation consistent with the rest of this work.

In Chapter 4 the realizability conditions for the pole-pair immittances and voltage transfer functions are discussed and explicit realizations for them are given. The real-part padding technique for the synthesis of approximate driving-point circuits is also addressed, and an explicit expression for the amount of padding necessary, in terms of the SEM parameters, is derived. Most of the material of

24

this chapter is original to the present work.

Chapters 5 and 6 present an application of the developed synthesis procedures to the thin-wire loop and dipole antennas, respectively. Practical, physically realizable active equivalent networks are presented and analyzed in the time domain with the help of a circuit analysis program. The results are compared with known repsonses or with responses obtained by the classical frequency domain technique. In addition, in Chapter 6 a sinusoidal current mode approximation is used to develop a particularly simple, and yet reasonably accurate, equivalent circuit for a symmetrical dipole, or a cylindrical post over a ground plane. An application of the equivalent circuits developed in Chapters 5 and 6 to the analysis of antennas with nonlinear loads is described in Appendix B where representative equivalent circuit responses for a thin-wire loop and a dipole antenna loaded with a semiconductor diode are included. The calculation of these responses with other methods, though tractable, is quite tedious.

Chapter 7 is devoted to the equivalent circuit synthesis for a spherical antenna. The dominant pole-pair circuits are synthesized by the real-part padding technique and the quality of the dominant pole approximation is examined. In Appendix C the static capacitance of the spherical antenna is computed both analytically and numerically.

The conclusions from this work are summarized in Chapter 8.

THE SEM REPRESENTATION FOR EM SCATTERING

2.1 Introduction

In Sections 2.2-2.4 of this chapter the SEM formalism is defined
and the SEM expansion for the current density on a scattering object
is derived formally via the eigenfunction expansion. In Section 2.5
the convergence properties of the two SEM coupling coefficient forms
(termed class 1 and class 2) are investigated as a function of the
time origin location. Then, in Section 2.6, the optimal choice of the
time origin location for the purposes of SEM equivalent circuit synthesis
is determined. Finally, in Section 2.7 the dominant pole approximation
is discussed and numerical evidence is presented that it can be success-
fully used, at least in the case of highly-resonant structures.

2.2 Integral Equation Formulation

The integral equation for the current density $\tilde{\vec{J}}(\vec{r},s)$ on a surface
S of a perfectly-conducting object immersed in a lossless, homogeneous
medium may be formulated as

$$\langle \tilde{\overleftrightarrow{\Gamma}}(\vec{r},\vec{r}',s); \tilde{\vec{J}}(\vec{r}',s) \rangle = \tilde{\vec{I}}^i(\vec{r},s) \ , \ \vec{r} \in S \tag{2.1}$$

where $\tilde{\vec{I}}^i(r,s)$ is the known incident or source field and $\overleftrightarrow{\Gamma}(\vec{r},\vec{r}',s)$ is the
dyadic kernel of the integral equation. The symmetric product
notation

$$\langle \vec{F}(\vec{r}); \ \vec{G}(\vec{r}) \rangle \equiv \iint_S \vec{F}(\vec{r}) \cdot \vec{G}(\vec{r}) dS$$

is used to denote integration over the surface S of the object.[1]

[1] If two or more ranges of integration are used then subscripts can
be placed on $\langle,\rangle$.

As in [*Marin and Latham*, 1972] it is assumed that S is a smooth surface of finite extent enclosing a simply-connected region. The solution of (2.1) can then be sought in $L^2(S)$, the Hilbert space of all square-integrable functions with support S. The frequency variable is $s = \sigma + j\omega$ and is that associated with the Laplace transform pair[1]

$$L\{f(t)\} \equiv \tilde{f}(s) = \int_0^\infty f(t)\bar{e}^{st}dt \qquad (2.2a)$$

and

$$f(t) \equiv L^{-1}\{\tilde{f}(s)\} = \frac{1}{2\pi j} \int_{C_B} \tilde{f}(s)e^{st}ds \qquad (2.2b)$$

where tildes (~) over quantities distinguish Laplace domain members of transform pairs and C_B is the Bromwich contour.

This work deals specifically witn the electric field integral equation (EFIE) characterization for a conducting object. In this case the kernel of eq. (2.1) becomes the symmetric impedance kernel[2]

$$\overset{\leftrightarrow}{\tilde{Z}}(\vec{r},\vec{r}',s) = Z_0\gamma\left[\overset{\leftrightarrow}{1}+\frac{\nabla\nabla'}{\gamma^2}\right]\tilde{G}_0(\vec{r},\vec{r}',s) \qquad (2.3)$$

where

$$G_0(\vec{r},\vec{r}'s,) = \frac{\bar{e}^{\gamma|\vec{r}-\vec{r}'|}}{4\pi|\vec{r}-\vec{r}'|} \qquad (2.4)$$

---

[1] The unilateral Laplace transform is used since only causal functions of time are dealth with. This is accomplished by a judicious choice of the time origin of the problem (see Section 2.5).

[2] The primed and unprimed differential operators act, respectively, on the primed and unprimed variables. Strictly speaking (2.1) is only meaningful when interpreted in terms of some sense of principal value integration. We use it and the kernel $\overset{\leftrightarrow}{Z}$ in a symbolic sense for efficiency of notation. Bringing the gradient operator in (2.3) outside of the integration leaves an integrable kernel, and it is upon this integro-differential operator that we may build a meaningful mathematical theory.

is the scalar Green function, $\overleftrightarrow{1}$ denotes the identity dyadic, $\gamma = s/c$ is the complex propagation constant, and Z_o is the intrinsic impedance of the medium. The speed of light is denoted by c. The EFIE incident field function is the tangential component of the incident electric field on S

$$\tilde{\vec{I}}^i(\vec{r},s) = \tilde{\vec{E}}^i(\vec{r},s) \cdot (\overleftrightarrow{1} - \hat{n}\hat{n}) \tag{2.5}$$

where $\hat{n} \equiv \hat{n}(\vec{r})$ is a unit vector normal at $\vec{r}$ to the object surface S. In most cases of practical interest the incident field is "factorable", *i.e.*, it can be written in the form

$$\tilde{\vec{E}}^i(\vec{r},s) = \vec{E}_o(\vec{r})\tilde{p}(\vec{r},s)\tilde{f}(s) \tag{2.6}$$

where $\vec{E}_o(\vec{r})$ indicates a spatial distribution factor, $\tilde{p}(\vec{r},s)$ is a propagation factor which links space and time dependencies, and $\tilde{f}(s)$ is the Laplace transform of the time history of the wave. It is assumed here that $\tilde{f}(s)$ is algebraic, which is also satisfied in most practical cases. For example, a plane wave carrying a time history f(t) may be written as

$$\tilde{\vec{E}}^i(\vec{r},s) = \vec{E}_o e^{-\gamma\hat{p} \cdot (\vec{r}-\vec{r}_o)}\tilde{f}(s) \tag{2.7}$$

where $\vec{E}_o$ is a constant polarization vector, $\hat{p}$ is a unit vector in the direction of propagation, and $\vec{r}_o$ is a vector pointing to a chosen phase reference point. The time domain counterpart of (2.7) is

$$\vec{E}^i(\vec{r},t) = \vec{E}_o \, \delta\left[t - \hat{p} \cdot (\vec{r}-\vec{r}_o)/c\right] * f(t)$$

$$= \vec{E}_o \, f\left[t - \hat{p} \cdot (\vec{r}-\vec{r}_o)/c\right]$$

$$= \vec{E}_o \, f(t - t_o - \hat{p} \cdot \vec{r}/c) \tag{2.8}$$

28

where $\delta(t)$ is the Dirac delta function, * denotes convolution in time, and

$$t_o = -\hat{p} \cdot \vec{r}_o / c \quad .$$
(2.9)

It is noted that, since the causality assumption is imposed on $f(t)$, *i.e.*, $f(t) = 0$ for $t < 0$, the excitation first reaches the point $\vec{r} = \vec{r}_0$ at the time $t = 0$. Hence, $\vec{r}_o$ defines the time origin of the problem: the time is counted beginning from the moment when the wave front passes the point $\vec{r} = \vec{r}_o$. The wave front reaches the coordinate origin $\vec{r} = \vec{0}$ at $t = t_o$.

2.3 Formal Solution of the EFIE

The kernel (2.3) is complex-symmetric [*Cochran*, 1972] and so one may define a set of eigenvalue/eigenfunction pairs through

$$\langle \tilde{\vec{J}}_n(\vec{r}',s); \tilde{\overleftrightarrow{Z}}(\vec{r}',\vec{r},s) \rangle = \langle \tilde{\overleftrightarrow{Z}}(\vec{r},\vec{r}',s); \tilde{\vec{J}}_n(\vec{r}',s) \rangle = \tilde{\lambda}_n(s) \tilde{\vec{J}}_n(\vec{r},s) \quad .$$
(2.10)

It follows, formally, that the kernel and its resolvent can be expanded as

$$\tilde{\overleftrightarrow{Z}}(\vec{r},\vec{r}',s) = \sum_n \tilde{\lambda}_n(s) \frac{\tilde{\vec{J}}_n(\vec{r},s) \, \tilde{\vec{J}}_n(\vec{r}',s)}{\langle \tilde{\vec{J}}_n(\vec{r},s); \tilde{\vec{J}}_n(\vec{r},s) \rangle}$$
(2.11)

and

$$\tilde{\overleftrightarrow{Z}}^{-1}(\vec{r},\vec{r}',s) = \sum_n \frac{1}{\tilde{\lambda}_n(s)} \frac{\tilde{\vec{J}}_n(\vec{r},s) \, \tilde{\vec{J}}_n(\vec{r}',s)}{\langle \tilde{\vec{J}}_n(\vec{r},s); \tilde{\vec{J}}_n(\vec{r},s) \rangle} \quad .$$
(2.12)

The solution to the integral equation (2.1) is thus written

$$\tilde{\vec{J}}(r,s) = \langle \tilde{\overleftrightarrow{Z}}^{-1}(\vec{r},\vec{r}',s) ; \tilde{\vec{I}}^{1}(\vec{r}',s) \rangle$$

$$= \sum_n \frac{1}{\tilde{\lambda}_n(s)} \frac{\langle \tilde{\vec{J}}_n(\vec{r}',s) ; \tilde{\vec{E}}^{1}(\vec{r}',s) \rangle}{\langle \tilde{\vec{J}}_n(\vec{r},s) ; \tilde{\vec{J}}_n(\vec{r},s) \rangle} \tilde{\vec{J}}_n(\vec{r},s) \ . \qquad (2.13)$$

The EEM representation (2.13) is formal in the sense that in
deriving it some tacit assumptions have been made which, in general,
may not be satisfied. Among other things, the major pitfall in the
expansions above is that since the kernel (2.3) is not Hermitian-symmetric,
there is nothing to guarantee the existence of a complete set of eigen-
vectors $\tilde{\vec{J}}_n(\vec{r},s)$, as defined in (2.10). One cannot even be sure that
the normalization factors in the denominators above do not vanish
[*Ramm*, 1973]. Perhaps the most common situation in practice in which
the eigenfunction representation fails is when the eigenvalues $\tilde{\lambda}_n(s)$
have branch points. At a branch point in the s-plane two or more
eigenvalues coalesce [*Cochran*, 1972], so that the inclusion of root
vectors[1] in the expansion may be necessary [*Ramm*, 1980]. In some
cases even for degenerate eigenvalues a set of independent eigenvectors

---

[1] Let A be a linear operator on the space considered and let $\phi_{i,1} \neq 0$
be an eigenvector associated with an eigenvalue λ_i, i.e., $(A-I\lambda_i)$
$\phi_{i,1} = 0$, where I denotes the identity operator. Consider the
subspace of all vectors that are annihilated by some power of
$(A-I\lambda_i)$. If for some power k there exists a vector $\phi_{i,k}$ in the
subspace such that $(A-I\lambda_i)^{k-1}\phi_{i,k} \neq 0$ and $(A-I\lambda_i)^k\phi_{i,k} = 0$, and such
that there is no vector in the subspace that is not annihilated at
least by $(A-I\lambda_i)^k$, then $\phi_{i,k}$ is a root vector (generalized eigenvector
[*Pease*, 1965]) of rank k, where k is the length of the longest chain
associated with eigenvalue λ_i. The chain $\{\phi_{i,1},\phi_{i,2},\ldots,\phi_{i,k}\}$, with
the elements defined by $\phi_{i,k-1} = (A-I\lambda_i)\phi_{i,k},\ldots,\phi_{i,1} = (A-I\lambda_i)^{k-1}\phi_{i,k}$,
is called a Jordan chain of length k. The union of all root vectors
of a linear operator A corresponding to all eigenvalues of A is called
the root system of A [*Ramm*, 1980].

can be found so that the root system coincides with the eigensystem.[1]
This is true for normal operators.[2] For example, it was shown by
Ramm [1973] that the scalar analog of the operator in (2.1) is normal
if S is a sphere. If the operator is not normal, it is not always
diagonalizable and considerable complexity arises in the computational
scheme *[Dolph et al., 1980]*.

There is an important class of bodies for which it can be shown
that branch points do not occur. These are structures such as the
sphere or circular loop, in which the eigenvectors are completely
determined by the geometrical symmetry of the structure and hence are
frequency independent. This follows from the Rayleigh quotient
representation of the eigenvalue,[3]

$$\dot{\tilde{\lambda}}_n(s) = \frac{<\dot{\tilde{\vec{J}}}_n(\vec{r}); \dot{\tilde{\overleftrightarrow{Z}}}(\vec{r}, \vec{r}', s); \tilde{\vec{J}}_n(\vec{r}')>}{<\tilde{\vec{J}}_n(\vec{r}); \tilde{\vec{J}}_n(\vec{r})>} \quad . \tag{2.14}$$

The kernel in (2.14) can be expanded in a Laurent series converging
for all $|s| > 0$, and integrated term-by-term to obtain a series with
the same region of convergence and analyticity. This argument is not
valid, however, if the body is not completely symmetric because the
eigenmodes $\tilde{\vec{J}}_n$ are then generally functions of s. To date, analytic

---

[1] In the language of finite-dimensional spaces this means that the
geometric multiplicity of an eigenvalue is equal to its algebraic
multiplicity *[Stakgold, 1967]*. We say that an eigenvalue λ_i has
algebraic multiplicity k if the term $(\lambda - \lambda_i)$ is repeated k times
in the characteristic equation of the operator. Geometric multiplicity
of λ_i denotes the number of independent eigenvalues corresponding to it.

[2] An operator A is called normal if $A^a A = AA^a$, where A^a is the adjoint
operator.

[3] The triple product notation is introduced for a triad of elements,
the middle element of which is dyadic: $< ; ; > = < ;< ; >>$.

properties of the eigenvalues of only rotationally-symmetric objects, such as the sphere and the circular loop, have been thoroughly examined.

2.4 Singularity Expansion of $\tilde{\vec{J}}(\vec{r},s)$

The singularity expansion for the surface current density on a scattering object can be obtained from the eigenfunction expansion by performing the residue series expansion of (2.12) or (2.13) in terms of the complex natural resonances s_n (the poles) of the object, defined as follows:

$$\left\{ s_{ni} : \tilde{\lambda}_n(s_{ni}) = 0 \right\} . \tag{2.15}$$

It is noted that for $s = s_{ni}$, in view of (2.10) and (2.15), the following is true:

$$\langle \overleftrightarrow{\tilde{Z}}(\vec{r},\vec{r}',s_{ni}) ; \tilde{\vec{J}}_n(\vec{r}',s_{ni}) \rangle = 0 . \tag{2.16}$$

Hence, $\tilde{\vec{J}}_n(\vec{r},s_{ni}) \equiv \vec{J}_{ni}(\vec{r})$ are the natural modes of the object associated with the poles s_{ni}. In practice the homogeneous integral equation (2.16) is replaced by a matrix equation by some approximate technique such as the method of moments (MoM) [Harrington, 1968], and the poles are sought as zeros of the determinant of the coefficient matrix.

Before expanding the reciprocal eigenvalue factor which appears in (2.12) and (2.13) in terms of its singularities in the complex frequency plane, it is expedient to subtract from $\tilde{\lambda}_n^{-1}(s)$ the possible pole at the origin and define

$$\tilde{h}_n(s) = \frac{1}{\tilde{\lambda}_n(s)} - \frac{r_{no}}{s} \tag{2.17}$$

where r_{no} denotes the residue of the pole at $s = 0$. Assuming first

order poles[1] one can postulate using the Mittag-Leffler

expansion [*Jeffreys and Jeffreys*, 1956] the representation

[*Pearson and Wilton*, 1980; *Pearson*, 1981]

$$\tilde{h}_n(s) = \tilde{h}_n(o) + \sum_i r_{ni} \left[\frac{1}{s - s_{ni}} + \frac{1}{s_{ni}} \right] + \tilde{b}_n(s) \qquad (2.18)$$

where $b_n(s)$ denote the branch-integral contributions which may occur

and r_{ni} are the residues which can be computed by using eq. (2.14)

as well as the orthogonality property of the eigenfunctions to yield

$$r_{ni} = \left[\frac{d}{ds} \tilde{\lambda}_n(s_{ni}) \right]^{-1} = \beta_{ni} <\vec{J}_{ni}(\vec{r}); \vec{J}_{ni}(\vec{r})> \qquad (2.19)$$

with the normalization constants β_{ni} given by

$$\beta_{ni} = <\vec{J}_{ni}(\vec{r}); \frac{\partial}{\partial s} \overset{\leftrightarrow}{\tilde{Z}}(\vec{r},\vec{r}',s_{ni}); \vec{J}_{ni}(\vec{r}')>^{-1} \quad . \qquad (2.20)$$

Marin and Latham [1972] have shown that for perfectly conducting

bodies of finite extent imbedded in a lossless medium $\overset{\leftrightarrow}{\tilde{Z}}{}^{-1}(\vec{r},\vec{r}'s)$ is

analytic in s except for pole singularities. This does not mean, however,

that there cannot be branch-integral contributions to (2.18) which

cancel out in the summation (2.14), *i.e.*,

$$\sum_n \tilde{b}_n(s) \frac{<\vec{\tilde{J}}_n(\vec{r},s); \vec{\tilde{E}}_o(\vec{r})\tilde{p}(\vec{r},s)>}{<\vec{\tilde{J}}_n(\vec{r},s); \vec{\tilde{J}}_n(\vec{r},s)>} \vec{\tilde{J}}_n(\vec{r},s) = 0 \quad . \qquad (2.21)$$

It is demostrated in Appendix A that such phenomena can, indeed, occur.

Only for bodies such as the sphere or the circular loop antenna, in

which geometrical symmetry completely determines the eigenfunctions

---

[1] It was conjectured by *Baum* [1971] that perfectly conducting, finite-extent bodies in homogeneous, lossless media possess only simple (first order) poles. A proof of this conjecture has been put forth recently by *Sancer and Varvatsis* [1980]. The simple pole restriction exludes also essential singularities in a finite complex plane since they can be regarded as infinite order poles.

(and hence they are frequency independent), has it been possible to show (Section 2.3) that branch points cannot occur, and poles are the only singularities of the reciprocal eigenvalue in the finite complex frequency plane, so that $\tilde{b}_n(s) = 0$. On the other hand, any losses in the medium always contribute a branch cut in the complex frequency plane. Although in the lossless medium case the branch-integral contributions ultimately cancel leaving the singularity expansion of current unaffected, they are likely to have bearing on SEM formulations where eigenmode-by-eigenmode expansion enters in, including the SEM equivalent circuit synthesis discussed in this work. *Pearson and Wilton* [1981] have shown that the reciprocal eigenvalues in (2.13) are positive real (PR)[1] functions of s; they have also speculated that the same may hold for the terminal admittances associated with individual current eigenmode contributions to total current. The PRness is a necessary condition for the realizability of driving-point functions. If the branch-integral constituent in (2.18) is non-zero, its ommission may lead to non-realizable immittances. This difficulty can potentially be circumvented by grouping terminal eigenadmittances which share common branch points, so that the branch-integral constituents add to zero and PRness is preserved. Since in most practical cases the branch-integral terms cannot be explicitly identified, the $\tilde{b}_n(s)$ factors in (2.18) will be suppressed throughout the rest of this work.

The expansion (2.18) is valid provided $\tilde{h}_n(s)$ is bounded on a set of circular contours centered at $s = 0$ and passing between the poles [*Jeffreys and Jeffreys*, 1956]. If $\tilde{h}_n(s)$ is not only bounded, but actually decays on this set of contours, one can show that [*Pearson*, 1981]

[1] See Section 4.2 for the definition of a positive real function.

34

$$\tilde{h}_n(0) = - \sum_i \frac{r_{ni}}{s_{ni}} \tag{2.22}$$

and

$$\tilde{h}_n(s) = \sum_i \frac{r_{ni}}{s - s_{ni}} \quad . \tag{2.23}$$

It is noted that even when $\tilde{b}_n(s) = 0$ in (2.18), the poles and the residues alone do not determine $\tilde{h}_n(s)$ and some additional information is necessary to determine the constant term $\tilde{h}_n(0)$. Often it can be argued from the high freuqency and/or low frequency considerations that $\tilde{h}_n(0) = 0$. In that case it follows

$$\frac{1}{\tilde{\lambda}_n(s)} = \frac{r_{no}}{s} + \sum_i r_{ni}\left[\frac{1}{s - s_{ni}} + \frac{1}{s_{ni}}\right] = \frac{r_{no}}{s} + \sum_i \left[\frac{s\, r_{ni}}{s_{ni}(s - s_{ni})}\right] \quad . \tag{2.24}$$

Similarly, using (2.17) and (2.23) yields

$$\frac{1}{\tilde{\lambda}_n(s)} = \frac{r_{no}}{s} + \sum_i \left[\frac{r_{ni}}{s - s_{ni}}\right] \quad . \tag{2.25}$$

Following the terminology introduced by *Baum* [1976a], the terms in brackets in (2.24) and (2.25) are referred to as, respectively, the modified and unmodifeid pole modules. Both forms have been used in the SEM equivalent circuit synthesis to date. Throughout most of this work the modified pole modules are used since they impose less stringent conditions on the behavior of $\tilde{\lambda}_n(s)$. It is of interest to point out, that the unmodified pole modules expansion (2.25) was proved by *Umashankar and Wilton* [1974] to be valid for the circular loop in a lossless medium. However, in the actual computations the truncated series (2.25) converged very slowly at low frequencies and they were forced to use, in effect, the modified from (2.24).

35

The substitution of the expansion (2.24) into (2.13) yields

$$\tilde{\vec{J}}(\vec{r},s) = \frac{1}{s}\,\beta_{oo}\tilde{\eta}_{oo}(s)J_{oo}(\vec{r})\tilde{f}(s)$$

$$+ \sum_n \sum_i \frac{s}{s_{ni}(s-s_{ni})}\,\beta_{ni}\tilde{\eta}_{ni}(s)\vec{J}_{ni}(\vec{r})\tilde{f}(s) \qquad (2.26)$$

with the coupling coefficients $\tilde{\eta}_{ni}(s)$ defined as

$$\tilde{\eta}_{ni}^{(1)} = <\vec{J}_{ni}(\vec{r});\vec{E}_o(\vec{r})\tilde{p}(\vec{r},s_{ni})> \qquad (2.27)$$

-- the class 1 coupling coefficient, or

$$\tilde{\eta}_{ni}^{(2)}(s) = <\tilde{J}_{ni}(\vec{r});\vec{E}_o(\vec{r})\tilde{p}(\vec{r},s)> \qquad (2.28)$$

-- the class 2 coupling coefficient[1] [*Baum*, 1972; *Baum*, 1976b]. It is noted that the class 1 form is simply a specialization of the class 2 coupling coefficient: $\tilde{\eta}_{ni}^{(1)} = \tilde{\eta}_{ni}^{(2)}(s_{ni})$. Also, both forms are identical for nonpropagating excitation fields, when $\tilde{p}(\vec{r},s)=1$. For the plane wave incident field the two classes of coupling coefficients take the form

$$\tilde{\eta}_{ni}^{(1)} = e^{-s_{ni}t_o}\,<\vec{J}_{ni}(r);E_o\,e^{-\gamma_{ni}\hat{p}\cdot\vec{r}}> \qquad (2.29)$$

and

$$\tilde{\eta}_{ni}^{(2)}(s) = e^{-st_o}\,<\vec{J}_{ni}(\vec{r});E_o e^{-\gamma\hat{p}\cdot\vec{r}}>\ . \qquad (2.30)$$

---

[1] The coupling coefficients defined here differ slightly in form from the ones originally introduced by *Baum* [1976b]. In Baum's work the time origin coincides with the space origin but the SEM series can be "turned on" in negative time, if necessary, by choosing the value of the turn-on time parameter. In the present formulation, which follows naturally from the assumed form of the incident field (27), the time origin $\vec{r}_o$ is chosen independently from the space origin and the SEM series is always turned on at $t=0$.

In the next sections the convergence properties of both coupling coefficient forms are discussed and what is believed to be the best choice of the coupling coefficient for the purposes of SEM circuit synthesis is determined. Meanwhile the generic notation $\tilde{\eta}_{ni}(s)$ is used to embrace both forms.

Several comments are in order concerning eq. (2.26). First, the term associated with the pole at the origin is shown explicitly and it is assumed that this pole belongs to the zeroth eigenmode. It can be argued from the form of the integral equation that this mode must be divergenceless (solenoidal). If the structure is not capable of supporting a solenoidal current mode, it can not have a pole at the origin. Second, it is noted that a concellation of a pole can occur if it coincides with a zero of the corresponding coupling coefficient. A limiting procedure should be used in such case to determine the contribution of such a pole-zero pair. Finally, it should be noted that perhaps the most improtant feature of the representation given in (2.26) is that the set of complex natural frequencies $\{s_n\}$, the set of complex natural modes $\{\vec{J}_{ni}(\vec{r})\}$, and the set of complex normalization coefficients $\{\beta_{ni}\}$ are dependent on the object parameters only but are independent on the excitation. The effect of the exciting field is contained entirely within the set of coupling coefficients $\{\tilde{\eta}_{ni}(s)\}$.

2.5 Convergence Properties of Class 1 and Class 2 Coupling Coefficients

In this section are investigated the convergence properties as $\mathrm{Re}\{s_{ni}\} \to \infty$ of the singularity expansion (2.26) with both coupling coefficient forms, as a function of the choice of the location

of the time origin $\vec{r}_o$. The tools for this analysis were provided in a recent paper by *Baum and Pearson* [1981]. It is helpful to follow them in defining the following characteristic dimensions for use subsequently: the largest linear dimension of the scatterer

$$L_o = \sup_{\vec{r},\vec{r}'\varepsilon S} |\vec{r}-\vec{r}'| , \qquad (2.31)$$

the "clearance distance

$$L_1 = \sup_{\vec{r}\varepsilon S} \hat{p} \cdot \vec{r} , \qquad (2.32)$$

and the "contact distance"

$$L_2 = \inf_{\vec{r}\varepsilon S} \hat{p} \cdot \vec{r} . \qquad (2.33)$$

The latter two distances define, respectively, the signed distance from the coordinate origin to the point at which the wave front clears the object, and the signed distance from the coordinate origin to the point at which the wave front first contacts the object (see Figure 2.1).

To investigate the convergence properties of the SEM expansion (2.26) the asymptotic properties of the terms $\beta_{ni} \tilde{\eta}_{ni}(s)$ need to be examined. The behavior of β_{ni} for $\text{Re}\{s_{ni}\} \to -\infty$ was argued by *Baum and Pearson* [1981] to be

$$\beta_{ni} \sim e^{s_{ni}L_o/c} . \qquad (2.34)$$

The behavior of the class 1 coupling coefficient is governed by

$$\tilde{\eta}_{ni}^{(1)} \sim e^{-s_{ni}(L_1 - \hat{p} \cdot \vec{r}_o)/c} \qquad (2.35)$$

so that

$$\beta_{ni} \tilde{\eta}_{ni}^{(1)} \sim e^{s_{ni}(L_o - L_1 + \hat{p} \cdot \vec{r}_o)/c} . \qquad (2.36)$$
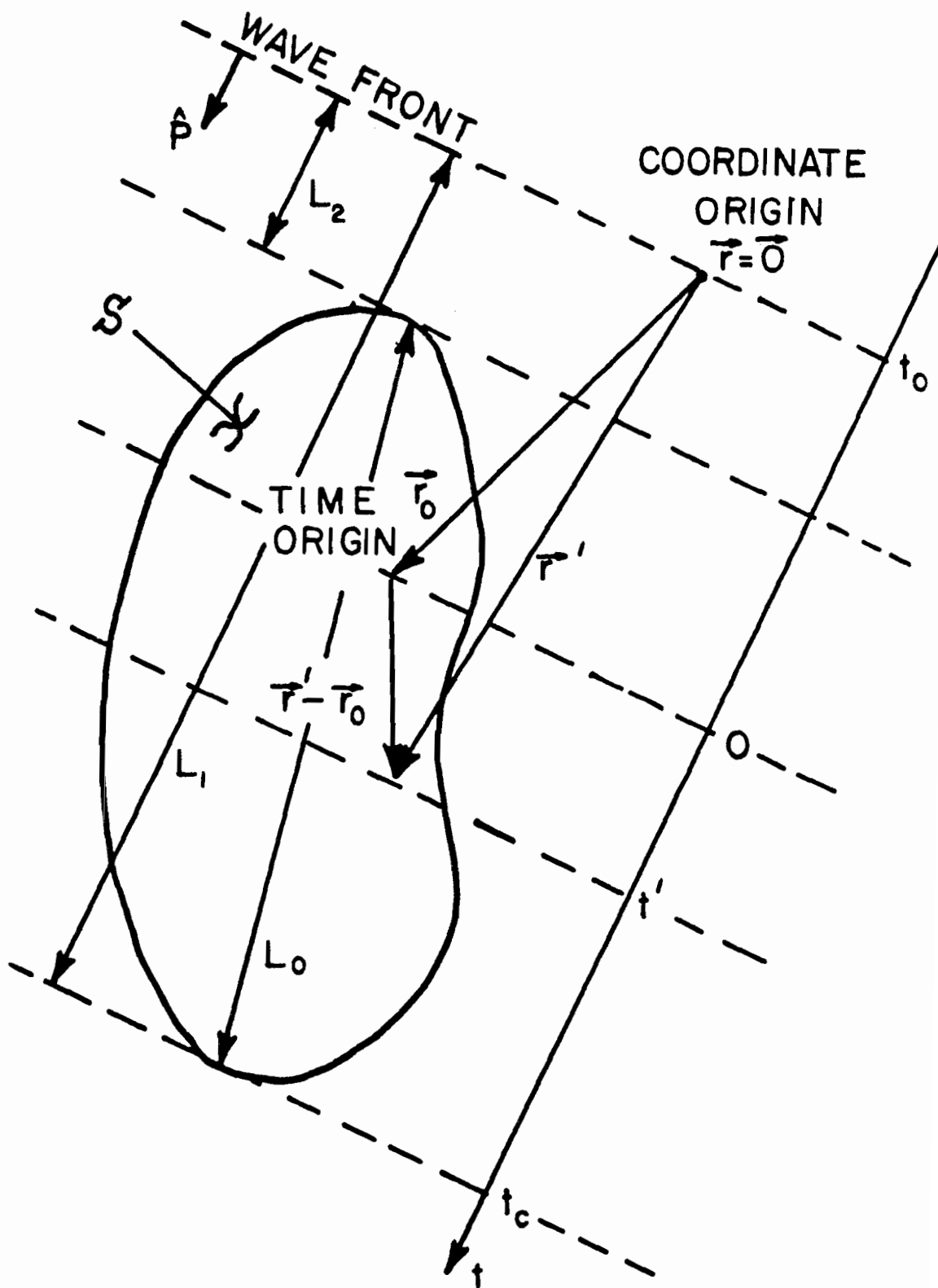
Figure 2.1 Portrayal of a scatterer in a plane-wave field. Indicated are the maximum extent of the object L_0, the clearance distance L_1 relative to the coordinate origin, and the contact distance L_2.

This term decays provided

$$\hat{p} \cdot \vec{r}_o > L_1 - L_o. \tag{2.37}$$

This condition is most stringent when the direction of propagation of the incident plane wave is along the largest dimension of the object. In this case (2.37) reduces to

$$\hat{p} \cdot \vec{r}_o > L_2 . \tag{2.38}$$

Hence, if the time origin is placed on the surface of the scattering object the convergence of the class 1 SEM expansion term is assured.

Similar analysis of the class 2 coupling coefficient form shows that

$$\beta_{ni} \ \tilde{\eta}_{ni}^{(2)}(s) \sim e^{s_{ni} L_o / c} . \tag{2.39}$$

Since L_o is always positive, one can conclude from the last expression that the class 2 form is always convergent, independet of the choice of the time origin.

2.6 Optimal Choice of the Time Origin

In this section are discussed the numerical properties of the two classes of coupling coefficients in the case of plane wave incident field. Also, the most convenient choice of the time origin $\vec{r}_o$ for SEM circuit synthesis if determined.

Although both class 1 and class 2 coupling coefficients give valid representation for the surface current density when used in (2.26), they exhibit quite different properties from the practical computation point of view. This is evident when one performs the Laplance inversion

40

of (2.26) to obtain the time domain response[1]

$$\vec{J}(\vec{r},t) = L^{-1}\{\tilde{\vec{J}}(\vec{r},s)\} \quad . \tag{2.40}$$

In this process terms like

$$\frac{1}{2\pi j} \int_{C_B} \frac{\tilde{\eta}_{ni}(s)}{s - s_{ni}} \, e^{st} ds \tag{2.41}$$

must be evaluated. Using the class 1 coupling coefficient (2.29) in (2.41) gives

$$\frac{1}{2\pi j} \int_{C_B} \frac{e^{-s_{ni}t_o} <\vec{J}_{ni}(\vec{r}); E_o e^{-\gamma_{ni}\hat{p} \cdot \vec{r}}>}{s - s_{ni}} \, e^{st} ds$$

$$= e^{-s_{ni}t_o} <\vec{J}_{ni}(\vec{r}); \vec{E}_o e^{-\gamma_{ni}\hat{p} \cdot \vec{r}}> u(t) e^{s_{ni}t} \tag{2.42}$$

whereas the class 2 coupling coefficient (2.30) gives

$$\frac{1}{2\pi j} \int_{C_B} \frac{<\vec{J}_{ni}(\vec{r}); \vec{E}_o e^{-\gamma \hat{p} \cdot (\vec{r}-\vec{r}_o)}>}{s - s_{ni}} \, d^{st} ds$$

$$= <\vec{J}_{ni}(\vec{r}); \vec{E}_o \frac{1}{2\pi j} \int_{C_B} \frac{e^{s[t - \hat{p} \cdot (\vec{r}-\vec{r}_o)/c]}}{s - s_{ni}} \, ds>$$

$$= e^{-s_{ni}t_o} <\vec{J}_{ni}(r); E_o e^{-\gamma_{ni}\hat{p} \cdot \vec{r}} u(t - t_o - \hat{p} \cdot \vec{r}/c)> e^{s_{ni}t} . \tag{2.43}$$

Thus, in the time domin the class 1 and class 2 coupling coefficients take, respectively, the form

---

[1] It should be kept in mind that any singularities of $\tilde{f}(s)$ must be taken into account in this process.

$$\eta_{ni}^{(1)}(t) = e^{-s_{ni}t_o} <\vec{J}_{ni}(\vec{r});E_o e^{-\gamma_{ni}\hat{p}\cdot\vec{r}}>u(t) \qquad (2.44)$$

and

$$\eta_{ni}^{(2)}(t) = e^{-s_{ni}t_o} <\vec{J}_{ni}(\vec{r});\vec{E}_o e^{-\gamma_{ni}\hat{p}\cdot\vec{r}} u(t - t_o - \hat{p}\cdot\vec{r}/c)> . \qquad (2.45)$$

It should be noted that the integrand in (2.45) gives a nonzero

contribution only when

$$\hat{p}\cdot\vec{r}/c < t - t_o \qquad (2.46)$$

or, equivalently, when

$$\hat{p}\cdot(\vec{r}-\vec{r}_o)/c < t . \qquad (2.47)$$

These expressions can be interpreted with the help of Figure 2.1 as

follows. The pole terms in (2.40) are "turned on" at $t = 0$, $i.e.$,

as soon as the wave front passes the time origin $\vec{r} = \vec{r}_o$. However, they

are computed differently depending on whether class 1 or class 2 coupling

coefficients are used. The class 1 coupling coefficients are constants

resulting from the integration over the entire object, as indicated in

(2.44). The class 2 coefficients (2.45), however, are obtained by

integrating only over that part of the object illuminated at the given

moment by the incident plane wave. Thus, they are time dependent

until $t=t_c$, when the edge of the incident wave has cleared the object.

After that time they take on constant values identical with those of

the class 1 coefficients. It is evident from the above discussion,

that the class 2 coupling coefficients form is much more expensive

computationally than the class 1 form. It is also unsuitable for the

purposes of SEM circuit synthesis because of its s-dependence in the

frequency domain. It has, however, some advantages, as discussed below.

It should be noted that the series (2.40) must sum to zero in the period of time before the leading edge of the incident wave arrives at the observation point (port location). However, the terms of the series contain the factors $\exp\left\{s_{ni}[t - \hat{p} \cdot (\vec{r} - \vec{r}_o)/c]\right\}$ which take on large values in early times, because $\text{Re}\{s_{ni}\} < 0$. Since these large numbers must sum to zero, the result is sensitive to errors in the pole values [*Marin*, 1972; *Pearson*, 1979]. The class 1 form requires also that a possibly full collection of poles belonging to a given eigenmode be included in the time domain counterpart of (2.26) [*Pearson*, 1979]. To illustrate this point, in Figure 2.2 are shown current responses at $\phi = 180°$ of a loop antenna of radius b illuminated by a step function plane wave polarized as indicated in the inset, computed in three ways. The first two curves were obtained by using class 1 coupling coefficients, but different collections of poles. In one case (solid line) all poles belonging to eigenmodes 0 - 10 for which $\text{Im}\{s_{ni}\} \lesssim 10c/b$ were included, while in the second case (dotted line) only one, "dominant" pole (the pole closest to the $j\omega$ axis) from each eigenmode collection was taken. The third curve (dashed line) was obtained by using class 2 coupling coefficients and dominant poles only. The time origin was chosen in all cases at $\phi = 0°$, the point of the first contact with the incident field. As can be seen in the figure, using class 1 coupling coefficient form and incomplete collection of poles results in a non-causal behavior of the response. The class 2 form is more tolerant and gives accurate responses for this case. Since in most practical situations the full eigenmode collections of poles are not at one's disposal, this last example would suggest that the class 1 coupling coefficient is of no value and that one must resort to the class 2 form. It should be noted,
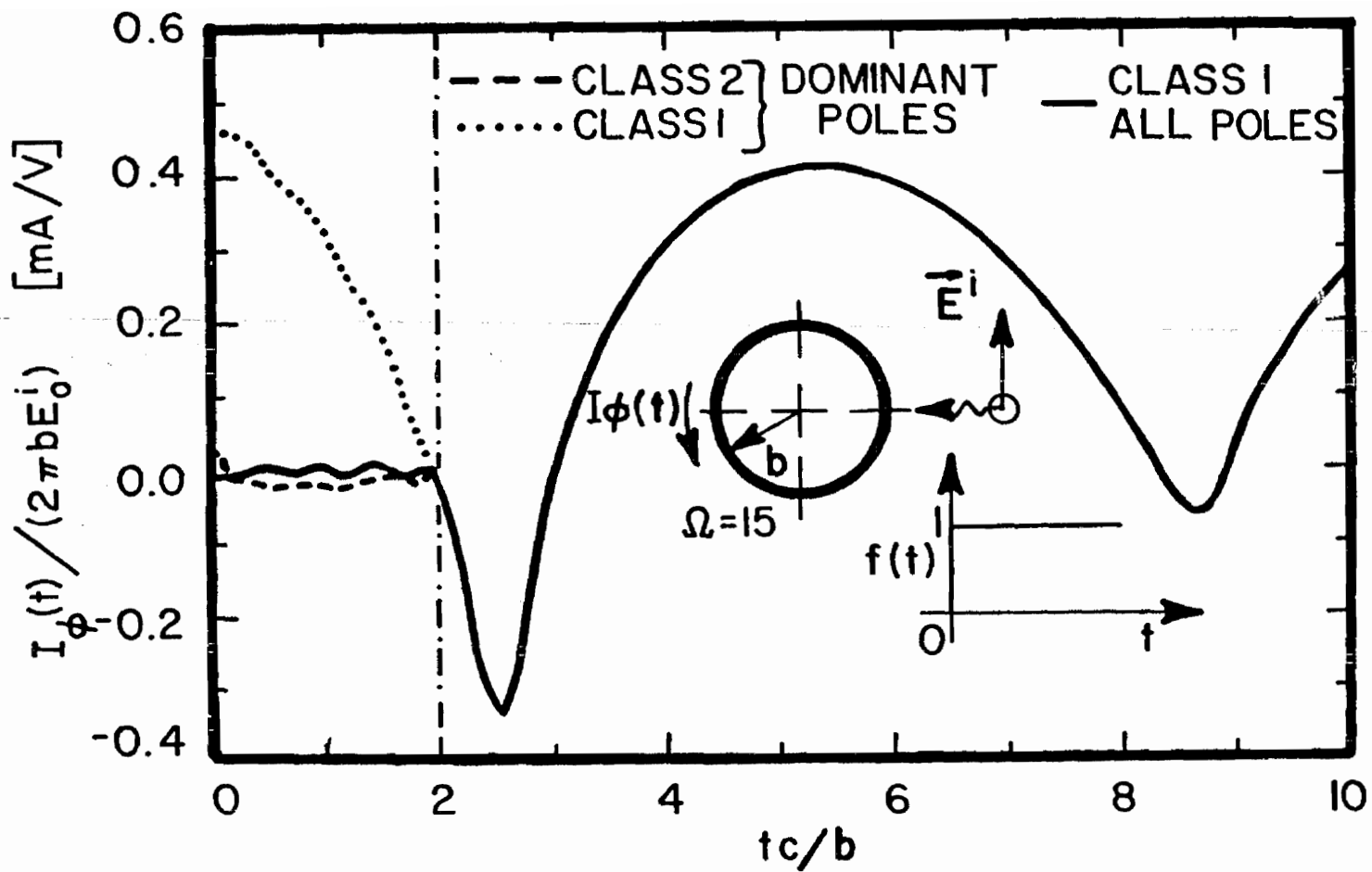
Figure 2.2 Short-circuit current excited in the circular loop at $\phi = 180°$ by a step function plane wave. Time domain SEM expansions using class 1 and class 2 coupling coefficients and different collections of poles are compared.

however, that the three curves in Figure 2.2 agree favorably for $t \leq 2b/c$ after the wave first arrives at the observation point. The response in the period $0 \leq t \leq 2b/c$ is not of much interest, since it is known *a priori* to be zero. Why not then move the time origin to the observation coordinate (port zone) and use the simple class 1 coupling coefficient? This point is supported by further examples presented below.

In Figure 2.3 and 2.4 are compared current responses of a loop antenna computed at $\phi = 90°$ and $\phi = 0°$, respectively, by using class 1 (dotted line) and class 2 (solid line) coupling coefficients and dominant poles satisfying $Im[s_{ni}] \leq 10c/b$. The excitation conditions are identical to that of the previous example. Again, one observes good agreement of the responses beginning from the time when the wave front reaches the observation point. It is seen, however, that the class 1 responses deteriorate slightly for observation points closer to the point of first contact of the plane wave with the loop. This can be attributed to the fact that in the process of moving the observation point toward the point first illuminated by the incident field increases the area of the object surface which in early time lies ahead of the wave front in the integral (2.44).

The conclusions drawn from the loop example also appear to be valid in a thin cylinder case, as demonstrated in Figure 2.5-2.7. The incident field is a step function plane wave whose angle of incidence $\theta = 30°$. In the numerical procedure the length ℓ of the cylinder was divided into 72 equal-size zones and the time origin was placed at the 72nd zone—the one first illuminated by the incident field. In Figures 2.5, 2.6, and 2.7 are shown, respectively, the current responses evaluated at zones $18(1/4\ell)$, $36(1/2\ell)$, and $54(3/4\ell)$. Only the

45
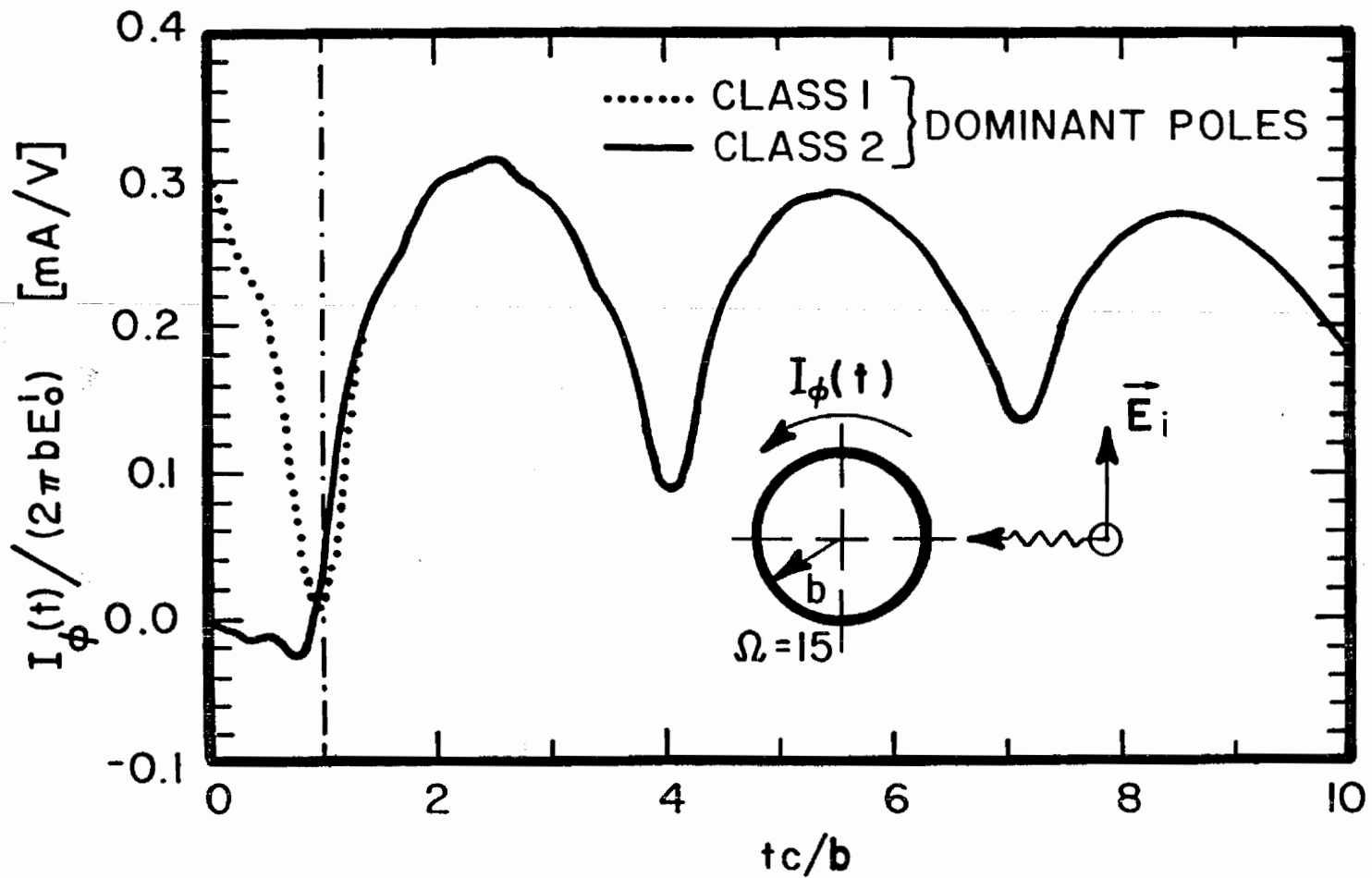
Figure 2.3 Short-circuit current excited in the circular loop at $\phi = 90°$ by a step function plane wave. Time domain SEM expansions using class 1 and class 2 coupling coefficients and dominant poles are compared.
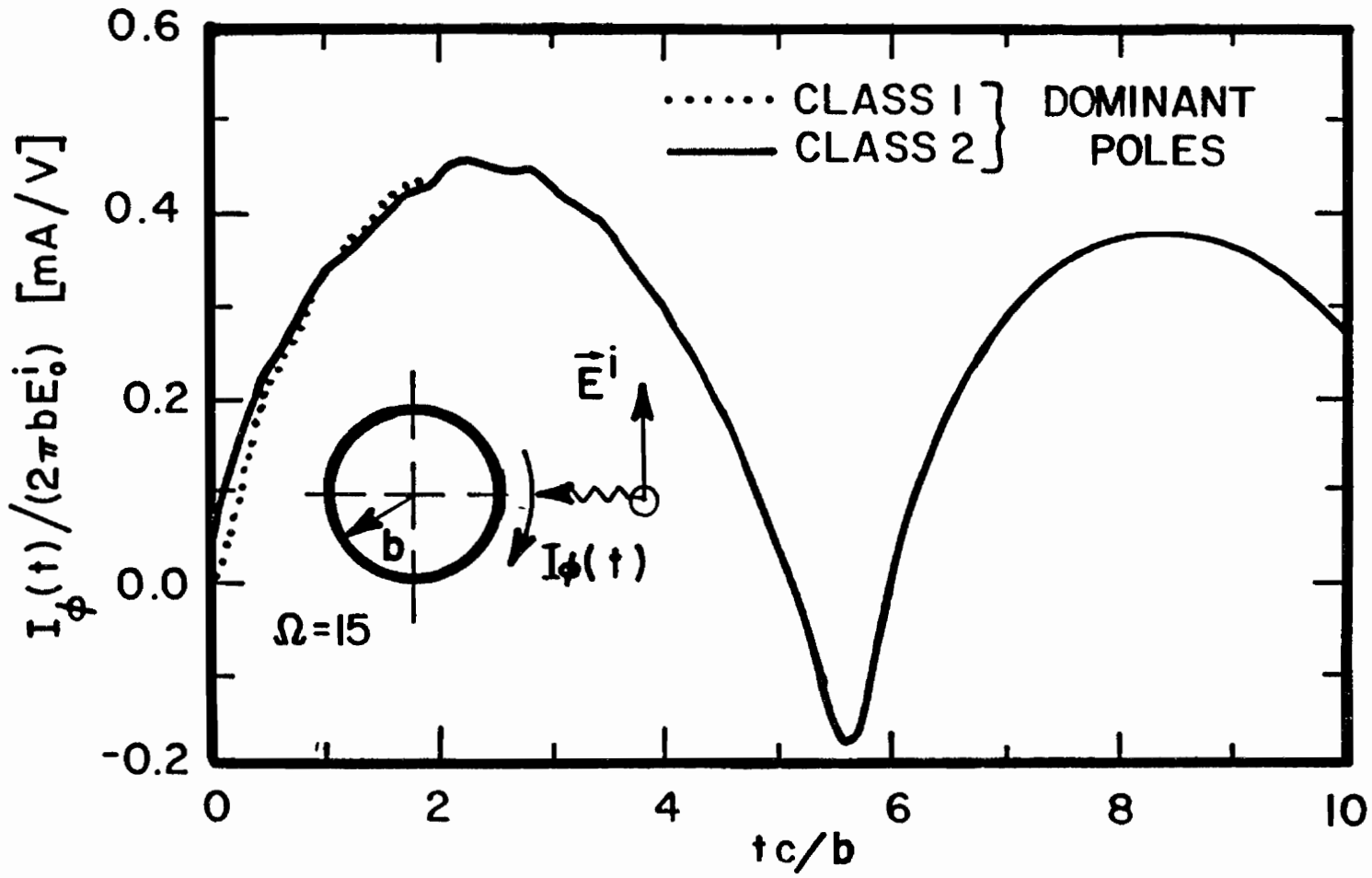
Figure 2.4   Short-circuit current excited in the circular loop at $\phi = 0^o$ by a step function plane wave.   Time domain SEM expansions using class 1 and class 2 coupling coefficients and dominant poles are compared.
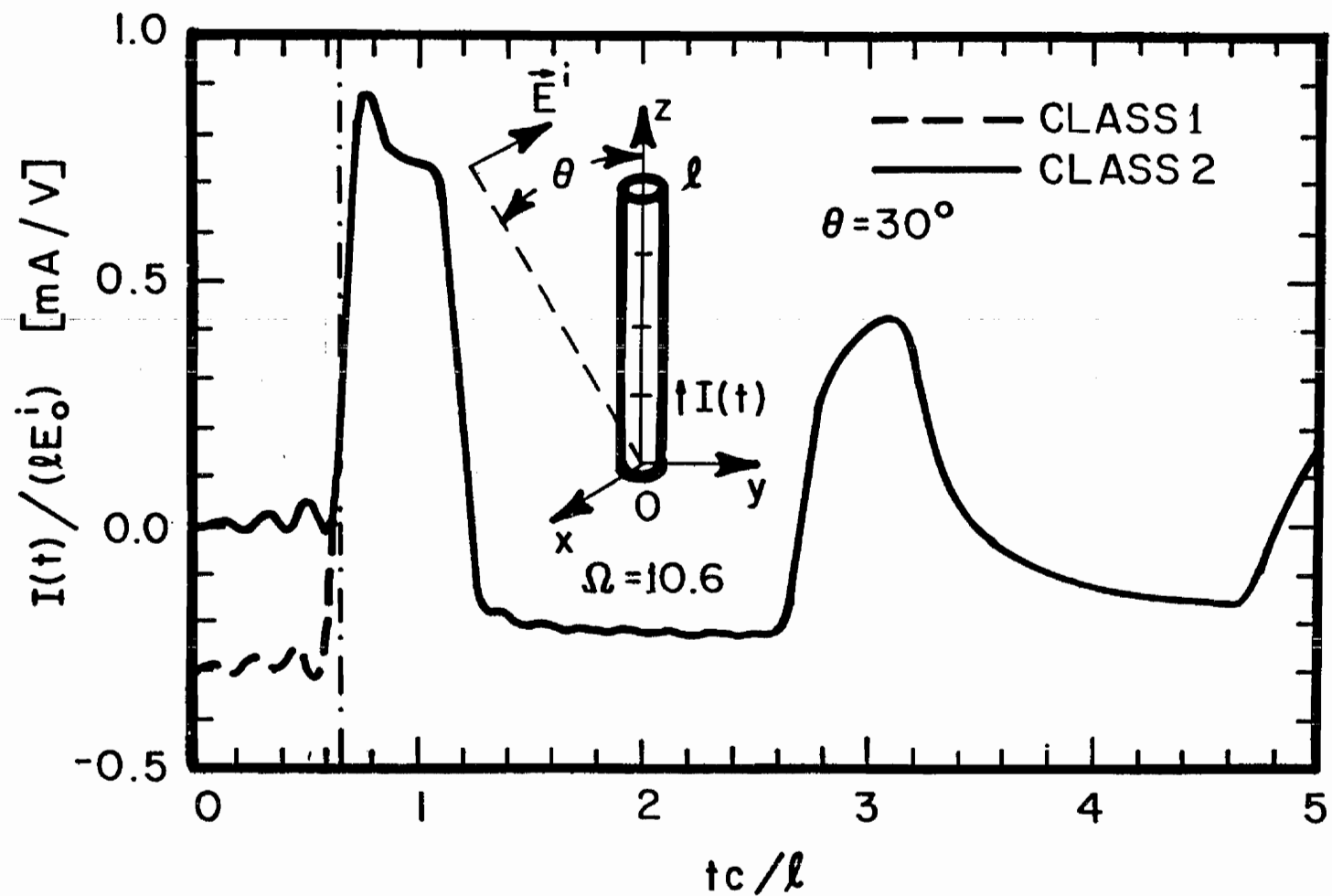
Figure 2.5 Short-circuit current excited in the thin cylinder at $z = 1/4\ell$ by a step function plane wave. Time domain SEM expansions using class 1 and class coupling coefficients and dominant poles are compared.
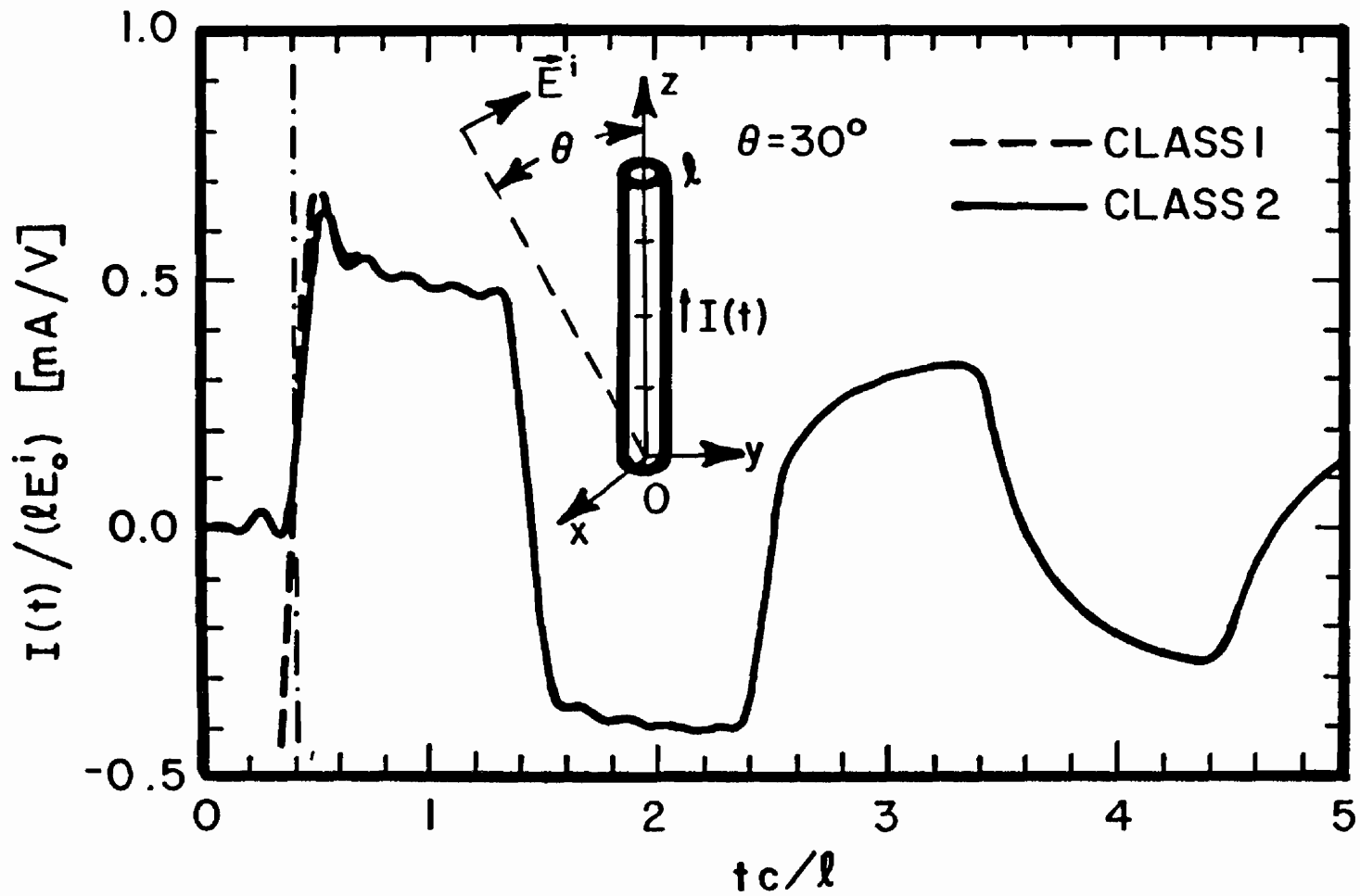
Figure 2.6 Short-circuit current excited in the thin cylinder at $z = 1/2\ell$ by a step function plane wave. Time domain SEM expansions using class 1 and class 2 coupling coefficients and dominant poles are compared.
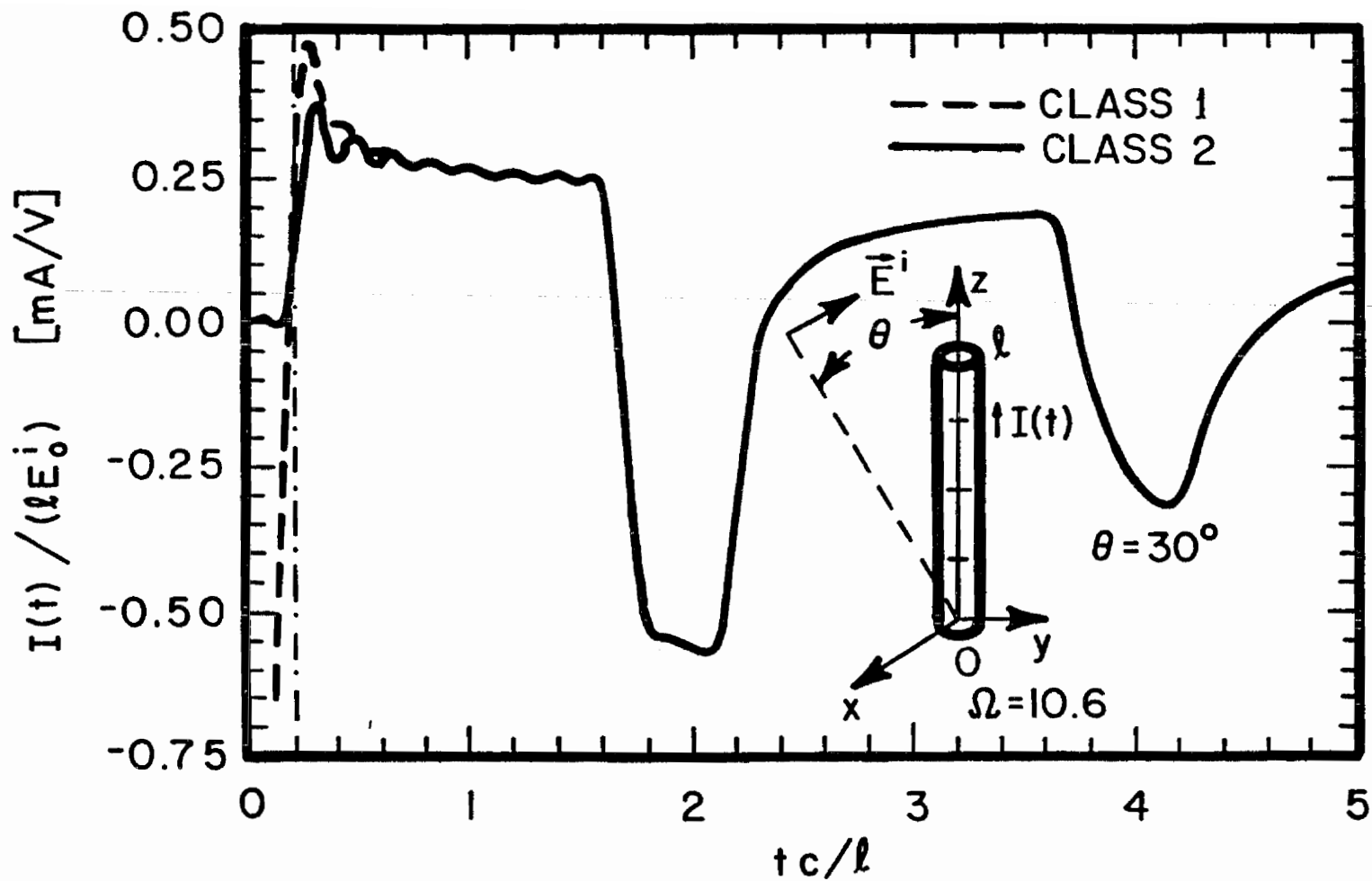
Figure 2.7 Short-circuit current excited in the thin cylinder at $z = 3/4\ell$ by a step function plane wave. Time domain SEM expansions using class 1 class 2 coupling coefficients and dominant poles are compared.

dominant poles for which $Im[s_{ni}] \lesssim 10\pi c/\ell$ were used in the SEM expansion

for the current. It is seen from these figures that class 1 responses

(dashed lines) agree favorably with class 2 responses (solid lines)

beginning from the time when the leading edge of the plane wave reaches

the observation point. As in the loop case the agreement deteriorates

somewhat when the observation point is moved toward the point of first

contact of the incoming wave with the cylinder. The discrepancy

between the class 1 and class 2 responses in the present case is greater

than in the loop case, which can be attributed to the fact that the poles

of the cylinder are computed less accurately than the poles of the loop,

and to the sensitivity of the class 1 coupling coefficient form to

errors in pole values [*Baum and Pearson*, 1981].

The following observations can be made from the above examples.

1. Using an incomplete pole collection in the SEM expansion
    together with class 1 coupling coefficients gives non-
    causal responses in the period of time before the leading
    edge of the incident field reaches the observation point.

2. The class 2 coupling coefficient form gives correct (causal)
    responses in a similar situation. It is reasonable to assume
    that it gives also more accurate responses than the class 1
    form for intermediate times, before $t = t_c$.

3. Beginning from the time when the incident wave first reaches
    the observation point the class 1 and class 2 responses
    agree very favorably, so that the class 1 coupling coefficient
    can be used if the time origin is placed at the observation
    point.

4. The class 1 response becomes less accurate when the observation
    point (port zone) is moved closer to the point of first contact
    of the incident field with the object. However, the deteriora-
    tion of the response is not significant (*cf.* Figures 2.4 and
    2.7).

5. The responses obtained by using dominant poles only agree
    favorably with the responses obtained by including more complete
    collections of poles. (This fact is exploited in the next
    section where the dominant pole approximation is discussed in
    more detail.)

From the above discussion we conclude that the class 1 coupling coefficient with the time origin at the port location is the best choice for the SEM equivalent circuit synthesis. In *Baum's* [1976b] formulation this is equivalent to choosing the turn-on time at the instant when the wave front reaches the observation point.

2.7 Dominant Pole Approximation

It is noted that the singularity expansion for the surface current density on the object (2.26) contains a potentailly double infinite summation of terms associated with an infinite number of eigenmodes and potentially infinite collection of poles belonging to a given eigen-mode [*Pearson and Wilton*, 1981]. For many problems of practical interest one can recover by numerical methods [*Tesche*, 1973; *Crow et al.*, 1972; *Singaraju et al.*, 1976], analytical methods [*VanBlaricum and Mittra*, 1975; *Pearson and Roberson*, 1980; *Pearson and Lee*, 1982; *Cho and Cordaro*, 1979] a finite number of poles which dominate the frequency and time responses for excitations whose spectra are bandlimited. These poles are the ones located closest to the $j\omega$-axis and are referred to as the dominant poles of the structure [*Pearson and Wilton*, 1981]. In the case of the few structures for which the distribution of poles among the eigenmodes can be explicitly determined (*e.g.*, the circular loop and the sphere) the collection of dominant poles can be obtained by taking only one "dominant" pole from the number of poles belonging to each eigenmode. There are strong indications that this is true in general. Denoting by s_n the dominant pole of the nth eigenmode, one can rewrite (2.26) in the dominant pole approximation as

52

$$\tilde{\vec{J}}(\vec{r},s) = \frac{1}{s} \beta_0 \tilde{\eta}_0(s)\vec{J}_0(\vec{r})\tilde{f}(s) + \sum_n \frac{s}{s_n(s-s_n)} \beta_n \tilde{\eta}_n(s)\vec{J}_n(\vec{r})\tilde{f}(s) \qquad (2.48)$$

with

$$\tilde{\eta}_n(s) = <\vec{J}_n(\vec{r}); \vec{E}_0(\vec{r})\tilde{p}(\vec{r},s)> . \qquad (2.49)$$

It is understood in (2.48) that complex conjegate poles are included in the summation. It is noted that the term associated with the pole at the origin is shown explicitly in (2.48). As pointed out in Section 2.3, this term is present only in the case of multiply-connected objects, such as the loop antenna. It is absent, for example, in the case of the thin dipole antenna, which can be considered as a member of the singly-connected class of structures.

It is important to note that in the case of a multiply-connected object immersed in an external incident filed, one expects a cancellation of the pole at the origin to occur. This is so, because in the limit as $s \to 0$ the coupling coefficient $\tilde{\eta}_0(s)$ is obtained by integrating along a closed path a conservative (in the limit) field against the constant natural mode. One may rewrite (2.48) in such cases as

$$\tilde{\vec{J}}(\vec{r},s) = \mu_0 \beta_0 \vec{J}_0(\vec{r})\tilde{f}(s) + \sum_n \frac{s}{s_n(s-s_n)} \beta_n \tilde{\eta}_n(s)\vec{J}_n(\vec{r})\tilde{f}(s) \qquad (2.50)$$

where

$$\mu_0 = \lim_{s \to 0} \left(\frac{\tilde{\eta}_0(s)}{s} \right) . \qquad (2.51)$$

For example, in the plane wave case, in the limit as $s \to 0$, one arrives at

$$\tilde{\eta}_o(s) = \langle \vec{J}_o(\vec{r}); \vec{E}_o e^{-\gamma \hat{p} \cdot (\vec{r} - \vec{r}_o)} \rangle$$

$$\cong \langle \vec{J}_o(\vec{r}); \vec{E}_o [1 - \gamma \hat{p} \cdot (\vec{r} - \vec{r}_o)] \rangle$$

$$= -s \langle \vec{J}_o(\vec{r}); \vec{E}_o \hat{p} \cdot (\vec{r} - \vec{r}_o)/c \rangle \tag{2.52}$$

so that

$$\mu_o = -\langle \vec{J}_o(\vec{r}); \vec{E}_o \hat{p} \cdot (\vec{r} - \vec{r}_o)/c \rangle \quad . \tag{2.53}$$

2.8 Conclusions

The SEM representation for the surface current density on a scattering object is derived formally by way of the eigenfunction expansion, and the potenital limitations of this procedure are addressed. Since the expansion is performed on the eigenmode-by-eigenmode basis, there may be branch-integral contributions present [*Pearson and Wilton*, 1981] which, in the case of finite-extent perfectly-conducting objects in lossless media, must cancel in the eigenmode summation, to give a meromorphic current response in accord with [*Marin and Latham*, 1972]. It is demonstrated by specific examples in Appendix A that such phenomenon can, indeed, occur. Only for highly symmetric objects, having frequency independent eigenfunctions, has it been possible to show (Section 2.3) that the eigenvalues are meromorphic in s. The omission of the branch-integral constituent in the SEM exapnsion can adversely affect the realizability of the terminal eigenadmittances [*Pearson and Wilton*, 1981].

Two basic SEM expansion forms arise in the SEM expansion of the current, the so-called modified and unmodified forms. Since the modified form imposes less stringent conditions on the large-s asymptotic properties of the inverse eigenvalues [*Pearson*, 1981], it is suggested

that the modified poles modules are preferable in the case of problems dealth with on a purely numerical basis.

Two forms of coupling coefficients have been used to date, the so-called class 1 and class 2 forms [*Baum*, 1976b]. For the SEM equivalent circuit synthesis one is forced to use the class 1 SEM expansion form. It is demonstrated that this form gives good results provided the time origin is placed at the gap zone. The convergence of this representation is assured since it is shown that the class 1 expansion form is always convergent as $\text{Re}\{s_{ni}\} \to \infty$ if the time origin is located on the surface of the scattering object.

It is also demonstrated that for the thin-wire loop antenna the dominant-pole approximation [*Pearson and Wilton*, 1980] gives very accurate short-circuit current responses. It is conjectured that this is true for all highly resonant structures.

CHAPTER 3

FORMAL DEVELOPMENT OF EQUIVALENT CIRCUITS

3.1 Introduction

In this chapter is discussed a formal development[1] of SEM equivalent circuits for energy collecting structures with definable ports. With some exceptions, this development essentially follows that presented by *Baum* [1976a] and, in a more recent paper, by *Pearson and Wilton* [1980]. It is reiterated here, for the sake of completeness, in notation consistent with the rest of this work.

The objective of this work is to derive an equivalent circuit at a port[2] of an antenna or scatterer from its SEM description. Since the problem is linear, one can construct the Norton and Thévenin equivalent networks, as shown in Figure 3.1. It is noted that the Norton circuit requires the knowledge of the driving-point admittance $\tilde{Y}(s)$ and the short-circuit current $\tilde{I}^{sc}(s)$. To define the Thévenin circuit one needs to know the driving-point impedance $\tilde{Z}(s)$ and the open-circuit voltage $\tilde{V}^{oc}(s)$. These quantities are not independent and are related by

$$Y(s) = \frac{1}{\tilde{Z}(s)} \tag{3.1}$$

and

$$Z(s) = \frac{\tilde{V}^{oc}(s)}{\tilde{I}^{sc}(s)} . \tag{3.2}$$

---

[1] The issues of physical realizability of the equivalent circuits are addressed in Chapter 4.

[2] A port is here understood in the usual circuit sense as a pair of terminals with the property that the current entering one terminal is equal to the current leaving the other terminal.
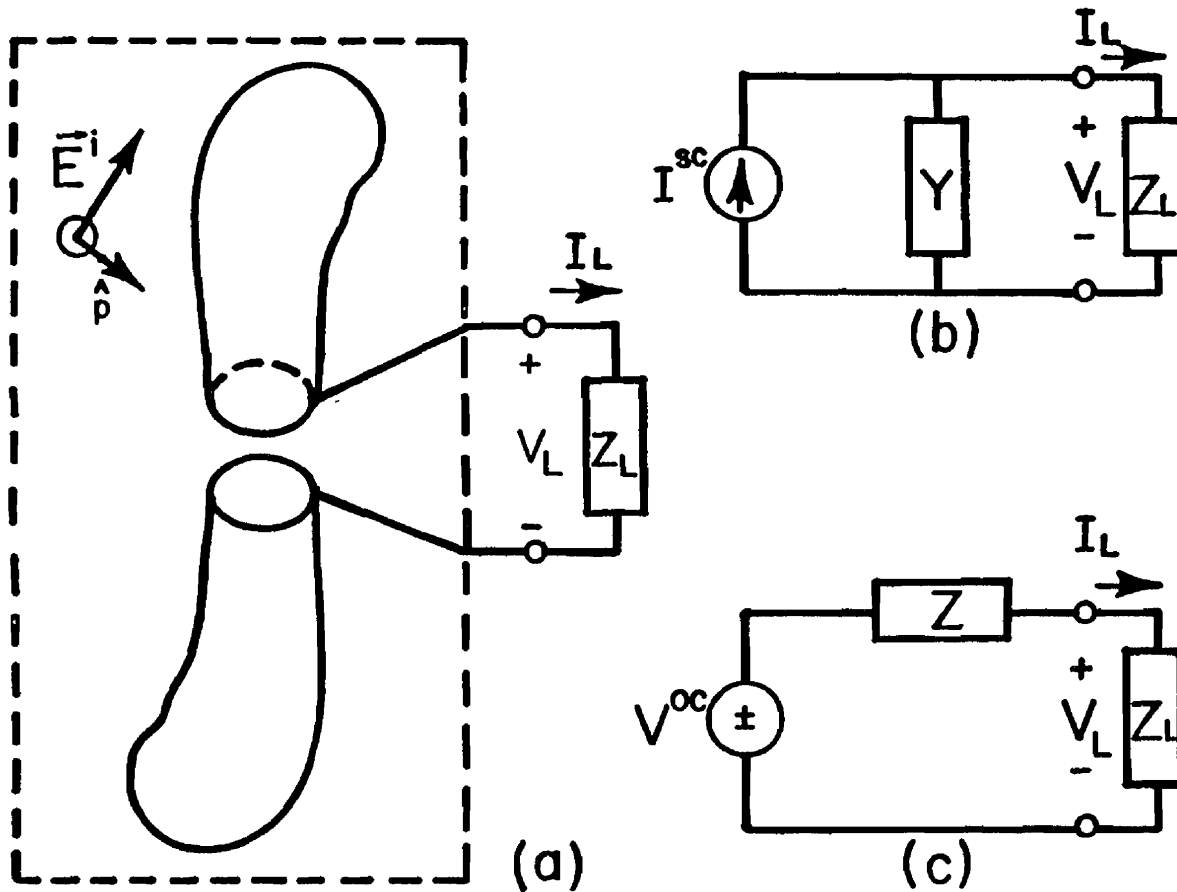
Figure 3.1 (a) Single-port electromagnetic energy collecting structure and (b) its Norton and (c) Thévenin equivalent circuit representations.

The process of constructing the Norton (Thévenin) equivalent network can thus be naturally divided into two steps: the computation of $\tilde{Y}(s)(\tilde{Z}(s))$ -- the immittance problem, and the computation of $\tilde{I}^{sc}(s)(\tilde{V}^{oc}(s))$ -- the source problem.

In order that the circuit quantities   voltage and current, could be uniquely defined, the field in the gap region must be conservative. This means that the gap must be electrically small in some sense. In most cases this requirement restricts the class of tractable objects to slender structures with narrow gaps (in terms of wavelengths or, equivalently, the rate of variation of the transient waveshapes of interest).[1]

A typical gap region of width Δ and perimeter P is shown in Figure 3.2. The gap is defined such that there are two sides or terminals separated by the gap region with surface S_g. The antenna or scatterer surface is designated by S_a so that $S = S_a \cup S_g$. $\hat{a}_g$ is a unit vector oriented from one gap side to the other on S_g. Following *Baum* [1976a] we define the gap current and voltage as the averaged quantities

$$I(s) = \frac{1}{\Delta} <\tilde{\vec{J}}(\vec{r},s); \hat{a}_g(\vec{r})>_{S_g} \tag{3.3}$$

and

$$\tilde{V}(s) = -\frac{1}{P} <\tilde{\vec{E}}(\vec{r},s); \hat{a}_g(\vec{r})>_{S_g} . \tag{3.4}$$

Since a slow spatial variation of the field in the gap is assumed, the expressions (3.3) and (3.4) can be simplified to, respectively,

---

[1] There are exceptions to this rule, *e.g.*, the symmetrically excited spherical antenna or the thick cylindrical antenna. One can even allow non-symmetric excitations (*e.g.*, plane wave) if the results are interpreted properly.
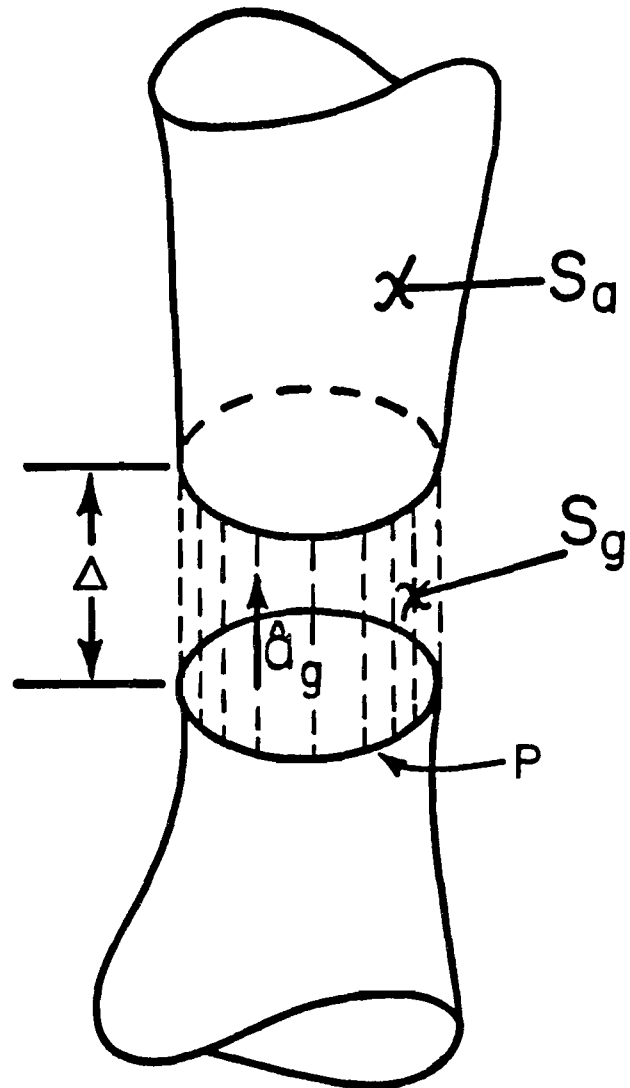
Figure 3.2 Detail of the feed gap of a radiating structure.

$$\tilde{I}(s) \cong P \; \tilde{\vec{J}}(\vec{r}_g, s) \cdot \hat{a}_g(\vec{r}_g) \qquad (3.5)$$

and

$$\tilde{V}(s) \cong - \Delta \; \tilde{\vec{E}}(\vec{r}_g, s) \cdot \hat{a}_g(\vec{r}_g) \qquad (3.6)$$

with $\vec{r}_g$ denoting a point in the gap region.

The Norton and Thévenin equivalent circuits resulting, respectively, from the short-circuit and the open-circuit boundary value problems are derived in the next sections. These circuits are based on the dominant pole expansion (2.48) for the current density on the object. In his original work *Baum* [1976a] also derived the eigenmode expansion networks obtained from (2.13). These networks, however, are of little practical value, since in most cases the quantities $\tilde{\vec{J}}_n(\vec{r}, s)$ and $\tilde{\lambda}_n(s)$ are not explicitly known.

3.2 Norton Equivalent Circuit

The Norton equivalent circuit consists of the driving-point admittance $\tilde{Y}(s)$ and the short-circuit current $\tilde{I}^{sc}(s)$ (Figure 3.1(a)). The driving-point admittance of the structure is determined by solving the short-circuit boundary value problem indicated in Figure 3.3(a). The incident field is that due to the voltage $\tilde{V}(s) = V_o \tilde{f}(s)$ impressed across the gap, so that the coupling coefficients (2.49) take the form

$$\tilde{\eta}_n = \langle \vec{J}_n(\vec{r}); \frac{V_o}{\Delta} \hat{a}_g(\vec{r}) \rangle_{S_g} = V_o \, I_n \qquad (3.7)$$

where the notation

$$I_n \equiv \frac{1}{\Delta} \langle \vec{J}_n(\vec{r}); \hat{a}_g(\vec{r}) \rangle_{S_g}$$

$$\cong P \; \vec{J}_n(\vec{r}_g) \cdot \hat{a}_g(\vec{r}_g) \qquad (3.8)$$
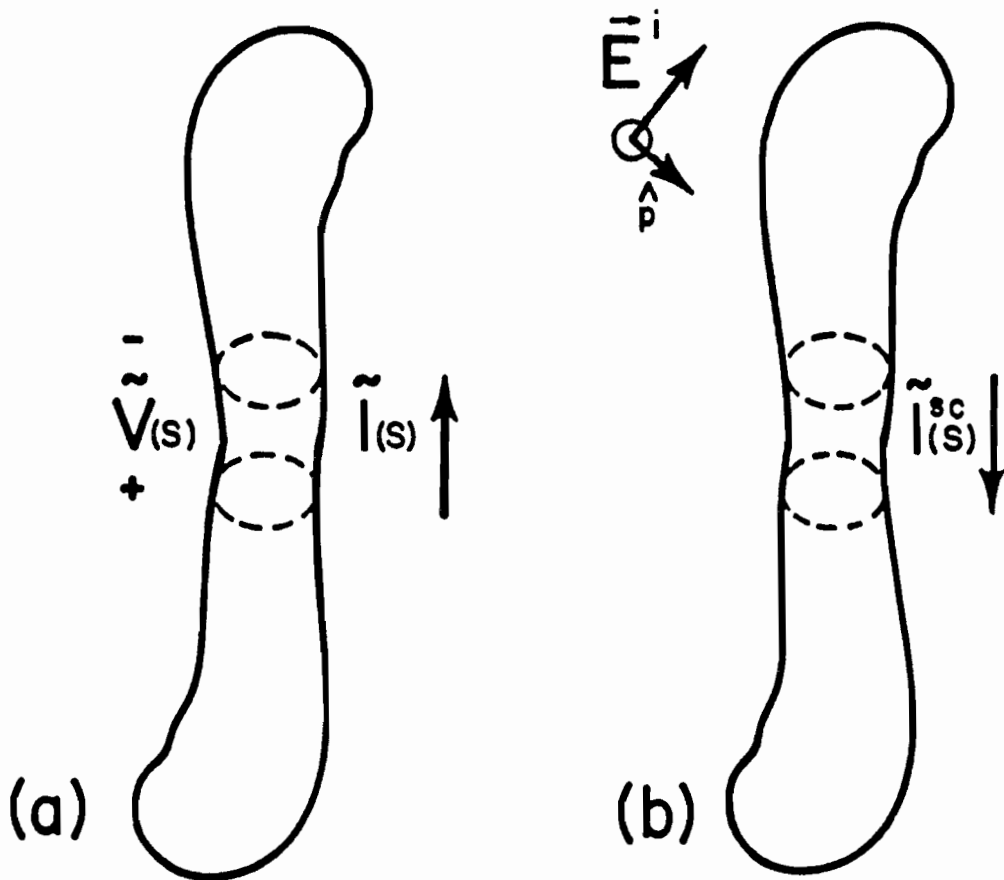
Figure 3.3 Short-circuit boundary value problem. (a) Determination of the driving-point admittance and (b) determination of the short-circuit current.

has been introduced. Using the coupling coefficients (3.7) in (2.48) the port current can be determined from (3.3) as

$$\tilde{I}(s) = \frac{1}{s} \beta_o I_o^2 \tilde{V}(s) + \sum_n \frac{s}{s_n(s - s_n)} \beta_n I_n^2 \tilde{V}(s) \quad . \tag{3.9}$$

The driving-point admittance $\tilde{Y}(s) = \tilde{I}(s)/\tilde{V}(s)$ follows directly from (3.9):

$$\tilde{Y}(s) = \frac{1}{sL_o} + \sum_n \tilde{Y}_n(s) \tag{3.10}$$

where the $\tilde{Y}_n(s)$ are defined by

$$\tilde{Y}_n(s) = \frac{a_n}{s - s_n} + \frac{a_n}{s_n} = \frac{a_n s}{s_n(s - s_n)} \quad . \tag{3.11}$$

These are the so-called modified pole admittances, as distinguished from the unmodified pole admittances

$$\tilde{Y}_n(s) = \frac{a_n}{s - s_n} \tag{3.12}$$

which result if the expansion (2.25) is used. The admittance residues a_n are given by

$$a_n = \beta_n I_n^2 \tag{3.13}$$

and the magnetostatic inductance L_o is defined as

$$L_o = \frac{1}{a_o} \quad . \tag{3.14}$$

One can combine conjugate pole terms in (3.10) to get[1]

---

[1] For simplicity, only complex conjugate poles are assumed. A trivial modification of (3.15) is necessary to avoid the double accounting of purely real poles.

$$\tilde{Y}(s) = \frac{1}{sL_o} + \sum_n \left[\tilde{Y}_n(s) + \tilde{Y}_{-n}(s) \right]$$

$$= \frac{1}{sL_o} + \sum_n \hat{\tilde{Y}}_n(s) \tag{3.15}$$

with the conjugate pole-pair admittances defined as

$$\hat{\tilde{Y}}_n(s) = \tilde{Y}_n(s) + \tilde{Y}_{-n}(s) . \tag{3.16}$$

In (3.15) - (3.16) the notation is adopted that n and -n constitute the indices for a conjugate pair of poles $(s_{-n} = s_n^*)$.[1]

The short-circuit current can be found from the boundary value problem shown in Figure 3.3(b). The incident field is now that due to a plane wave and the coupling coefficients η_n are given by

$$\tilde{\eta}_n = \langle \vec{J}_n(\vec{r}); \vec{E}_o \, e^{-\gamma_n \hat{p} \cdot (\vec{r} - \vec{r}_g)} \rangle_S . \tag{3.17}$$

Note that the class 1 coupling coefficient form is used with the time origin at the gap region, as suggested in Section 2.5. The short-circuit current can be obtained from (2.50) and (3.3) as

$$\tilde{I}^{sc}(s) = \mu_o \beta_o I_o \tilde{f}(s) + \sum_n \frac{s}{s_n(s - s_n)} \beta_n \tilde{\eta}_n I_n \tilde{f}(s) . \tag{3.18}$$

This expression can be conveniently rewritten as

$$\tilde{I}^{sc}(s) = g_o \tilde{f}(s) + \sum_n \tilde{Y}_n(s) \, T_n \tilde{f}(s) \tag{3.19}$$

where the source coefficients

$$g_o = \mu_o \beta_o I_o \tag{3.20}$$

and

_____

[2] Complex conjugate value is denoted by superscript asterisk (*).

63

$$T_n = \frac{\tilde{\eta}_n}{I_n} \qquad (3.21)$$

have been introduced. Combining conjugate pole terms in (3.19) gives

$$\tilde{I}^{sc}(s) = g_o \tilde{f}(s) + \sum_n \left[\tilde{Y}_n(s)T_n + \tilde{Y}_{-n}(s)T_n^* \right] \tilde{f}(s) \ . \qquad (3.22)$$

It is fruitful to express $\tilde{I}^{sc}(s)$ in terms of the pole-pair admittances $\hat{\tilde{Y}}_n(s)$ as follows:

$$\tilde{I}^{sc}(s) = g_o \tilde{f}(s) + \sum_n \hat{\tilde{Y}}_n(s)\hat{\tilde{T}}_n(s)\tilde{f}(s)$$

$$= g_o \tilde{f}(s) + \sum_n \hat{\tilde{Y}}_n(s)\tilde{V}_n(s) \qquad (3.23)$$

where the pole-pair voltage transfer functions $\hat{\tilde{T}}_n(s)$ are defined as

$$\hat{\tilde{T}}_n(s) = \frac{\tilde{Y}_n(s)\hat{T}_n + \tilde{Y}_{-n}(s)T_n^*}{\tilde{Y}_n(s) + \tilde{Y}_{-n}(s)} = \text{Re}\{T_n\} + j\ \text{Im}\{T_n\} \frac{\tilde{Y}_n(s) - \tilde{Y}_{-n}(s)}{\hat{\tilde{Y}}_n(s)} \qquad (3.24)$$

and the pole-pair source voltages $\tilde{V}_n(s)$ as

$$\tilde{V}_n(s) = \hat{\tilde{T}}_n(s)\tilde{f}(s) \qquad . \qquad (3.25)$$

The driving-point admittance (3.15) and the short-circuit current (3.23) can be combined according to the Norton's theorem to give the equivalent network shown in Figure 3.4(a). By pairing pole-pair admittances with the corresponding pole-pair source voltages and applying the Thévenin's transformation to each pole-pair circuit this network can be recast into the form shown in Figure 3.4(b). This very fruitful transformation was first introduced by *Baum* [1976a].
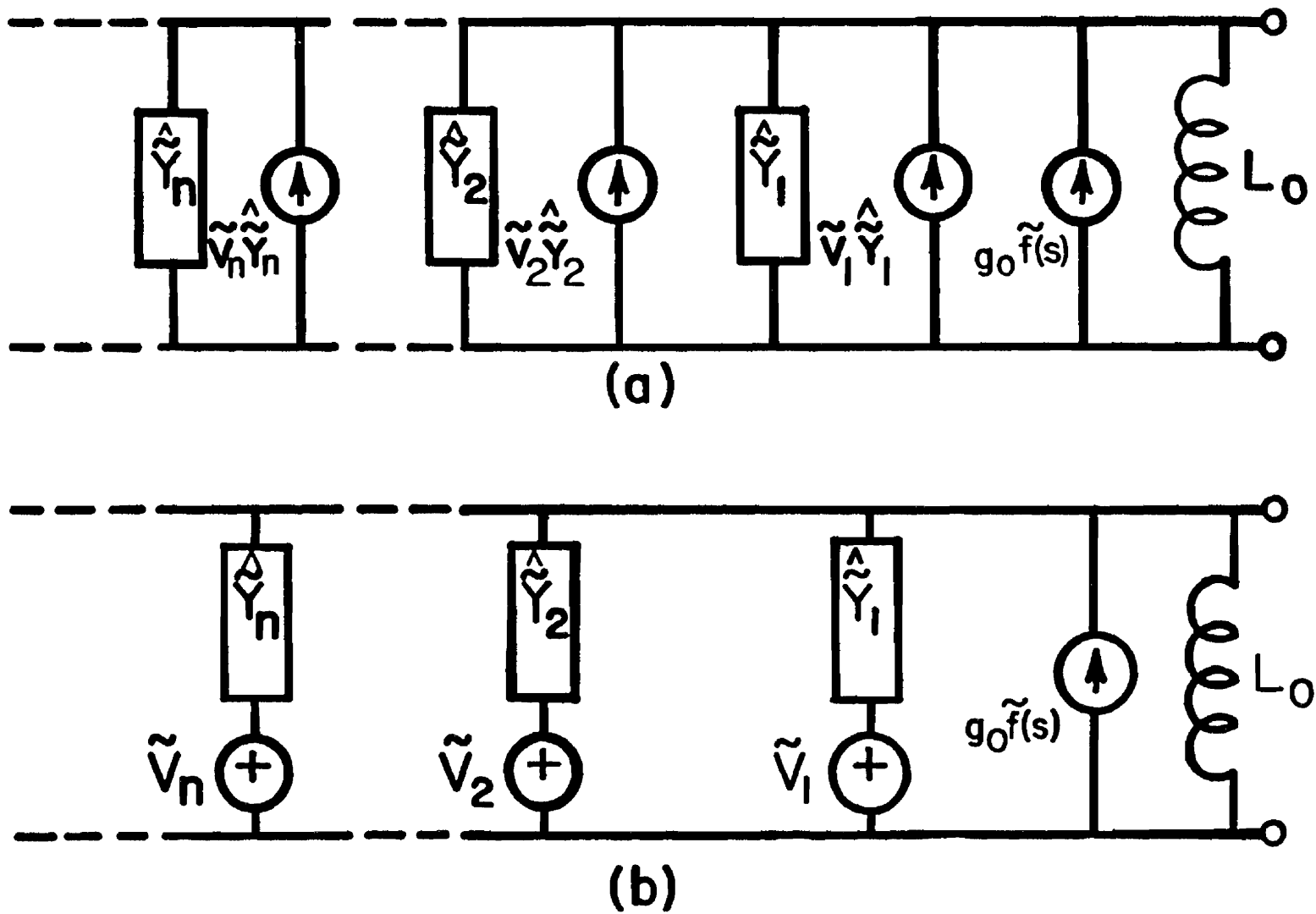
Figure 3.4 (a) Norton circuit representation and (b) its alternative form.

3.3 Thévenin Equivalent Circuit

The Thévenin equivalent circuit results from the open-circuit
boundary value problem shown in Figure 3.5. The solution for the
open-circuit SEM parameters is in practice a much more difficult
task than the solution for the short-circuit parameters of the same
structure. Thus, it is probably more practical to derive the Thévenin
circuit indirectly, from the short-circuit parameters. This last
approach, which was pursued recently by *Tesche and Giri* [1981], is
briefly discussed at the end of this section.

The forcing function in the impedance problem (Figure 3.5(a))
is the impressed gap current

$$\vec{\tilde{J}}_g(\vec{r},s) = \vec{J}_g(\vec{r})\tilde{f}(s) \cong \frac{1}{P} \hat{a}_g(r_g) I_o \tilde{f}(s)$$

$$= \frac{1}{P} \hat{a}_g(\vec{r}_g)\tilde{I}(s) \ , \ \vec{r} \, \epsilon \, S_g \qquad . \qquad (3.26)$$

The field due to this current can be otained from the integral
equation as

$$\vec{\tilde{E}}^i(\vec{r},s) = - <\vec{\tilde{Z}}(\vec{r},\vec{r}',s);\vec{\tilde{J}}_g(\vec{r},s)>_{S_g}$$

$$= -I_o \frac{1}{P} <\vec{\tilde{Z}}(\vec{r},\vec{r}'s,);\hat{a}_g(\vec{r}')>_{S_g} \tilde{f}(s) \qquad (3.27)$$

and the coupling coefficients are given by

$$\tilde{\eta}_n(s) = -I_o \frac{1}{P} <\vec{J}_n(\vec{r});<\vec{\tilde{Z}}(\vec{r},\vec{r}',s);\hat{a}_g(\vec{r}')>_{S_g}>_{S_a} \equiv -I_o \tilde{\alpha}_n(s) \qquad (3.28)$$

where, for notational convenience, a new quantity has been defined:

$$\tilde{\alpha}_n(s) = \frac{1}{P} <\vec{J}_n(\vec{r});<\vec{\tilde{Z}}(\vec{r},\vec{r}',s);\hat{a}_g(\vec{r}')>_{S_g}>_{S_a} \qquad . \qquad (3.29)$$

66
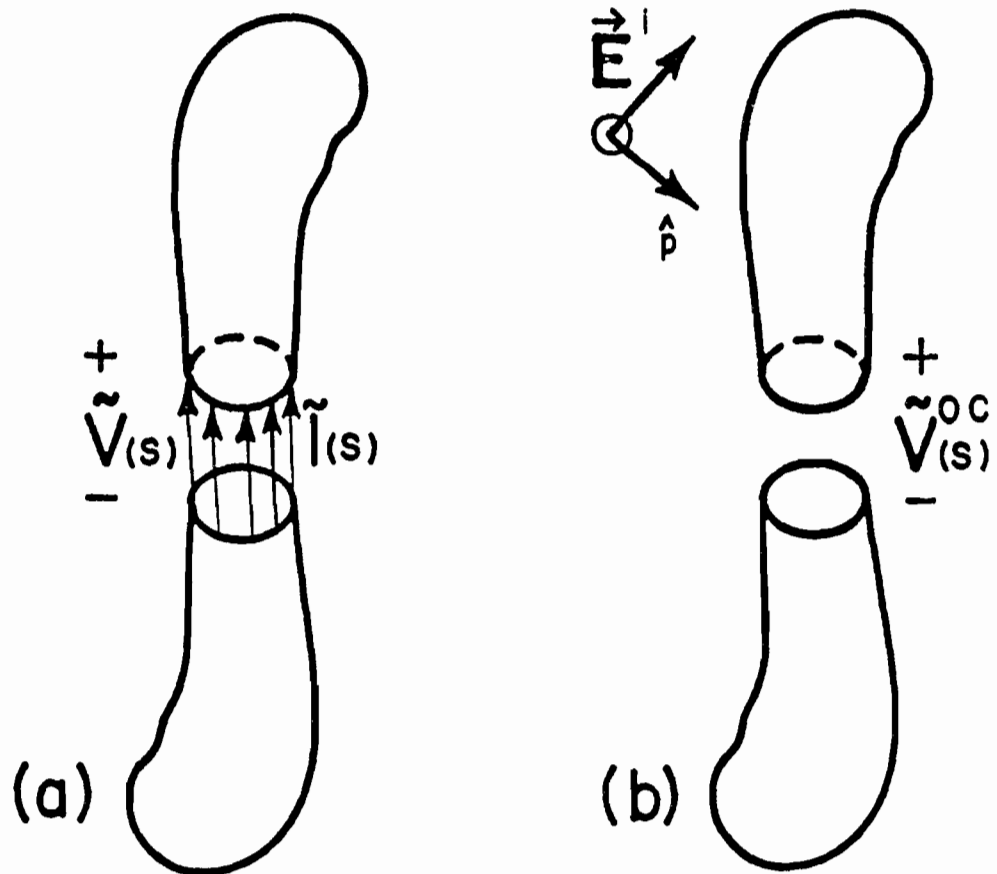
Figure 3.5 Open-circuit boundary value problem. (a) Determination of the driving-point impedance and (b) determination of the open-circuit voltage.

The current on the object can be now expressed with the help of (2.48) as[1)]

$$\tilde{\vec{J}}(\vec{r},s) = -\frac{1}{s}\beta_o\tilde{\alpha}_o(s)\vec{J}_o(\vec{r})\tilde{I}(s) - \sum_n \frac{s}{s_n(s-s_n)}\beta_n\tilde{\alpha}_n(s)\vec{J}_n(r)\tilde{I}(s). \quad (3.30)$$

The electric field radiated by this current and the gap current is given by

$$\tilde{\vec{E}}^s(\vec{r},s) = -\langle\tilde{\overleftrightarrow{Z}}(\vec{r},\vec{r}',s);\tilde{\vec{J}}(\vec{r}',s)\rangle_{S_a}$$
$$- \langle\tilde{\overleftrightarrow{Z}}(\vec{r},\vec{r}',s);\tilde{\vec{J}}_t(\vec{r}',s)\rangle_{S_g} \quad \cdot \quad (3.31)$$

Using the last expression in (3.4) gives the voltage across the gap as

$$\tilde{V}(s) = \frac{1}{P}\langle\langle\tilde{\overleftrightarrow{Z}}(\vec{r},\vec{r}',s);\tilde{\vec{J}}(\vec{r}',s)\rangle_{S_a};\hat{a}_g(\vec{r})\rangle_{S_g}$$
$$+ \frac{1}{P}\langle\langle\tilde{\overleftrightarrow{Z}}(\vec{r},\vec{r}'s);\tilde{\vec{J}}_g(\vec{r},s)\rangle_{S_g};\hat{a}_g(\vec{r}')\rangle_{S_g} \quad \cdot \quad (3.32)$$

Substituting (3.26) and (3.30) into (3.32) and using the symmetry properties of the impedance kernel yields

$$\tilde{V}(s) = \tilde{\alpha}_g(s) - \frac{1}{s}\beta_o\tilde{\alpha}_o^2(s) - \sum_n \frac{s}{s_n(s-s_n)}\beta_n\tilde{\alpha}_n^2(s)\tilde{I}(s) \quad (3.33)$$

where a new quantity has been defined:

$$\tilde{\alpha}_g(s) = \frac{1}{P^2}\langle\hat{a}_g(\vec{r});\tilde{\overleftrightarrow{Z}}(\vec{r},\vec{r}',s);\hat{a}_g(\vec{r}')\rangle_{S_g} \quad \cdot \quad (3.34)$$

Since $\vec{J}_o(\vec{r})$ is solenoidal, it can be seen from (3.29) and (2.3) that $\tilde{\alpha}_o(s) \to s$ as $s \to 0$, so that the second term of (3.33) goes to zero at this frequency. For $n > 0$, however, $\tilde{\alpha}_n(s)$ introduces a pole at zero. Also, $\tilde{\alpha}_g(s)$ has a pole at the origin. Expression (3.33) can be reexpanded

---

[1)] It should be kept in mind that the SEM parameters s_n, $\vec{J}_n(r)$, and β_n are computed with the gap open and are, in general, different from the short-circuit quantities used in the previous section.

to give the driving-point impedance $\tilde{Z}(s) = \tilde{V}(s)/\tilde{I}(s)$ in the form

$$\tilde{Z}(s) = \frac{1}{s}\left[\alpha_g' + \sum_n \frac{\beta_n \alpha_n'^2}{s^2_n}\right] - \sum_n \frac{s}{s_n(s - s_n)} \beta_n \alpha_n^2 \tag{3.35}$$

where

$$\alpha'_{\binom{n}{g}} \equiv \lim_{s \to 0} \left[s\, \tilde{\alpha}_{\binom{n}{g}}(s)\right] \tag{3.36}$$

and $\alpha_n \equiv \tilde{\alpha}_n(s_n)$. It is convenient to define new quantities, the electrostatic capacitance

$$C_o = \frac{1}{\alpha_g' + 2 \sum_n \text{Re}\left\{\frac{\beta_n \alpha_n'^2}{s^2_n}\right\}} \tag{3.37}$$

and the impedance residues

$$a_n' = \beta_n \alpha_n^2 \tag{3.38}$$

and rewrite (3.35) as

$$\tilde{Z}(s) = \frac{1}{sC_o} + \sum_n \tilde{Z}_n(s) \tag{3.39}$$

with the modified pole impedances $\tilde{Z}_n(s)$ given by

$$\tilde{Z}_n(s) = \frac{a_n' s}{s_n(s - s_n)} \quad . \tag{3.40}$$

The impedance counterpart of (3.12), the unmodified pole impedances, are defined as

$$\tilde{Z}_n(s) = \frac{a_n'}{s - s_n} \quad . \tag{3.41}$$

Combining the conjugate pole terms in (3.39) gives

69

$$\tilde{Z}(s) = \frac{1}{sC_o} + \sum_n \left[\tilde{\tilde{Z}}_n(s) + \tilde{Z}_{-n}(s) \right]$$

$$= \frac{1}{sC_o} + \sum_n \hat{\tilde{Z}}_n(s) \tag{3.42}$$

with the conjugate pole-pair impedances defined as

$$\hat{\tilde{Z}}_n(s) = \tilde{Z}_n(s) + \tilde{Z}_{-n}(s) \ . \tag{3.43}$$

Note that for multiply-connected objects, such as the loop antenna, (3.42) does not exhibit the proper behavior as $s \to 0$, unless $C_o = \infty$. This means that the denominator of (3.37) must sum to zero in such case. Also, note that all poles contribute to the static capacitance C_o, as given by (3.37). Numerical evaluation of this expression shows that if only dominant poles are included, (3.37) significantly underestimates the value of C_o. Much better results can be obtained by computing C_o apart from the SEM formulation, by solving for the static charge distribution on the structure.

The open-circuit voltage can be found from the boundary value problem shown in Figure 3.5(b). The incident field is that due to a plane wave and the coupling coefficients are given by

$$\tilde{\eta}_n = \langle \vec{J}_n(\vec{r}) ; \vec{E}_o e^{-\gamma_n \hat{p} \cdot (\vec{r} - \vec{r}_g)} \rangle_{S_a} \ . \tag{3.44}$$

The current on the object is given by (2.50) as

$$\tilde{\vec{J}}(\vec{r},s) = \mu_o \beta_o \vec{J}_o(\vec{r}) \tilde{f}(s) + \sum_n \frac{s}{s_n(s - s_n)} \beta_n \tilde{\eta}_n \vec{J}_n(\vec{r}) \tilde{f}(s) \tag{3.45}$$

and the open-circuit voltage is given by (3.4) as

$$\tilde{V}^{oc}(s) = \frac{1}{P} \langle\langle \tilde{\bar{\bar{Z}}}(\vec{r},\vec{r}',s) ; \tilde{\vec{J}}(\vec{r}',s) \rangle_{S_a} ; \hat{a}_g(\vec{r}) \rangle_{S_g} \ . \tag{3.46}$$

Substituting (3.45) into (3.46) gives

$$\tilde{V}^{OC}(s) = \mu_o \beta_o \tilde{\alpha}_o(s) f(s) + \sum_n \frac{s}{s_n(s - s_n)} \beta_n \tilde{\eta}_n \tilde{\alpha}_n(s) \tilde{f}(s) \ . \tag{3.47}$$

Again, $\tilde{\alpha}_o(s)$ has a zero at zero and $\tilde{\alpha}_n(s)$, $n > 0$, introduces a pole at the origin. Reexpanding (3.47) gives

$$\tilde{V}^{OC}(s) = k_o' \ \tilde{f}(s) + \sum_n \frac{s}{s_n(s - s_n)} \beta_n \tilde{\eta}_n \alpha_n \tilde{f}(s) \tag{3.48}$$

where

$$k_o' = - \sum_n \frac{\alpha_n' \beta_n \tilde{\eta}_n}{s_n^2} \ . \tag{3.49}$$

This series should sum to zero in the case of loop-like (multiply-connected) structures. By introducing

$$T_n' = - \frac{\tilde{\eta}_n}{\alpha_n} \tag{3.50}$$

(3.48) can be rewritten in a form

$$\tilde{V}^{OC}(s) = k_o' \tilde{f}(s) + \sum_n \tilde{Z}_n(s) T_n' \tilde{f}(s) \tag{3.51}$$

or, after pairing the conjugate pole terms, as

$$\tilde{V}^{OC}(s) = k_o \tilde{f}(s) + \sum \left[\tilde{Z}_n T_n + \tilde{Z}_{-n}(s) T_n^* \right] \tilde{f}(s) \tag{3.52}$$

with

$$k_o = 2 \ \text{Re}\{k_o'\} \ . \tag{3.53}$$

It is fruitful to express $\tilde{V}^{OC}(s)$ in terms of the pole-pair impedances as follows

$$\tilde{V}^{OC}(s) = k_o \tilde{f}(s) + \sum_n \hat{\tilde{Z}}_n(s) \hat{\tilde{T}}_n'(s) \tilde{f}(s)$$

$$= k_o \tilde{f}(s) + \sum_n \hat{\tilde{Z}}_n(s) \tilde{I}_n(s) \tag{3.54}$$

71

where the pole pair transfer function $\hat{\tilde{T}}'_n(s)$ are defined by

$$
\begin{aligned}
\hat{\tilde{T}}'_n(s) &= \frac{\tilde{Z}_n(s)T'_n + \tilde{Z}_{-n}(s)T'^*_n}{\tilde{Z}_n(s) + \tilde{Z}_{-n}(s)} \\
&= \text{Re}\{T'_n\} + j\, I_m\{T'_n\}\, \frac{\tilde{Z}_n(s) - \tilde{Z}_{-n}(s)}{\hat{\tilde{Z}}_n(s)}
\end{aligned}
\tag{3.55}
$$

and the pole-pair source currents by

$$
\tilde{I}_n(s) = \hat{\tilde{T}}_n(s)\tilde{f}(s) .
\tag{3.56}
$$

The driving-point impedance and the open-circuit voltage can be now combined according to the Thévenin's theorem to give the circuit shown in Figure 3.6(a). By pairing pole-pair impedances with the corresponding pole-pair source currents and applying the Norton's transformation to each pole-pair circuit this network can be recast into the form shown in Figure 3.6(b).

As mentioned at the beginning of this section, the open-circuit SEM parameters are much more difficult to obtain than the short-circuit parameters of the same problem. This is so because the highly localized charge interaction effects between the two parts of the structure in the vicinity of the gap must be modeled precisely in the open-circuit boundary value problem. Furthermore, it is enough to solve only one short-circuit boundary value problem for all possible gap locations on the structure, whereas the open-circuit problem must be resolved each time the gap is moved. Thus, if for any reason the Thévenin equivalent circuit is preferred over the Norton equivalent, it is likely to be expedient to derive it from the short-circuit parameters using the relations (3.1) and (3.2). Using (3.15) in (3.1) gives the driving-point impedance as
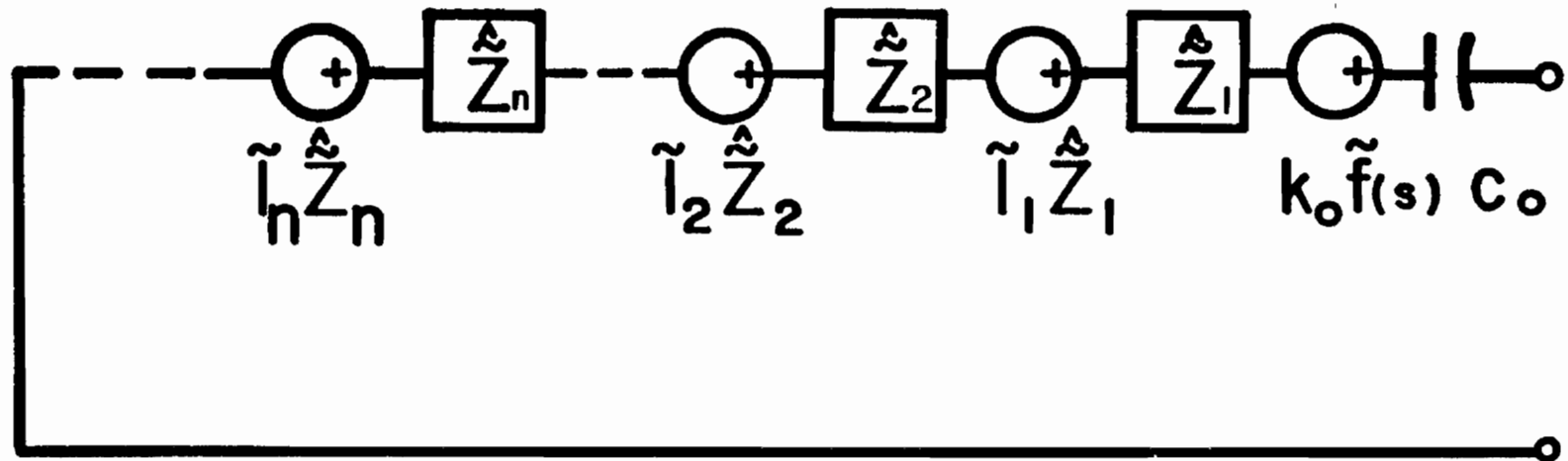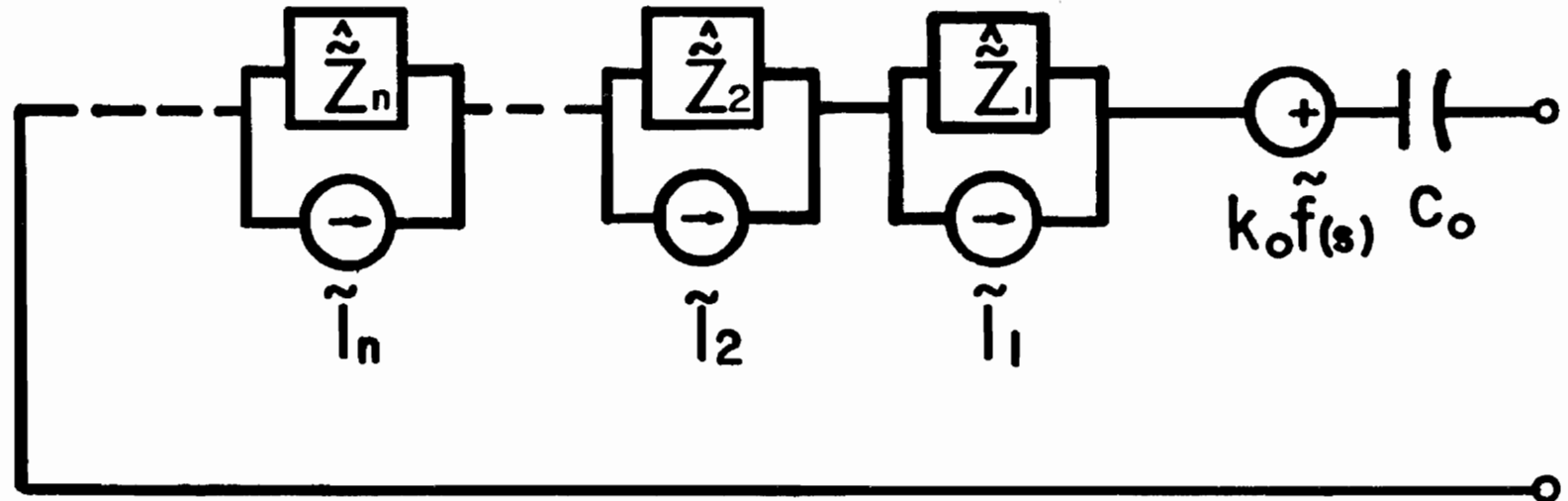
Figure 3.6 (a) Thévenin circuit representation and (b) its alternative form.

$$\tilde{Z}(s) = \frac{1}{\tilde{Y}(s)} = \frac{1}{\frac{1}{sL_o} + \sum_n \hat{\tilde{Y}}_n(s)} \cdot \qquad (3.57)$$

This expression can be easily recast in a form of a ratio of two polynomials in s, and the open-circuit poles can be found by solving for the roots of the denominator polynomial. Expanding $\tilde{Z}(s)$ in terms of these poles gives the input impedance in the desired form (3.39). It should be noted that the inductive term in (3.57) is not present in the case of a simply-connected structure, such as the dipole antenna. Such a structure exhibits a capacitive behavior at low frequencies, with the static capacitance given by[1]

$$C_o = -2 \sum_n \text{Re}\left\{\frac{a_n}{s_n^2}\right\} \qquad (3.58)$$

where a_n are the admittance residues and s_n are the short-circuit poles.

In like fashion, the open-circuit voltage can be otained by substituting (3.15) and (3.23) into (3.2) as

$$\tilde{V}^{oc}(s) = \frac{\tilde{I}^{sc}(s)}{\hat{\tilde{Y}}(s)} = \frac{g_o \tilde{f}(s) + \sum_n \hat{\tilde{Y}}_n(s)\tilde{V}_n(s)}{\frac{1}{sL_o} + \sum_n \hat{\tilde{Y}}_n(s)} \cdot \qquad (3.59)$$

In the case of dipole-like structures (simply-connected objects) the first terms in the numerator and the denominator of (3.59) are not present, and this expression can be easily recast into the form of (3.54) with the coefficient k_o given by

---

[1] Complex conjugate poles are assumed. The extension to purely real poles is trivial.

74

$$k_o = \frac{2}{C_o} \sum_n \text{Re}\left\{\frac{a_n T_n}{s_n^2}\right\} \qquad (3.60)$$

where C_o is given by (3.58) and T_n are the source coefficients defined by (3.21).

CHAPTER 4

SYNTHESIS OF THE POLE-PAIR CIRCUITS

4.1 Introduction

The formal equivalent networks developed in Chapter 3 have the
form of a connection of simple modules associated with conjugate pole
pairs. This network topology simplifies considerably the synthesis
process. Furthermore, it has the advantage that it can be easily
expanded by adding more pole-pair modules without repeating the whole
synthesis process. Since the pole-pair modules are simple, one can
hope to give simple prescriptions for their physical realization. To
define such prescriptions is the main objective of this chapter.

As the first step toward this goal, the Norton and Thévenin
networks from Figures 3.4(b) and 3.6(b) are recast into the form given
in Figures 4.1 and 4.2, respectively. These networks are in a physically
realizable form provided the admittances $\hat{\hat{Y}}_n(s)$ and transfer functions
$\hat{\hat{T}}_n(s)$ in the Norton network, and the impedances $\hat{\hat{Z}}_n(s)$ and transfer
functions $\hat{\hat{T}}'_n(s)$ in the Thevenin network, can be physically realized.
It should be noted that these networks contain controlled sources.
In a hardware realization they can be implemented by active devices,
such as operational amplifiers.

The next sections are devoted to the synthesis of the $\hat{\hat{Y}}_n(s)$ and
$\hat{\hat{Z}}_n(s)$ (driving-point function synthesis), and the synthesis of $\hat{\hat{T}}_n(s)$
and $\hat{\hat{T}}'_n(s)$ (voltage transfer function synthesis). Both modified and
unmodified pole modules are considered.

Some of the material of this chapter is not new and is included
here, for the sake of continuity, in the notation consistent with the
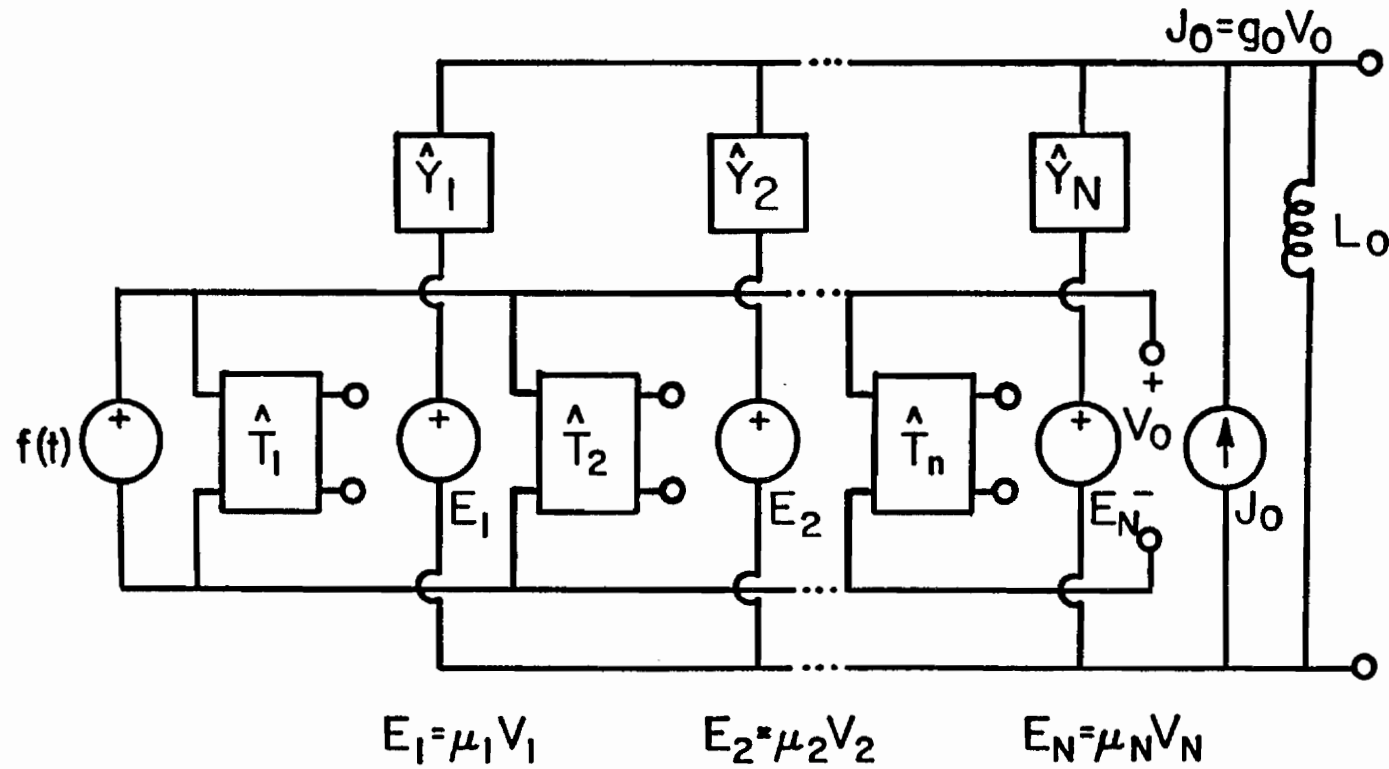
Figure 4.1 Topology of the Norton-based equivalent circuit.
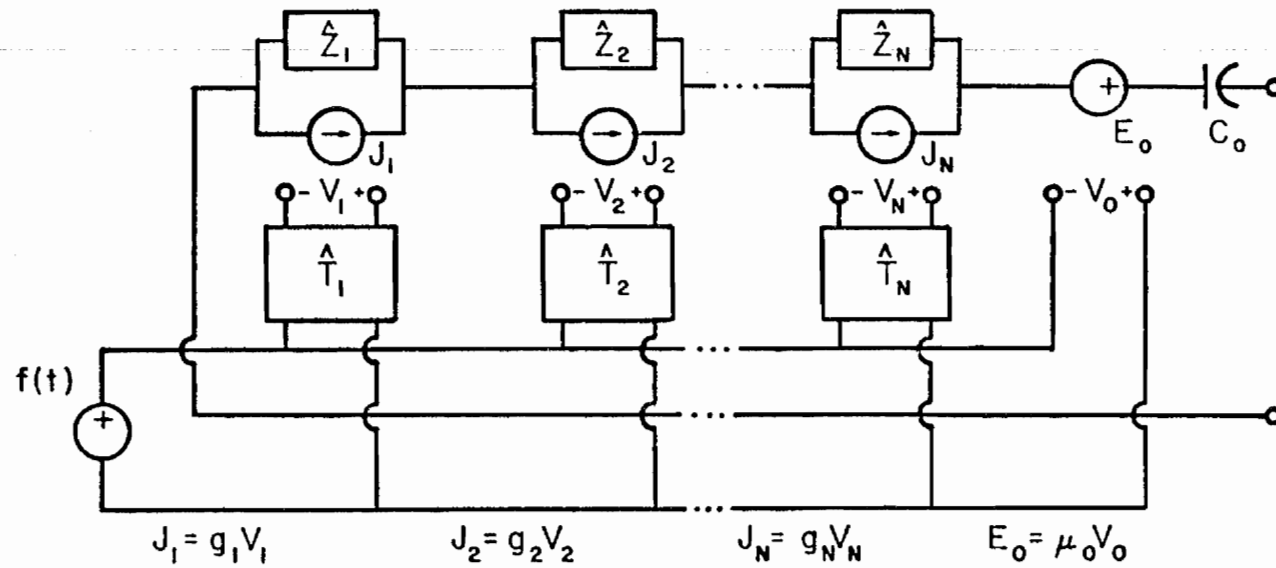
Figure 4.2 Topology of the Thévenin-based equivalent circuit.

rest of this work. This is true in particular of the realizability

conditions of the unmodified pole-pair modules and their interpretation.

Analogous conditions which we give for the modified pole-pair immittances

are believed to be new, however. Similarly, the padding procedure

addressed in Section 4.3 and the approximate Bott-Duffin modules were

used previously, but the explicit expressions for the necessary padding

and network element values in terms of the SEM parameters appear here

for the first time. In deriving them we benefited from an early work

by *Foster* [1955]. Most of the material on the pole-pair transfer

function synthesis in Section 4.4 is also original.

4.2 Driving-Point Function Synthesis

The conjugate pole-pair admittance (2.16) can be written explicitly

in a form of a biquadratic function of s as follows:

$$\hat{\hat{Y}}_n(s) = \frac{A_n s^2 + B_n s + C_n}{D_n s^2 + E_n s + F_n} \tag{4.1}$$

with the coefficients defined differently depending on whether the modified

or unmodified pole admittances are used. For the unmodified modules

the numerator coefficients of (4.1) are given by

$$A_n = 0 \quad , \tag{4.2a}$$

$$B_n = \frac{2c_n}{|s_n|} \quad , \tag{4.2b}$$

and

$$C_n = \frac{c_n - d_n q_n}{Q_n} \quad , \tag{4.2c}$$

and the denominator coefficients by

$$D_n = |s_n|^{-1} , \qquad (4.3\ a)$$

$$E_n = Q_n^{-1} , \qquad (4.3\ b)$$

$$F_n = |s_n| . \qquad (4.3\ c)$$

For the modified modules the numerator coefficients of (4.1) are given by

$$A_n = \frac{d_n q_n - c_n}{Q_n |s_n|^2} , \qquad (4.4a)$$

$$B_n = \frac{c_n (2Q_n^2 - 1) + d_n q_n}{Q_n^2 |s_n|} , \qquad (4.4b)$$

and
$$C_n = 0, \qquad (4.4c)$$

with the denominator coefficients still given by (4.3). In (4.2)-(4.4) the following notation is introduced:

$$s_n = -\sigma_n + j\omega_n , \qquad (4.5)$$

$$a_n = c_n + jd_n , \qquad (4.6)$$

$$Q_n = \frac{|s_n|}{2\sigma_n} , \qquad (4.7)$$

and
$$q_n = \frac{\omega_n}{\sigma_n} = \sqrt{4Q_n^2 - 1} , \qquad (4.8)$$

where the residues a_n are defined by (3.13) and where Q_n are the quality factors of the poles s_n.

The conjugate pole-pair impedances $\hat{Z}_n(s)$, defined in (3.43), can also be written in the form (4.1) with the only difference that the residues a_n are given by (3.38) and the poles are, of course, the open-circuit poles. In what follows we deal specifically with the driving-point admittance function (4.1). However, all conclusions

hold also for the impedance function $\hat{Z}_n(s)$. The circuits which realize $\hat{Z}_n(s)$ are just the duals of the circuits for $\hat{Y}_n(s)$.

The necessary (but not sufficient) condition for the physical realizability of $\hat{Y}_n(s)$ is that the denominator coefficients of (4.1) be positive and that the numerator coefficients be non-negative. This requirement leads to the following restriction on the residue location if the unmodified pole modules are used:

$$c_n \geq 0 \tag{4.9a}$$

and

$$c_n - d_n q_n \geq 0 \quad . \tag{4.9b}$$

If the modified pole modules are employed, the conditions are

$$d_n q_n - c_n \geq 0 \tag{4.10a}$$

and

$$c_n(2Q_n^2 - 1) + d_n q_n \geq 0 \quad . \tag{4.10b}$$

The following discussion can be simplified considerably by assuming

$$Q_n > \frac{1}{\sqrt{2}} \cong 0.707 \quad . \tag{4.11}$$

This assumption does not seem to be restrictive since the dominant poles of all structures considered so far satisfy (4.11). Even the dominant poles of a sphere, which is an extremely low-Q structure, satisfy $Q_n \geq 1$. Assuming that (4.11) holds, (4.10) can be rewritten as

$$-\frac{q_n}{2Q_n^2 - 1} \leq \frac{c_n}{d_n} \leq q_n \tag{4.12a}$$

and

$$d_n \geq 0 \quad . \tag{4.12b}$$

81

The driving-point admittance function $\hat{\tilde{Y}}_n(s)$ is physically realizable if it is positive real (PR) [*Brune*, 1931], *i.e.*, if it satisfies the following conditions:

1. $Re\{\hat{\tilde{Y}}_n(s)\} > 0$ for $Re\{s\} > 0$; and

2. $\hat{Y}_n(s)$ is real when s is real.

Since it is extremely difficult to apply these conditions directly, the following equivalent requirements, which are easier to check, can be employed:

A. $\hat{Y}_n(s)$ cannot have any poles or zeros in the right half of the complex frequency plane;

B. any $j\omega$-axis poles of $\hat{\tilde{Y}}_n(s)$ must be simple and have positive real residues; and

C. $Re\{\hat{\tilde{Y}}_n(j\omega)\} \geq 0$ for all ω.

In the case of the biquadratic function (4.1) the conditions A and B above are automatically satisfied if (4.9) and (4.12) hold, respectively, for the case of unmodified and modified pole modules. It only remains to check the condition C.

The behavior of $Re\{\hat{\tilde{Y}}_n(j\omega)\}$ can be investigated with the help of the function

$$\tilde{F}_n(s) = \frac{1}{2}\left[\hat{\tilde{Y}}_n(s) + \hat{\tilde{Y}}_n(-s)\right] \tag{4.13}$$

which on the $j\omega$ axis is equal to the real part of $\hat{\tilde{Y}}_n(s)$ there [*Guillemin*, 1977]. For the unmodified pole modules case $\tilde{F}_n(s)$ has the form

$$F_n(s) = \frac{(C_n D_n - B_n E_n)s^2 + C_n F_n}{D_n^2 s^4 + (2D_n F_n - E_n^2)s^2 + F_n^2} . \tag{4.14}$$

In addition to a double zero at infinity this function has two zeros given by

82

$$s_o = \pm \sqrt{\frac{C_n F_n}{B_n E_n - C_n D_n}} \quad . \tag{4.15}$$

If the zeros are real, *i.e.*, if

$$B_n E_n - C_n D_n \geq 0 \tag{4.16}$$

the pole-zero pattern of $\tilde{F}_n(s)$ is that shown in Figure 4.3(a) and the corresponding behavior of $\text{Re}\{\hat{\tilde{Y}}_n(j\omega)\}$ is that shown in Figure (4.3(b)).[1] If the condition (4.16) is violated, the zeros (4.15) become purely imaginary, as shown in Figure 4.3(c), and the character of the real part of $\hat{\tilde{Y}}_n(j\omega)$ changes to that shown in Figure 4.3(d). It is evident from this figure that in this case there is a negative excursion in the real part of $\hat{\tilde{Y}}_n(s)$ on the $j\omega$-axis, and the condition C is violated. Hence, (4.16) is a necessary condition for the PR-ness of (4.1) for the case of unmodified pole modules. Expressed in terms of the SEM parameters this condition takes the form

$$c_n + d_n q_n \geq 0 \quad . \tag{4.17}$$

Combining (4.9) and (4.17) yields

$$\frac{c_n}{|d_n|} \geq q_n \tag{4.18}$$

which is, therefore, the necessary and sufficient condition for the physical realizability of the unmodified pole pair admittances. This condition was stated previously by *Guillemin* [1977].

For the modified pole modules, $\tilde{F}_n(s)$ takes the form

---

[1] If (4.16) is satisfied with the equality sign, ˄the zeros (4.12) move to infinity. However, the character of $\text{Re}\{\tilde{Y}_n(j\omega)\}$ is still that shown in the Figure 4.3(b).
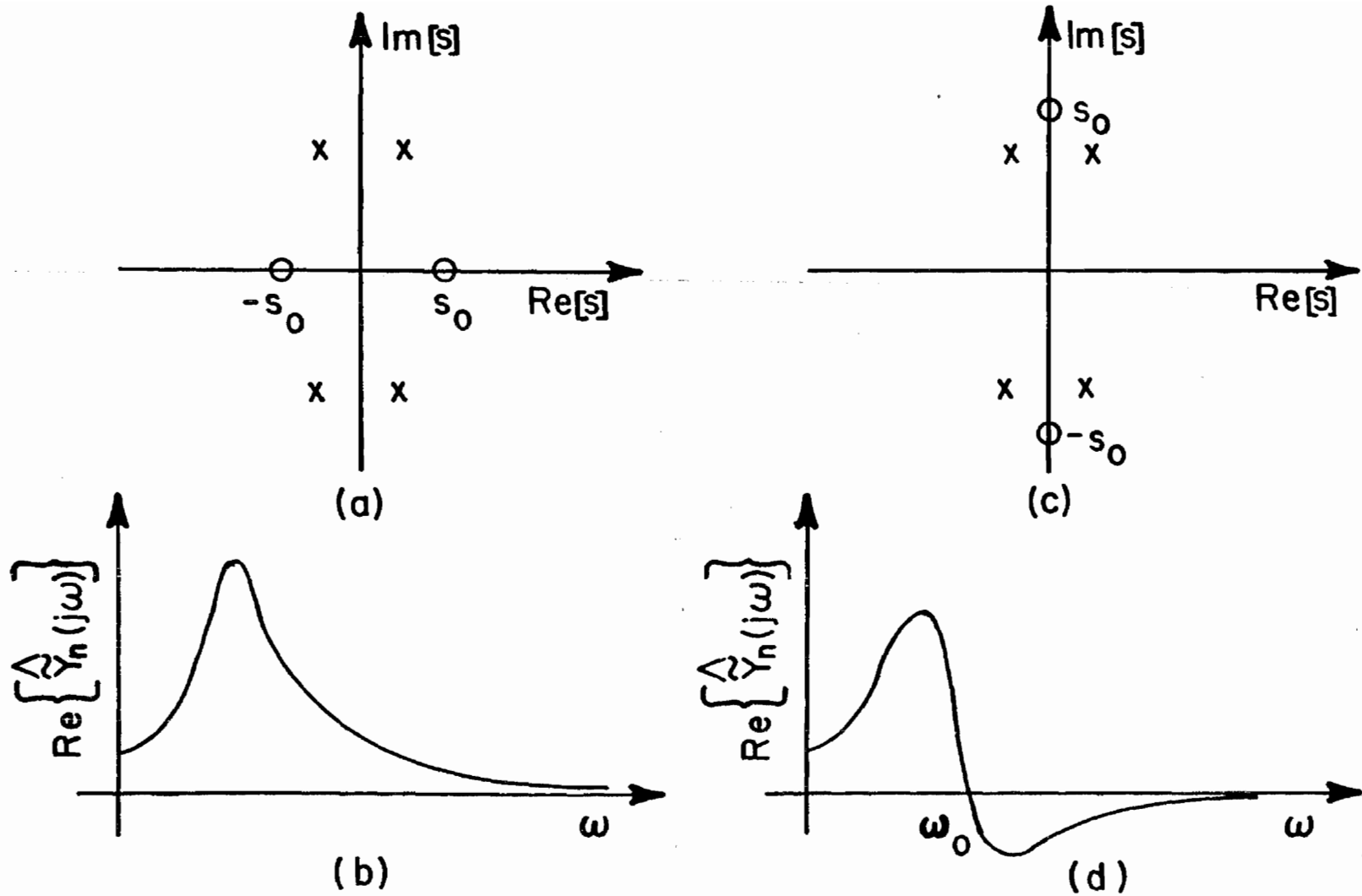
Figure 4.3 Pole-zero patterns of the even-part function of the unmodified pole module and the corresponding $j\omega$-axis behavior of the real part.

$$\tilde{F}_n(s) = s^2 \frac{A_n D_n s^2 + (A_n F_n - B_n E_n)}{D_n^2 s^4 + (2D_n F_n - E_n^2) s^2 + F_n^2} \quad . \tag{4.19}$$

This function has a double zero at the origin and a pair of zeros given by

$$s_o = \pm \sqrt{\frac{B_n E_n - A_n F_n}{A_n D_n}} \quad . \tag{4.20}$$

If the condition

$$B_n E_n - A_n F_n \geq 0 \tag{4.21}$$

is satisfied, the pole-zero pattern of $\tilde{F}_n(s)$ and the character of the real part of $\hat{\tilde{Y}}_n(j\omega)$ are that shown in Figure 4.4(a) and (4.4(b)), respectively. If the condition (4.21) is violated, the pole-zero pattern of $\tilde{F}_n(s)$ and the character of the real part become that shown in Figure 4.4(c) and (4.4(d)), respectively. Again in this case, there is a negative excursion of the real part on the $j\omega$-axis. Hence, (4.21) is a necessary condition for the realizability of (4.1) in the modified pole-pair admittances case. This condition may be written in terms of the poles and residues as

$$c_n(3Q_n^2 - 1) - d_n(Q_n^2 - 1)q_n \geq 0 \tag{4.22}$$

or, through the use of (4.11) and (4.12a) as

$$\frac{c_n}{d_n} \geq \frac{Q_n^2 - 1}{3Q_n^2 - 1} q_n \quad . \tag{4.23}$$

Combining (4.12) and (4.23) gives the necessary and sufficient condition for the physical realizability of the modified pole-pair admittances as

$$\frac{Q_n^2 - 1}{3Q_n^2 - 1} q_n \leq \frac{c_n}{d_n} \leq q_n \tag{4.24a}$$

85
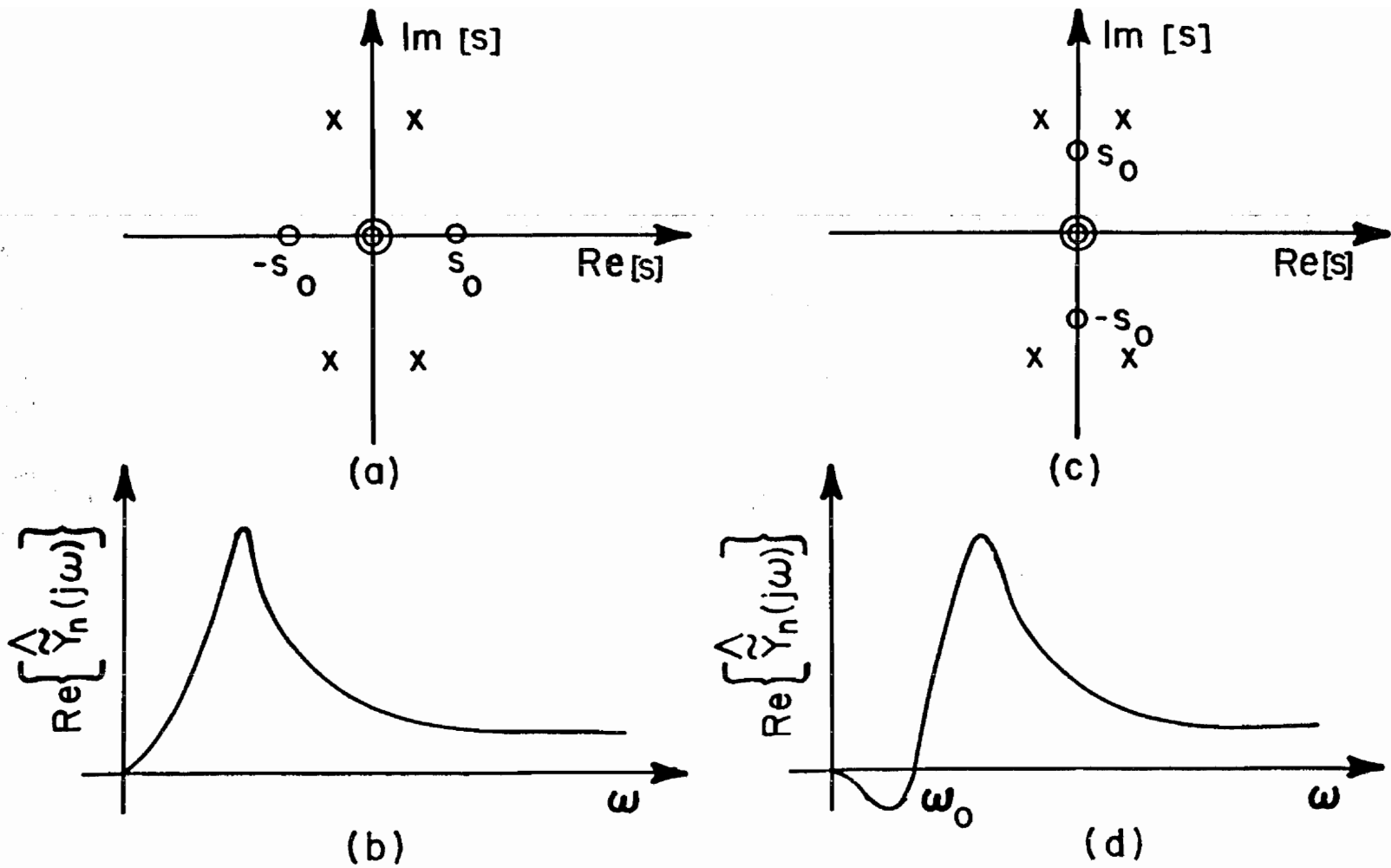
Figure 4.4 Pole-zero patterns of the even-part function of the modified pole module and the corresponding jω-axis behavior of the real part.

with

$$d_n \geq 0 \quad . \tag{4.24b}$$

If $Q_n \gg 1$, which is satisfied for most dominant poles of highly-resonant structures, the first condition above is given approximately by

$$\frac{2}{3} Q_n \leq \frac{c_n}{d_n} \leq 2Q_n. \tag{4.25}$$

The conditions for realizability of the unmodified and modified pole-pair modules can be interpreted geometrically in the a_n-plane as shown in Figure 4.5. If the residue a_n falls into region I, the unmodified pole-pair admittance is realizable; if it falls in region II, the modified pole-pair admittance is realizable; if the residue lies outside the regions I and II, neither form is realizable.

The realizability conditions for the modified pole-pair admittances were given previously by *Streable and Pearson* [1981] in a form not amenable to any geometrical interpretation. Similar conditions derived by *Baum and Singaraju* [1980] are necessary but not sufficient.

If the PR-ness conditions are satisfied, the unmodified and modified pole-pair admittances can be synthesized by a continued-fraction expansion [*Matthaei*, 1954; *Michalski and Pearson*, 1979] in a form shown in Figures 4.6 and 4.7, respectively. (The index n on the coefficients of (4.1) is dropped in the circuits given in Figures 4.6 and 4.7, and other figures in this chapter.) It should be noted that two equivalent realizations are possible in each case.

4.3 Synthesis of Approximate Driving-Point Circuits

It has been found that for most poles of the thin-wire dipole and loop antennas, as well as the spherical antenna, the residue a_n falls outside the regions I and II of Figure 4.5, *i.e.*, the pole-pair
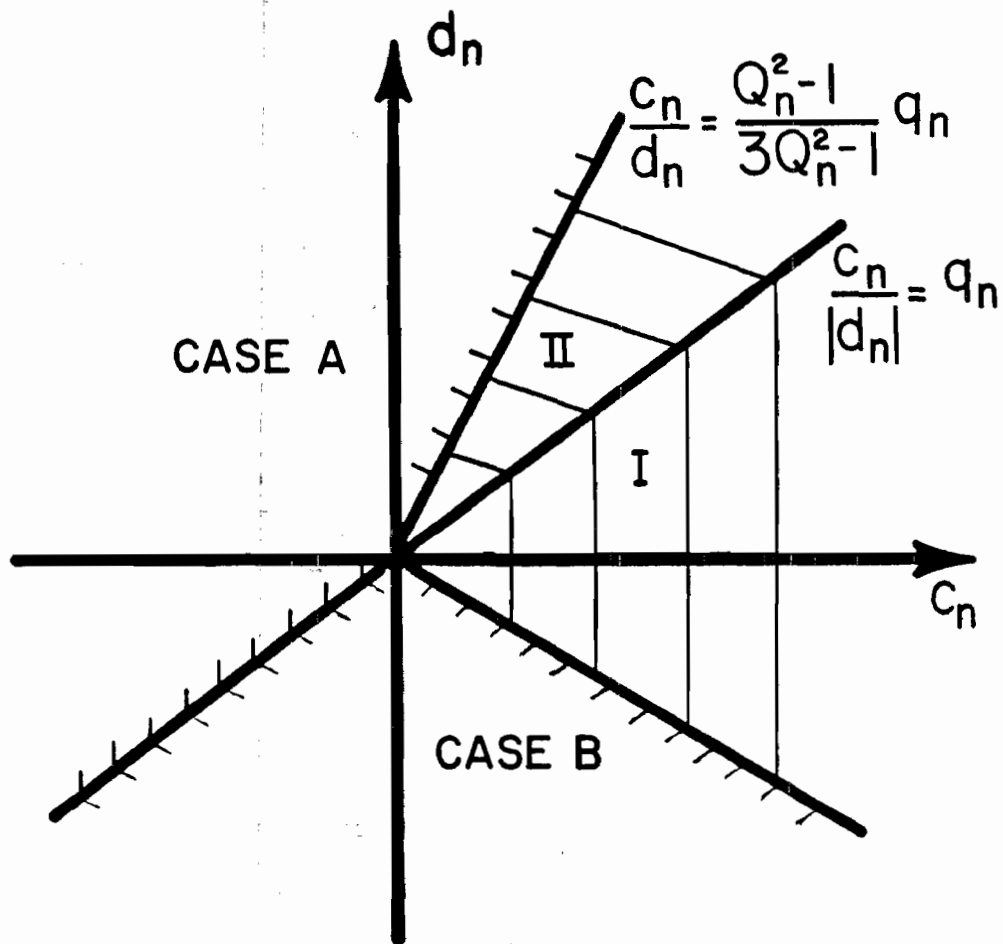
Figure 4.5 Geometrical interpretation of the realizability conditions for the modified and unmodified pole-pair admittances.

$$\frac{Q}{B^2} \leq \frac{F}{C} \qquad\qquad \frac{Q}{B^2} > \frac{F}{C}$$

(a)

$$L_1 = \frac{D}{B} \qquad R_1 = \frac{Q}{B^2}$$

$$C_1 = \frac{B^3}{B^2 F - QC} \qquad R_2 = \frac{F}{C} - \frac{Q}{B^2}$$

(c)

$$L_1 = \frac{D}{B} \qquad R_1 = \frac{F}{C}$$

$$L_2 = \frac{QC - B^2 F}{BC^2} \qquad R_2 = \frac{Q}{B^2} - \frac{F}{C}$$

(b)

$$L_1 = \frac{D}{B} \qquad C_1 = \frac{B^2 F - CQ}{BF^2}$$

$$R_1 = \frac{F}{C} \qquad R_2 = \frac{FQ}{B^2 F - CQ}$$

(d)

$$L_1 = \frac{D}{B} \qquad L_2 = \frac{Q^2}{CQ - B^2 F}$$

$$R_1 = \frac{Q}{B^2} \qquad R_2 = \frac{QF}{CQ - B^2 F}$$
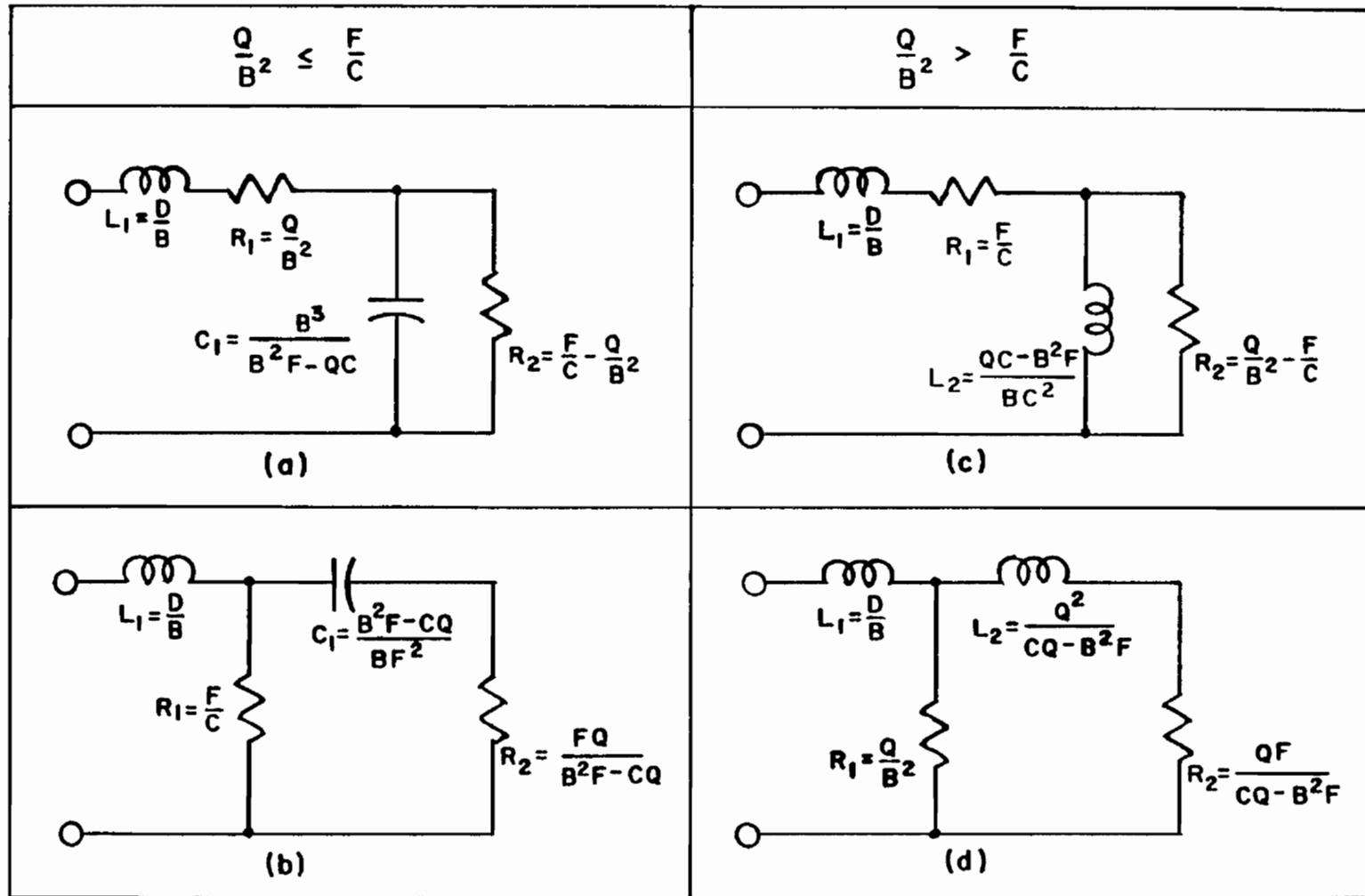
Figure 4.6 Practical realizations of the pole-pair admittance function when the residue lies in region I of Figure 4.5.   (Q = BE–CD)
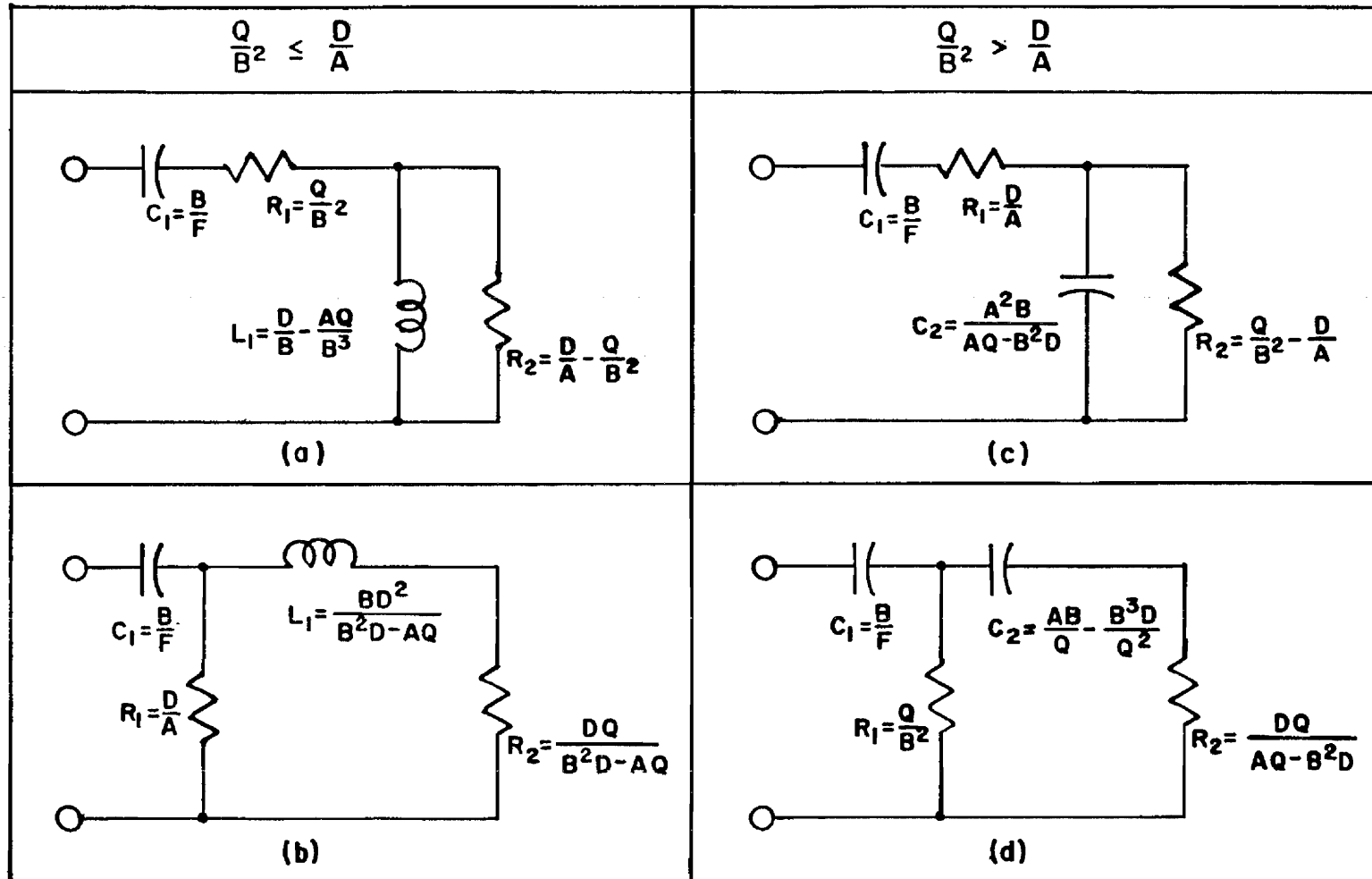
Figure 4.7 Practical realizations of the pole-pair admittance function when the residue lies in region II of Figure 4.5. (Q = BE-AF)

admittance is, in most cases, not physically realizable. This manifests
itself as a negative excursion in the real part of the driving-point
function on the $j\omega$-axis, as discussed in Section 4.2. It has been
observed, however, that in the case of modified pole modules this
negative excursion is in most cases negligible, or at least small, in
comparison with the value of the real part near the resonance. Thus,
if a small conductance G_n is added $\hat{\tilde{Y}}_n(s)$, the resulting function can be
rendered PR without introducing appreciable error. This procedure is
called a real-part padding by *Guillemin* [1977] and was first applied
in the present context by *Streable and Pearson* [1981] in synthesizing
driving-point equivalent circuits for the thin-wire dipole and loop
antennas. It should be noted that neither the poles nor the residues
are affected in the padding process. Only the zeros of the pole-pair
module are changed.

The amount of padding G_n which must be added to a pole-pair
admittance, so that the condition C of Section 4.2 is satisfied,
can be found explicitly in terms of the poles and residues to be

$$G_n = \frac{Q_n(2Q_n|a_n| + d_n - c_n q_n)}{q_n|s_n|} \tag{4.26}$$

for the unmodified pole-pair module, and

$$G_n = \frac{2Q_n^3|a_n| - d_n(3Q_n^2 - 1) - c_n(Q_n^2 - 1)q_n}{Q_n|s_n|q_n} \tag{4.27}$$

for the modified module. The numerator coefficients of the padded
pole-pair admittance (4.1) can be expressed in terms of the poles and
residues as follows:

$$A_n = \frac{Q_n(2Q_n|a_n| + d_n - c_n q_n)}{q_n|s_n|^2} , \tag{4.28a}$$

91

$$B_n = \frac{2Q_n|a_n| + d_n + c_n q_n}{q_n|s_n|} \, , \tag{4.28b}$$

and

$$C_n = \frac{2Q_n^3|a_n| - c_n(Q_n^2 - 1)q_n - d_n(3Q_n^2 - 1)}{q_n Q_n} \, . \tag{4.28c}$$

The denominator coefficients are not affected and are given by (4.3). It should be noted that after padding all coefficients of the biquadratic function (4.1) are nonzero, which makes the synthesis of it more difficult.

It can be shown [*Foster*, 1955] that the necessary and sufficient condition for the physical realizability of (4.1) is

$$\left(\sqrt{A_n F_n} - \sqrt{C_n D_n} \right)^2 \leq B_n E_n \, . \tag{4.29}$$

It is easy to see that this condition is consistent with (4.16) in the case when $A_n = 0$, and with (4.21) when $C_n = 0$. The padded pole-pair admittance is a minimum-real-part function, *i.e.*, the real part is zero at some finite frequency [*Balabanian*, 1958]. For such functions (4.29) is satisfied with the equality sign, *i.e.*,

$$\sqrt{A_n F_n} - \sqrt{C_n D_n} = \pm \sqrt{B_n E_n} \, . \tag{4.30}$$

It appears [*Michalski and Pearson*, 1979] that the only general synthesis methods which can be applied in this case are the Brune method [*Brune*, 1931] and the Bott-Duffin method [*Bott and Duffin*, 1949]. The synthesis of (4.1) by these methods is described in considerable detail in [*Michalski and Pearson*, 1979]. Here, we quote only the principal results.

The Brune network realizing (4.1) is shown in Figure 4.8 with

explicit expressions for the element values in terms of the coefficients

of (4.1). The Brune network is simple and can be successfully used

for analysis purposes. It is less attractive for a physical realization,

because of the presence of a unity-coupled transformer. Even a slight

deviation of the coupling coefficient from unity gives rise to an

additional zero of $\hat{\hat{Y}}_n(s)$ at infinity. This does not seem to have a

very drastic effect on the behavior of the function, however.

An application of the Bott-Duffin procedure to (4.1) results

in two different network topologies depending on the sign on the right

hand side of (4.30). For the "+" sign the network shown in Figure

4.9(a) results, whereas for the "-" sign the network in Figure 4.9(b)

is applicable. These two situations will be referred to as cases A

and B, respectively. An explicit network for the case B (or, rather,

the dual of it) was given previously by *Foster* [1955]. Note that the

Bott-Duffin networks are in a form of a balanced bridge, *i.e.*, the

points "A" and "B" in Figures 4.9(a) and 4.9(b) are at the same potential,

and any impedance (even a short-circuit) can be inserted between them

without affecting the terminal admittance. This fact can be used to

reduce by one the number of reactive elements by inserting a capacitor

or an inductor of a proper value into the bridge arm, and performing

a delta-wye or a wye-delta transformation. The resulting networks for

the two cases above are shown in Figure 4.10 and 4.11. Again, the

explicit reduced networks for the case B were given previously by

Foster [1955].

Even in the simplified form the Bott-Duffin networks are rather

complicated. They are generally considered unattractive from the point
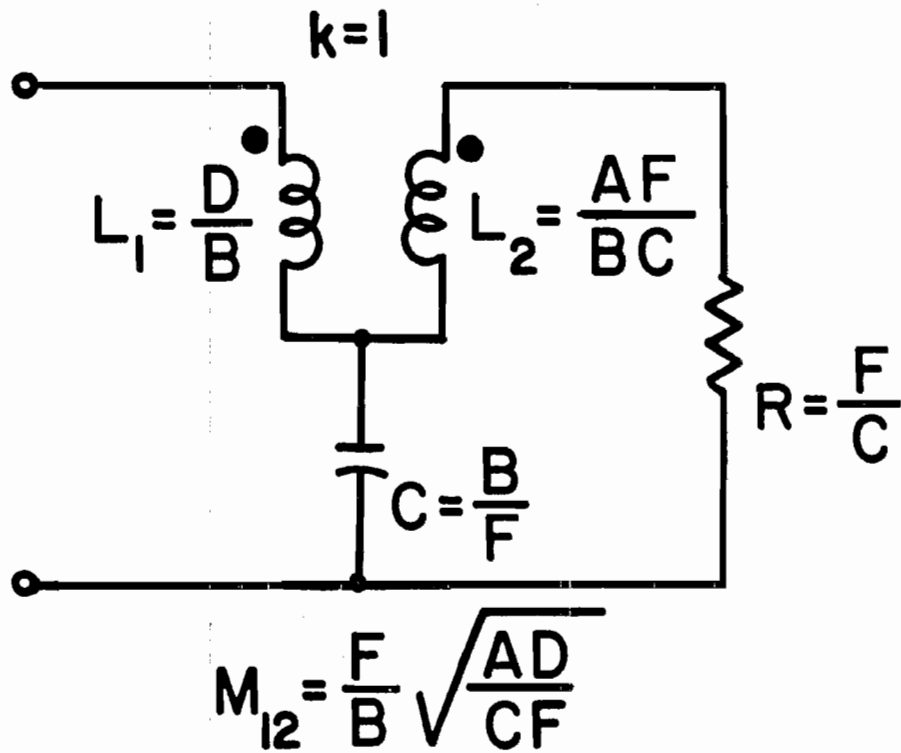
Figure 4.8 Brune realization of the padded pole-pair admittance
function.
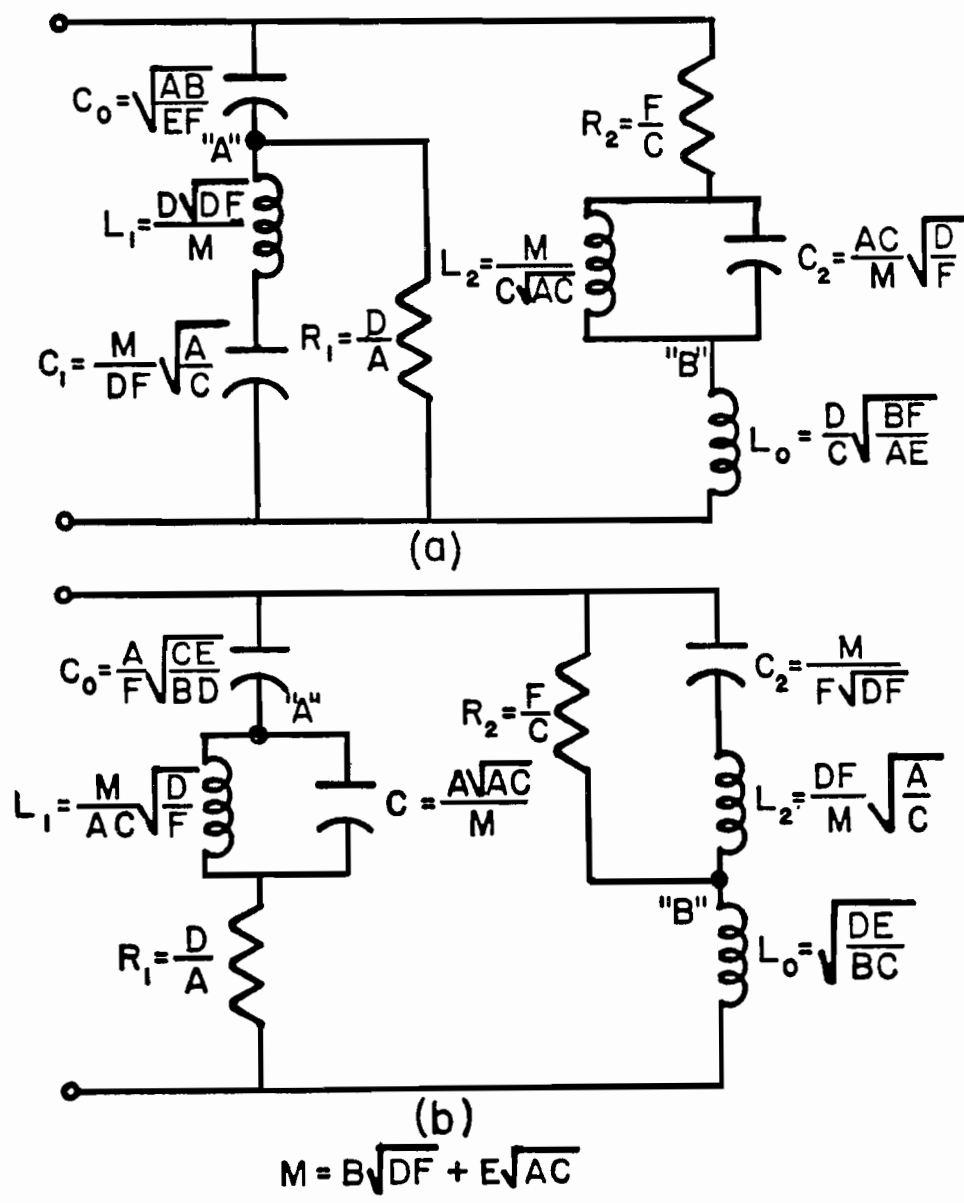
Figure 4.9   Bott-Duffin realizations of the padded pole-pair
admittance function for (a) case A and (b) case B.

$C_o = \sqrt{\dfrac{AB}{EF}}$

$R_2 = \dfrac{F}{C}$

$C_2 = \dfrac{AC}{R}\sqrt{\dfrac{DE}{AF}}$

$L_1 = \dfrac{RD\sqrt{BD}}{M^2}$

$R_1 = \dfrac{D}{A}$

$L_o = \dfrac{R}{C\sqrt{CE}}$

$C_1 = \dfrac{M^2}{RCD}\sqrt{\dfrac{AC}{BF}}$

$R = F\sqrt{BD} + E\sqrt{CE}$ (a)

$C_o = \sqrt{\dfrac{AB}{EF}}$

$R_2 = \dfrac{F}{C}$

$L_2 = \dfrac{M^2}{QC\sqrt{EC}}$

$C_2 = \dfrac{QAC}{M^2}\sqrt{\dfrac{DE}{AF}}$

$R_1 = \dfrac{D}{A}$

$C_1 = \dfrac{Q}{CD}\sqrt{\dfrac{AC}{BF}}$

$L_o = \dfrac{D\sqrt{BD}}{Q}$

$Q = A\sqrt{CE} + B\sqrt{BD}$ (b)
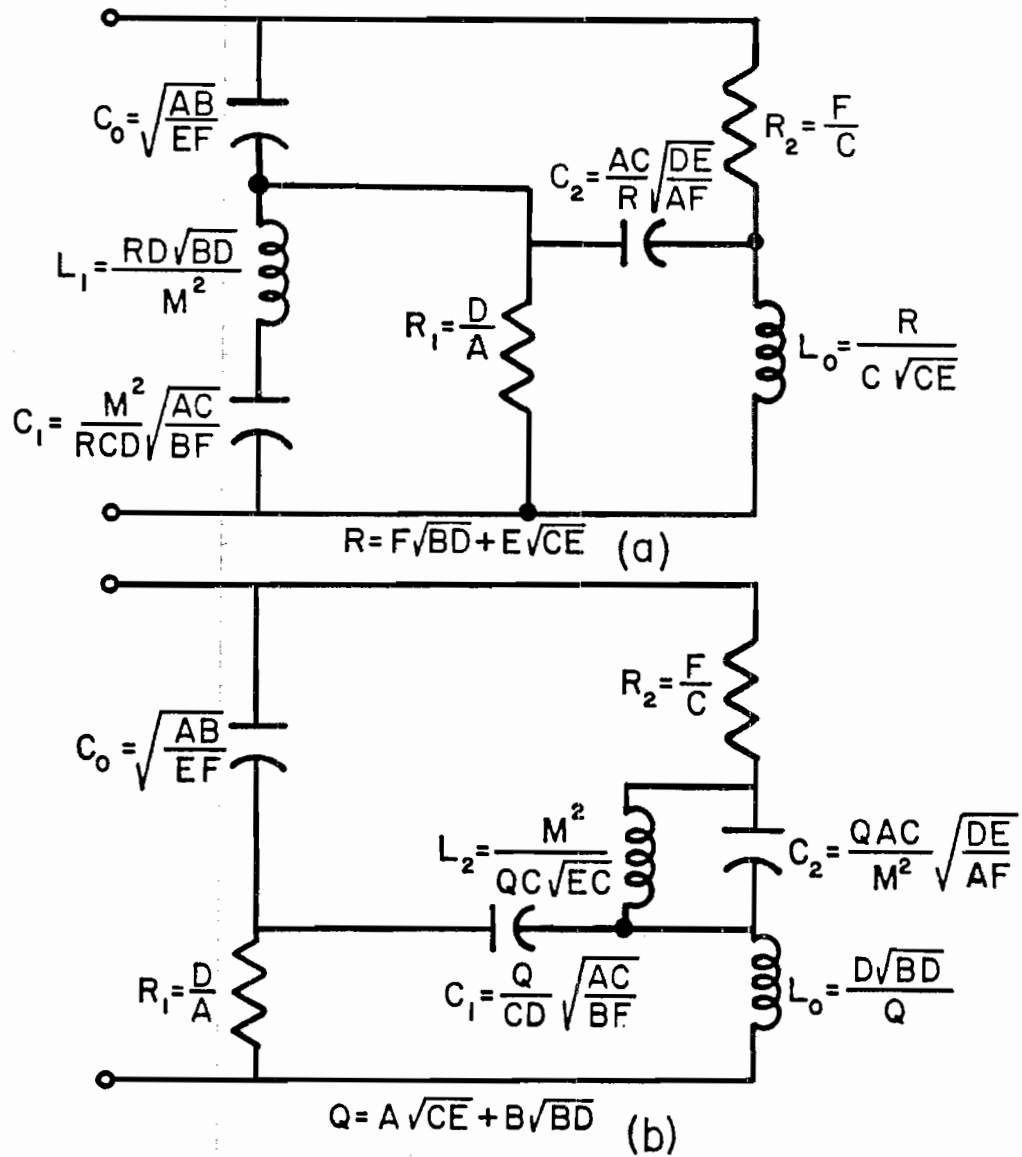
Figure 4.10 Modified Bott-Duffin networks for the padded pole-pair admittance function -- case A.

96

$$C_0 = \frac{A\sqrt{AE}}{Q}$$

$$R_2 = \frac{F}{C}$$

$$C_2 = \frac{M^2}{QF\sqrt{BF}}$$

$$L_2 = \frac{QAF}{M}\sqrt{\frac{BD}{AC}}$$

$$R_1 = \frac{D}{F}$$

$$L_1 = \frac{Q}{AC}\sqrt{\frac{CD}{EF}}$$

$$L_0 = \sqrt{\frac{DE}{BC}}$$

$$Q = D\sqrt{BF} + E\sqrt{AE}$$

(a)

$$C_0 = \frac{R}{F\sqrt{BF}}$$

$$L_2 = \frac{AF}{R}\sqrt{\frac{BD}{AC}}$$

$$R_2 = \frac{F}{C}$$

$$L_1 = \frac{M^2}{RAC}\sqrt{\frac{CD}{EF}}$$

$$C_1 = \frac{RA\sqrt{AE}}{M^2}$$

$$L_0 = \sqrt{\frac{DE}{BC}}$$

$$R_1 = \frac{D}{A}$$

$$R = B\sqrt{DF} + E\sqrt{AC}$$

(b)
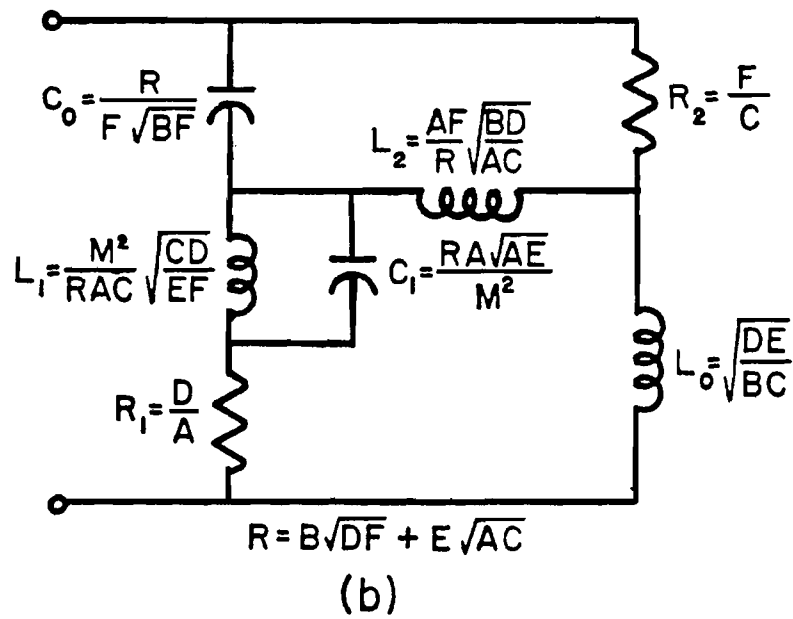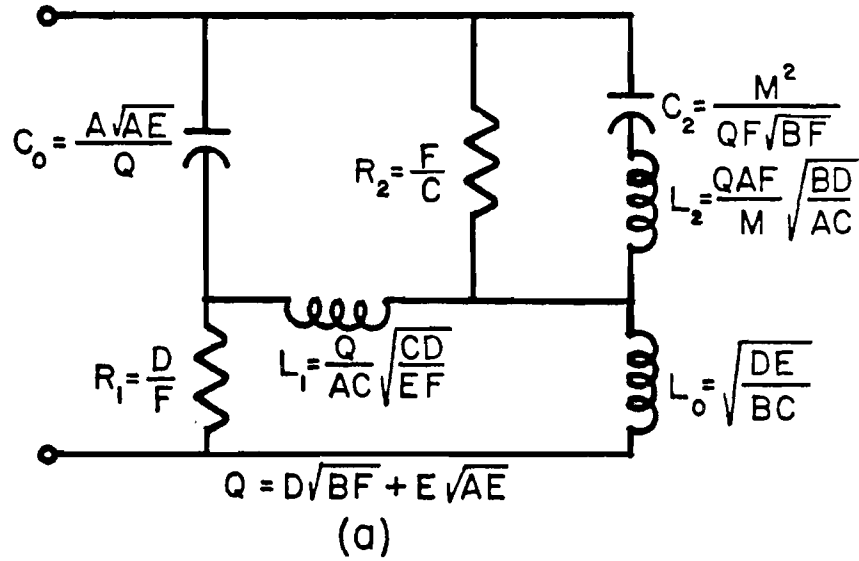
Figure 4.11 Modified Bott-Duffin networks for the padded pole-pair admittance function -- case B.

97

of view of sensitivity, as element variations from their nominal values give rise to three additional poles and zeros in the driving-point function.

In order to determine which of the two cases A or B is applicable for a given set of SEM parameters, it is helpful to consider the expression

$$A_n F_n - C_n D_n = \frac{d_n q_n - c_n}{|s_n| Q_n} \quad . \tag{4.31}$$

It is easy to see from (4.30) that the case A arises when (4.31) is positive; if it is negative, the case B is applicable. This can be summarized as follows:

$$d_n q_n - c_n \begin{cases} \geq 0 & , \quad \text{case A} \\ < 0 & , \quad \text{case B} \end{cases} \quad . \tag{4.32}$$

The geometrical interpretation of this condition in the a_n-plane is given in Figure 4.5 with the regions of applicability of the two cases explicitly indicated.

It can be shown that the resistances R_2 in Figure 4.9(a) and R_1 in Figure 4.9(b) are reciprocals of G_n - the amount of padding used. Thus, if the pole-pair admittance is almost PR, so that the padding is negligible, these resistances are large and the entire circuit legs in series with them can be neglected. The Bott-Duffin networks simplified in this way are shown in Figure 4.12. The approximate pole-pair module for the case A (Figure 4.12(a)) was first derived by *Streable and Pearson* [1981]. They did not give explicit expressions for the element values, however.

$$C_0 = \sqrt{\frac{AB}{EF}}$$

$$L_1 = \frac{D\sqrt{DF}}{M}$$

$$R_1 = \frac{D}{A}$$

$$C_1 = \frac{M}{DF}\sqrt{\frac{A}{C}}$$

$$\sqrt{AF} - \sqrt{CD} = +\sqrt{BE}$$

(a)

$$L_0 = \sqrt{\frac{DE}{BC}}$$

$$L_1 = \frac{DF}{M}\sqrt{\frac{A}{C}}$$

$$R_2 = \frac{F}{C}$$

$$C_1 = \frac{M}{F\sqrt{DF}}$$

$$\sqrt{AF} - \sqrt{CD} = -\sqrt{BE}$$

(b)
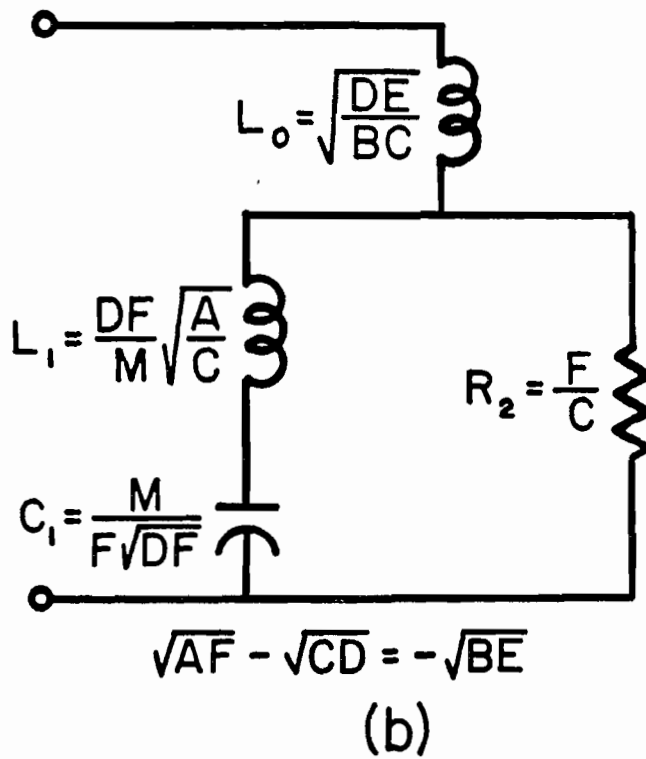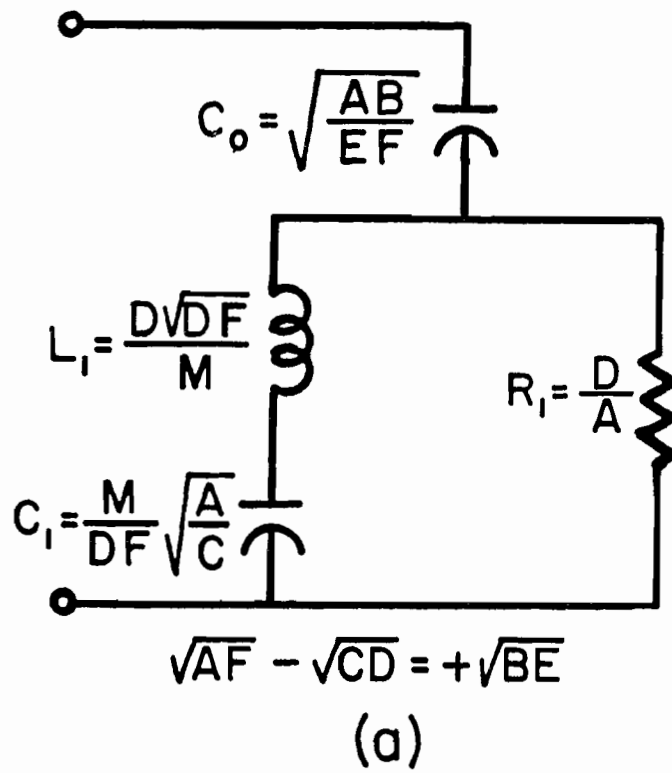
Figure 4.12 Simplified Bott-Duffin circuits approximating the padded
pole-pair admittance function in the case of negligible padding.
(a) circuit for case A and (b) circuit for case B.

99

In all cases considered to date (the thin-wire dipole and loop antennas, the spherical antenna) only the case A has arisen. It seems, however, that this cannot be generalized, and situations where the case B is appropriate cannot be excluded *a priori*.

4.4 Voltage Transfer Function Synthesis

The voltage transfer function of the Norton network (3.24) and its Thévenin network counterpart (3.55) can both be written in the form

$$\hat{\tilde{T}}_n(s) = \frac{A_n s + B_n}{C_n s + D_n} \tag{4.33}$$

with the coefficients (which should not be confused with the coefficients of (4.1)) given by

$$A_n = \text{Re}\{a_n T_n\}, \tag{4.34a}$$

$$B_n = - \text{Re}\{a_n T_n s_n^*\}, \tag{4.34b}$$

$$C_n = c_n, \tag{4.34c}$$

and

$$D_n = \frac{|s_n|(c_n - d_n q_n)}{2Q_n} \tag{4.34d}$$

if the unmodified pole-pair modules are used, and by

$$A_n = \text{Re}\{a_n s_n^* T_n\},$$

$$B_n = - \text{Re}\{a_n s_n^{*2} T_n\},$$

$$C_n = \frac{|s_n|}{2Q_n}(d_n q_n - c_n), \tag{4.35c}$$

and

$$D_n = \frac{|s_n|^2}{2Q_n^2}\left[d_n q_n + c_n(2Q_n^2 - 1)\right] \tag{4.35d}$$

if the modified pole-pair modules are employed. In (4.34)-(4.35) a_n are the immittance residues given either by (3.13) for the Norton formulation, or by (3.38) for the Thévenin formulation. The source coefficients T_n are defined in these two cases by (3.21) and (3.50), respectively.

Before proceeding with the synthesis of (4.33), several comments are in order. First, note that the equivalent circuits transformations due to *Baum* [1976a] indicated in Figures 3.4 and 3.6 lead to very simple pole-pair voltage transfer functions which are bilinear in s. Without this transformation one would have to deal with biquadratic transfer functions, which would be a more difficult task. Second, note that each transfer network in Figures 4.1 and 4.2 is followed by a controlled source. The main purpose of these controlled sources is to provide the impedance buffering which is required because synthesis techniques do not exist which realize a given transfer function for a general, unspecified loading conditions. In addition, these controlled sources serve as amplifiers. The amplifier function is necessary because, in general, most synthesis techniques realize a given transfer function only to within a constant multiplier, with the expectation that the gain can be restored at a later stage.

The theory of transfer function synthesis is a vast and mature field [*e.g.*, *Balabanian*, 1958]. Fortunately, the function (4.33) is so simple that only a small part of the accumulated knowledge needs to be applied. Before attempting to synthesize (4.33) it is appropriate to quote some of the conditions which a general voltage transfer function, say $\tilde{T}(s)$, must satisfy in order to be physically realizable [*Balabanian*, 1958]. First of all, no poles of $\tilde{T}(s)$ can lie in the

right half plane. In addition, no poles of $\tilde{T}(s)$ can lie at zero or infinity. The zeros, however, can lie anywhere in the s plane. If all the zeros of $\tilde{T}(s)$ are confined to the left half plane, $\tilde{T}(s)$ is called a minimum-phase function; otherwise it is called a nonminimum-phase function. The conditions imposed on $\tilde{T}(s)$ depend on the network topology desired. Here we will seek a transformerless realization. Also, we will prefer an unbalanced (common ground) topology over a balanced (no common input and output terminals) realization, whenever possible. Following *Balabanian* [1958] we summarize these conditions as follows.

For unbalanced two-ports with no mutual inductance:

1. Transmission zeros may lie anywhere except on the positive real axis.

2. For real positive values of s, the value of the transfer function lies between 0 and 1. The maximum value of unity can be attained only at zero or infinity, or both.

3. The numerator coefficients of the transfer function are positive (or zero) and no greater than the corresponding denominator coefficients, assuming no cancellation of factors.

4. For a ladder network realization, which is a special form of an unbalanced network, the transmission zeros cannot lie in the right half plane.

For balanced two-ports with no mutual inductance:

1. Transmission zeros may lie anywhere, including the positive real axis.

2. For real positive values of s the value of the transfer function lies between -1 and +1. The extremities of the range can be attained only at zero or infinity, or both.

3. The numerator coefficients of the transfer function may be negative, but they are no greater in magnitude than the corresponding denominator coefficients, assuming no cancellation of factors.

As discussed above, for physical realizability one requires that the pole of (4.33) lie in the left half of the complex frequency plane. This is satisfied only if the denominator coefficients of (4.33) are of equal sign. In the unmodified pole module case this imposes the following restrictions on the location of the residue a_n:

$$\frac{d_n}{c_n} < \frac{1}{q_n} \quad . \tag{4.36}$$

The geometrical interpretation of this condition is given in Figure 4.13(a). The transfer function is realizable if the a_n lies in the shaded region of the figure. If the modified pole modules are employed, and (4.11) is satisfied, the residue location is restricted as follows:

$$-\frac{q_n}{2Q_n^2 - 1} < \frac{c_n}{d_n} \leq q_n \quad . \tag{4.37}$$

The realizability region associated with this condition is the shaded region in Figure 4.13(b).

The comparison of Figures 4.5 and 4.13 reveals that the voltage transfer function is always realizable if the associated pole-pair immittance function is realizable. If the pole-pair immittance is initially non-PR, $i.e.$, the residue falls outside the regions I and II of Figure 4.5 so that the padding procedure described in Section 4.3 is employed, the associated voltage transfer function is still realizable in at least one of the two forms: modified or unmodified. There is a region in the a_n-plane where the realizability regions of Figures 4.13(a) and 4.13(b) overlap, so that both forms could be realized. We have found that for all dominant poles of the thin-wire dipole and loop antennas the residues a_n fall into that part of the realizability
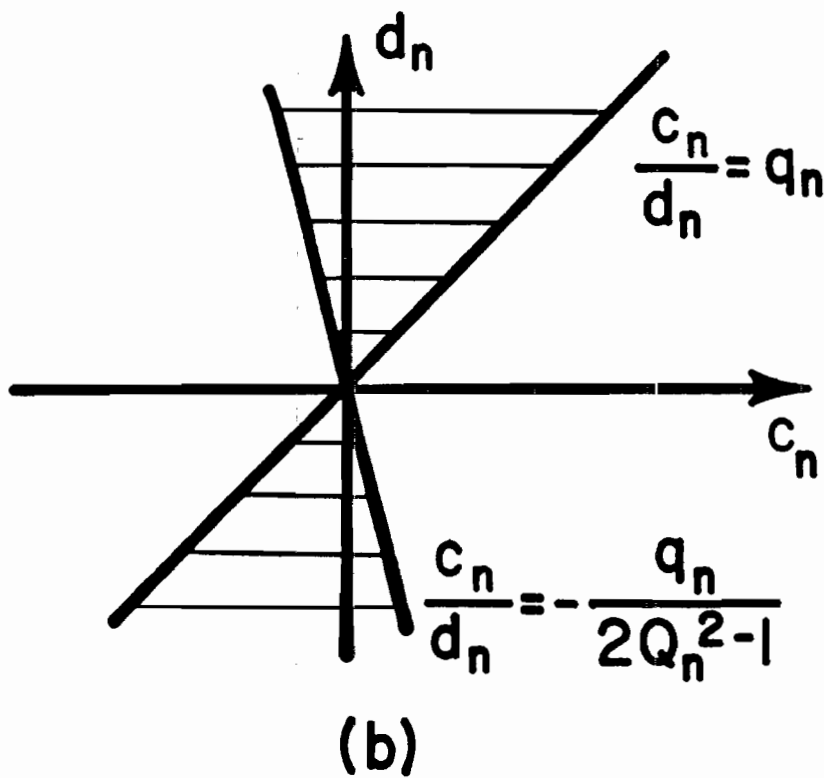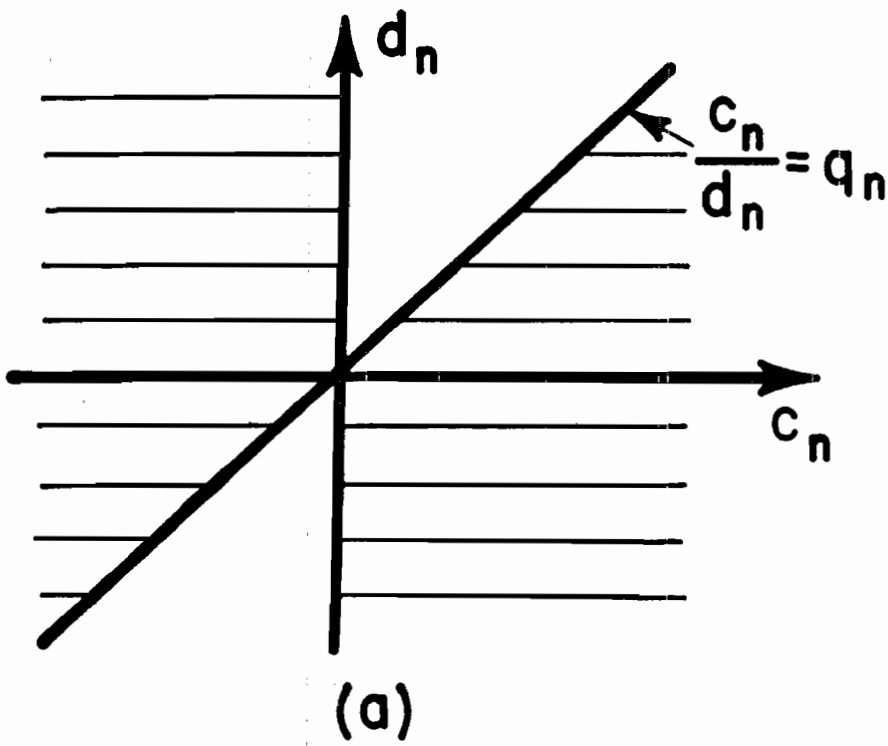
Figure 4.13 Regions of realizability (shaded) of the pole-pair voltage transfer function for (a) the unmodified and (b) modified pole modules.

region lying in the first quadrant of Figure 4.13(b), so that the modified form of the voltage transfer function is realizable.

For notational convenience the index n on the coefficients of (4.33) is dropped throughout the rest of this section. Also it is convenient to introduce a scaling factor k and rewrite (4.33) as

$$\hat{\tilde{T}}_n(s) = \frac{1}{k} \frac{kAs + kB}{Cs + D} = \frac{\tilde{z}_{12}}{\tilde{z}_{11}} = -\frac{\tilde{y}_{12}}{\tilde{y}_{22}} \tag{4.40}$$

where $\tilde{z}_{ij}$ and $\tilde{y}_{ij}$ denote, respectively, the open-circuit impedance parameters and the short-circuit parameters of the two-port [*Balabanian, 1958*]. If (4.40) is realizable, the coefficients C and D are of the same sign, as discussed above. It will be assumed here that they are positive, which can always be accomplished by multiplying the numerator and the denominator of (4.40) by -1. The following discussion can also be simplified if the sign of k is chosen such that kA is positive. Then it is only necessary to consider separately two situations: $kB \geq 0$ ($\hat{\tilde{T}}_n(s)$ is a minimum-phase function), and $kB < 0$ ($\hat{\tilde{T}}_n(s)$ is a nonminimum-phase function). In each case two circuit topologies are obtained depending on the choice of the impedance or admittance parameters representation in (4.40).

Case 1. $kB \geq 0$

In this case one can make the associations

$$\tilde{z}_{12} = kAs + kB \tag{4.41a}$$

and

$$\tilde{z}_{11} = Cs + D = (kAs + kB) + (C - kA)s + (D - kB) . \tag{4.41b}$$

To this set of parameters corresponds the RL ladder circuit shown in
Figure 4.14(a). This circuit is physically realizable if the value
of the unspecified constant k is restricted to

$$k \leq \min \left(\frac{C}{A} , \frac{D}{B} \right) .$$ (4.42)

It is easy to see that by choosing the maximum allowed value of k
one can eliminate either L_A or R_A from the circuit in Figure 4.14(a).

If the admittance representation is used in (4.40) one can
write

$$-\tilde{y}_{12} = kAs + kB$$ (4.43a)

and

$$\tilde{y}_{22} = Cs + D = (kAs + kB) + (C - kA)s + (D - kB) .$$ (4.43b)

This set of parameters can be realized by the RC ladder network shown
in Figure 4.14(b). This network is physically realizable if k satisfies
(4.42). Again, by a judicious choice of the value of k one can eliminate
either C_B or R_B.

Case 2. kB < 0

Since in this case the voltage transfer function has a positive
real zero, it cannot be realized in an unbalanced form [*Balabanian*,
1958]. Instead, one must resort to the symmetrical lattice topology
shown in Figure 4.15(a). If this network is unwrapped to the equivalent
form of Figure 4.15(b), it is recognized that the symmetrical lattice
is identical with a bridge network.

The lattice arm impedances $\tilde{Z}_a$ and $\tilde{Z}_b$ can be expressed in terms
of the open-circuit impedance parameters as
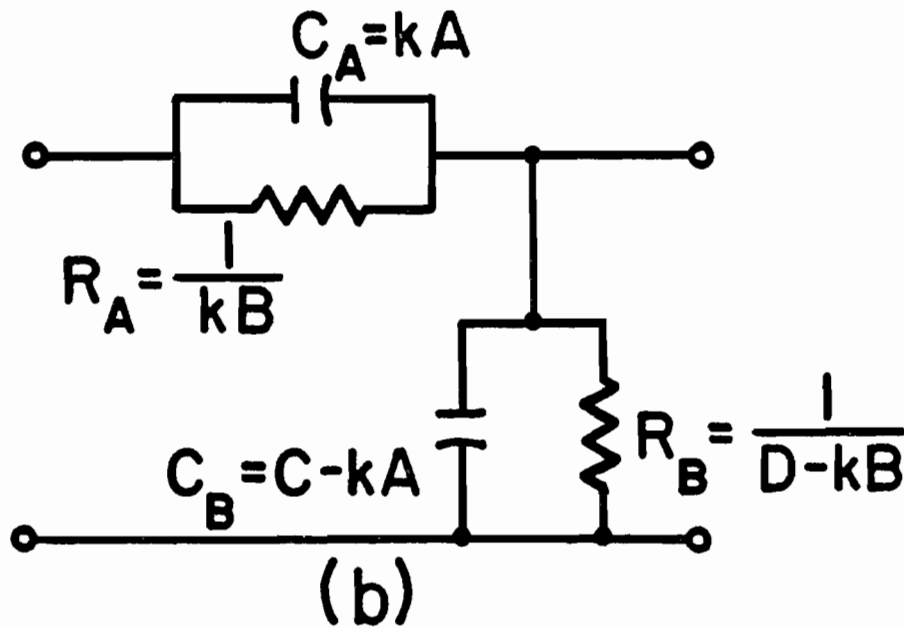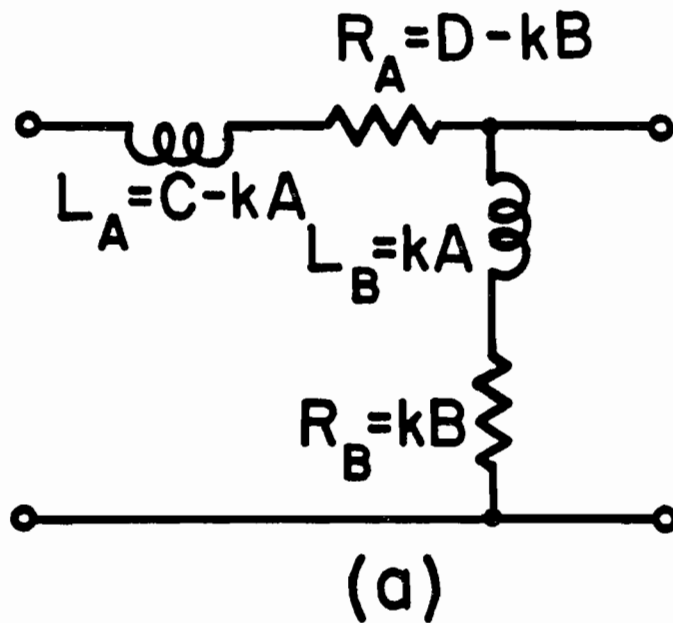
Figure 4.14 Ladder network realizations of (a) the RL and (b) RC type for the pole-pair voltage transfer function -- negative transmission zero case.

107
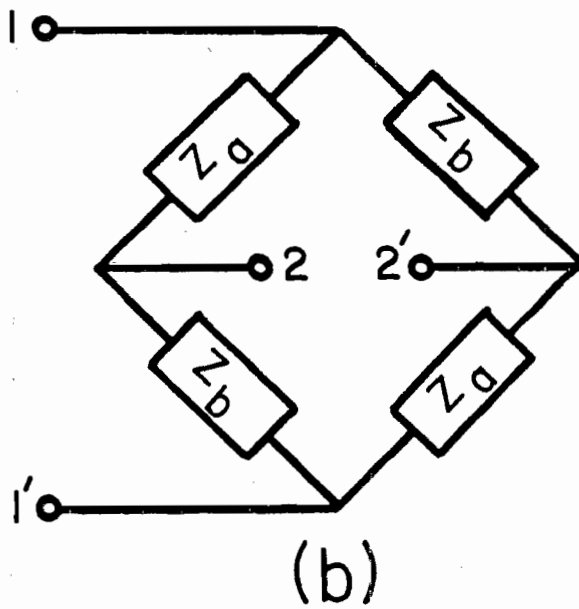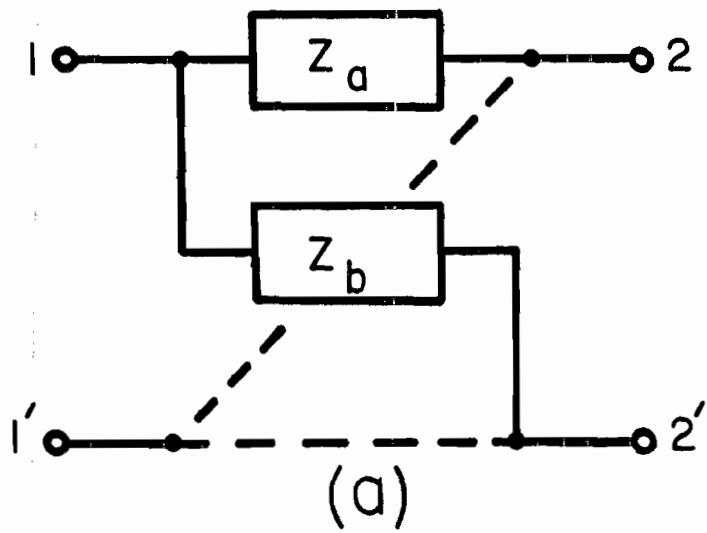
Figure 4.15 (a) Standard and (b) bridge form representation of the symmetrical lattice.

$$\tilde{Z}_a = \tilde{z}_{11} - \tilde{z}_{12} \qquad (4.44a)$$

and

$$\tilde{Z}_b = \tilde{z}_{11} + \tilde{z}_{12} \quad . \qquad (4.44b)$$

Alternatively, the lattice arm admittances $\tilde{Y}_a = 1/\tilde{Z}_a$ and $\tilde{Y}_b = 1/\tilde{Z}_b$ can be expressed in terms of the short-circuit parameters as

$$\tilde{Y}_a = \tilde{y}_{22} - \tilde{y}_{12} \qquad (4.45a)$$

and

$$\tilde{Y}_b = \tilde{y}_{22} + \tilde{y}_{12} \quad . \qquad (4.45b)$$

Using (4.41) in (4.44) gives

$$\tilde{Z}_a = (C - kA)s + (D - kB) \qquad (4.46a)$$

and

$$\tilde{Z}_b = (C + kA)s + (D + kB) \quad . \qquad (4.46b)$$

This set of parameters can be realized by the network shown in Figure 4.16(a). For physical realizability it is required that

$$k \leq \min\left(\frac{C}{A}, \ -\frac{D}{B}\right) \quad . \qquad (4.47)$$

By giving k the maximum value allowed by (4.47) one can make either L_A or R_B disappear.

In like fashion, using (4.43) in (4.45) gives

$$\tilde{Y}_a = (C + kA)s + (D + kB) \qquad (4.48a)$$

and

$$\tilde{Y}_b = (C - kA)s + (D - kB) \quad . \qquad (4.48b)$$

To this set of parameters corresponds the network shown in Figure 4.16(b). The value of k is still restricted by (4.47). Again, either
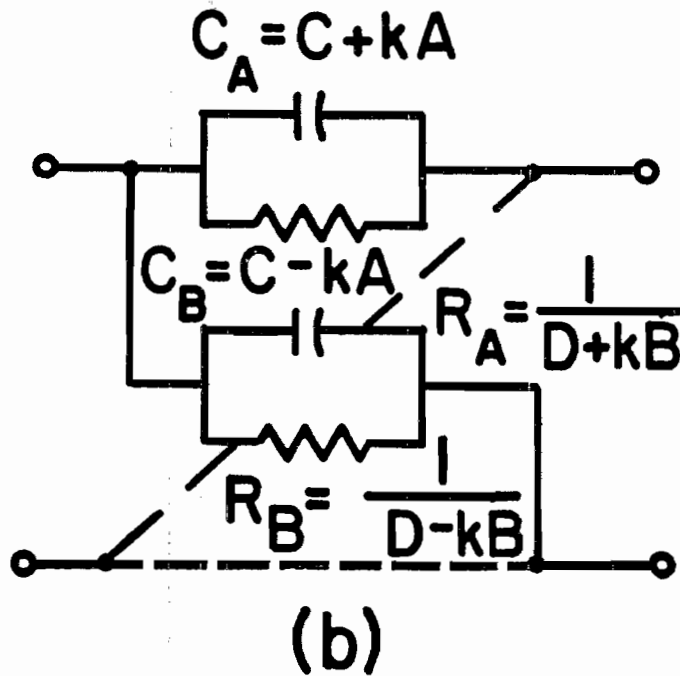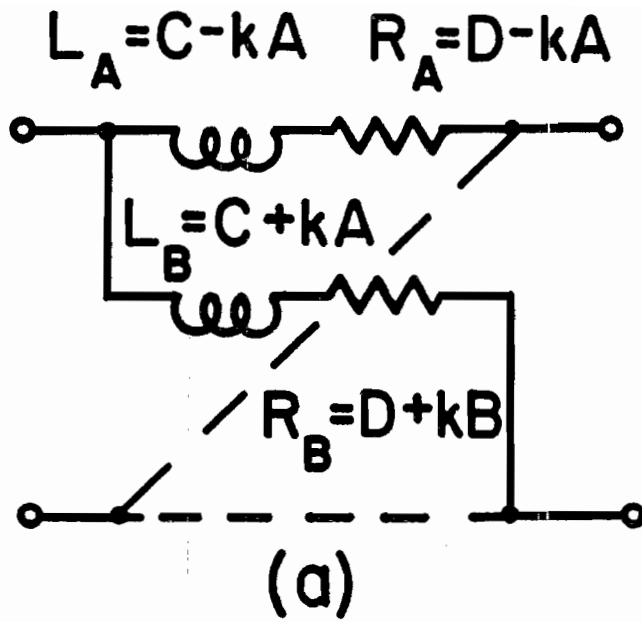
Figure 4.16 Symmetrical lattice realizations of (a) the RL and (b) RC type for the pole-pair voltage transfer function -- positive transmission zero case.

R_A or C_B can be removed by a judicious choice of the value of k.

The circuits given above do not realize the multiplicative factor 1/k in (4.40). The gain lost can be restored in the controlled source stage following each voltage transfer network. The amplification factor of this controlled source must have the value $\mu = 1/k$.

Still different realizations in the case when kB < 0 can be obtained by writing (4.40) as a product of an all-pass function[1] and a minimum-phase function as follows

$$\hat{T}_n(s) = \frac{1}{k} \frac{kAs + kB}{kA - kB} \cdot \frac{kAs - kB}{C + D} \quad . \qquad (4.49)$$

Now the all-pass function can be realized as a simple constant-resistance[2] LC lattice, and the minimum-phase function can be synthesized as a constant-resistance ladder [*Balabanian*, 1958]. A cascade connection of these two-ports realizes (4.49). This realization, however, is more complicated than the networks shown in Figure 4.16.

4.5 Conclusions

In this chapter simple procedures are developed for the synthesis of physically realizable active equivalent circuits for energy collecting structures from their SEM description. The general network topology is that shown in Figure 4.1 for the short-circuit boundary value problem (the Norton equivalent), or that shown in Figure 4.2 for the open-circuit boundary value problem (the Thévenin equivalent). These networks

---

[1] An all-pass function is defined as a transfer function whose zeros are all in the right half plane and whose poles are the negatives of its zeros.

[2] A constant-resistance two-port is defined as one whose driving-point impedance is equal to a constant R when the two-port is terminated in a resistance R.

have the form of a connection of simple modules associated with conjugate pole pairs of the structure. These pole-pair circuits are synthesized one at a time, so if the need arises the network can be easily expanded by adding more pole-pair modules without repreating the whole synthesis process. By using the network topologies of Figures 4.1 and 4.2 the synthesis process if reduced to the realization of a driving-point function biquadratic in s and a voltage transfer function bilinear in s. The realizability conditions and explicit circuit realizations are given for these functions. If the pole-pair driving-point function is initially nonrealizable, a simple padding procedure is described to synthesize an approximating network. It is shown that the pole-pair voltage transfer function can be always realized either in the form of a ladder circuit or of a symmetrical lattice circuit. Unfortunately, the applicability of each of the two topologies is dependent on the direction of arrival of the incident plane wave, so that the circuit topology may change when excitation conditions are changed. The equivalent network does not depend on the time history carried by the incident field, however. Also, the autonomic voltage source is connected to only one port, which is a desirable feature. As the Figures 4.1 and 4.2 indicate, the controlled sources could not be avoided. They can be implemented in practice with active devices which, however, usually can not sustain very high voltages.

In the next chapters the procedures developed here are used to synthesize practical equivalent circuits for the loop, dipole, and spherical antenna.

112

CHAPTER 5

EQUIVALENT CIRCUIT SYNTHESIS FOR A CIRCULAR LOOP

5.1 Introduction

In this chapter the procedures developed in Chapters 2-4 are
used to synthesize an SEM Norton-type, dominant pole-pair equivalent
circuit for a thin-wire loop antenna. The thin-wire circular loop
is one of the few structures for which an explicit solution for the
current can be found (subject to the thin-wire approximation). The
development presented here differs in details from the general theory
developed in Chapter 3 because of the occurrence of the eigenvalue
degeneracy in the present case.

The performance of the developed SEM equivalent circuits is
compared with responses obtained by the classical frequency domain—
inverse Fourier transform approach. The application of these circuits
to the analysis of antennas with nonlinear loads is demonstrated in
Appendix B.

5.2 Preliminary Theory

The geometry of the loop is defined in Figure 5.1. It is assumed
that the radius of the wire a is much smaller than the radius of the
loop $b(a \ll b)$ and that $\omega_{max} a/c \ll 1$, where $\omega = \omega_{max}$ is the largest
significant spectral component of the excitation. As a consequence,
it can be assumed that there is only a ϕ-component of the surface
current density, $i.e.$, $\tilde{\vec{J}}(\vec{r},s) = \tilde{J}_\phi(\vec{r},s)\hat{\phi}$, where $\hat{\phi}$ denotes the unit
vector in the ϕ direction, and that the current density is uniform around
the wire, $i.e.$, $\tilde{J}_\phi(\vec{r},s) = \tilde{J}_\phi(\phi,s)$. The total current can be defined as

113
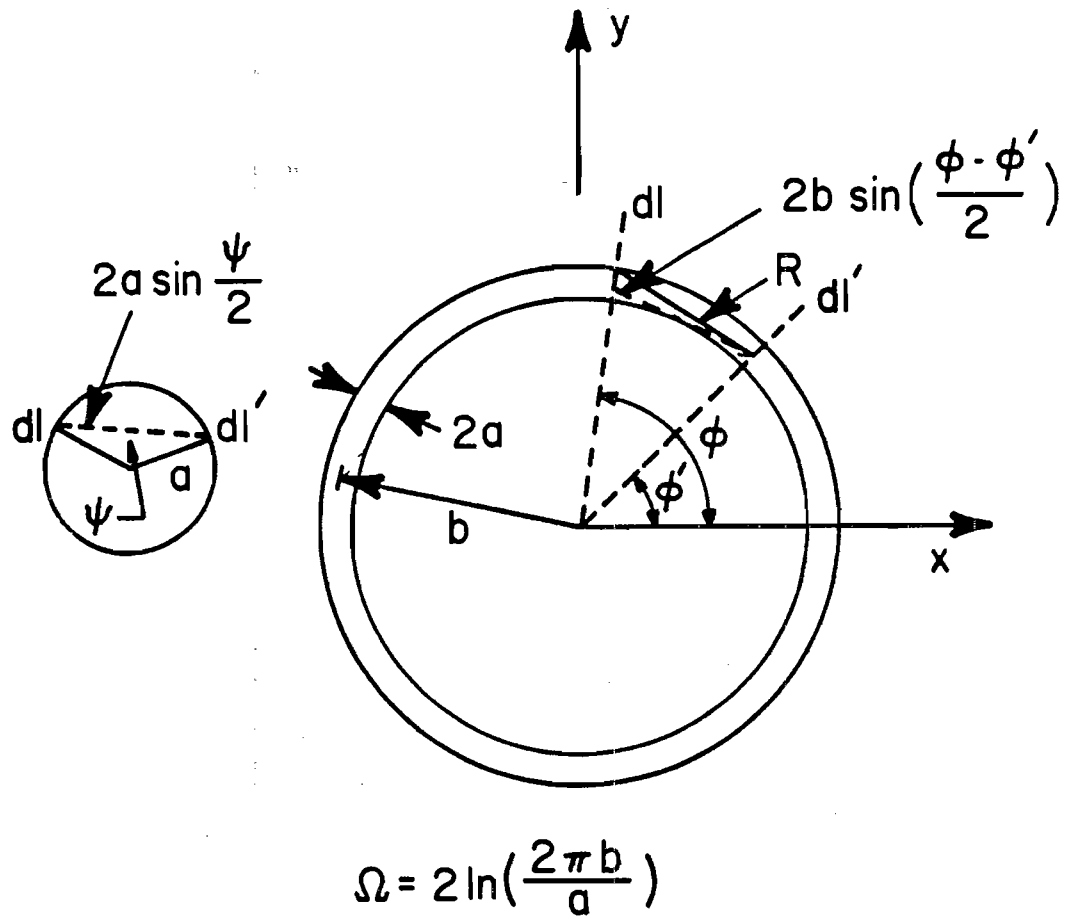
Figure 5.1 Geometry of the circular loop.

$$\tilde{I}(\phi, s) = 2\pi a \tilde{J}_\phi(\phi, s) .\qquad(5.1)$$

The EFIE for the total current becomes one-dimensional with the kernel defined by

$$\tilde{Z}(\phi, \phi', s) = \frac{Z_o}{b}\left[s \cos(\phi - \phi') - \frac{1}{s}\frac{\partial}{\partial\phi'}\frac{\partial}{\partial\phi}\right]\frac{e^{-sR}}{4\pi bR}\qquad(5.2)$$

$s = \gamma b$ is the normalized complex frequency, γ being the complex propagation constant, and R is the normalized distance between the source point and the observation point on the surface of the wire (see Figure 5.1) given by

$$R = \sqrt{4 \sin^2\left(\frac{\phi - \phi'}{2}\right) + \left(\frac{A}{b}\right)^2}\qquad(5.3)$$

with

$$A = 2a \sin\left(\frac{\psi}{2}\right) .\qquad(5.4)$$

The suitable symmetric product is defined as

$$<[\ ];[\ ]> \equiv \int_{-\pi}^{\pi}[\ ]\cdot[\ ]b\ d\phi .\qquad(5.5)$$

The eigenvalues of the EFIE can be found as [*Harrington*, 1968; *King*, 1969]

$$\tilde{\lambda}_n(s) = \frac{jZ_o}{2b}\ \tilde{a}_n(s)\qquad(5.6)$$

where

$$\tilde{a}_n(s) = -js\left[\frac{\tilde{K}_{n-1}(s) + \tilde{K}_{n+1}(s)}{2} + \left(\frac{n}{s}\right)^2\tilde{K}_n(s)\right]\qquad(5.7)$$

and

$$\tilde{K}_n(s) = \frac{1}{4\pi^2} \int\limits_{-\pi}^{\pi} d\psi \int\limits_{-\pi}^{\pi} \frac{e^{jn(\phi-\phi')} e^{-sR}}{R} \, d(\phi-\phi') \; . \tag{5.8}$$

As shown by *Wu* [1962], eq. (5.8) may be approximately written in terms of integrals of Anger-Weber functions for unrestricted n, as

$$\tilde{K}_o(s) = \frac{1}{\pi} \ln\left(\frac{8b}{a}\right) - \frac{1}{2} \int\limits_0^\zeta \left[\Omega_o(z) + j \, J_o(z)\right] dz \tag{5.9a}$$

$$\tilde{K}_n(s) = \frac{1}{\pi}\left[I_o\left(\frac{na}{b}\right)K_o\left(\frac{na}{b}\right) + C_n\right] - \frac{1}{2} \int\limits_0^\zeta \left[\Omega_{2n}(z) + j \, J_{2n}(z)\right] dz \tag{5.9b}$$

with

$$C_n = \ln(4\Gamma) - 2 \sum\limits_{m=0}^{n-1} (2m+1)^{-1} \tag{5.10}$$

where $\zeta = -j2s$ and I_o and K_o are the modified Bessel functions of the first and second kind, respectively, and $\Gamma = 1.781...$ is the Euler's constant. This representation was originally obtained by Wu for the real frequency case ($s = j\omega$); it was generalized to the complex frequency case by *Umashankar and Wilton* [1974].

The eigenfunctions associated with the eigenvalues (5.6) are

$$I_{n,\substack{e\\o}}(\phi) = \begin{Bmatrix} \cos(n\phi) \\ \sin(n\phi) \end{Bmatrix} \; , \tag{5.11}$$

so that there is an eigenvalue degeneracy for $n \geq 1$.

The current $\tilde{I}(s) \equiv \tilde{I}(\phi_g, s)$ at the location $\phi = \phi_g$ can be expanded in terms of the eigenfunctions as

$$\tilde{I}(s) = \frac{-j2b}{Z_o} \left\{ \frac{1}{\tilde{a}_o(s)} \frac{\langle I_{o,e}(\phi), \tilde{E}_\phi^i(\phi,s)\rangle}{\langle I_{o,e}(\phi), I_{o,e}(\phi)\rangle} \right.$$

$$\left. + \sum\limits_{n=1}^\infty \sum\limits_\sigma \frac{1}{\tilde{a}_n(s)} \frac{\langle I_{n,\sigma}(\phi), \tilde{E}_\phi^i(\phi,s)\rangle}{\langle I_{n,\sigma}(\phi), I_{n,\sigma}(\phi)\rangle} I_{n,\sigma}(\phi_g) \right\} \tag{5.12}$$

where the subscript σ indicates e (for "even") or o (for "odd").
Noting that

$$<I_{o,e}(\phi),I_{o,e}(\phi)> = 2\pi b \qquad (5.13a)$$

and

$$<I_{n,\substack{e\\o}}(\phi),I_{n,\substack{e\\o}}(\phi)> = \pi b \qquad (5.13b)$$

one can rewrite (5.12) as

$$\tilde{I}(s) = \frac{-j}{\pi Z_o}\left\{\frac{1}{\tilde{a}_o(s)} <I_{n,e}(\phi),\tilde{E}^i(\phi,s)> \right.$$

$$\left. + 2\sum_{n=1}^{\infty}\sum_{\sigma}\frac{1}{\tilde{a}_n(s)} <I_{n,\sigma}(\phi),\tilde{E}_\phi^i(\phi,s)>I_{n,\sigma}(\phi_g)\right\} \quad . \qquad (5.14)$$

5.3 Derivation of the Driving-Point Admittance of the Loop Antenna

For the driving-point admittance computation a delta function generator located at $\phi = \phi_g$ is assumed, with the field defined by

$$\tilde{E}_\phi^i(\phi,s) = \frac{\tilde{V}(s)}{b}\delta(\phi-\phi_g) \quad . \qquad (5.15)$$

Using (5.15) in (5.14) the admittance $\tilde{Y}(s) = \tilde{I}(s)/\tilde{V}(s)$ can be written as

$$\tilde{Y}(s) = \frac{-j}{\pi Z_o}\left\{\frac{1}{\tilde{a}_o(s)} + 2\sum_{n=1}^{\infty}\sum_{\sigma}\frac{1}{\tilde{a}_n(s)} I_{n,\sigma}^2(\phi_g)\right\} \quad . \qquad (5.16)$$

Umashankar and Wilton [1974] have shown that the term $1/\tilde{a}_n(s)$ can be expanded in a residue series

$$\frac{-j}{\tilde{a}_n(s)} = \frac{R_{no}}{s} + \sum_{i=1}^{\infty}\left[\frac{R_{ni}}{s-s_{ni}} + \frac{R_{ni}^*}{s-s_{ni}^*}\right] \qquad (5.17)$$

where the term associated with the pole at $s = 0$ is present only for

117

$n = 0$, *i.e.*, $R_{no} = 0$ for $n \geq 1$, and the residues R_{ni} are given by

$$R_{ni} = \lim_{s \to s_{ni}} \frac{s - s_{ni}}{\tilde{a}_n(s)} = \left[\frac{d\, a_n(s_{ni})}{ds} \right]^{-1} . \qquad (5.18)$$

In actual computations this series must be truncated after some finite number of terms (say M). *Umashankar and Wilton* [1974] have found that the truncated series (5.17) converged very slowly at low frequencies and they were forced, in effect, to use the modified pole expansion (see Section 2.3)

$$-\frac{j}{a_n(s)} \cong \frac{R_{no}}{s} + \sum_{i=1}^{M} s \left[\frac{R_{ni}}{s_{ni}(s - s_{ni})} + \frac{R_{ni}^*}{s_{ni}^*(s - s_{ni}^*)} \right] . \qquad (5.19)$$

They also observed that the poles belonging to a given eigenmode could be divided into three categories:

1. Type I - A single pole of each eigenset nearest the $j\omega$-axis at approximately $\omega = n$. This pole is the principal contributor to the response of the loop - it is the dominant pole (see Section 2.7).

2. Type II - A set of (n+1) poles (including conjugate pairs) which lie roughly along an elliptic arc centered at $s = 0$ and with a semi-major axis somewhat larger than n.

3. Type III - A group of an infinite number of poles lying almost parallel to the $j\omega$-axis. The spacing of these poles is asymptotic to $\Delta\omega = \pi c/b$.

This classification is illustrated in Figure 5.2 for a loop with the shape factor $\Omega = 2\ln(2\pi b/a)$. In this figure all fourth eigenmode poles with $\text{Im}\{s_{ni}\} \leq 20b/c$ are shown together with the dominant (Type I) poles of the eigenmodes 0-19. More recently *Blackburn* [1976] (see also [*Blackburn and Wilton*, 1978]) has provided an extensive tabulation of the poles and associated residues for the loop for several different shape parameters Ω.
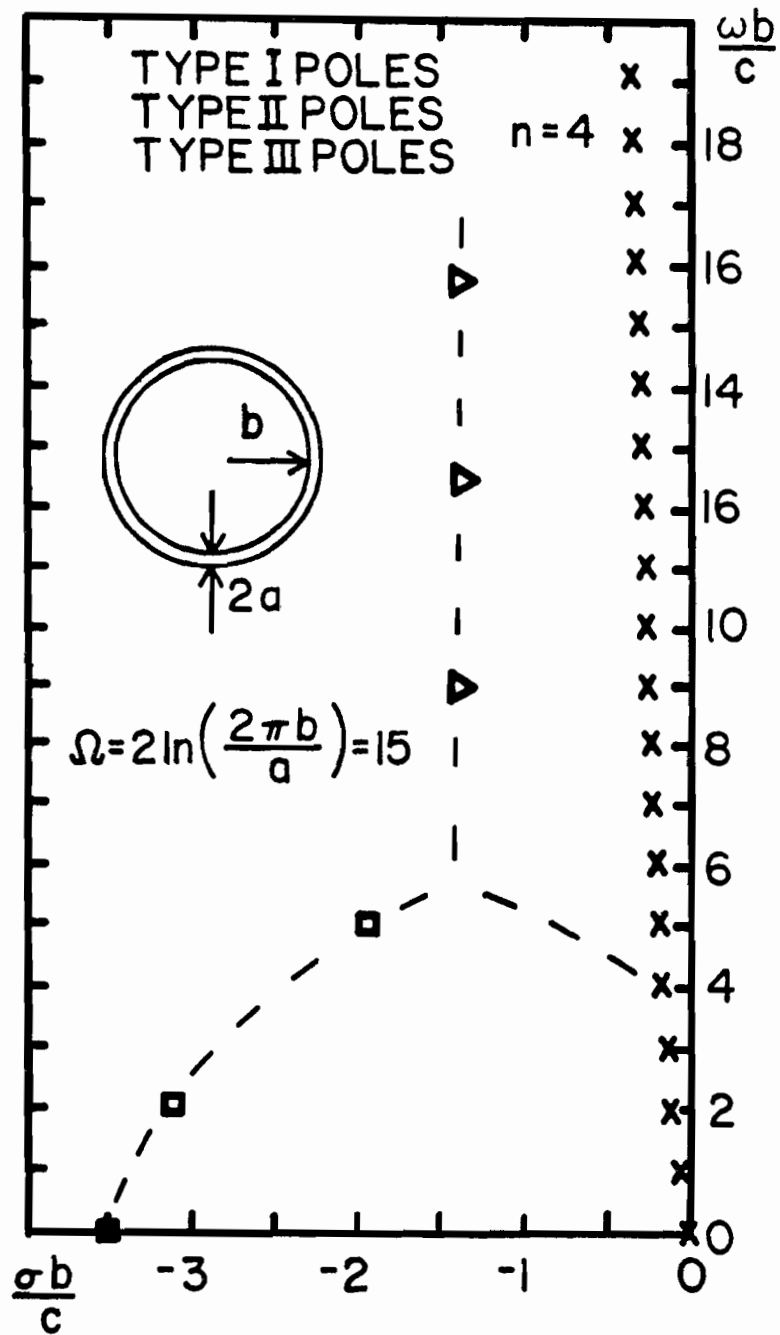
Figure 5.2 Type I, Type II, and Type III poles of the fourth eigenmode, and Type I poles of eigenmodes 0-19 of a circular loop with the shape factor $\Omega = 15$.

Denoting by s_n the dominant pole of the nth eigenmode and by R_n' the associated residue, one can write

$$\frac{-j}{\tilde{a}_o(s)} \cong \frac{R_o'}{s} \tag{5.20a}$$

and

$$\frac{-j}{\tilde{a}_n(s)} \cong s \left[\frac{R_n'}{s_n(s-s_n)} + \frac{R_n'^*}{s_n^*(s-s_n^*)} \right] \text{ , } n \geq 1. \tag{5.20b}$$

To simplify notation, it is convenient to define a normalized residue by

$$R_n = \frac{R_n'}{\pi Z_o} \text{ .} \tag{5.21}$$

Using (5.19) and (5.20) in (5.16) yields

$$\tilde{Y}(s) \cong \frac{1}{sL_o} + \sum_{n=1}^{N} \hat{\tilde{Y}}_n(s) \tag{5.22}$$

where $L_o = 1/R_o$, N is the number of dominant poles used, and

$$\hat{\tilde{Y}}_n(s) = \hat{\tilde{Y}}_{n,e}(s) + \hat{\tilde{Y}}_{n,o}(s), \tag{5.23}$$

$$\hat{\tilde{Y}}_{n,\sigma}(s) = \tilde{Y}_{n,\sigma}(s) + \tilde{Y}_{-n,\sigma}(s),$$

$$\tilde{Y}_{n,\sigma}(s) = s \frac{a_n I_{n,\sigma}^2(\phi_g)}{s_n(s-s_n)} \text{ ,} \tag{5.25}$$

with

$$a_n = 2R_n \text{ , } n \geq 1 \text{ .} \tag{5.26}$$

As discussed in Section 3.2, the index $-n$ indicates the term associated with the conjugate pole. Note that since

$$I_{n,e}^2(\phi) + I_{n,o}^2(\phi) \equiv 1 \tag{5.27}$$

for all values of ϕ, it follows that

$$\tilde{Y}_n(s) = \tilde{Y}_{n,e}(s) + \tilde{Y}_{n,o}(s) = s \frac{a_n}{s_n(s - s_n)} \tag{5.28}$$

and

$$\hat{\tilde{Y}}_n(s) = \tilde{Y}_n(s) + \tilde{Y}_{-n}(s) \tag{5.29}$$

is independent on the port location. This could be anticipated, of course, because of the symmetry of the loop.

The quality of the dominant-pole approximation to the driving point admittance of the loop antenna with $\Omega = 15.0$ is illustrated in Figure 5.3 which shows the comparison of the behavior of $\tilde{Y}(s)$ on the $j\omega$-axis computed both from the approximate formula (5.22), with $N = 10$, and from the exact expression (5.16). It is seen that the agreement is satisfactory, in particular in the real parts. The agreement in the imaginary parts deteriorates for $\omega \geq 3c/b$.

5.4 Derivation of the Short-Circuit Current of the Loop Antenna

For the short-circuit current computation at $\phi = \phi_g$ a plane wave incident field is assumed with the geometry defined in Figure 5.4. The ϕ component of the incident field on the wire is given by

$$\tilde{E}_\phi^i(\phi,s) = E_o^i Q(\phi) \tilde{p}(\phi,s) \tilde{f}(s) \tag{5.30a}$$

with

$$Q(\phi) = \sin\psi \cos\theta \sin(\phi-\phi_i) - \cos\psi \cos(\phi-\phi_i) \tag{5.30b}$$

and

$$\tilde{p}(\phi,s) = e^{s \sin\theta[\cos(\phi-\phi_i) - \cos(\phi_g - \phi_i)]} . \tag{5.30c}$$

In (5.30a) E_o^i denotes the magnitude of the field strength and $\tilde{f}(s)$ is the Laplace transform of the time history carried by the plane wave.

121
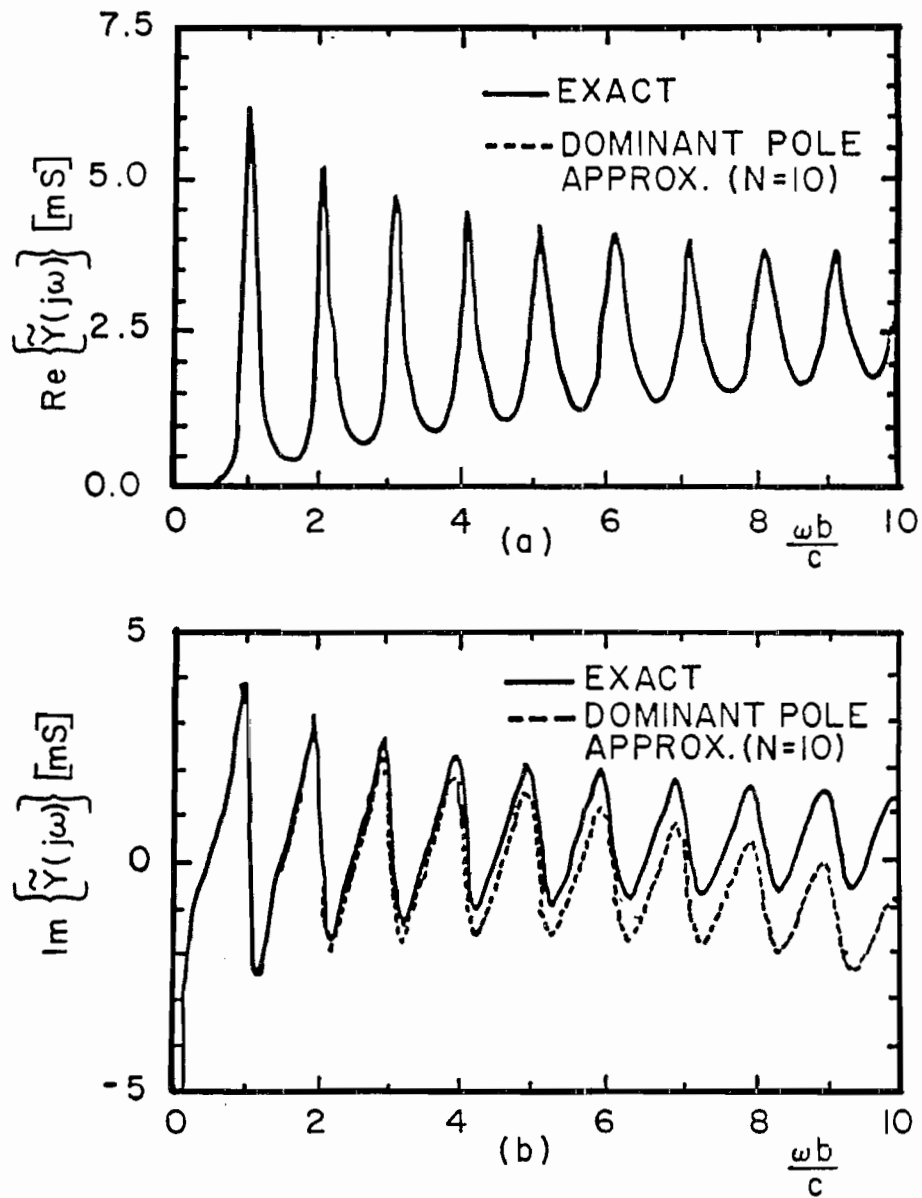
Figure 5.3 (a) The real part and (b) the imaginary part of the spectrum of the driving-point admittance of the loop antenna. The dominant pole approximation (5.22) is compared with the exact expression (5.16).
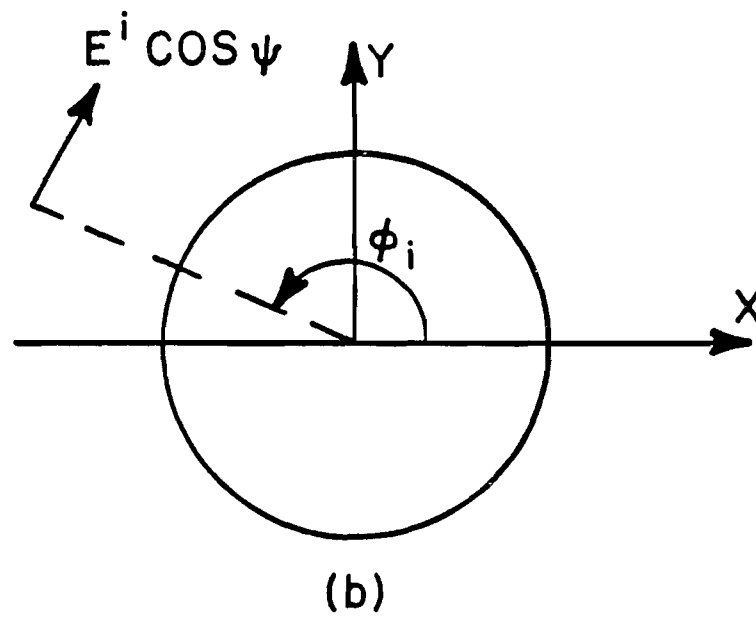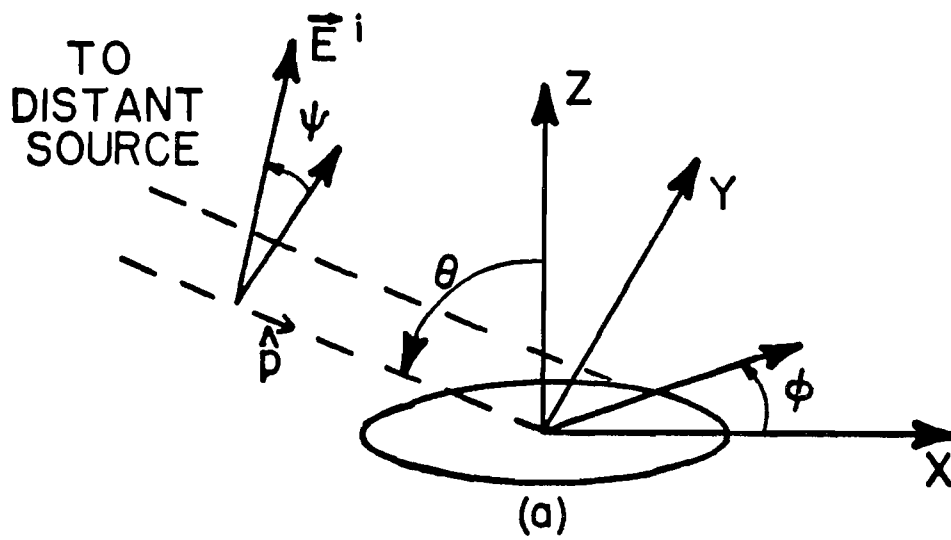
Figure 5.4 Circular loop in a plane-wave incident field. (a) The
general view; (b) the plane containing the loop.

The time origin is placed at the port location $\phi = \phi_g$, as discussed in Section 2.5. Using (5.30) in (5.14) and normalizing the current to $2\pi b E_o^i$ yields

$$\tilde{I}^{sc}(s) = \frac{-j}{\pi Z_o} \left\{ \frac{\tilde{\eta}_o(s)}{\tilde{a}_o(s)} + 2 \sum_{n=1}^{\infty} \sum_{\sigma} \frac{\tilde{\eta}_{n,\phi}(s)}{\tilde{a}_n(s)} I_{n,\sigma}(\phi_g) \right\} \tilde{f}(s) \qquad (5.31)$$

with the coupling coefficients given by

$$\tilde{\eta}_o(s) = \cos \psi \ I_1(s \sin\theta) e^{-s \sin\theta \cos(\phi_g - \phi_i)} \qquad (5.32a)$$

and

$$\tilde{\eta}_{n,\begin{subarray}{l} e \\ o \end{subarray}}(s) = \left[\cos\psi \left\{ \begin{matrix} \cos(n\phi_i) \\ \sin(n\phi_i) \end{matrix} \right\} I_n'(s \sin\theta) \right.$$

$$\left. - \sin\psi \cos\theta \left\{ \begin{matrix} -\sin(n\phi_i) \\ \cos(n\phi_i) \end{matrix} \right\} \frac{n \ I_n(s \sin\theta)}{s \sin\theta} \right] e^{-s \sin\theta \cos(\theta_g - \theta_i)},$$

$$n \geq 1 \ . \qquad (5.32b)$$

In the dominant-pole approximation the short-circuit current becomes

$$\tilde{I}^{sc}(s) \cong R_o \lim_{s \to 0} \left(\frac{\tilde{\eta}_o(s)}{s} \right) \tilde{f}(s) + 2 \sum_{n=1}^{\infty} \sum_{\sigma} \frac{s \ R_n \ \tilde{\eta}_{n,\sigma}(s_n)}{s_n(s - s_n)} I_{n,\sigma}(\phi_g) \tilde{f}(s). \qquad (5.33)$$

Combining N conjugate pole-pairs in (5.33) results in

$$\tilde{I}^{sc}(s) \cong g_o \tilde{f}(s) + \sum_{n=1}^{N} \sum_{\sigma} \left[\tilde{Y}_{n,\sigma}(s) T_{n,\sigma} + \tilde{Y}_{-n,\sigma}(s) T_{n,\sigma}^* \right] \tilde{f}(s) \qquad (5.34)$$

where

$$g_o = R_o \lim_{s \to 0} \left(\frac{\tilde{\eta}_o(s)}{s} \right) = R_o \frac{\cos\psi \ \sin\theta}{2} \qquad (5.35)$$

and

$$T_{n,\sigma} = \frac{\tilde{\eta}_{n,\sigma}(s_n)}{I_{n,\sigma}(\phi_g)} \ . \qquad (5.36)$$

124

Eq. (5.34) can be rewritten with the help of (5.32) as

$$\tilde{I}^{SC}(s) \cong g_o \tilde{f}(s) + \sum_{n=1}^{N} \left[\tilde{\bar{Y}}_n(s) T_n + \tilde{Y}_{-n}(s) T_n^* \right] \tilde{f}(s) \tag{5.37}$$

where the source coefficients T_n are defined by

$$T_n = I_{n,e}^2(\phi_g) T_{n,e} + I_{n,o}^2(\phi_g) T_{n,o} = \left\{ \cos\psi \, \cos[n(\phi_g - \phi_i)] I_n'(s_n \, \sin\theta) \right.$$

$$\left. - \sin\psi \, \cos\theta \, \sin[n(\phi_g - \phi_i)] \, \frac{n \, I_n(s_n \sin\theta)}{s_n \sin\theta} \right\} e^{-s_n \sin\theta \, \cos(\phi_g - \phi_i)} . \tag{5.38}$$

As discussed in Section 3.2, eq. (5.37) can be further transformed to

$$\tilde{I}^{SC}(s) \cong g_o \tilde{f}(s) + \sum_{n=1}^{N} \hat{\tilde{Y}}_n(s) \hat{\tilde{T}}_n(s) \tilde{f}(s) \tag{5.39}$$

with the voltage transfer functions $\hat{\tilde{T}}_n(s)$ defined by (3.24).

The quality of the dominant pole approximation to the short-circuit current of a loop antenna with $\Omega = 15.0$ is illustrated in Figure 5.5 which shows the comparison of the behavior of $\tilde{I}^{SC}(s)$ on the $j\omega$-axis computed both from the approximate formula (5.39), with $N = 10$, and from the exact expression (5.31). It is seen that the agreement is satisfactory.

The expressions (5.22) for the driving-point admittance, and (5.39) for the short-circuit current, are now in a form suitable for the application of the synthesis procedures developed in Chapter 4.

5.5 Equivalent Circuits for the Loop Antenna With $\Omega = 15$

In this section Norton-type equivalent circuits are presented for a loop antenna with the shape factor $\Omega = 15$. The general layout of the equivalent circuit is shown in Figure 4.1. It was found that only 10

125
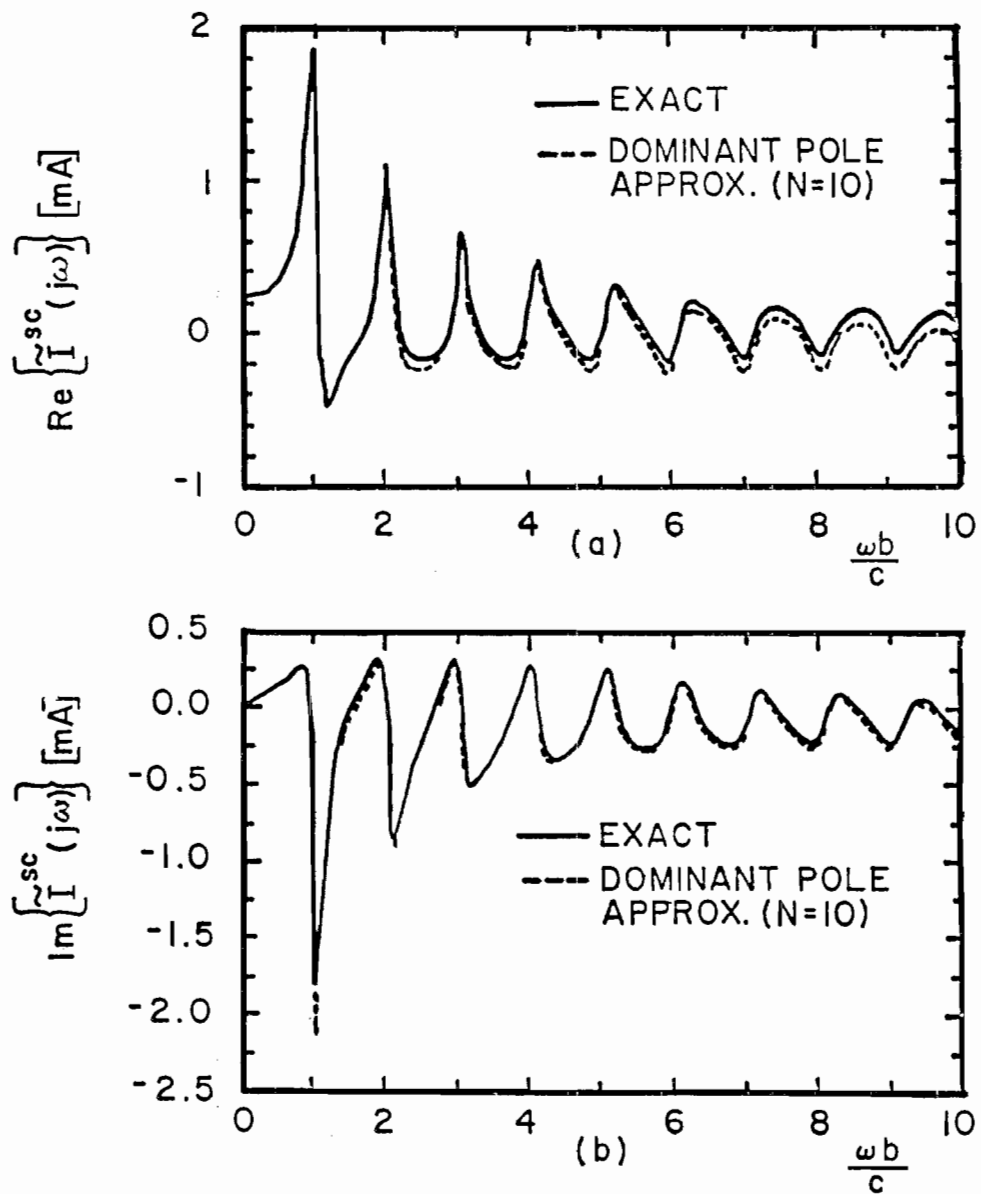
Figure 5.5 (a) The real part and (b) the imaginary part of the spectrum of the short-circuit current of the loop antenna. The dominant pole approximation (5.31) is compared to the exact expression (5.39).

or less dominant pole-pair modules model the structure adequately for the excitations used. The SEM data employed (the poles and the admittance residues) were taken from [*Blackburn*, 1976] and are listed in Table 5.1. Also indicated in this table for each pole are the quality factor Q_n, the residue location—as referred to Figure 4.5, and the padding necessary to restore the PR-ness of the associated pole-pair admittance $\hat{Y}_n(s)$. The column denoted "%" gives the ratio (in %) of the padding conductance G_n to the maximum value of the real part of $\hat{\tilde{Y}}_n(j\omega)$. It is evident from Table 5.1 that only $\hat{\tilde{Y}}_1(s)$ is initially PR and can be realized by one of the ladder circuits shown in Figure 4.7. For all other pole-pair admittances the residues lie outside the regions I and II, in the area denoted "case A" (see Figure 4.5), so that padding is required. However, the amount of padding is insignificant as compared to the value of the real part of $\hat{\tilde{Y}}_n(j\omega)$ near the resonance. The padded pole-pair admittances can be realized by the simplified Bott-Duffin modules, as discussed in Section 4.3. The element values of the first 10 dominant pole-pair modules are listed in Table 5.2. Similar driving-point admittance network for the loop was synthesized previously by *Streable and Pearson* [1981].

The current response of the equivalent network defined in Table 5.2 due to a Gaussian voltage pulse, computed by the SCEPTRE [*Jensen and McNamee*, 1976] circuit analysis program, is shown in Figure 5.6. This response is compared to a waveform obtained from the TWTD [*VanBlaricum and Miller*, 1972] computer code, which solves an integral equation for the current in the time domain. It requires, however, that the structure be modeled by a connection of straight wire segments. Only about 50 segments were employed to model the loop for the TWTD run

Table 5.1 Admittance residues a_n, quality factors Q_n, and the padding conductances G_n associated with the dominant poles $s_n^{*)}$ of a circular loop antenna with $\Omega = 15$.

n	$s_n = -\sigma_n + j\omega_n$	Q_n	$a_n = c_n + jd_n$ [mS]	Region -Case	Padding G_n [mS]	%
0	0.0 +j 0.0	–	0.4620 +j 0.0	–	–	–
1	-0.0749 +j 1.0388	13.87	0.5301 +j 0.0893	II	–	–
2	-0.1083 +j 2.0526	18.94	0.5726 +j 0.0939	III-A	$2.6211 * 10^{-5}$	$4.89 * 10^{-4}$
3	-0.1340 +j 3.0625	22.86	0.6033 +j 0.0987	III-A	$1.0999 * 10^{-3}$	0.024
4	-0.1558 +j 4.0706	26.13	0.6279 +j 0.1033	III-A	$2.3856 * 10^{-3}$	0.058
5	-0.1751 +j 5.0777	29.00	0.6489 +j 0.1076	III-A	$3.4936 * 10^{-3}$	0.093
6	-0.1927 +j 6.0840	31.57	0.6672 +j 0.1118	III-A	$4.4191 * 10^{-3}$	0.126
7	-0.2091 +j 7.0897	33.90	0.6837 +j 0.1157	III-A	$5.1984 * 10^{-3}$	0.157
8	-0.2245 +j 8.0950	36.06	0.6987 +j 0.1195	III-A	$5.8646 * 10^{-3}$	0.186
9	-0.2390 +j 9.0999	38.07	0.7126 +j 0.1231	III-A	$6.4430 * 10^{-3}$	0.213
10	-0.2529 +j10.1046	39.05	0.7255 +j 0.1267	III-A	$6.9521 * 10^{-3}$	0.239

*) The Poles s_n and residues a_n are normalized to c/b.

Table 5.2 Element values of the dominant pole-pair admittance networks for a loop antenna with $\Omega = 15$.[*]

LADDER CIRCUIT (Figure 4.7(a))			
n	$C_1/b[pF/m]$	$R_1[\Omega]$	$L_1/b[\mu H/m]$	$R_2[k\Omega]$
1	3.3034	47.374	3.0865	10.164

BOTT-DUFFIN CIRCUIT-CASE A (Figure 4.12(a))			
n	$C_0/b[pF/m]$	$L_1/b[\mu H/m]$	$C_1/b[pF/m]$	$R_1[k\Omega]$
2	0.9333	2.8764	44.3967	16.144
3	0.5095	2.7291	2.8702	20.727
4	0.3355	2.6209	1.0626	24.225
5	0.2443	2.5355	0.5527	26.998
6	0.1893	2.4648	0.3384	29.254
7	0.1531	2.4045	0.2284	31.125
8	0.1276	2.352	0.1645	32.701
9	0.1089	2.3055	0.1242	35.042
10	0.0946	2.2637	0.0971	35.197

[*] The static inductance $L_0/b = 7.215$ [$\mu H/m$].
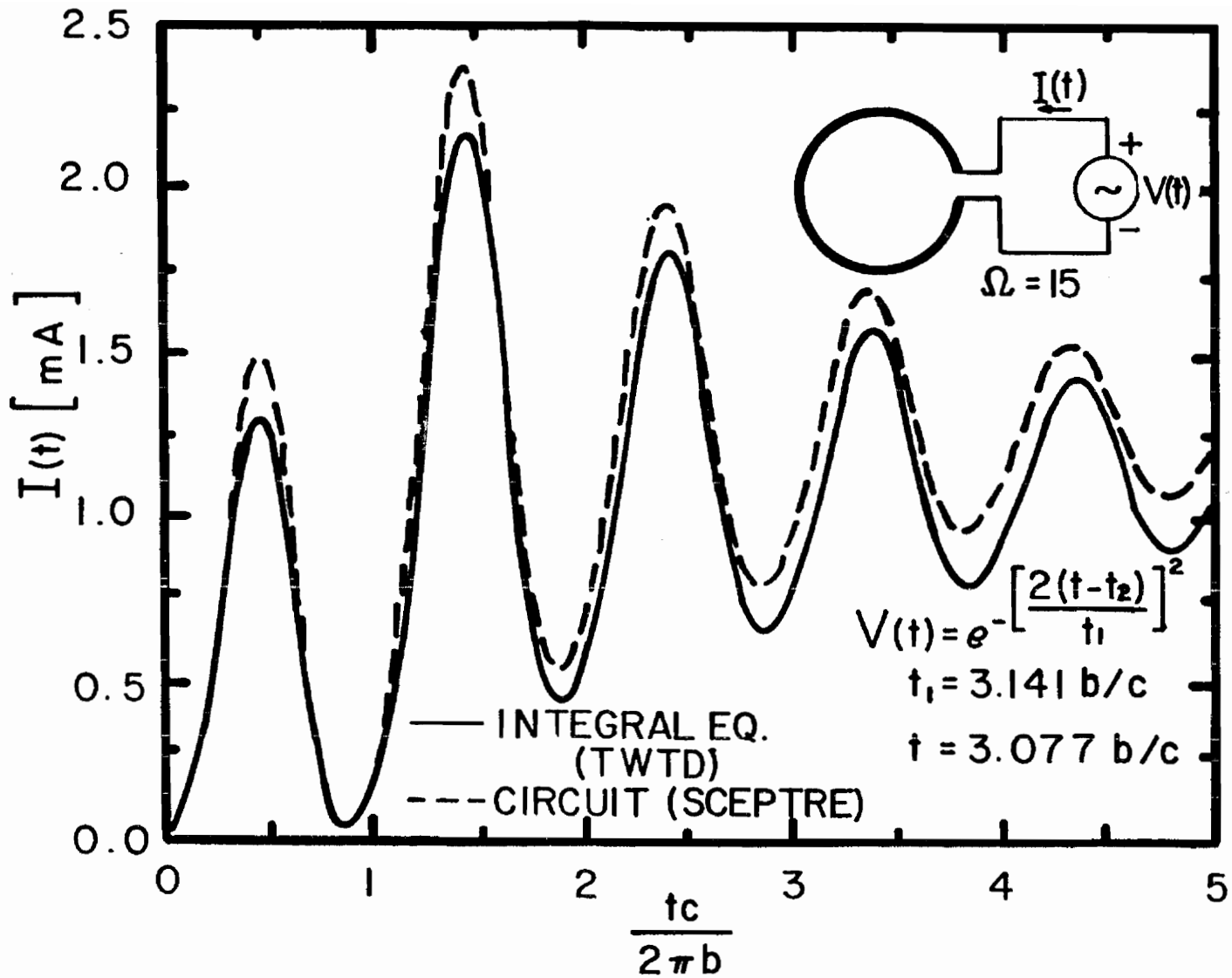
Figure 5.6 Input current of the circular loop antenna excited by a Gaussian voltage pulse. SCEPTRE and TWTD results are compared.

with the gap width equal to the length of one segment. This crude modeling is a possible explanation of the quite significant disagreement (about 15% in the worse case) of the SCEPTRE and TWTD curves.

Because of the symmetry of the loop, the driving-point part of the equivalent network does not depend on the gap location ϕ_g; neither does it depend on the direction of propagation of the plane wave incident field, of course. The transfer function part of the equivalent network does depend on the angles of incidence and the polarization of the incident plane wave, as discussed in Chapter 4. Not only the element values of the active part of the network change when the direction of incidence is changed, but also the network topology can be affected. However, it is shown in Chapter 4 that at most two network topologies can result: a ladder network or a symmetrical lattice network. For both cases explicit expressions for the element values in terms of the poles s, the admittance residues a_n and the source coefficients T_n are given in Chapter 4. The expression for T_n in the loop case is derived in Section 5.4, eq. (5.38). The topologies and element values of the corresponding transfer networks are listed in Tables 5.3-5.6. Note that we have chosen to use the RC networks rather than the RL networks. This choice was made because the element values of the RC networks turned out to be more realistic than the element values of the equivalent RL networks.

The short-circuit current responses of the complete equivalent networks computed by SCEPTRE are compared in Figures 5.7-5.12 with responses obtained by other means for different excitation conditions.

131

Table 5.3 Element values of the dominant pole-pair voltage transfer networks for a loop antenna $(\Omega = \overline{15})$ with a port at $\phi_g = 0°$, excited by a plane wave with the angles of incidence $\theta = 90°$, $\phi_1 = 0°$, and $\psi = 180°$.*)

n	TOPOLOGY	C_A/b [pF/m]	R_A [Ω]	C_B/b [pF/m]	R_B [Ω]	$\dfrac{\mu}{2\pi b E_o^i}$ [V^{-1}]
1	RC LATTICE	0.3541	$1.807*10^3$	–	$1.622*10^3$	3.0464
2	RC LATTICE	0.2053	531.47	–	331.86	0.9368
3	RC LADDER	0.7384	212.85	–	970.85	−0.2431
4	RC LADDER	1.0757	643.79	–	111.52	−0.9129
5	RC LADDER	1.4432	$1.410*10^3$	–	61.759	−1.1433
6	RC LATTICE	3.6760	41.602	–	38.711	−1.0055
7	RC LATTICE	4.5160	34.216	–	24.916	−0.6149
8	RC LATTICE	5.370	–	$3.305*10^{-2}$	10.826	−0.1207
9	RC LADDER	3.1672	52.597	–	24.696	0.3325
10	RC LADDER	3.6543	135.56	–	14.857	0.6233

*) The gain of the associated voltage-controlled current source $(\mathrm{VCCS}) g_o/(2\pi b E_o^i) = 0.231$ [mS/V].

Table 5.4 Element values of the dominant pole-pair voltage transfer networks for a loop antenna ($\Omega = 15$) with a port at $\phi_g = 90°$, excited by a plane wave with the angles of incidence $\theta = 90°$, $\phi_i = 0°$, and $\psi = 180°$.*)

n**)	TOPOLOGY	$C_A/b[pF/m]$	$R_A[\Omega]$	$C_B/b[pF/m]$	$R_B[\Omega]$	$\dfrac{\mu}{2\pi b E_o^i}[V^{-1}]$
2	RC LADDER	0.436	$838.53*10^3$	–	408.79	1.9989
4	RC LATTICE	2.151	95.512	–	94.602	1.1836
6	RC LATTICE	3.676	40.432	–	39.782	0.8619
8	RC LATTICE	5.403	21.884	–	21.423	0.6849
10	RC LATTICE	7.308	13.562	–	13.222	0.5713

*) The gain of the associated VCCS $g_o/(2\pi b E_o^i) = 0.231[mS/V]$.

**) The transfer networks associated with poles s_n for $n = 1,3,5,...$ are not present.

Table 5.5 Element values of the dominant pole-pair voltage transfer networks for a loop antenna ($\Omega = 15$) with a port at $\phi_g = 180°$, excited by a plane wave with the angles of incidence $\theta = 90°$, $\phi_i = 0°$, and $\psi = 180°$.

n	TOPOLOGY	C_A/b[pF/m]	$R_A[\Omega]$	C_B/b[pF/m]	$R_B[\Omega]$	$\dfrac{\mu}{2\pi b E_o^i}[V^i]$
1	RC LADDER	0.1770	$28.305 * 10^3$	–	1.8259	2.6702
2	RC LADDER	0.4360	$2.117 * 10^3$	–	506.28	0.9079
3	RC LATTICE	0.825	–	0.6518	87.288	-0.15302
4	RC LATTICE	2.1514	117.65	–	79.741	-0.5442
5	RC LATTICE	2.8864	62.836		55.904	-0.7547
6	RC LADDER	1.8380	$2.134 * 10^3$		40.872	-0.7097
7	RC LADDER	2.2579	254.90	–	32.513	-0.4883
8	RC LADDER	2.7015	53.930	–	36.173	-0.1851
9	RC LATTICE	6.3343	48.144	–	10.179	0.1068
10	RC LATTICE	7.3087	15.682	–	11.682	0.3140

*) The gain of the associated VCCS $g_o/(2\ b E_o^i) = 0.231$[mS/V].

134

Table 5.6 Element values of the dominant pole-pair voltage trnasfer networks for a loop antenna ($\Omega = 15$) with a port at $\phi_g = 90°$, excited by a plane wave with the angles of incidence $\theta = 30°$, $\phi_i = 180°$, and $\psi = 60°$.

n	TOPOLOGY	$C_A/b[pF/m]$	$R_A[\Omega]$	$C_B/b[pF/m]$	$R_B[\Omega]$	$\dfrac{\mu}{2\pi bE_o^i}[V^{-1}]$
1	RC LADDER	0.1679	$1.7152*10^3$	$2.746*10^{-3}$	–	0.3626
2	RC LATTICE	0.872	41.269	–	40.456	-0.9664
3	RC LADDER	0.7384	28.523	–	45.00	0.1538
4	RC LATTICE	2.1514	97.223	–	92.981	-0.2499
5	RC LADDER	1.4432	114.43	–	122.52	$5.873*10^{-2}$
6	RC LATTICE	3.676	41.423	–	38.867	$-7.747*10^{-2}$
7	RC LADDER	2.258	61.777	–	54.074	$2.256*10^{-2}$
8	RC LATTICE	5.403	22.558	–	20.814	$-2.586*10^{-2}$
9	RC LADDER	3.1672	38.799	–	29.646	$8.748*10^{-3}$
10	RC LATTICE	7.3087	14.064	–	12.777	$-8.993*10^{-3}$

*) The gain of the associated VCCS $g_o/(2\pi bE_o^i) = -0.0578$ [mS/V].
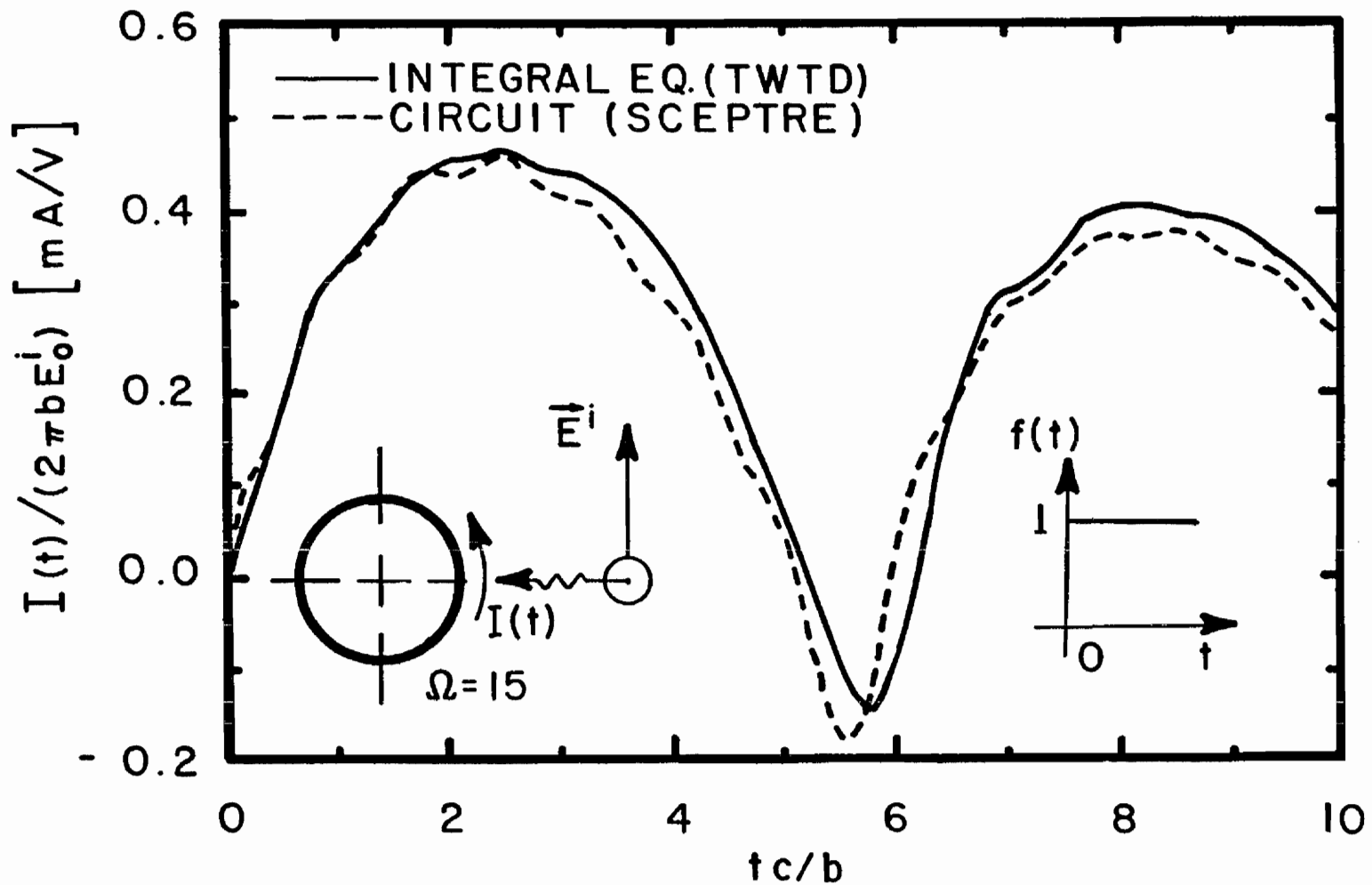
Figure 5.7 Short-circuit current excited in the circular loop at $\phi = 0°$ by a step function plane wave. SCEPTRE and TWTD results are compared.
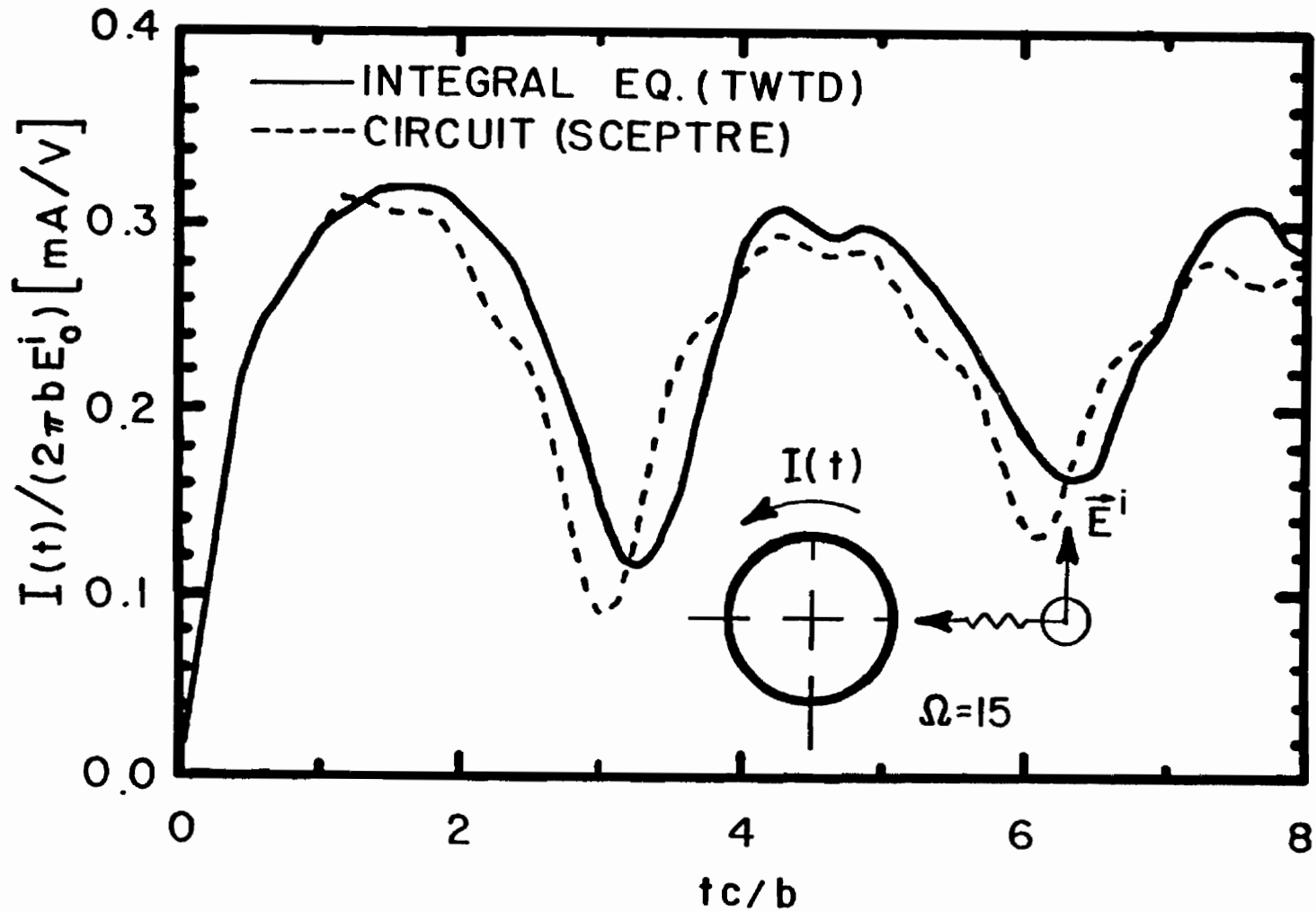
Figure 5.8 Short-circuit current excited in the circular loop at $\phi = 90°$ by a step function plane wave. SCEPTRE and TWTD results are compared.
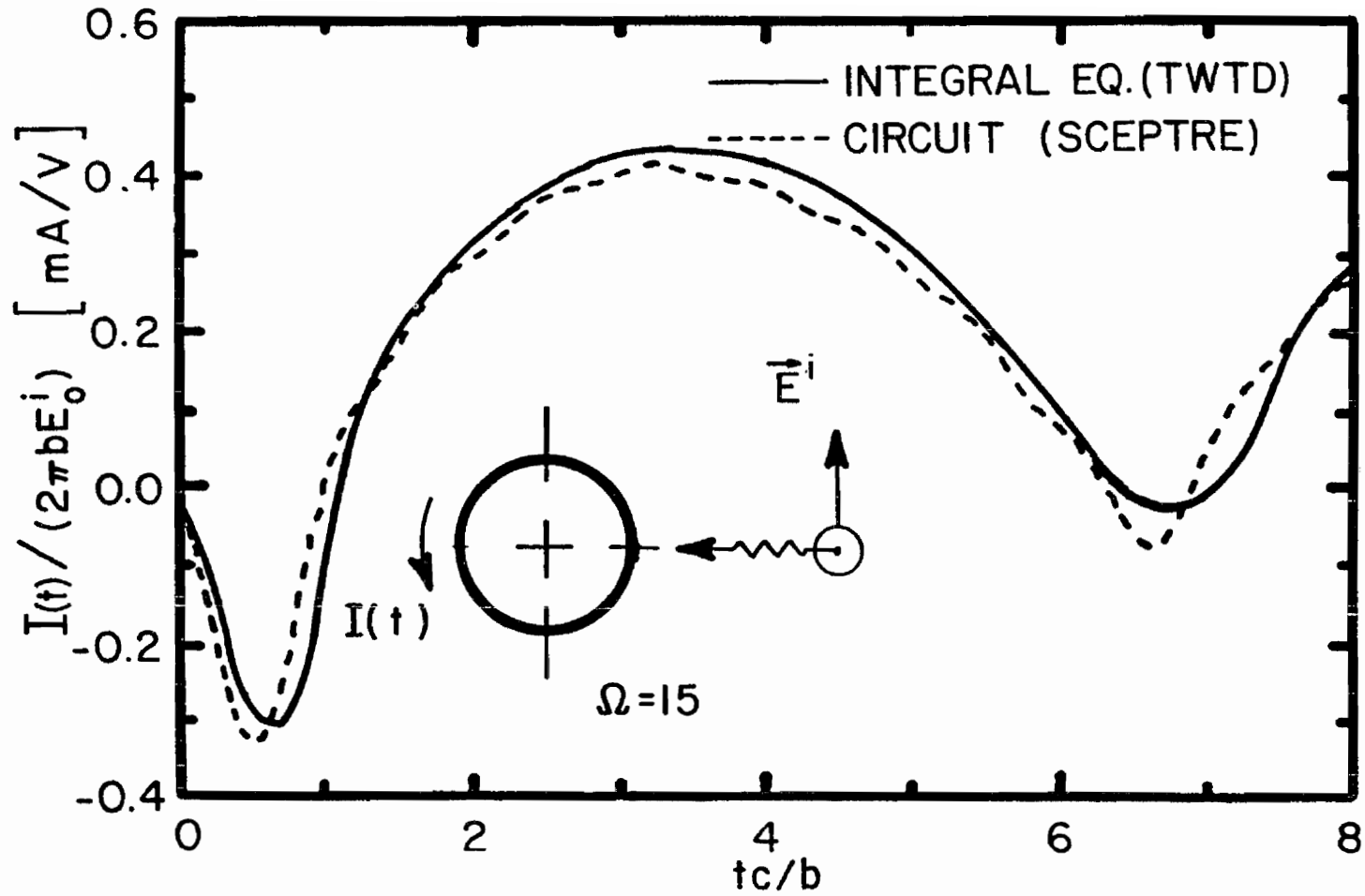
Figure 5.9 Short—circuit current excited in the circular loop at $\phi = 180°$ by a step function plane wave. SCEPTRE and TWTD results are compared.
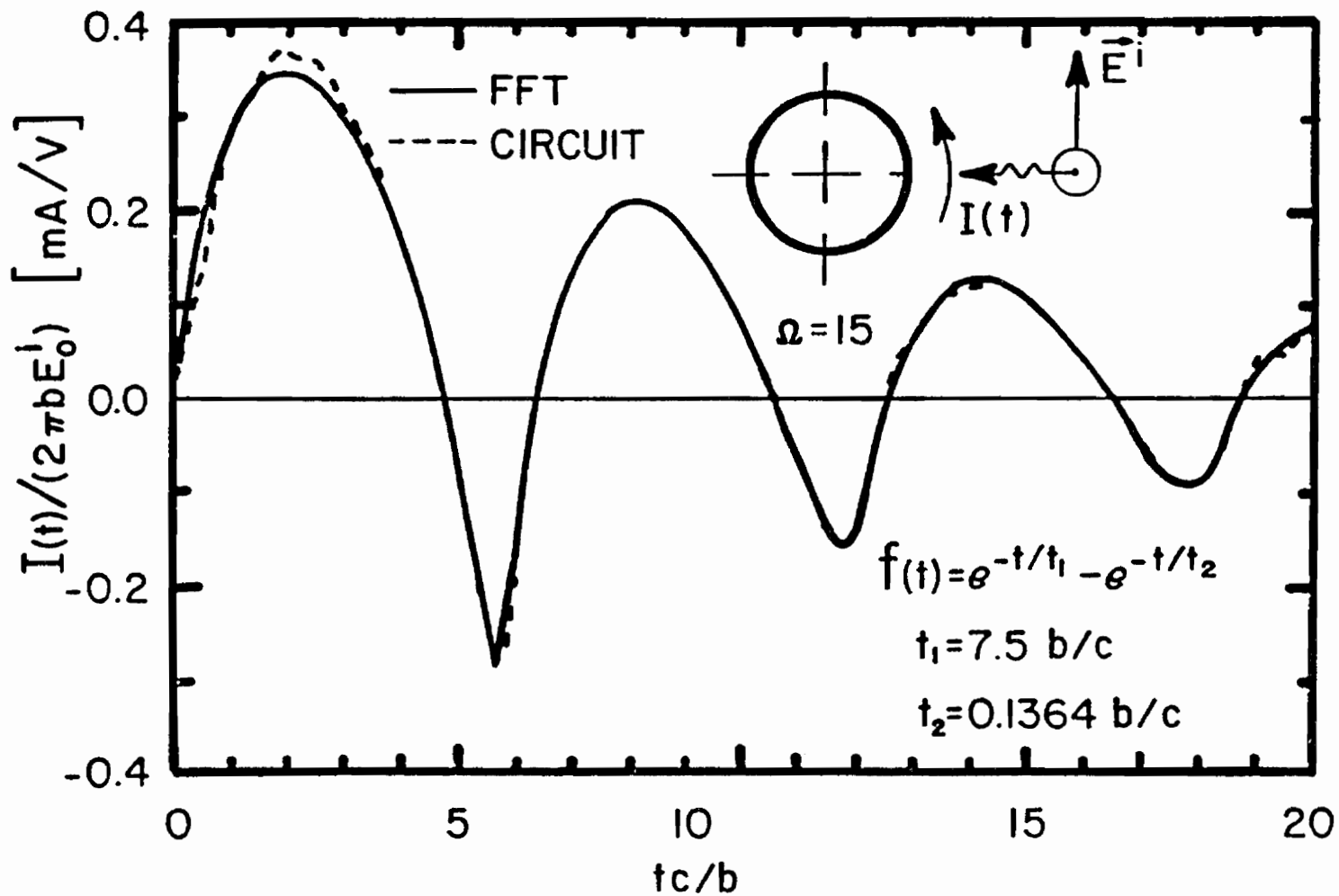
Figure 5.10 Short-circuit current excited in the circular loop at $\phi = 0°$ by a double-exponential function plane wave. SCEPTRE and FFT results are compared.
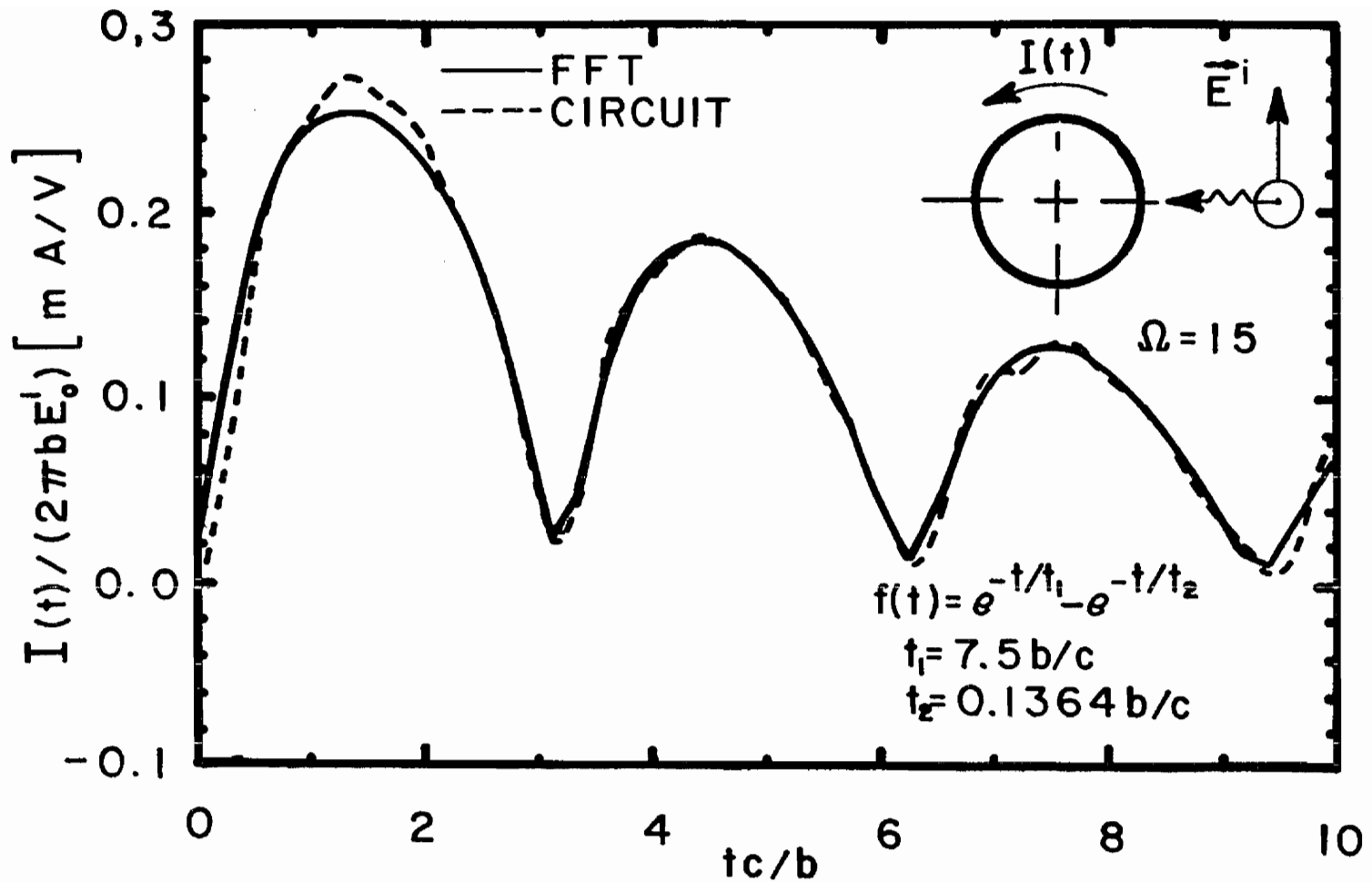
Figure 5.11 Short-circuit current excited in the circular loop at $\phi = 90°$ by a double-exponential plane wave. SCEPTRE and FFT results are compared.
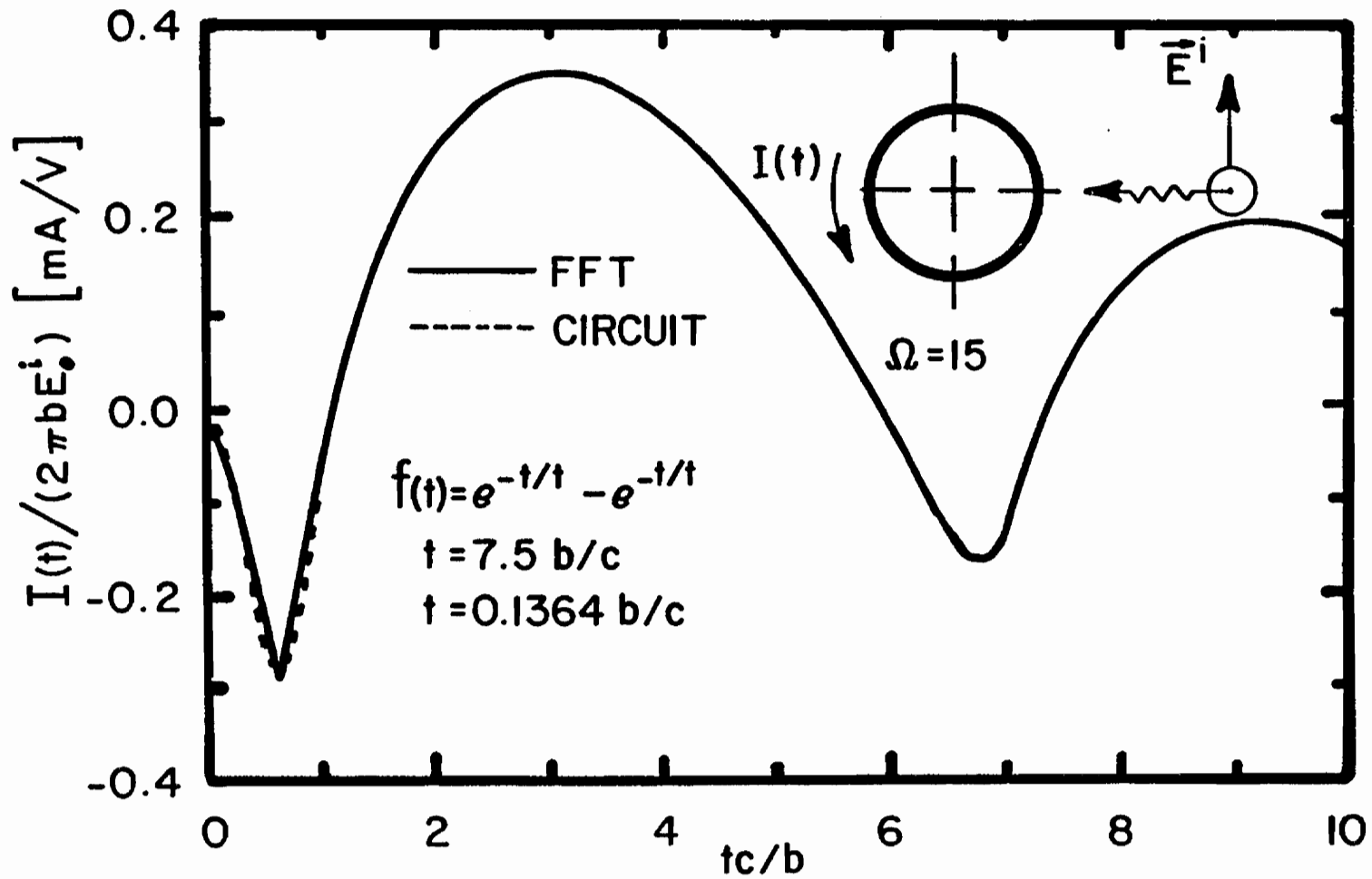
Figure 5.12   Short—circuit current excited in the circular loop at $\phi = 180°$ by a double—exponential plane wave.   SCEPTRE and FFT results are compared.

SCEPTRE responses are compared with TWTD results in Figures
5.7-5.9. The time history carried by the plane wave is a step function.
As in the case of the admittance network, there is a significant
discrepancy between these two curves. Again, one can attribute this
discrepancy to the relatively crude modeling of the loop by the
straight pieces of wire. It is of interest to note that the current
waveform approaches a constant non-zero value for late times. This
phenomenon is possible because there is a d-c (direct-current)
component in the incident waveform spectrum and the loop is perfectly
conducting.

The circuit responses are compared with the results of the
classical frequency domain—Fourier transform method in Figures 5.10-
5.12. The time history of the incident wave is a double exponential
function. In computing the frequency domain response the series
(5.31) for the short-circuit current was evaluated for $s = j\omega$ with 30
terms included. The subroutine developed by *Blackburn et al.* [1978]
was used to evaluate the $\tilde{a}_n(j\omega)$ factors. The time domain response was
obtained by applying the Fast Fourier Transform (FFT) algorithm
[*Brigham*, 1974]. It is seen from Figures 5.10-5.12 that the SCEPTRE and
FFT responses agree favorably (the maximum discrepancy is less than 8%).

5.6 Conclusions

The responses of the dominant pole-pair equivalent circuits for
a thin-wire loop antenna agree favorably with the exact responses
obtained from the frequency domain—inverse FFT approach. The amount
of the real-part padding necessary for physical realizability of the
pole pair admittances is negligible in comparison to the value of the
real part at the resonance.

CHAPTER 6

EQUIVALENT CIRCUIT SYNTHESIS FOR A CYLINDRICAL DIPOLE

6.1 Introduction

In this chapter the procedures developed in Chapters 2-4 are applied to the synthesis of the dominant pole-pair, Norton-based, equivalent circuits for a thin cylindrical dipole antenna. The cylindrical dipole is a member of the class of structures for which an exact analytical solution is not available. Instead, the SEM data are derived numerically by the MoM technique. Simplified equivalent circuits based on the sinusoidal mode approximation are also derived. For a symmetrical dipole antenna or a cylindrical post over a ground plane, particularly simple and yet reasonably accurate equivalent circuits result. The responses of the SEM equivalent circuits are compared with the results of the classical frequency domain—inverse FFT approach. An application of the derived equivalent circuits to the analysis of antennas with nonlinear loads is illustrated in Appendix B.

6.2 Preliminary Theory

The geometry of the dipole is defined in Figure 6.1. It is assumed that the cylinder is slender ($a \ll \ell$) and electrically thin, *i.e.*, $\omega_{max} a/c \ll 1$, where $\omega = \omega_{max}$ is the largest significant spectral component of the excitation. As a consequence, it can be assumed that there is only a z-component of the surface current density, *i.e.*, $\tilde{\vec{J}}(\vec{r},s) = \tilde{J}_z(\vec{r},s)\hat{z}$, where $\hat{z}$ denotes the unit vector in the z direction. It can be further assumed that the current density is uniform around the cylinder, *i.e.*, $\tilde{J}_z(\vec{r},s) \equiv \tilde{J}_z(z,s)$, so that the total current is given by
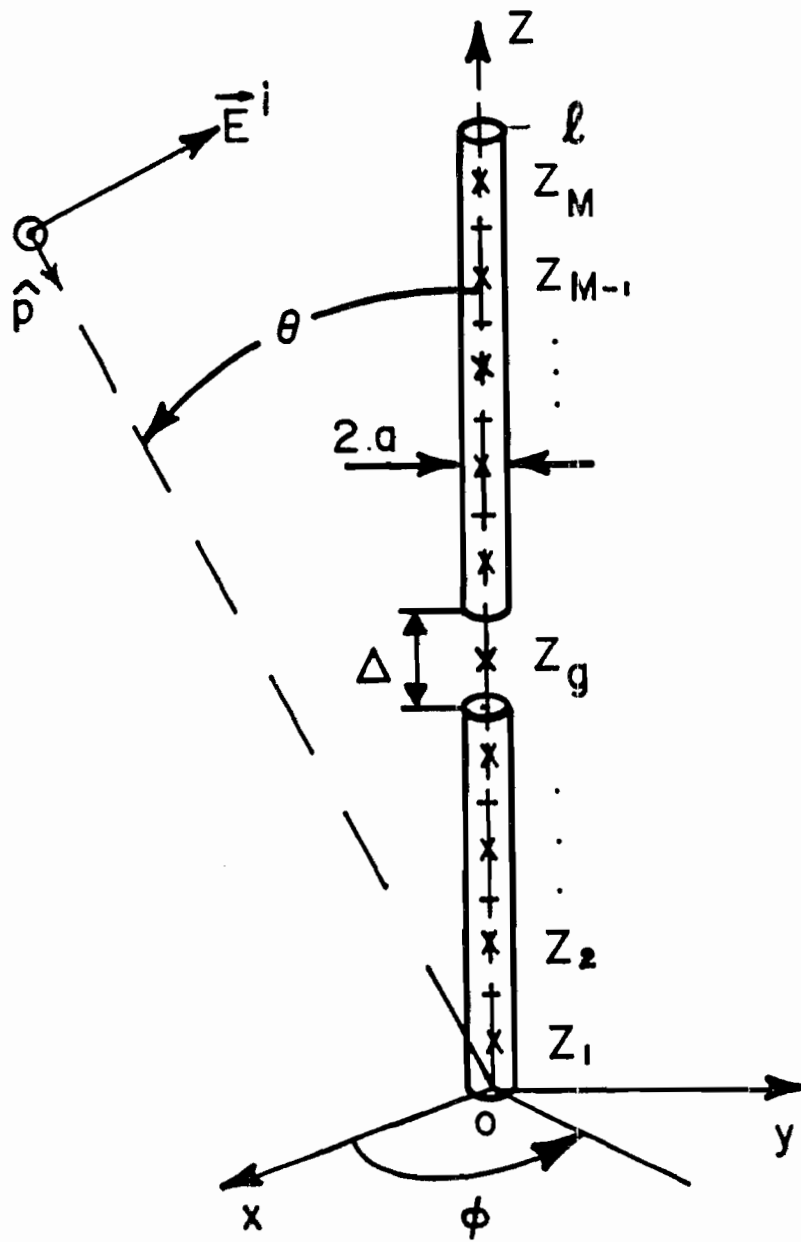
$$\Omega = 2\ell n \ (\ell/a)$$

Figure 6.1 Geometry of the cylindrical dipole.

$$\tilde{I}(z,s) = 2\pi a \tilde{J}_z(z,s) \ . \tag{6.1}$$

The current on the dipole can be found from the so-called "Pocklington's equation"

$$-\frac{Z_o}{4\pi\gamma} \left[\frac{d^2}{dz^2} - \gamma^2\right] \int_0^{\ell} \tilde{I}(z,s)\tilde{K}(z,z',s)dz' = \tilde{E}_z^i(z,s) \tag{6.2}$$

where

$$\tilde{K}(z,z',s) = \frac{1}{2\pi} \int_{-\pi}^{\pi} \frac{e^{-\gamma R}}{R} \, d\phi' \tag{6.3}$$

with

$$R = \sqrt{(z-z')^2 + 4a^2 \, \sin^2(\phi'/2)}. \tag{6.4}$$

$\tilde{E}_z^i(z,s)$ denotes the z component of the incident electric field and $\gamma = s/c$ is the complex propagation constant.

In order to find the short-circuit SEM parameters of the dipole the gap is closed (Figure 6.1) and the integro-differential operator in (6.2) is matricized by using the method of moments (MoM) technique [*Harrington*, 1968]. In a simple variation of this method, as applied to the present problem, the cylinder is divided into a number, say M, of equal size zones of width $\Delta = \ell/M$ and the current distribution within a zone is approximated by a constant. By replacing the differential operator in (6.2) by finite differences [*Wilton and Butler*, 1976] and enforcing the integral equation at the match points z_k, $k = 1, 2, \ldots, N$ (collocation testing), a linear matrix equation is obtained for the expansion coefficients of the current. The natural frequencies (the poles) are found as the zeros of the determinant of the MoM matrix. At these freqeuncies the homogeneous eq. (6.2) has nontrivial solutions— the natural modes. The natural mode associated with the pole s_n can be expressed as

145

$$\tilde{I}_n(z) \cong \sum_{k=1}^{M} \tilde{I}_{n,k} \, P_k(z) \tag{6.5}$$

where $\tilde{I}_{n,k}$ are the current expansion coefficients obtained from the MoM solution and $P_k(z)$ are the pulse expansion functions defined by

$$P_k(z) = \begin{cases} 1 & , \quad z_k - \Delta/2 \le z \le z_k + \Delta/2 \\ 0 & , \quad \text{otherwise} \end{cases} \tag{6.6}$$

From the MoM matrix and the natural modes one can compute the normalization constants β_n according to eq. (2.20).

6.3 Derivation of the Driving-Point Admittance of the Dipole Antenna

The driving-point admittance of the dipole is determined by computing the current $\tilde{I}(s)$ in the gap region due to a voltage $\tilde{V}(s) = V_o \tilde{f}(s)$ impressed across the gap, as discussed in Section 3.2. The incident field due to this voltage can be approximated by

$$\tilde{E}_z^i(z,s) \cong \frac{V_o}{\Delta} P_g(z) \tilde{f}(s) \tag{6.7}$$

where $k = g$ is the index of the gap zone. The coupling coefficients can be found from (see Section 3.2)

$$\tilde{\eta}_n = \int_0^\ell \tilde{I}_n(z) \frac{V_o}{\Delta} P_g(z) dz \cong V_o \tilde{I}_{n,g} \tag{6.8}$$

and the admittance residues from

$$a_n \cong \beta_n \tilde{I}_{n,g}^2 \quad . \tag{6.9}$$

The driving-point admittance $\tilde{Y}(s) = \tilde{I}(s)/\tilde{V}(s)$ has the form

$$\tilde{Y}(s) \cong \sum_{n=1}^{N} \hat{\tilde{Y}}_n(s) \tag{6.10}$$

where $\hat{\tilde{Y}}_n(s)$ are the pole-pair admittances defined in (3.16) and N is the number of dominant poles employed. Note that the inductive term of eq. (3.15) is not present in the dipole case.

The poles and natural modes of a thin cylinder with the shape factor $\Omega = 2\ln(\ell/a) = 10.6$ were first found by *Tesche* [1973] by the procedure described in the previous section. In this work, however, the natural modes are given in a graphical form only. Since the numerical values of the coefficients $\tilde{I}_{n,k}$ were needed for the circuit synthesis purposes, Tesche's data were reproduced using 72 pulses in the current expansion. The gap width was taken to be one zone. The results are summarized in Figure 6.2 and Table 6.1. It can be seen from Figure 6.2 that the poles lie in layers roughly parallel to the jω-axis. The first layer poles are the dominant ones. Also shown in this figure is a grouping of poles according to eigensets, conjectured by D. R. Wilton [*Streable and Pearson,* 1981]. Note that, unlike in the loop case, there are only a finite number of poles belonging to each eigenmode in this representation.

The quality of the dominant-pole approximation to the driving-point admittance of a cylindrical dipole antenna with $\Omega = 10.6$ is illustrated in Figure 6.3 which shows the comparison of the behavior of $\tilde{Y}(s)$ on the jω-axis computed from the approximate formula (6.10) with $N = 10$, and by solving the integral equation (6.2) numerically. It is seen that the agreement is quite good in the real parts case while it is not as good in the imaginary parts, especially for $\omega \gtrsim 2\pi \, c/\ell$.

147
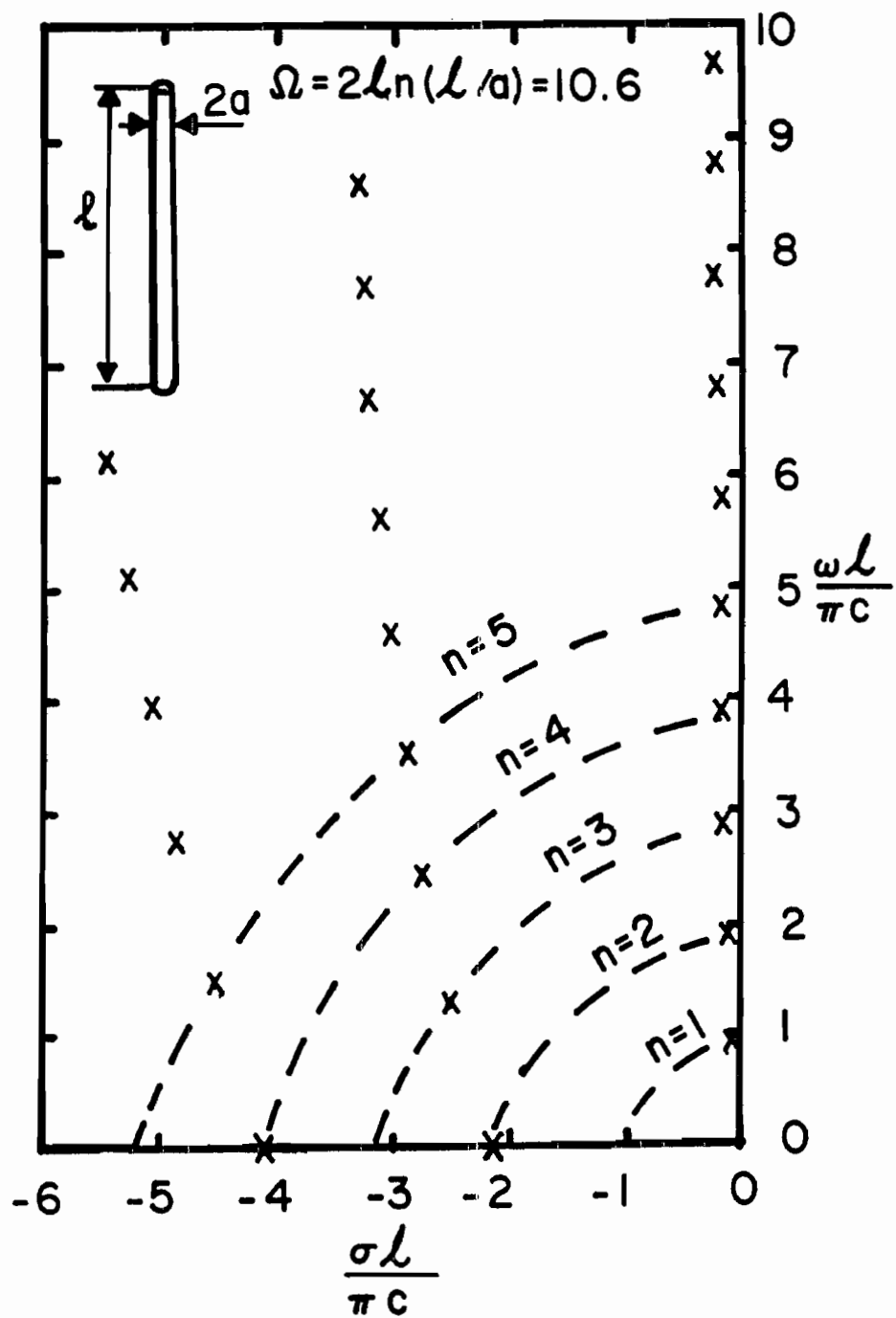
Figure 6.2 Pole distribution of a thin cylinder with the
shape factor $\Omega = 10.6$.
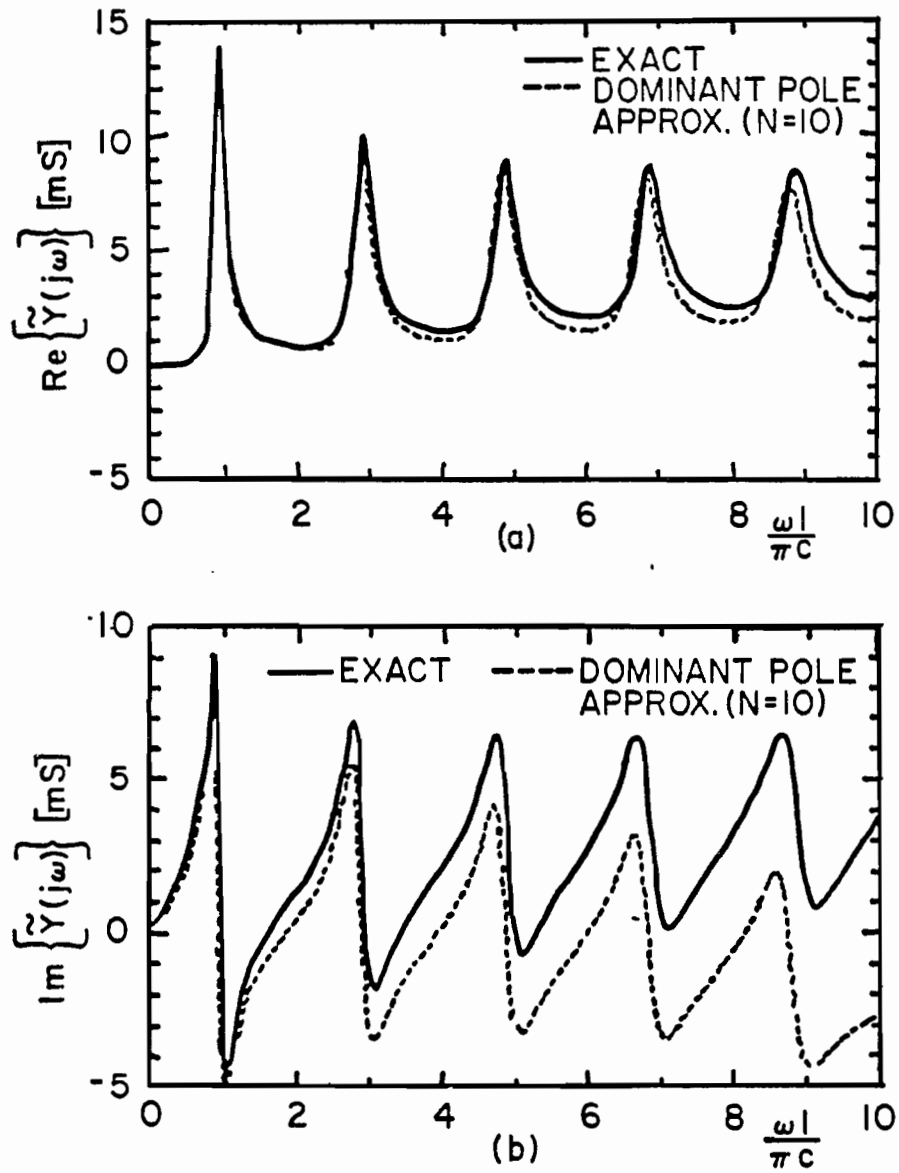
Figure 6.3 (a) The real part and (b) the imaginary part of the spectrum of the driving-point admittance of the dipole antenna. The dominant pole approximation (6.10) is compared with the "exact" curves obtained by solving the integral eq. (6.2) numerically.

6.4 Derivation of the Short-Circuit Current of the Dipole Antenna

For the short-circuit current computation the incident field is that due to a plane wave carrying a time history $f(t)$. The z-component of the electric field evaluated on the z-axis is given by

$$\tilde{E}_z^i(z,s) = E_o^i \sin\theta \, e^{\gamma(z-z_g)\cos\theta} \tilde{f}(s) \tag{6.11}$$

with the time origin chosen in the gap zone, as discussed in Section 2.6. With the current normalized to ℓE_o^i, the coupling coefficients can be computed as

$$\tilde{\eta}_n = -\frac{\sin\theta}{\ell} \int_0^\ell \tilde{I}_n(z) e^{\gamma_n(z-z_g)\cos\theta} dz$$

$$\cong -\frac{\Delta\sin\theta}{\ell} \sum_{k=1}^M \tilde{I}_{n,k} e^{\gamma_n(z_k-z_g)\cos\theta} \tag{6.12}$$

with the source coefficients given by

$$T_n = \frac{\tilde{\eta}_n}{\tilde{I}_{n,g}} \, . \tag{6.13}$$

The short-circuit current can be expressed as

$$\tilde{I}^{sc}(s) \cong \sum_{n=1}^N \hat{\tilde{Y}}_n(s)\hat{\tilde{T}}_n(s)\tilde{f}(s) \tag{6.14}$$

with the voltage transfer functions $\hat{\tilde{T}}_n(s)$ defined in (3.24). Note that the first term of eq. (3.23) is not present in the dipole case.

The quality of the dominant-pole approximation to the short-circuit current of a cylindrical dipole antenna with $\Omega = 10.6$ is illustrated in Figure 6.4, in which the behavior of $\tilde{I}^{sc}(j\omega)$ computed from the approximate formula (6.14) with $N = 10$ is compared with the "exact" waveform obtained from the solution of the integral equation (6.2) numerically by the MoM

150
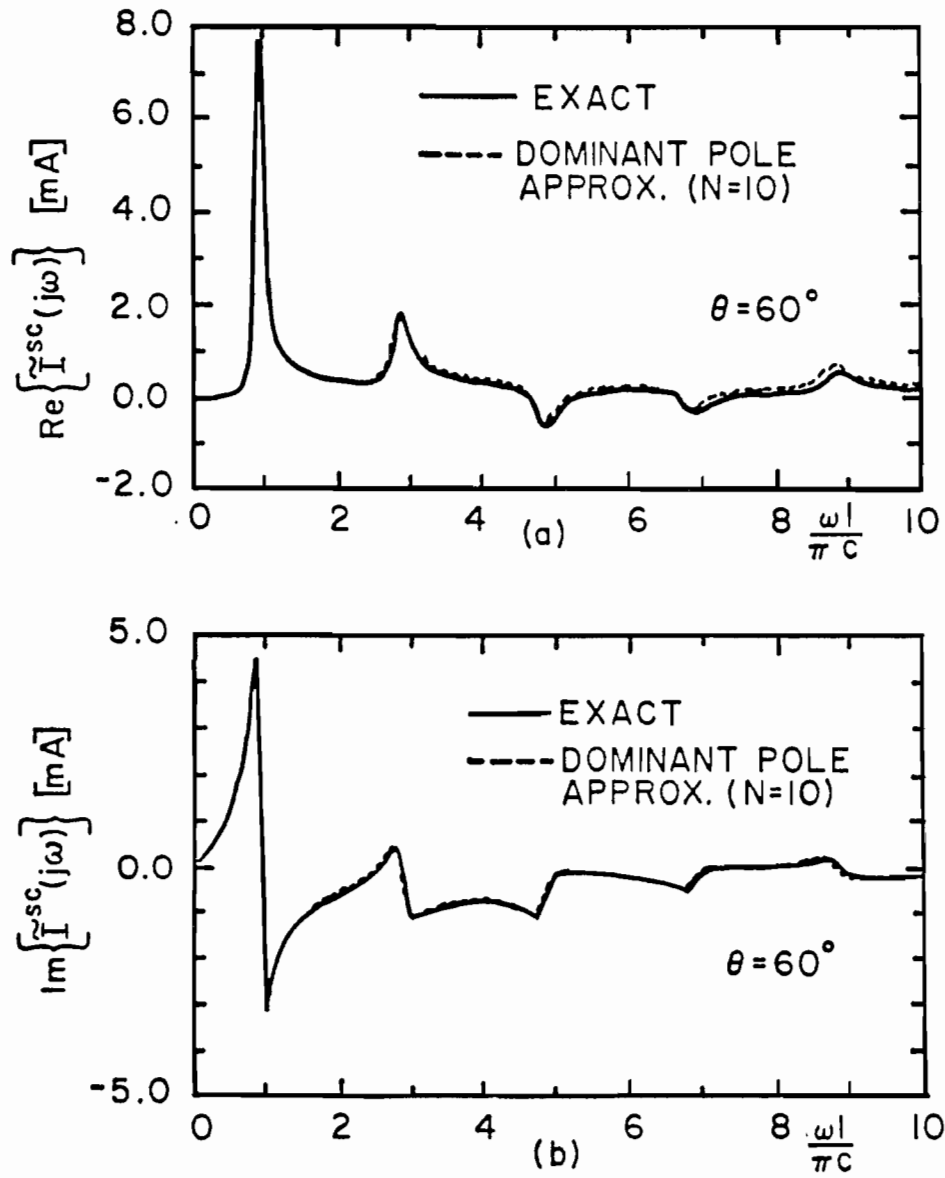
Figure 6.4 (a) The real part and (b) the imaginary part of the spectrum of the short-circuit current of the dipole antenna. The dominant pole approximation (6.14) is compared with the "exact" curves obtained by solving the integral eq. (6.2) numerically.

technique. The time history is the delta function and the angle of incidence $\theta = 60°$. It is seen that the agreement is excellent, both in the real and imaginary parts.

6.5 Equivalent Circuits for the Cylindrical Dipole with $\Omega = 10.6$

In Table 6.1 are listed for each pole s_n the quality factor Q_n, the admittance residue a_n and its location—as referred to Figure 4.5, and the padding G_n necessary to restore the PR-ness of the associated pole-pair admittance $\hat{Y}_n(s)$. The column denoted "%" gives the ratio (in %) of the padding conductance G_n to the maximum value of the real part of $\hat{Y}_n(j\omega)$. Data are provided for two gap location: $z_g = 1/2\ell$ and $z_g = 1/4\ell$. As can be seen from this table, for most poles the residues fall outside the regions I and II, in the area denoted "case A" (see Figure 4.5), so that after padding the Bott-Duffin module can be employed to realize $\hat{Y}_n(s)$. For two dominant poles the residues lie in region II, so that one of the ladder networks from Figure 4.7 can be directly used. The element values of the driving-point equivalent networks for the two gap locations are listed in Tables 6.2 and 6.3, respectively. These networks were first obtained by *Streable and Pearson* [1981]. We include them here for the sake of completeness, since they are part of the active equivalent networks. The responses of the equivalent networks for a center- and a quarter-driven dipole due to a Gaussian voltage pulse, computed by the SCEPTRE [*Jensen and McNamee*, 1976] circuit analysis program, are compared to the TWTD [*VanBlaricum and Miller*, 1972] time domain integral equation solutions in Figures 6.5 and 6.6, respectively. Except for the early time, the agreement is seen to be quite good. The early time response of the SEM

Table 6.1 Admittance residues a_n, quality factors Q_n, and padding conductances G_n associated with the dominant poles s_n^*) of a center-driven (quarter-driven) dipole antenna with $\Omega = 10.6$.

n	$s_n = -\sigma_n + j\omega_n$	Q_n	$a_n = c_n + jd_n$ [mS]	Region -Case	Padding G_n [mS]	%
1	$-0.2575 + j\ 2.8750$	5.60	$3.5126 + j\ 0.9949$ $(1.9577 + j\ 0.5162)$	III-A (II)	$2.2831*10^{-4}$ (-)	$1.60*10^{-3}$ (-)
2	$-0.3796 + j\ 5.9349$	7.83	$0.0\quad + j\ 0.0$ $(4.0095 + j\ 1.1299)$	- (III-A)	- $(1.896*10^{-2})$	- (0.172)
3	$-0.4667 + j\ 9.0164$	9.67	$4.1748 + j\ 1.0559$ $(1.7375 + j\ 0.7224$	III-A (III-A)	$1.977*10^{-2}$ $(5.732*10^{-2})$	0.215 (1.440)
4	$-0.5368 + j12.104$	11.29	$0.0\quad + j\ 0.0$ $(0.0\quad + j\ 0.0\quad)$	- (-)	- (-)	- (-)
5	$-0.5962 + j15.193$	12.75	$4.5001 + j\ 1.1287$ $(2.9059 + j\ 0.3601)$	III-A (III-A)	$3.191*10^{-2}$ $(3.901*10^{-5})$	0.411 $(7.94*10^{-4})$

Table 6.1 (continued)

n	$s_n = -\sigma_n + j\omega_n$	Q_n	$a_n = c_n + jd_n$	Region –Case	Padding G_n [mS]	%
6	−0.6478 +j18.279	14.12	0.0 +j 0.0 (4.7478 +j 1.3671)	− (III–A)	− $(5.768*10^{-2})$	− (0.761)
7	−0.6932 +j21.359	15.41	4.7326 +j 1.1908 (1.7368 +j 1.0094)	III–A (III–A)	$3.911*10^{-2}$ $(1.315*10^{-1})$	0.558 (4.747)
8	−0.7335 +j24.430	16.66	0.0 +j 0.0 (0.0 +j 0.0)	− (−)	− (−)	− (−)
9	−0.7689 +j27.490	17.88	4.9214 +j 1.2392 (3.3935 +j 0.2283)	III–A (II)	$4.365*10^{-2}$ (−)	0.665 (−)
10	−0.7999 +j30.539	19.10	0.0 +j 0.0 (5.1541 +j 1.5688)	− (III–A)	− $(7.880*10^{-2})$	− (1.183)

*) The poles s_n and residues a_n are normalized to c/ℓ.

Table 6.2 Element values of the dominant pole-pair admittance networks for a center-driven dipole antenna ($\Omega = 10.6$).

BOTT-DUFFIN CIRCUIT-CASE A (Figure 4.12(a))				
n [*)	$C_o/\ell[pF/m]$	$L_1/\ell[\mu H/m]$	$C_1/\ell[pF/m]$	$R_1[k\Omega]$
1	2.9728	0.4584	131.99	2.1290
3	0.5063	0.3875	1.134	4.8650
5	0.2412	0.3595	0.2966	6.3673
7	0.1519	0.3417	0.1329	7.3458
9	0.1089	0.3285	$7.529 * 10^{-2}$	8.0824

[*) Resonant frequencies s_n, $n = 2,4,\dots$ do not contribute to the driving-point network.

Table 6.3 Element values of the dominant pole-pair admittance
networks for a quarter-driven dipole antenna with $\Omega = 10.6$.

LADDER CIRCUIT (Figure 4.7(a))				
$n^{*)}$	$C_1/\ell[pF/m]$	$R_1[\Omega]$	$L_1/\ell[\mu H/m]$	$R_2[k\Omega]$
1	1.6149	7.307	0.8243	4.244
9	$2.998*10^{-2}$	67.612	0.4897	103.08
BOTT-DUFFIN CIRCUIT-CASE A (Figure 4.12(a))				
n	$C_0/\ell[pF/m]$	$L_1/\ell[\mu H/m]$	$C_1/\ell[pF/m]$	$R_1[k\Omega]$
2	1.0326	0.4009	3.1783	3.2045
3	0.3246	0.8869	0.2850	5.0706
5	$8.738*10^{-2}$	0.5696	2.4309	30.882
6	0.2171	0.3375	0.1780	5.3000
7	0.1209	0.8301	$3.797*10^{-2}$	4.5332
10	0.1166	0.3095	$5.693*10^{-2}$	5.7955

*) 4th and 8th resonant frequencies do not contribute to the
driving-point network.

$$V(t) = e^{-\left(\frac{2(t-t_2)}{t_1}\right)^2}$$

$$t_2 = 0.186\ell/c$$

$$t_1 = 0.208\ell/c$$

$$\Omega = 10.6$$

— INTEGRAL EQ(TWTD)

---- CIRCUIT (SCEPTRE)

— — CIRCUIT WITH A SHUNT
CAPACITOR $C_o = 0.7\ell$ pF (SCEPTRE)
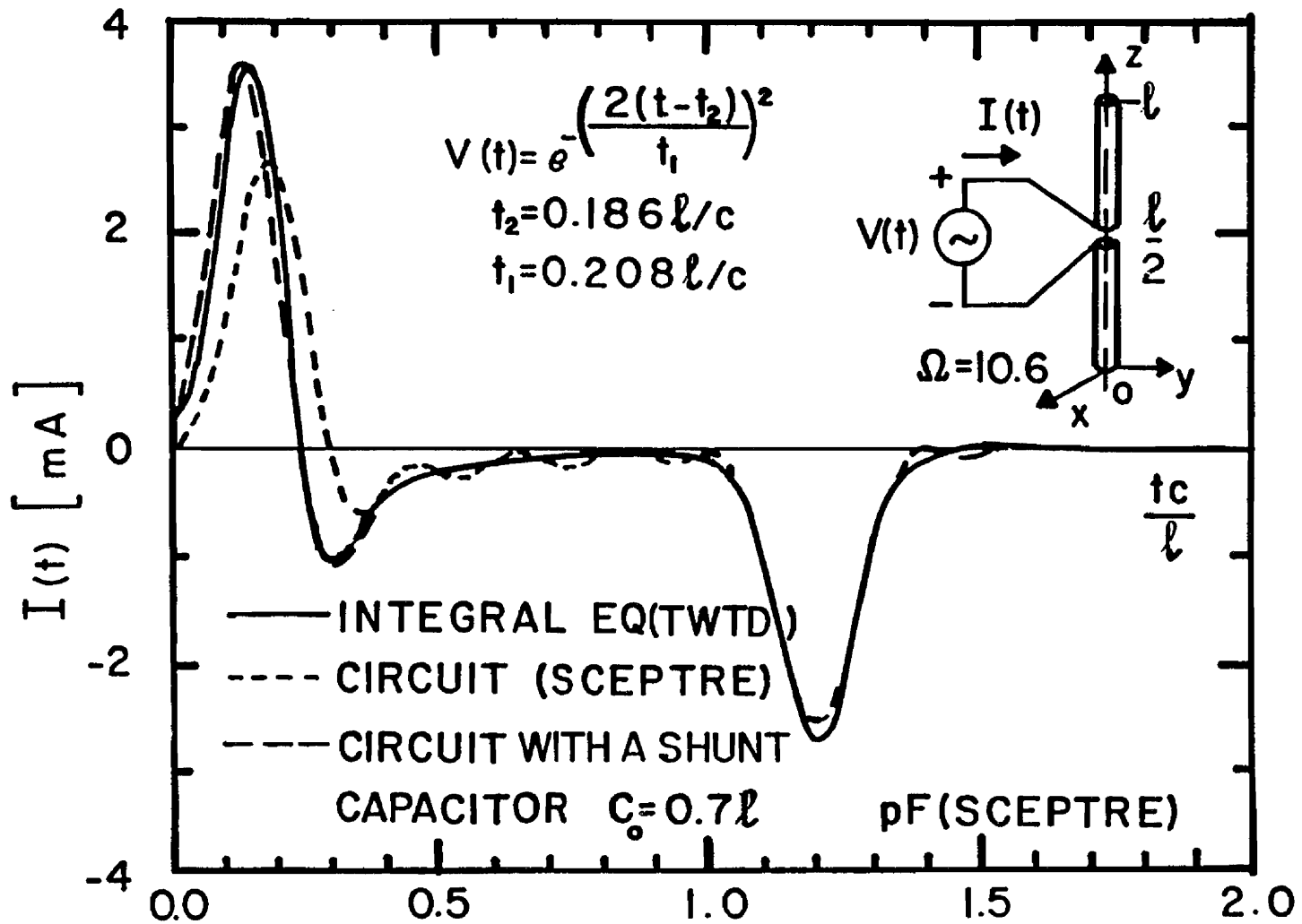
Figure 6.5 Input current of a symmetrical dipole antenna excited by a Gaussian voltage
pulse. SCEPTRE and TWTD results are compared.
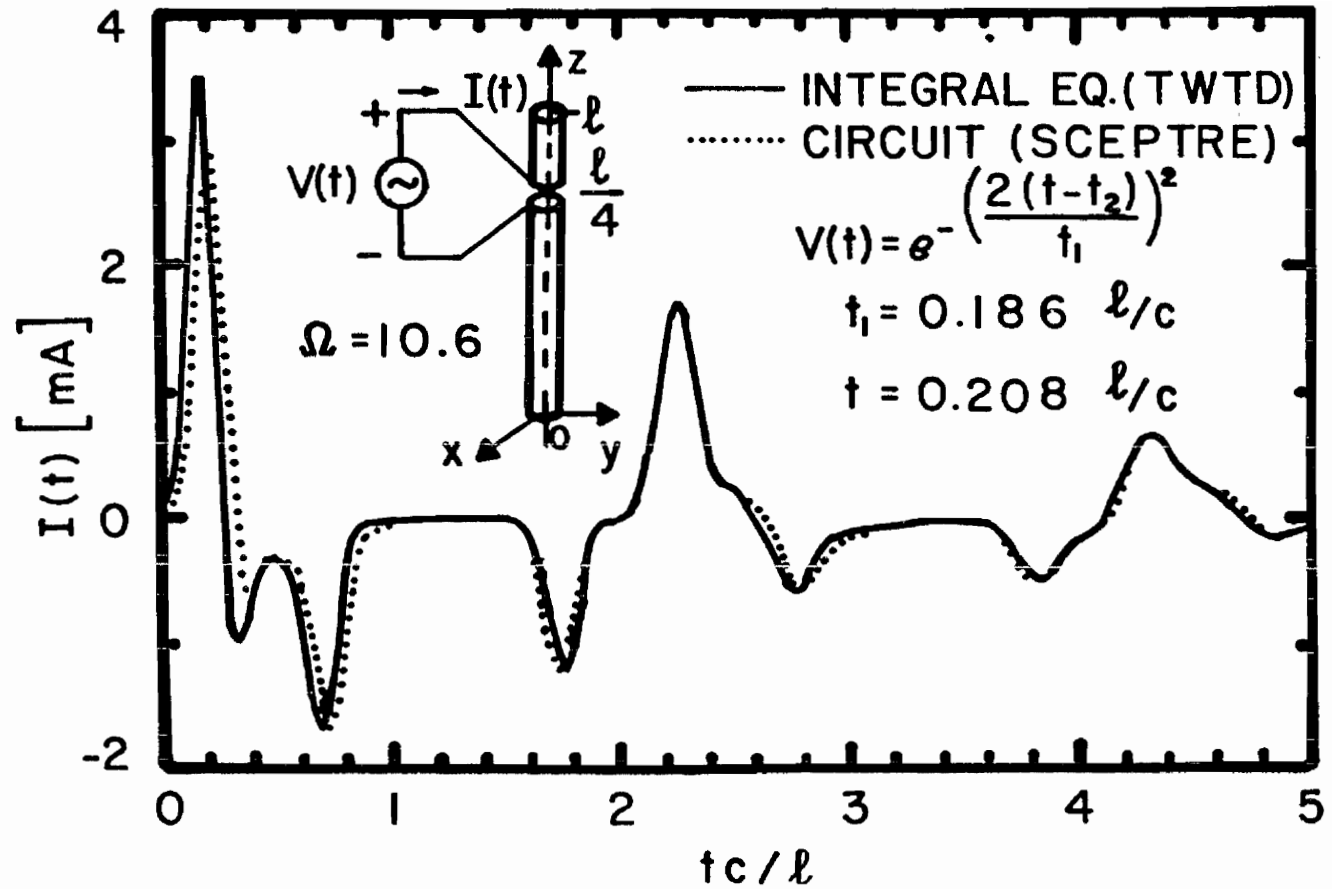
Figure 6.6 Input current of a quarter-driven dipole antenna excited by a Gaussian voltage pulse. SCEPTRE and TWTD results are compared.

equivalent circuit can be significantly improved by augmenting it by a shunt capacitor of a proper value as discussed in Section 3.3. The value of the capacitor must be computed apart from the SEM representation, *e.g.*, by solving for the static charge distribution on the object. The effectiveness of this procedure is illustrated by Figure 6.5 for the center-driven dipole case.

The active part of the equivalent network depends not only on the gap location z_g, but also on the angle of incidence θ of the plane wave. As discussed in Chapter 4, the voltage transfer network realizing $\hat{T}_n(s)$ can be always synthesized in one of the two forms: as a ladder circuit or as a symmetrical lattice circuit. For both cases explicit expressions for the element values in terms of the poles s_n, the admittance residues a_n, the the source coefficients T_n are given in Chapter 4. The expressions for a_n and T_n in the dipole case are given in Sections 6.3 and 6.4, respectively.

The topologies and element values of the first ten dominant pole-pair voltage transfer networks of a dipole ($\Omega = 10.6$) for three gap locations ($z_g = 1/4\ell$, $1/2\ell$, and $3/4\ell$) and three angles of incidence ($\theta = 30°$, $60°$, and $90°$) are listed in Tables 6.4-6.11. As in the loop case, we have chosen to use the RC networks rather than the equivalent RL realizations (see Section 4.4). It was found that less than 10 dominant pole-pair modules were enough to model properly the dipole behavior for the excitations used. To give the reader the idea of the complexity of a typical equivalent circuit for a cylindrical dipole, we show explicitly in Figure 6.7 the topology of the equivalent circuit for the case $z_g = 3/4\ell$ and $\theta = 60°$.

Table 6.4 Element values of the dominant pole-pair voltage transfer networks for a symmetrical dipole antenna $(\Omega = 10.6)$ excited by a plane wave with the angle of incidence $\theta = 30°$.

$n^{*)}$	TOPOLOGY	C_A/ℓ[pF/m]	$R_A[\Omega]$	C_B/ℓ[pF/m]	$R_B[\Omega]$	$\dfrac{\mu}{\ell E_o^i}[V^{-1}]$
1	RC LADDER	5.2643	33.021	1.2561	–	0.2856
3	RC LADDER	25.242	3.261	–	24.501	0.2971
5	RC LADDER	48.227	1.261	–	3.773	0.3003
7	RC LADDER	73.857	0.699	–	1.311	0.2679
9	RC LADDER	100.96	0.474	–	0.603	0.2063

$^{*)}$The transfer networks associated with poles s_n for $n = 2,4,\ldots$ are not present.

Table 6.5 Element values of the dominant pole-pair voltage transfer networks for a symmetrical dipole antenna ($\Omega = 10.6$) excited by a plane wave with the angle of incidence $\theta = 60°$.

n [*]	TOPOLOGY	C_A/ℓ [pF/m]	R_A [Ω]	C_B/ℓ [pF/m]	R_B [Ω]	$\frac{\mu_1}{\ell E_o}$ [V^{-1}]
1	RC LADDER	5.9343	33.021	0.5862	–	0.5512
3	RC LADDER	25.242	4.461	–	8.108	0.2617
5	RC LADDER	48.227	1.285	–	3.576	−0.1600
7	RC LADDER	73.857	0.937	–	0.888	−0.140
9	RC LADDER	100.96	0.418	–	0.726	0.1095

[*] The transfer networks associated with poles s_n for $n = 2,4,...$ are not present.

Table 6.6 Element values of the dominant pole-pair voltage transfer networks for a symmetrical dipole antenna ($\Omega = 10.6$) excited by a plane wave with the angle of incidence $\theta = 90°$.

n [*]	TOPOLOGY	C_A/ℓ [pF/m]	R_A [Ω]	C_B/ℓ [pF/m]	R_B [Ω]	$\dfrac{\mu}{\ell E_o^i}$ [V^{-1}]
1	RC LADDER	6.255	33.021	0.2655	–	0.6705
3	RC LADDER	25.242	4.030	–	10.067	-0.3138
5	RC LADDER	48.227	1.519	–	2.500	0.2178
7	RC LADDER	73.857	0.803	–	1.056	-0.1709
9	RC LADDER	100.96	0.503	–	0.562	0.1431

[*] The transfer networks associated with poles s_n for $n = 2,4,\ldots$ are not present.

162

Table 6.7 Element values of the dominant pole-pair voltage transfer networks for a dipole antenna ($\Omega = 10.6$) with a port located at $z_g = 3/4\ell$, excited by a plane wave with the angle of incidence $\theta = 30°$.

$n^{*)}$	TOPOLOGY	$C_A/\ell[pF/m]$	$R_A[\Omega]$	$C_B/\ell[pF/m]$	$R_B[\Omega]$	$\dfrac{\mu}{\ell E_o^i}[V^{-1}]$
1	RC LATTICE	6.5343	85.682	–	45.512	–1.1166
2	RC LADDER	17.282	16.654	–	11.664	0.6601
3	RC LADDER	19.012	140.06	–	7.150	1.3076
5	RC LADDER	9.458	1.4783	3.0054	–	0.3270
6	RC LADDER	73.053	4.2765	–	0.7229	0.8391
7	RC LATTICE	135.72	1.7579	–	0.9308	0.5839
9	RC LADDER	12.222	6.9463	–	0.4117	2.5852
10	RC LATTICE	291.73	0.2098	–	0.2001	0.3905

$^{*)}$The transfer networks associated with poles s_n for $n = 4$ and $n = 8$ are not present.

Table 6.8 Element values of the dominant pole-pair voltage transfer networks for a dipole antenna ($\Omega = 10.6$) with a port located at $z_g = 3/4\ell$, excited by a plane wave with the angle of incidence $\theta = 60°$.

$n^{*)}$	TOPOLOGY	$C_A/\ell[pF/m]$	$R_A[\Omega]$	$C_B/\ell[pF/m]$	$R_B[\Omega]$	$\dfrac{\mu}{\ell E_o^i}[V^{-1}]$
1	RC LATTICE	6.5343	326.20	–	32.704	−0.8977
2	RC LADDER	17.282	53.300	–	7.873	1.6562
3	RC LATTICE	38.023	10.541	–	5.022	0.5635
5	RC LADDER	12.463	116.34	–	1.4973	−1.9172
6	RC LATTICE	146.11	1.8087	–	0.3729	−0.2019
7	RC LADDER	67.86	3.6660	–	1.8220	0.2238
9	RC LATTICE	24.444	2.3189	–	0.2121	0.1155
10	RC LADDER	145.87	2.7367	–	0.2214	−0.3172

$^{*)}$The transfer networks associated with poles s_n for $n = 4$ and $n = 8$ are not present.

Table 6.9 Element values of the dominant pole-pair voltage transfer networks for a dipole antenna $(\Omega = 10.6)$ with a port located at $z_g = 3/4\ell$, excited by a plane wave with the angle of incidence $\theta = 90°$.

$n^{*)}$	TOPOLOGY	$C_A/\ell[pF/m]$	$R_A[\Omega]$	$C_B/\ell[pF/m]$	$R_B[\Omega]$	$\frac{\mu}{\ell E_o^i}[V^{-1}]$
1	RC LADDER	3.2672	59.993	–	$6.6364*10^3$	0.9079
3	RC LADDER	19.012	6.8684	–	714.10	0.3468
5	RC LADDER	12.463	4.7306	–	2.1503	−0.5473
7	RC LADDER	67.86	1.2662	–	40.147	−0.1615
9	RC LADDER	12.22	3.1582	–	0.4432	0.7591

$^{*)}$The transfer networks associated with poles s_n for $n = 2,4,\ldots$ are not present.

Table 6.10 Element values of the dominant pole-pair voltage transfer networks for a dipole antenna $(\Omega = 10.6)$ with a port located at $z_g = 1/4\ell$, excited by a plane wave with the angle of incidence $\theta = 30°$.

$n^{*)}$	TOPOLOGY	$C_A/\ell [pF/m]$	$R_A[\Omega]$	$\dot{C}_B/\ell [pF/m]$	$R_B[\Omega]$	$\frac{\mu}{\ell E^i_o}[V^{-1}]$
1	RC LADDER	3.2672	313.324	–	73.372	1.4945
2	RC LATTICE	24.219	–	10.345	3.4298	−0.2503
3	RC LATTICE	38.023	9.2271	–	5.3876	−8.3631
5	RC LADDER	12.464	6.5353	–	1.9104	1.0599
6	RC LATTICE	146.11	1.2841	–	0.4072	−0.3074
7	RC LATTICE	135.72	1.5053	–	1.0216	−0.4721
9	RC LATTICE	24.444	9.5141	–	0.1984	−0.1299
10	RC LATTICE	291.74	0.2764	–	0.1628	−0.1993

*)The transfer networks associated with poles s_n for $n = 4$ and $n = 8$ are not present.

Table 6.11 Element values of the dominant pole-pair voltage transfer networks for a dipole antenna $(\Omega = 10.60)$ with a port located at $z_g = 1/4\ell$, excited by a plane wave with the angle of incidence $\theta = 60°$.

$n^{*)}$	TOPOLOGY	C_A/ℓ [pF/m]	$R_A[\Omega]$	C_B/ℓ [pF/m]	$R_B[\Omega]$	$\dfrac{\mu}{\ell E_o^i}[v^{-1}]$
1	RC LADDER	3.2672	193.37	–	85.835	2.1216
2	RC LATTICE	34.563	9.8594	–	5.2595	−0.9495
3	RC LADDER	19.012	159.23	–	7.1066	−0.7308
5	RC LATTICE	24.928	1.5523	–	1.4110	1.4206
6	RC LADDER	73.053	4.3125	–	0.7218	0.4333
7	RC LADDER	11.720	1.2171	56.14	–	0.1158
9	RC LADDER	12.222	5.8927	–	0.4161	−1.0491
10	RC LATTICE	291.74	0.4498	–	0.1326	0.1189

$^{*)}$The transfer networks associated with poles s_n for $n = 4$ and $n = 8$ are not present.
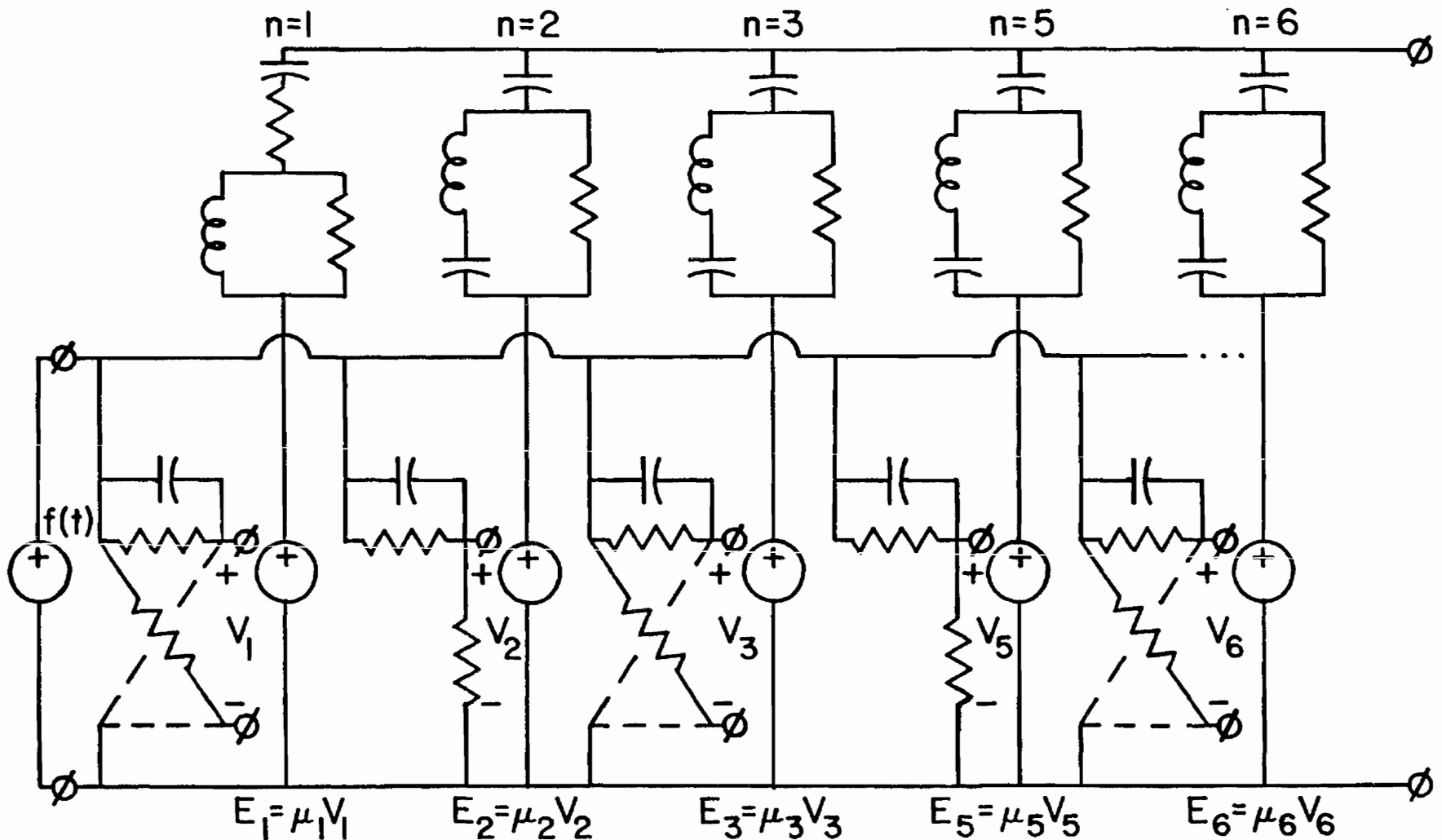
Figure 6.7 Topology of the equivalent circuit for a plane-wave excited cylindrical dipole antenna with the port located at $z = 3/4\ell$ and the angle of incidence $\theta = 60°$.

The short-circuit current responses of the equivalent circuits for a plane wave excited dipole ($\Omega = 10.6$) for various angles of incidence and various gap locations are compared in Figures 6.8-6.15 to results obtained by the TWTD code. The time history of the plane wave is a Gaussian pulse. As can be seen from these figures, the circuit responses computed by SCEPTRE agree favorably with the responses obtained from the time domain integral equation solution.

Finally, in Figure 6.16 is shown the port current of a symmetrical dipole antenna ($\Omega = 10.6$) loaded by a parallel RLC circuit with the quality factor $Q = 40$, the characteristic resistance $R_o = 25\Omega$, and the resonant frequency $\omega_o = \pi$, excited by a plane wave with the angle of incidence $\theta = 60°$ and a double exponential time history. The solid line represents the response obtained from the numerical solution of the integral equation (6.2) (modified by the loading impedance in the port zone) followed by an FFT inversion. The dashed line is the equivalent circuit response obtained from the SCEPTRE analysis. It is seen that the agreement between these two curves is satisfactory, but not as good as in the short-circuit conditions.

6.6 Simplified Equivalent Circuits for a Cylindrical Dipole Based on the Sinusoidal Mode Approximation

It has long been known that the natural current modes of a thin cylinder are approximately sinusoidal [*King*, 1967]. That this is indeed the case was recently confirmed by the numerical work by *Tesche* [1973] where he plotted the "exact" natural modes of a cylinder with $\Omega = 10.6$. *Hallén* [1930] used the sinusoidal approximation
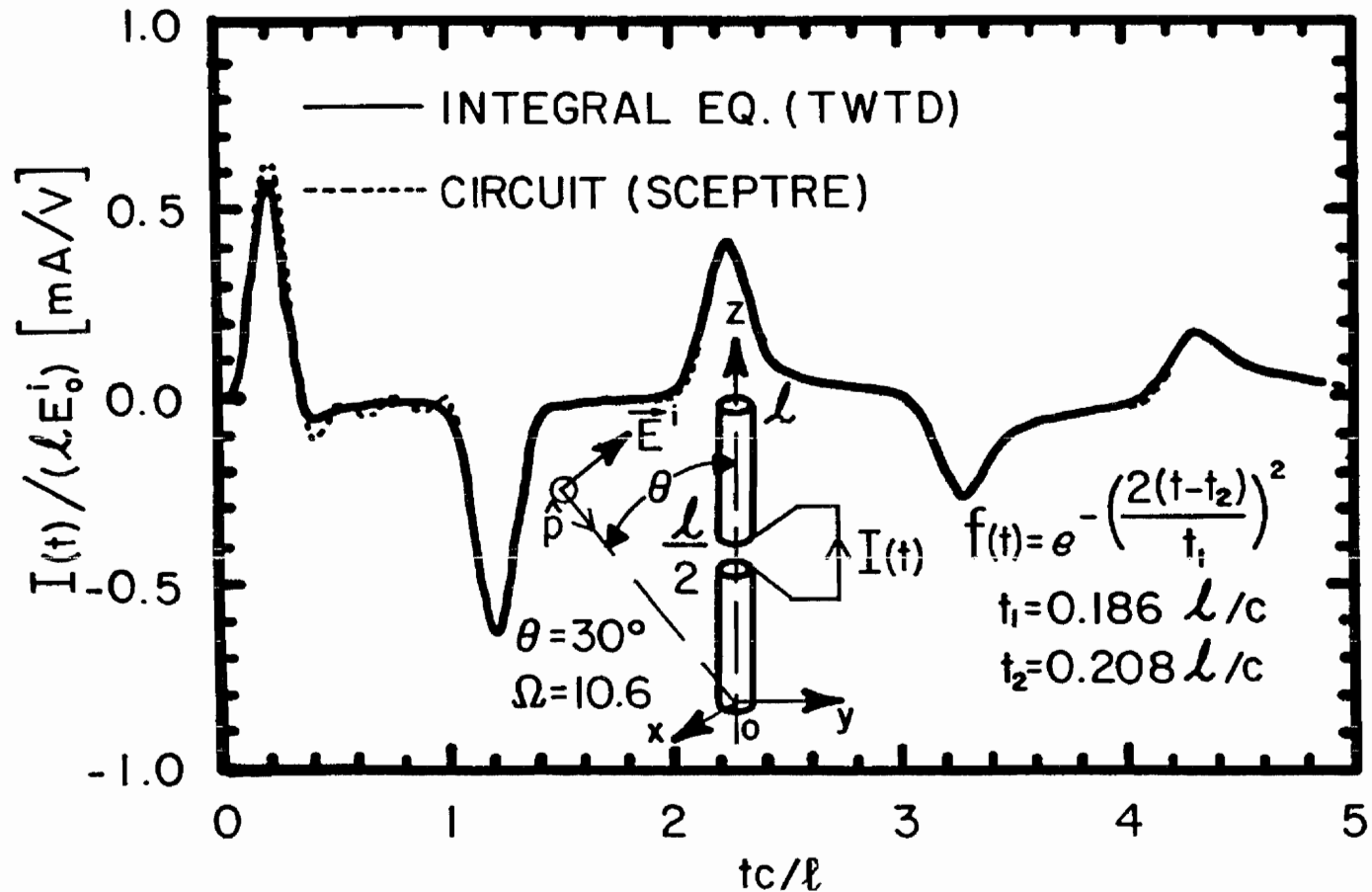
Figure 6.8 Short-circuit current excited in the symmetrical dipole antenna by a Gaussian function plane wave with the angle of incidence $\theta = 30°$. SCEPTRE and TWTD results are compared.
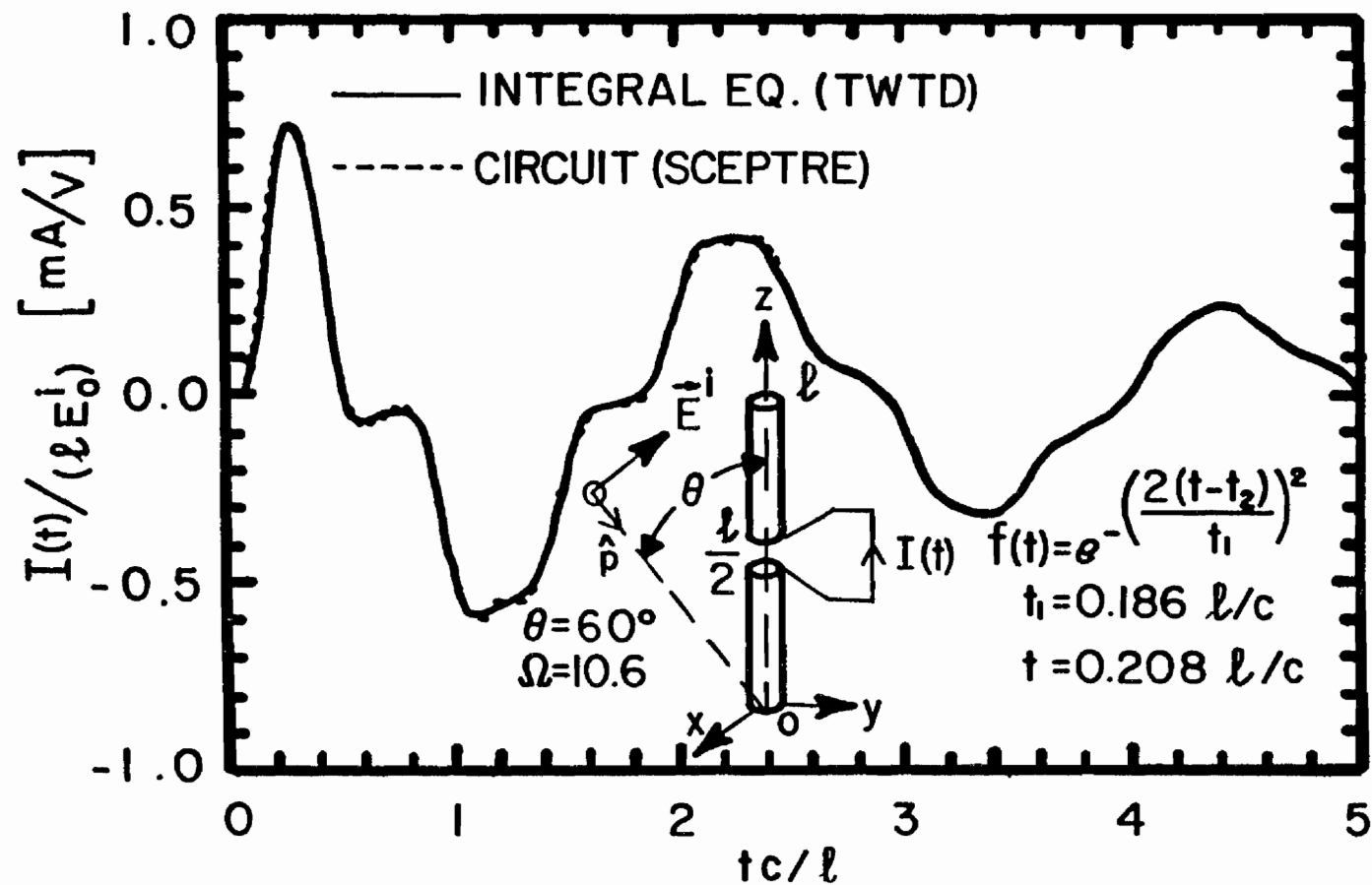
Figure 6.9 Short-circuit current excited in the symmetrical dipole antenna by a Gaussian function plane wave with the angle of incidence θ = 60°. SCEPTRE and TWTD results are compared.

Figure 6.10 Short-circuit current excited in the symmetrical dipole antenna by a Gaussian function plane wave with the angle of incidence $\theta = 90°$. SCEPTRE and TWTD results are compared.
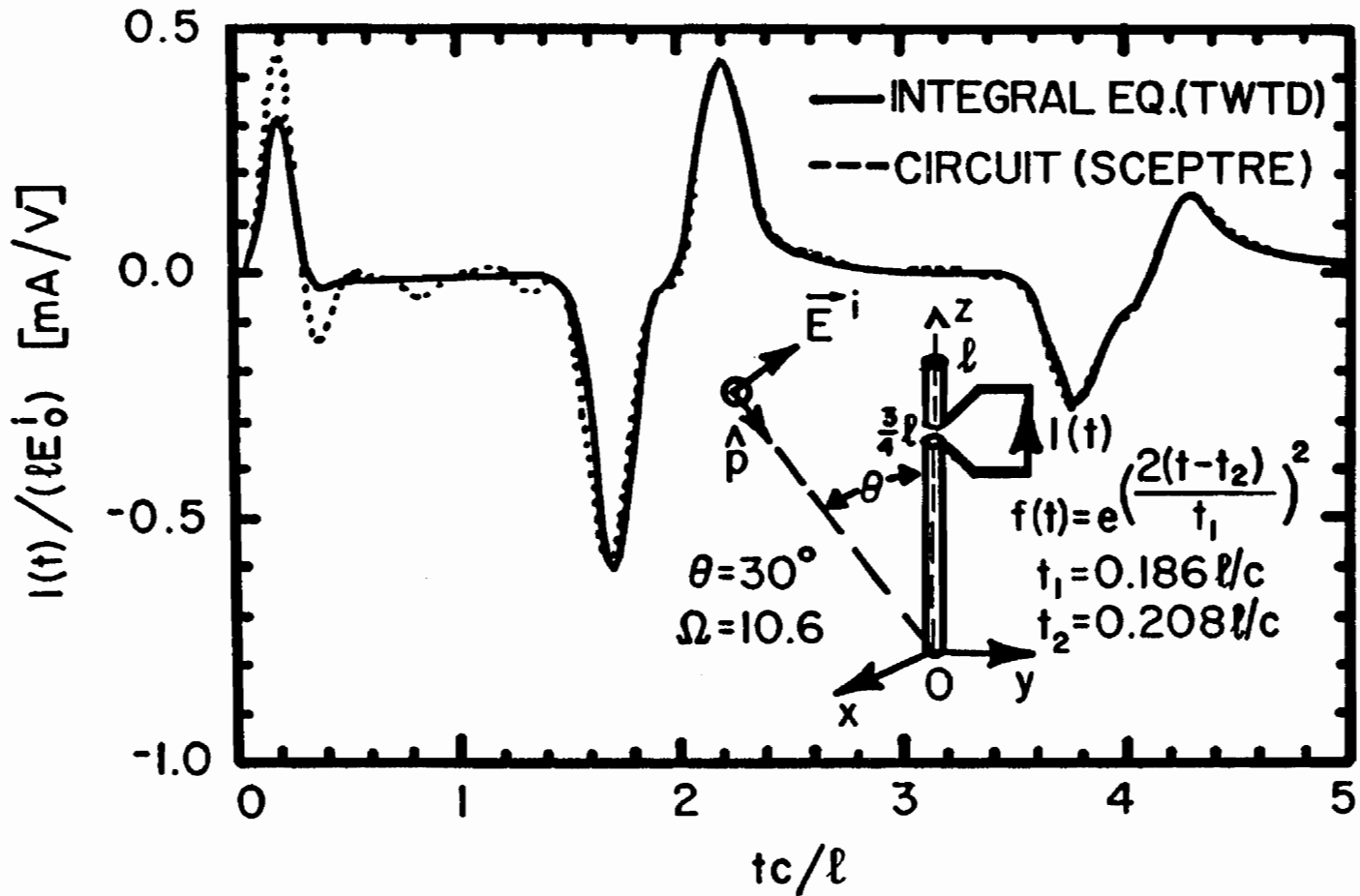
Figure 6.11 Short-circuit current excited in a dipole antenna with a port located at z = 3/4ℓ by a Gaussian function plane wave with the angle of incidence θ = 30°. SCEPTRE and TWTD results are compared.
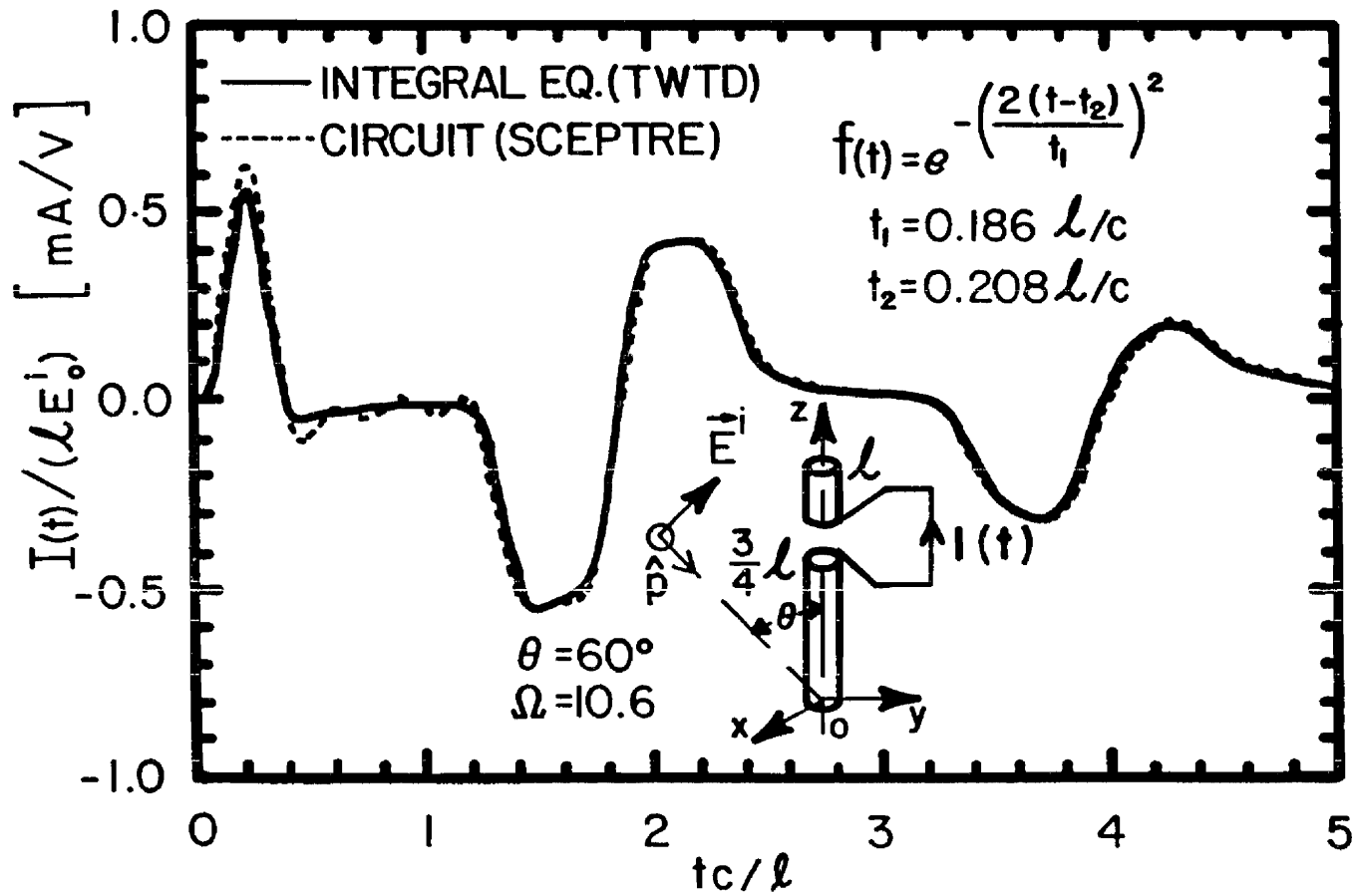
Figure 6.12 Short-circuit current excited in a dipole antenna with a port located at z = 3/4ℓ by a Gaussian function plane wave with the angle of incidence θ = 60°. SCEPTRE and TWTD results are compared.

Figure 6.13 Short-circuit current excited in a dipole antenna with a port located at z = 3/4ℓ by a Gaussian function plane wave with the angle of incidence θ = 90°. SCEPTRE and TWTD results are compared.

Figure 6.14 Short-circuit current excited in a dipole antenna with a port located at $z = 1/4\ell$ by a Guassian function plane wave with the angle of incidence $\theta = 30°$. SCEPTRE and TWTD results are compared.

Figure 6.15 Short-circuit current excited in a dipole antenna with a port located at $z = 1/4\ell$ by a Gaussian function plane wave with the angle of incidence $\theta = 60°$. SCEPTRE and TWTD results are compared.
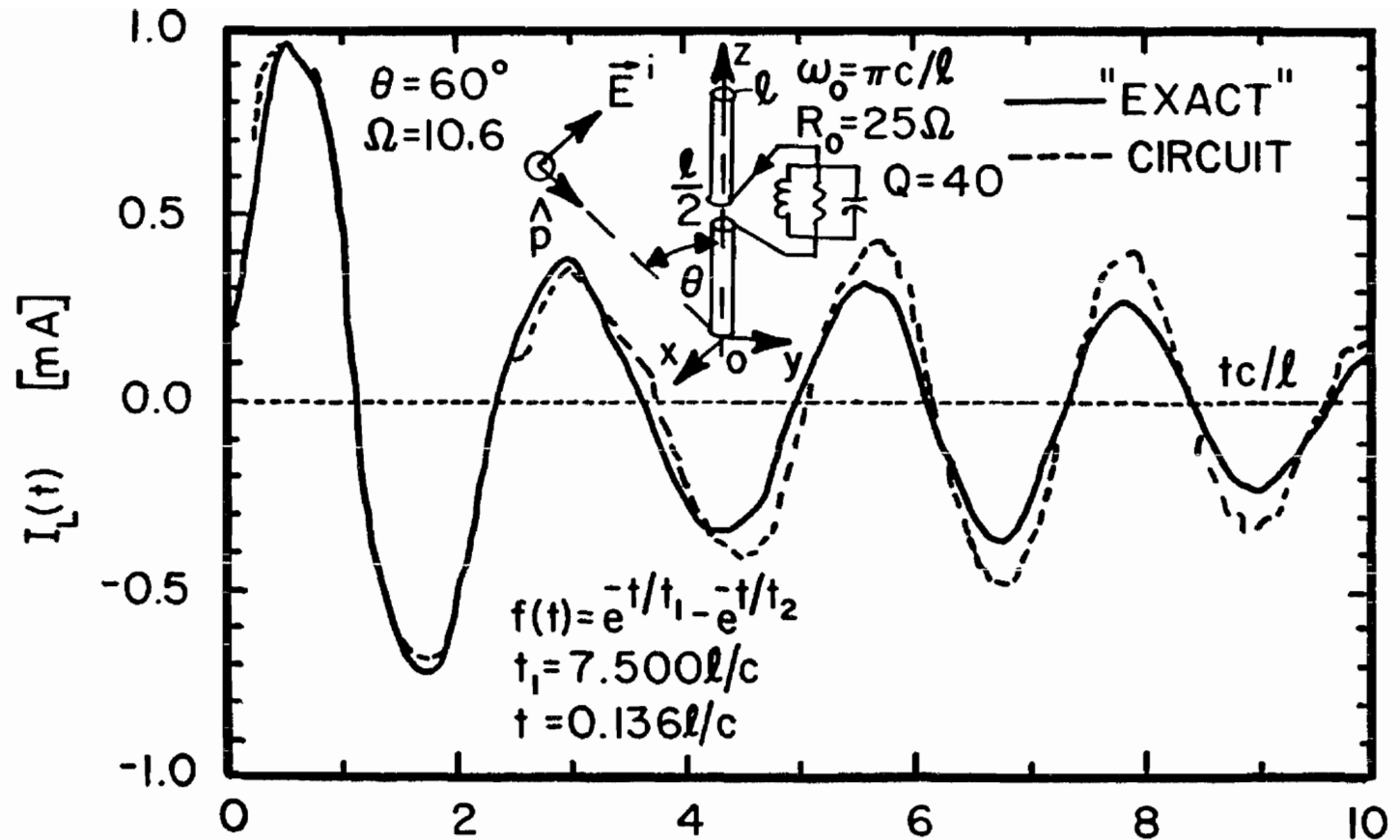
Figure 6.16 Port current of a symmetrical dipole antenna loaded by a parallel RLC resonant circuit and excited by a double-exponential plane wave with the angle of incidence $\theta = 60°$. The SCEPTRE response is compared with the response obtained by solving numerically the integral eq. (6.2) (modified for loading) in the frequency domain and FFT inversion.

$$\tilde{I}_n(z) \cong \sin\left[\frac{n\pi}{\ell} z\right] + O(\Omega^{-1}) \tag{6.15}$$

to derive by an iterative procedure an analytical expression for the
dominant poles of a thin cylinder. In a first order approximation he
obtained

$$s_n = -\frac{\ln(2n\pi\Gamma) - Ci(2n\pi)}{\Omega} + jn\pi\left[1 - \frac{Si(2n\pi)}{n\pi\Omega}\right] + O(\Omega^{-2}) \tag{6.16}$$

where Si and Ci denote the sine and cosine integrals [*Abramowitz and
Stegun*, 1965], respectively, $\Gamma = 1.781...$ is the Euler's constant, and the
poles s_n are normalized to c/ℓ. *Hallén* [1930] (and more recently *Marin*
[1974]) also carried the iteration one step further and obtained
expressions for $\tilde{I}_n(z)$ which are correct up to Ω^{-2} and expressions for
s_n correct up to Ω^{-3}. These expressions are rather complicated,
however. It was found by *Langenberg* [1978] that the first order formula
(6.16) can be used for the first few resonances for cylinders with
$\Omega \gtrsim 12$. The second order formula is good for $\Omega \gtrsim 8$.

The zeroth order approximation to the natural modes (6.15) and
the first order approximation to the poles (6.16) were used successfully
by *Marin and Liu* [1976] and *Langenberg* [1978] for the solution of
transient thin-wire problems and a similar approach was used by
Singaraju and Gardner [1976] for the computation of a transient response
of a helical antenna.

By using the so-called "reduced kernel" [*King*, 1956] in (6.2)
and the sinusoidal current modes (6.15) it can be shown [*Marin*, 1974]
that the normalization constants (normalized to c/ℓ) can be approximated
by

$$\beta_n \cong \frac{4\pi}{Z_o \Omega} \cong \frac{1}{30\Omega} \qquad (6.17)$$

with $Z_o \cong 120\pi$. The admittance residues are thus given by

$$a_n \cong \beta_n \tilde{I}_n^2(z_g) \cong \frac{\sin^2\left[\frac{n\pi}{\ell} z_g\right]}{30\Omega} \quad . \qquad (6.18)$$

For a symmetrical dipole $(z_g = 1/2\ell)$ (6.18) reduces to

$$a_n \cong \frac{1}{30\Omega} \quad , \quad n = 1,3,5,\ldots \qquad (6.19)$$

Note that these residues are real and equal for all poles. For $\Omega = 10.6$, $a_n = (3.145 + j0.0)$ mS, which differs rather significantly from the "exact" residues listed in Table 6.1.

Since the residues (6.19) are purely real, they fall into region I of Figure 4.5. Thus, the pole-pair admittances of a symmetrical dipole can be realized in the unmodified form

$$\hat{\tilde{Y}}_n(s) \cong \frac{1}{30\Omega} \left[\frac{1}{s - s_n} + \frac{1}{s - s_n^*}\right]$$

$$= \frac{1}{15\Omega} \frac{s + \sigma_n}{s^2 + 2\sigma_n s + |s_n|^2} \quad . \qquad (6.20)$$

A continued-fraction expansion [*Matthaei*, 1954] of (6.20) leads to the circuit in Figure 6.17(a) or to its equivalent shown in Figure 6.17(b). The first of these circuits was derived previously by *Baum and Singaraju* [1980].

By a slightly different procedure still another approximation to the pole-pair admittance can be derived:
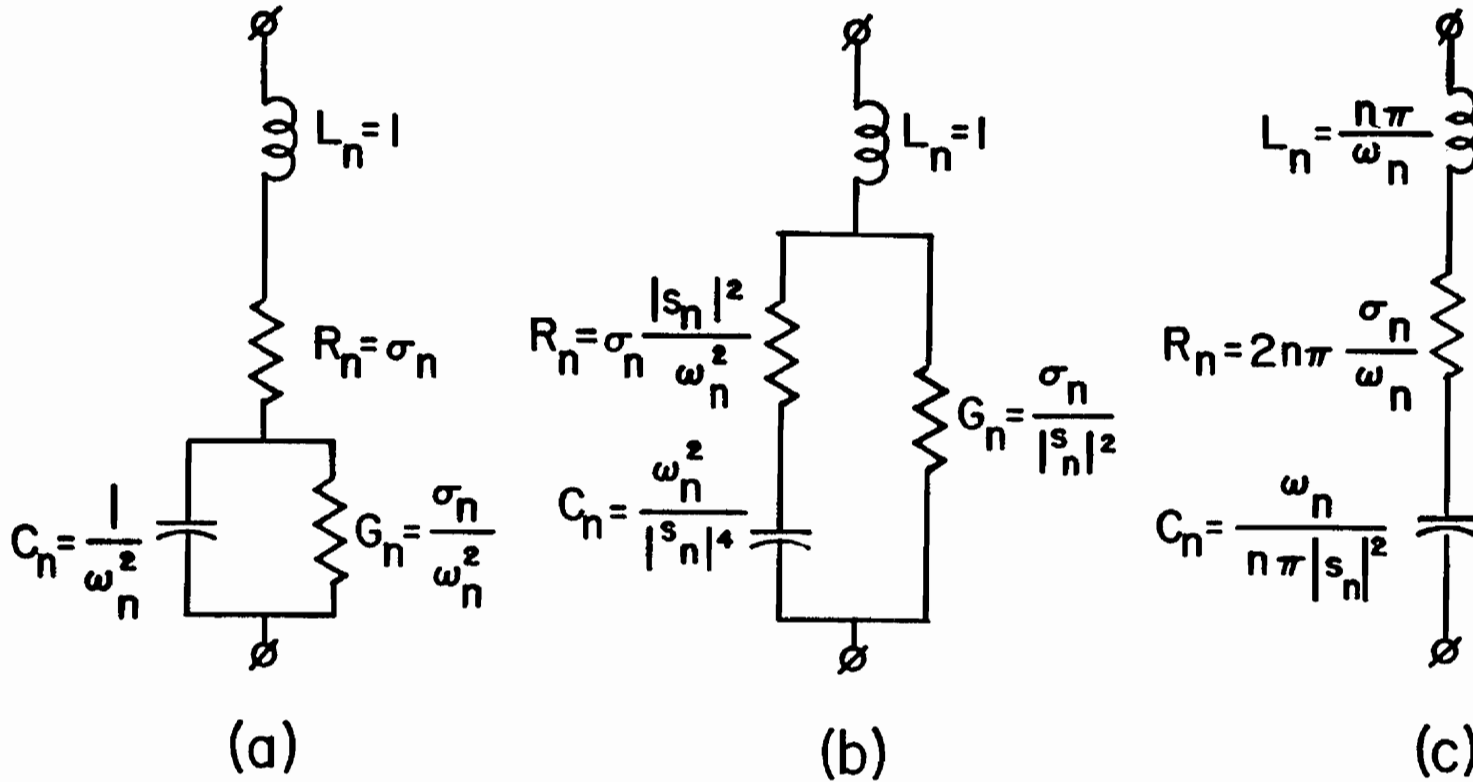
Figure 6.17 Simplified pole-pair admittance circuits derived by the sinusoidal mode approximation (frequency normalization to c/ℓ and impedance level normalization to 15Ω is understood).

$$\tilde{Y}_n(s) \cong \frac{1}{15\Omega} \frac{s}{\left(\frac{n}{\omega_n}\right)^2 s^2 + \left(\frac{2\sigma_n n}{\omega_n}\right)s + \frac{n|s_n|^2}{\omega_n}} \tag{6.21}$$

which can be realized by the circuit shown in Figure 6.17(c). This circuit resembles the circuit used by *Barnes* [1973], but the expressions for the element values are different.

The input current response of the simplified equivalent circuit for a symmetrical dipole ($\Omega = 10.6$) due to a Gaussian voltage pulse is compared in Figure 6.18 to the result of the TWTD code analysis. Also shown in this figure is the response of the "exact" equivalent circuit using the reduced Bott-Duffin modules. As can be seen from this comparison, the response of the simplified circuit is significantly worse than the response of the Bott-Duffin network. Since the complexities of the two circuit topologies are comparable, one can conclude that it is more expedient to employ the padding procedure and the Bott-Duffin realization rather than the sinusoidal mode approximation in the development of the driving-point equivalent circuits.

The sinusoidal natural-mode approximation can be also used to simplify the source synthesis problem of a plane wave illuminated dipole. Namely, the substitution of (6.15) into (6.12) gives

$$T_n = (-1)^{\frac{n-1}{2}} \frac{n\pi}{2} \sin\theta \frac{e^{-s_n(\xi_g - \frac{1}{2})\cos\theta}}{\cos[n\pi(\xi_g - \frac{1}{2})]} \frac{\cosh\left(\frac{s_n\cos\theta}{2}\right)}{\left(\frac{s_n\cos\theta}{2}\right)^2 + \left(\frac{n\pi}{2}\right)^2} \tag{6.22a}$$

for odd values of n, and

$$T_n = (-1)^{\frac{n-2}{2}} \frac{n\pi}{2} \sin\theta \frac{e^{-s_n(\xi_g - \frac{1}{2})\cos\theta}}{\sin[n\pi(\xi_g - \frac{1}{2})]} \frac{\sinh\left(\frac{s_n\cos\theta}{2}\right)}{\left(\frac{s_n\cos\theta}{2}\right)^2 + \left(\frac{n\pi}{2}\right)^2} \tag{6.22b}$$

$$V(t)=e^{-\left(\frac{2(t-t_2)}{t_1}\right)^2}$$

$t_1 = 0.186\ell/c$

$t_2 = 0.208\ell/c$

$\Omega = 10.6$

——— INTEGRAL EQ. (TWTD)

- - - - BOTT-DUFFIN CIRCUIT (SCEPTRE)

— — SINUSOIDAL MODE APPROX.
(SCEPTRE)
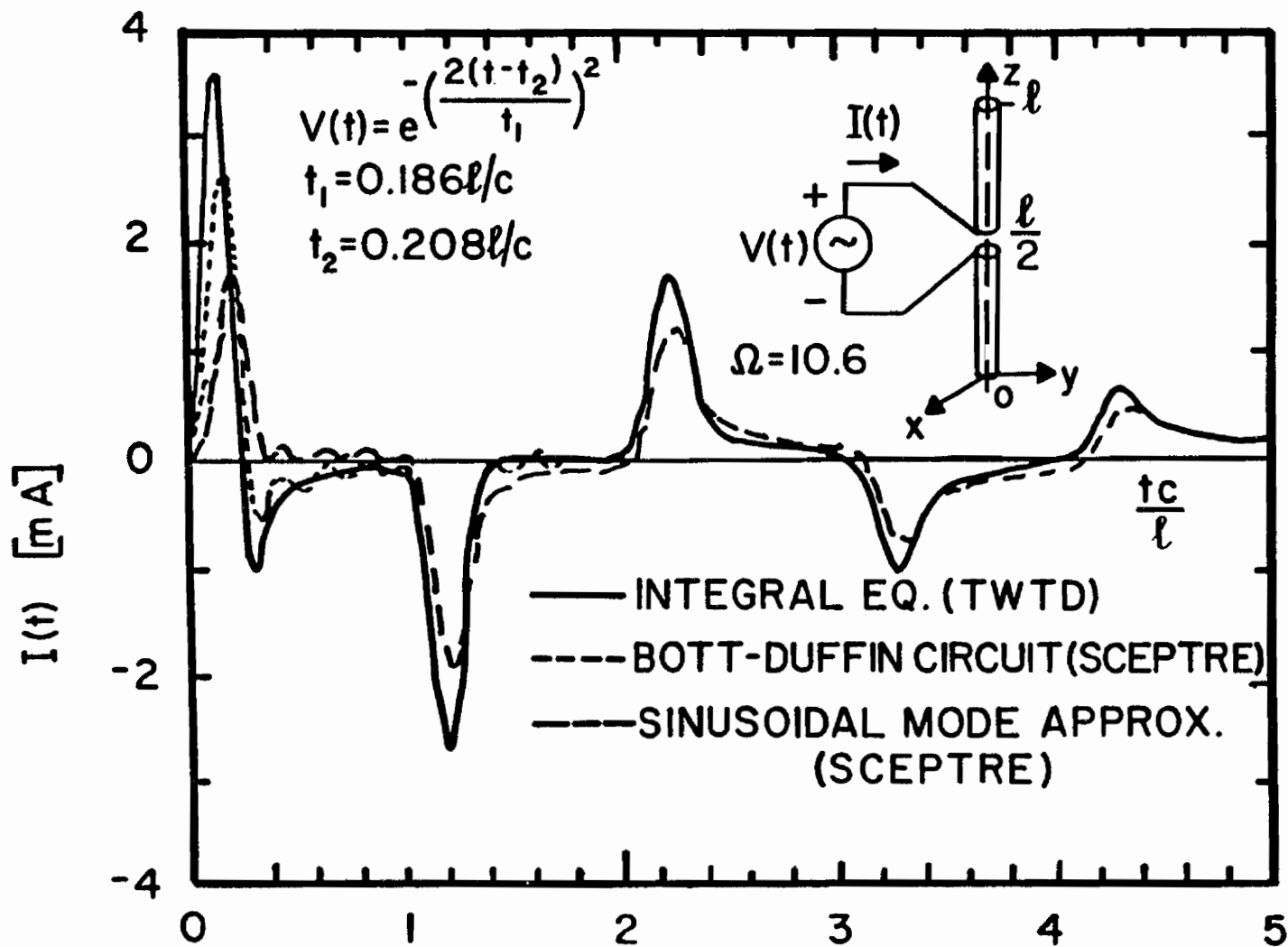
Figure 6.18 Input current of a symmetrical dipole antenna excited by a Gaussian voltage pulse. The TWTD response if compared with the responses of the equivalent circuits using the Bott-Duffin modules and the simplified modules resulting from the sinsoidal mode approximation.

for n even, where $\xi_g = z_g/\ell$. These expressions, which were obtained previously by *Pearson and Wilton* [1981], can be used to approximate the "exact" expressions (6.13) for the source coefficients.

For a symmetrical dipole ($\xi_g = 1/2$) the source coefficient (6.22b) corresponding to an even n has a reciprocal singularity. However, the assocaited admittance vanishes quadratically, so that the entire pole-pair module disappears. The source coefficients corresponding to odd n reduce in this case to

$$T_n = (-1)^{\frac{n-1}{2}} \frac{n\pi}{2} \sin\theta \frac{\cosh\left(\frac{s_n\cos\theta}{2}\right)}{\left(\frac{s_n\cos\theta}{2}\right)^2 + \left(\frac{n\pi}{2}\right)^2} . \tag{6.23}$$

These are still complex numbers, but a further approximation

$$s_n \cong jn\pi \tag{6.24}$$

leads to purely real source coefficients

$$T_n = (-1)^{\frac{n-1}{2}} \frac{2}{n\pi} \frac{\cos\left(\frac{n\pi}{2}\cos\theta\right)}{\sin\theta} . \tag{6.25}$$

Since the T_n's are real numbers, an examination of (3.24) reveals that the voltage transfer functions $\hat{T}_n(s)$ degenerate to real constants which can be realized by VCVS with gain factors given by (6.25).

The gain constants of the simplified dominant pole-pair transfer circuits for a symmetrical dipole ($\Omega = 10.6$) are listed for three different angles of incidence θ in Table 6.12. The topology of a simplified equivalent circuit using the reduced Bott-Duffin modules is shown in Figure 6.19. The short-circuit current response of this network for a plane wave with $\theta = 30°$ and a Gaussian time history is

184

Table 6.12 Gain constants $T_n^{*)}$ of the voltage controlled voltage sources associated with the dominant pole-pairs of a symmetrical dipole antenna (Ω=10.6) excited by a plane wave with the angle of incidence θ=30°, 60°, and 90°.

θ $n^{**)}$	30°	60°	90°
1	0.26598	0.51980	0.63662
3	0.25050	0.17327	-0.21221
5	0.22117	-0.10396	0.12732
7	0.18103	-0.07426	-0.09095
9	0.13415	0.05776	0.07074

$^{*)}$Normalized to (ℓE_o^i).

$^{**)}$Resonant frequencies s_n, n=2,4,..., do not contribute to the equivalent network.

185
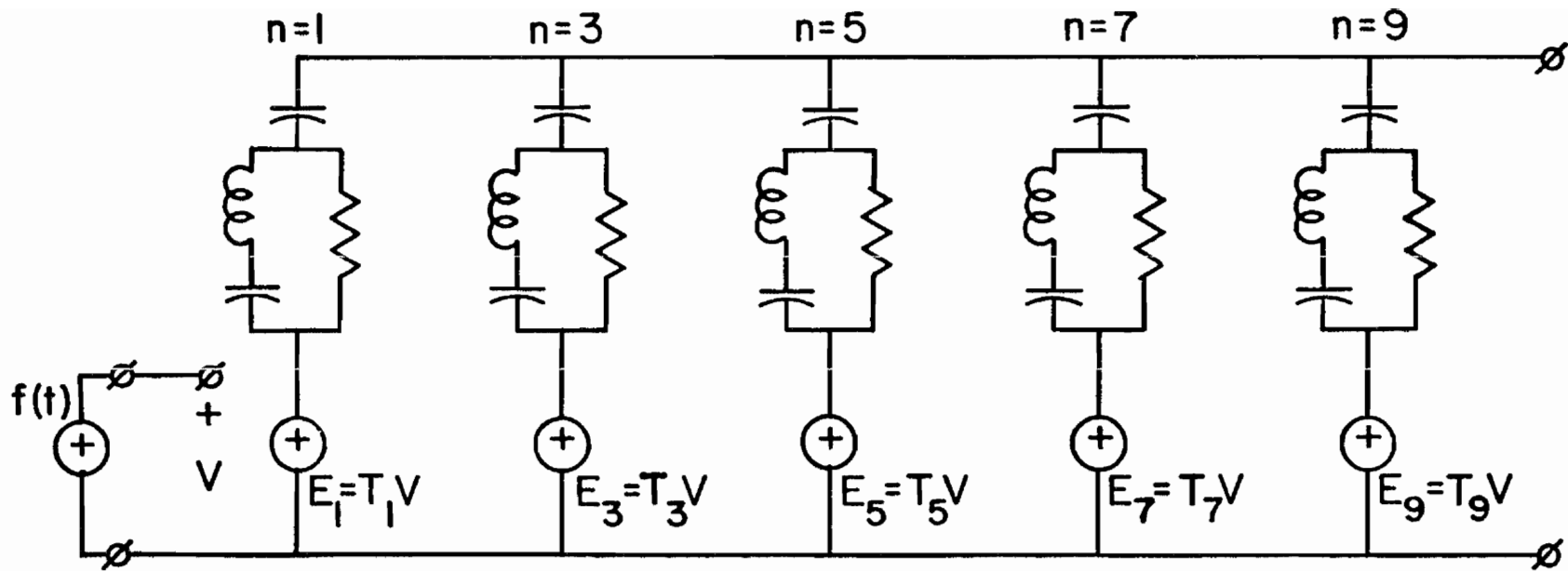
Figure 6.19 Topology of the equivalent circuit for a plane-wave excited symmetrical dipole antenna with simplified voltage transfer networks.

compared in Figure 6.20 to the response obtained from the TWTD code.

The agreement is seen to be very satisfactory. Short-circuit current

responses of the network from Figure 6.19 due to a double-exponential

wave with three angles of incidence: $\theta = 90°$, $60°$, and $30°$ are plotted

in Figure 6.21. These curves agree favorably with the responses

computed by the WT-MBA/LLL1B code [*Landt et al.*, 1974], included in

[*Cho and Cordaro*, 1979].

Finally, in Figure 6.22 we compare the response of the circuit

from Figure 6.19 with $\theta = 90°$ and a Gaussian time history to the response

of the same circuit with the Bott-Duffin modules replaced by the

simplified circuits from Figure 6.17(a). It is seen that there is a

significant deterioration of the circuit performance when the sinusoidal

mode approximation is used in the admittance modules. It appears,

however, that this approximation can be used successfully to simplify

the source modules of an equivalent circuit for a symmetrical dipole

or a cylindrical post over a ground plane.

6.7 Conclusions

The responses of the dominant pole-pair equivalent circuits for

the thin-wire dipole antenna agree favorably with the "exact" responses

obtained from the classical frequency domain—inverse FFT approach.

The amount of padding necessary for physical realizability of the pole-

pair admittances is negligible in comparison with the value of the real

part of the admittances at the resonance.

It is demonstrated that the sinusoidal mode approximation gives

poor results when used in the synthesis of the dominant pole-pair

admittances. However, it can be employed successfully in the synthesis
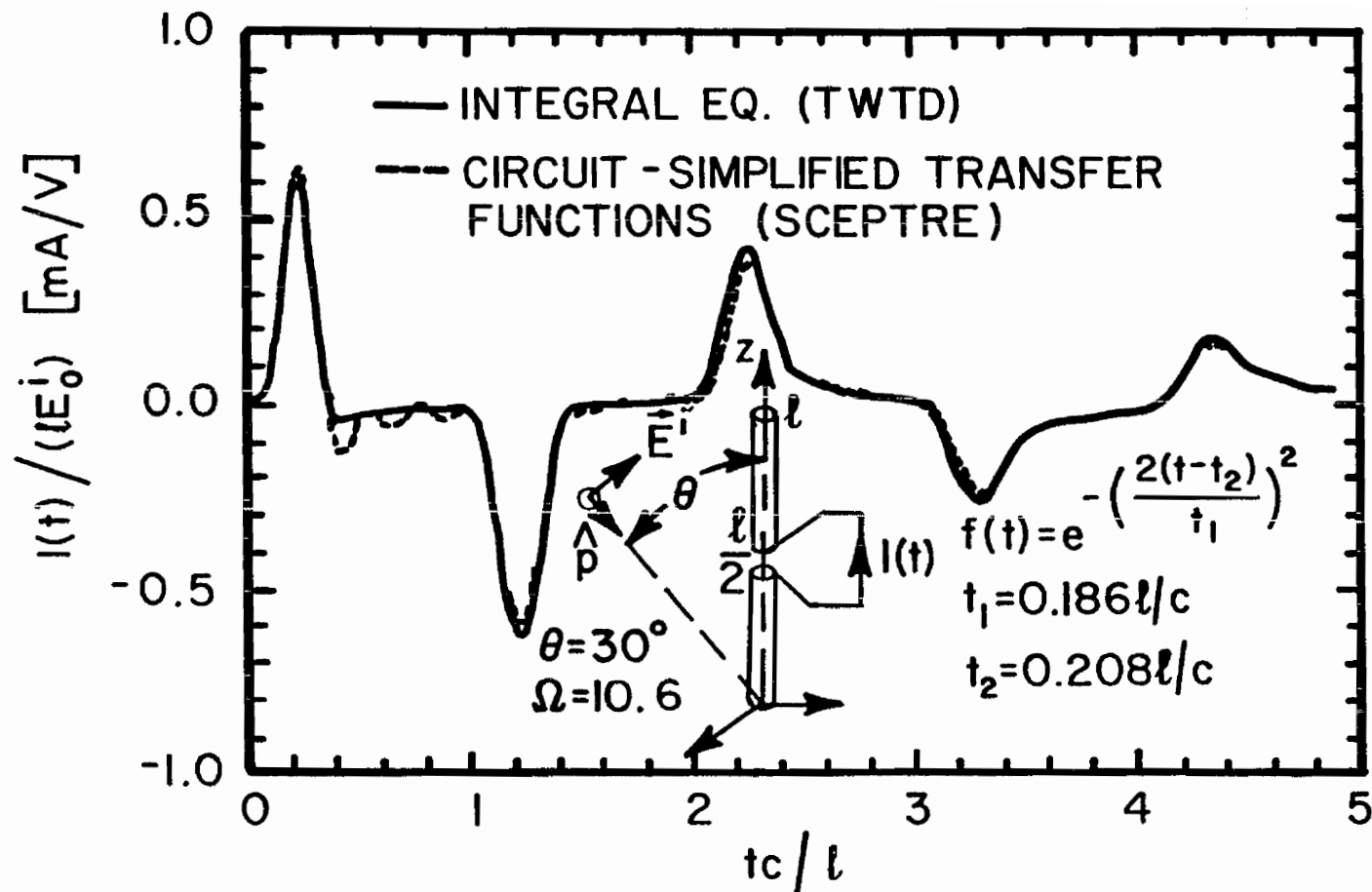
Figure 6.20 Short-circuit current excited in a symmetrical dipole antenna by a Gaussian function plane wave with the angle of incidence $\theta = 30°$. The response of the equivalent circuit with simplified transfer networks is compared with the result of the TWTD analysis.
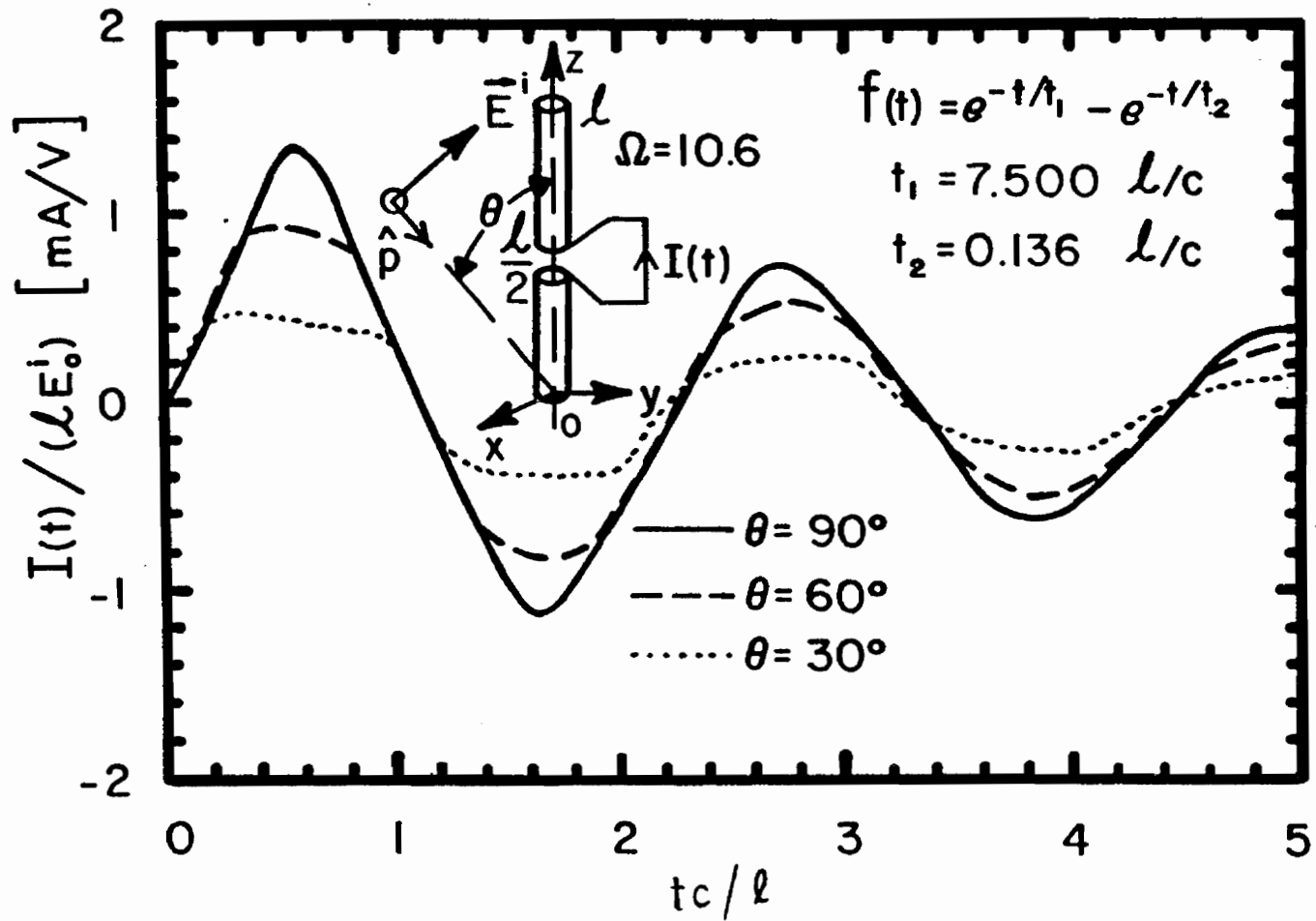
Figure 6.21 Short-circuit current responses excited in a symmetrical dipole antenna by a double-exponential plane wave with various angles of incidence.
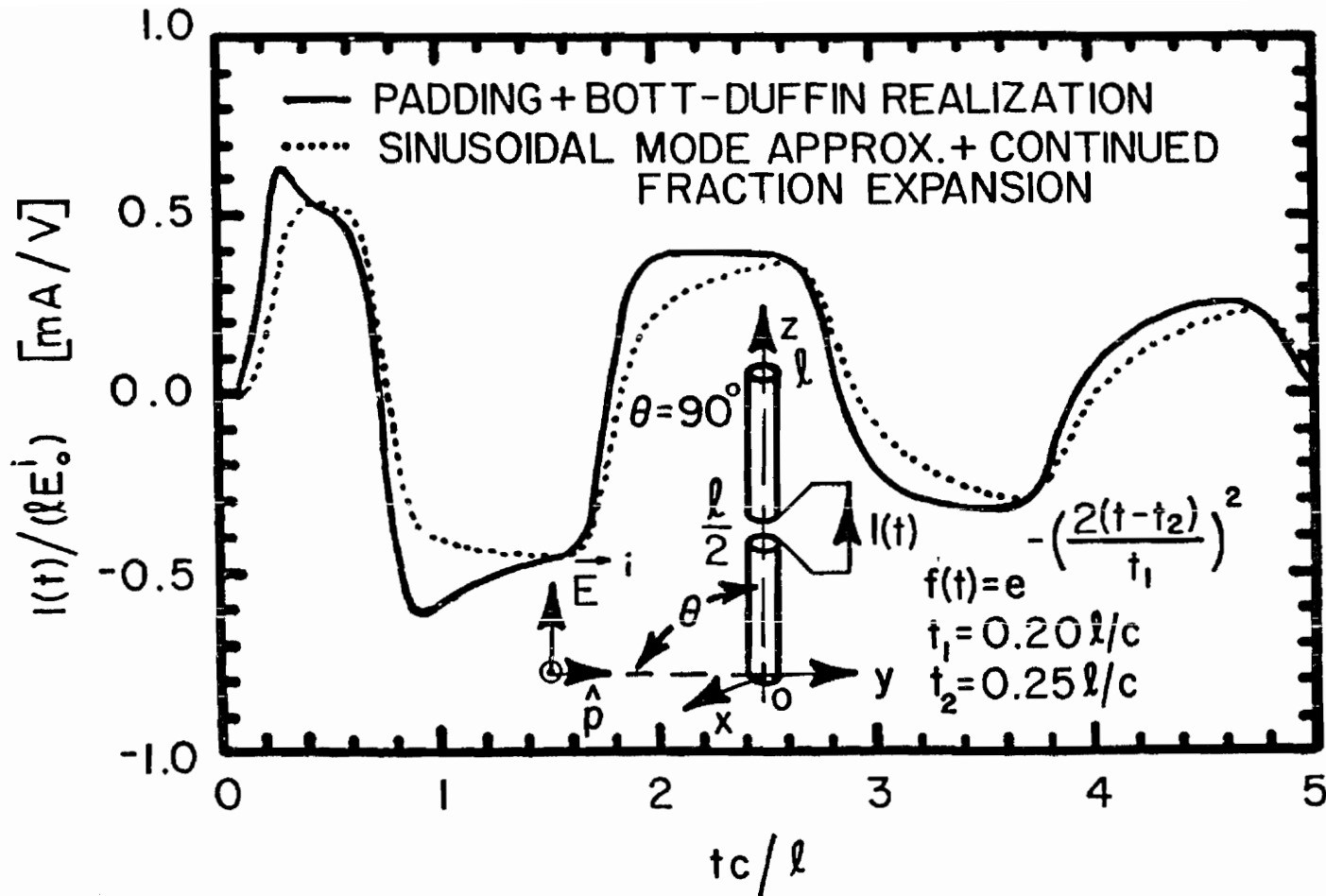
Figure 6.22 Short-circuit current excited in a symmetrical dipole antenna by a Gaussian function plane wave and the angle of incidence $\theta = 90°$. The response of the equivalent circuit with the Bott-Duffin modules is compared with the response of the circuit using simplified modules resulting from the sinusoidal mode approximation.

of the pole-pair voltage transfer networks. For a symmetrical cylin-
drical dipole or a cylindrical post over a ground plane, the pole-
pair transfer networks reduce to just voltage-controlled voltage
sources with gain constants dependent on the angle of incidence of the
impinging plane wave.

CHAPTER 7

EQUIVALENT CIRCUIT SYNTHESIS FOR A SPHERICAL ANTENNA

7.1 Introduction

Although the spherical antenna configuration is not one which

has been employed frequently in practice (its main application has

been in sensors for the electromagnetic pulse (EMP) measurements

[*Baum*, 1969; *Baum et al.*, 1978]), it is nevertheless worthwhile studying

this structure since it is one of the few finite shapes which can be

analyzed exactly. Also, with its resonances so highly damped, it provides

a stringent test for the dominant pole approximation introduced in

Chapter 2.

In the next sections SEM equivalent circuits are derived for a

spherical dipole with a slot along a longitudinal line. The develop-

ment presented here differs in details from the general theory

developed in Chapter 3 due to the explicit appearance of the internal

resonances of the structure in the formulation. This phenomenon,

which has not been taken into consideration in the derivations of

Chapter 3, posed no problem in the thin-wire loop and dipole cases,

since the cavity resonances of these structures lie well outside the

frequency range of interest. Another difficulty not encountered

before is the fact that the extent of the port region of the spherical

antenna is not electrically small. Therefore the time origin cannot

be located in the gap zone independently of the direction of arrival

of the incident field, as suggested in Chapter 2. This difficulty

is overcome by moving the time origin to the point of the first contact

of the gap region with the leading edge of the impinging plane wave.

The static capacitance of the structure can be considered, along with the poles and residues, as an important SEM parameter. If known, it can often be used to improve the early time response of the SEM equivalent circuit by augmenting it by a corrective capacitor of a proper value. Two methods of computation of the static capacitance of the spherical antenna are compared in Appendix C.

The analysis presented in this chapter is perhaps more detailed than the analyses of the loop and cylindrical dipole antennas included in Chapters 5 and 6. Some of the reasons for this are that the spherical geometry is amenable to an exact analysis, and that it provides the "worst case" estimate of the performance of the dominant pole-pair-at-a-time equivalent circuits.

7.2 Preliminary Theory

The surface current density $\tilde{\vec{J}}(\theta,\phi,s)$ on a perfectly conducting sphere of radius a centered at the origin of the spherical coordinate system (r,θ,ϕ) is given by an integral equation of the form

$$\langle \tilde{\overleftrightarrow{\Gamma}}(\theta,\phi,\theta',\phi',s); \tilde{\vec{J}}(\theta',\phi',s) \rangle = (\overleftrightarrow{1} - \hat{n}\hat{n}) \cdot \tilde{\vec{E}}^i(a,\theta,\phi,s) \qquad (7.1)$$

with the symmetric product defined as

$$\langle [\ ];[\ ] \rangle \equiv \int\limits_{-\pi}^{\pi} \int\limits_{0}^{\pi} [\ ]\cdot[\ ] a^2 \sin\theta \, d\theta \, d\phi \; . \qquad (7.2)$$

As in Chapter 2, $\overleftrightarrow{1}$ denotes the identity dyadic, $\hat{n} = \hat{n}(\theta,\phi)$ is a unit vector normal at (θ,ϕ) to the surface of the sphere, and $\tilde{\vec{E}}^i(a,\theta,\phi,s)$ is the factorable incident field evaluated on the sphere surface. As

before, the time history of the incident field is f(t) with the Laplace transform $\tilde{f}(s)$. The dyadic kernel $\overset{\leftrightarrow}{\tilde{\Gamma}}$ can be expanded in terms of the spherical wave functions, as shown by *Tai* [1971]. This representation, when particularized to r = a, as above, constitutes an eigenfunction expansion for $\overset{\leftrightarrow}{\tilde{\Gamma}}$ in the eigenfunctions of the integral operator in (7.1). From this expansion the resolvent kernel $\overset{\leftrightarrow}{\tilde{\Gamma}}{}^{-1}$ can be constructed by means of eigenvalue reciprocation, which leads to the solution of (7.1) in the form

$$
\begin{aligned}
\overset{\rightarrow}{\tilde{J}}(\theta,\phi,s) = \sum_{n=1}^{\infty} & \left\{ \frac{\beta_{n,o}}{\tilde{\lambda}_n^{TM}(s)} \overset{\rightarrow}{\theta}_{n,o,e}(\theta,\phi)\tilde{\eta}_{n,o,e}^{TM}(s) + \frac{\beta_{n,o}}{\tilde{\lambda}_n^{TE}(s)} \vec{R}_{n,o,e}(\theta,\phi)\tilde{\eta}_{n,o,e}^{TE}(s) \right. \\
& + \sum_{m=1}^{n} \sum_{\sigma} \left[\frac{\beta_{n,m}}{\tilde{\lambda}_n^{TM}(s)} \overset{\rightarrow}{\theta}_{n,m,\sigma}(\theta,\phi)\tilde{\eta}_{n,m,\sigma}^{TM}(s) + \frac{\beta_{n,m}}{\tilde{\lambda}_n^{TE}(s)} \vec{R}_{n,m,\sigma}(\theta,\phi)\tilde{\eta}_{n,m,.}^{TE}(s) \right] \Big\} \tilde{f}(s)
\end{aligned}
$$

(7.3)

where the index σ takes on the values "e" (for "even") and "o" (for "odd") and the superscripts TM and TE stand for "transverse magnetic to $\vec{r}$" and "transverse electric to $\vec{r}$", respectively. The meaning of the other symbols is explained below.

The $\tilde{\lambda}_n^{TM}(s)$ and $\tilde{\lambda}_n^{TE}(s)$ are the eigenvalues of the integral operator given by

$$\tilde{\lambda}_n^{TM}(s) = -Z_o[s\,i_n(s)]'[s\,k_n(s)]' \qquad (7.4)$$

and

$$\tilde{\lambda}_n^{TE}(s) = Z_o[s\,i_n(s)][s\,k_n(s)] \qquad (7.5)$$

194

where Z_o is the intrinsic impedance of the medium and the prime denotes differentiation with respect of the normalized complex frequency $s = \gamma a$, γ being the complex propagation constant. The functions $i_n(s)$ and $k_n(s)$ have been introduced by *Baum* [1971] and are related to the spherical Bessel and Hankel functions as

$$i_n(\xi) = j^n \, j_n(-j\xi) \tag{7.6}$$

$$k_n(\xi) = -j^{-n} \, h_n^{(2)}(-j\xi) \quad . \tag{7.7}$$

The eigenfunctions $\vec{Q}_{n,m,\substack{e \\ o}}(\theta,\phi)$ and $\vec{R}_{n,m,\substack{e \\ o}}(\theta,\phi)$ are given by

$$\vec{Q}_{n,m,\substack{e \\ o}}(\theta,\phi) = \frac{\partial P_n^m(\cos\theta)}{\partial\theta} \begin{Bmatrix} \cos(m\phi) \\ \sin(m\phi) \end{Bmatrix} \hat{\theta} + \frac{m}{\sin\theta} P_n^m(\cos\theta) \begin{Bmatrix} -\sin(m\phi) \\ \cos(m\phi) \end{Bmatrix} \hat{\phi} \tag{7.8}$$

and

$$\vec{R}_{n,m,\substack{e \\ o}}(\theta,\phi) = \frac{m}{\sin\theta} P_n^m(\cos\theta) \begin{Bmatrix} -\sin(m\phi) \\ \cos(m\phi) \end{Bmatrix} \hat{\theta} - \frac{\partial P_n^m(\cos\theta)}{\partial\theta} \begin{Bmatrix} \cos(m\phi) \\ \sin(m\phi) \end{Bmatrix} \hat{\phi} \tag{7.9}$$

where P_n^m denotes the associated Legendre functions of degree n and order m [*Abramowitz and Stegun*, 1965]. Note that the eigenfunctions are real and frequency independent. Also, there is a manifold eigenvalue degeneracy due to the sphere symmetry.

The normalization constants $\beta_{n,m}$ are defined as

$$\beta_{n,m} = \left[(1 + \delta_{o,m}) \pi a^2 \, \frac{2n(n+1)(n+m)!}{(2n+1)(n-m)!} \right]^{-1} \tag{7.10}$$

where δ is the Kronecker delta function and the coupling coefficients are given by

$$\eta_{n,m,\sigma}^{\begin{Bmatrix} TM \\ TE \end{Bmatrix}} = \left< \begin{Bmatrix} \vec{Q}_{n,m,\sigma}(\theta,\phi) \\ \vec{R}_{n,m,\sigma}(\theta,\phi) \end{Bmatrix} ; \vec{E}_o(a,\theta,\phi)\tilde{p}(a,\theta,\phi,s) \right> \tag{7.11}$$

where $\vec{\tilde{E}}_o$ is the spatial distribution factor and $\tilde{p}$ is the propagation factor of the incident field (*cf.* eq. (2.6) of Chapter 2).

For the purposes of equivalent circuit synthesis the port current $\tilde{I}(s)$ can be defined as the net surface current passing the specified longitudinal line $\theta = \theta_o$ which coincides with the edge of a narrow circumferential slot in the spherical shell (Figure 7.1). This is the component of current which would excite a load attached to the spherical antenna via a radial or a biconical transmission line. Thus, the port current is given by

$$\tilde{I}(s) = - \int_{-\pi}^{\pi} \hat{\theta} \cdot \vec{\tilde{J}}(\theta_o, \phi, s) \sin\theta_o \, a d\phi \quad . \tag{7.12}$$

An examination of (7.3) reveals that only the $m = 0$, $\sigma = e$ TM terms survive the integration in (7.12), so that

$$\tilde{I}(s) = \frac{\pi}{Z_o} \sum_{n=1}^{\infty} \frac{2n+1}{n(n+1)} \frac{P_n^1(\cos\theta_o)\sin\theta_o}{[s\, i_n(s)]'[s\, k_n(s)]'} \tilde{\eta}_n(s)\tilde{f}(s) \tag{7.13}$$

with the coupling coefficient

$$\tilde{\eta}_n(s) = \frac{1}{2\pi a} <P_n^1(\cos\theta)\hat{\theta}; \vec{\tilde{E}}_o(a,\theta,\phi)\tilde{p}(a,\theta,\phi,s)> \quad . \tag{7.14}$$

7.3 Derivation of the Driving-Point Admittance of the Spherical Antenna

We consider a spherical shell of radius a with a circumferential slot of width $d(d/a = 2\alpha_o)$ with the center located at $\theta = \theta_g$ (Figure 7.1). Let this structure be excited by a ϕ-independent electric field at the surface of the sphere

$$\tilde{E}_\theta(\theta,s) = - \frac{V_o}{a} g(\theta)\tilde{f}(s) \tag{7.15}$$

where

196

$$d/a \simeq 2\alpha_0$$

Figure 7.1 Geometry of the spherical antenna.

197

$$\int_0^\pi g(\theta)d\theta = 1 \qquad (7.16)$$

and where

$$\tilde{V}(s) = V_o \tilde{f}(s) = -\int_0^\pi \tilde{E}_o(\theta,s)ad\theta \qquad (7.17)$$

is the applied voltage. From (7.13) and (7.17) the driving-point admittance $\tilde{Y}(s) = \tilde{I}(s)/\tilde{V}(s)$ takes the form

$$\tilde{Y}(s) = -\frac{\pi}{Z_o}\sum_{n=1}^\infty \frac{2n+1}{n(n+1)} \frac{P_n^1(\cos\theta_o)\sin\theta_o}{[si_n(s)]'[sk_n(s)]'}$$

$$\times \int_0^\pi P_n^1(\cos\theta)g(\theta)\sin\theta d\theta \qquad (7.18)$$

where $\theta_o = \theta_g - \alpha_o$. By using the Wronskian relation for the functions $i_n(s)$ and $k_n(s)$ [*Baum*, 1971]

$$W\left\{i_n(s),k_n(s)\right\} \equiv i_n(s)k_n'(s) - i_n'(s)k_n(s) = -\frac{1}{s^2} \qquad (7.19)$$

it can shown that

$$\frac{-1}{[si_n(s)]'[sk_n(s)]'} = \frac{si_n(s)}{[si_n(s)]'} - \frac{sk_n(s)}{[sk_n(s)]'} . \qquad (7.20)$$

Thus, the driving-point admittance (7.18) can be divided into its internal and external parts [*Baum*, 1969]

$$\tilde{Y}^{int}(s) = \frac{\pi}{Z_o}\sum_{n=1}^\infty \frac{2n+1}{n(n+1)} s\left\{\frac{(n+1)i_n(s)}{[si_n(s)]'}\right\}V_n(\theta_g,\alpha_o) \qquad (7.21)$$

and

$$\tilde{Y}^{ext}(s) = \frac{\pi}{Z_o} \sum_{n=1}^{\infty} \frac{2n+1}{n^2} s\left\{- \frac{nk_n(s)}{[sk_n(s)]'}\right\} V_n(\theta_g, \alpha_o) \qquad (7.22)$$

where

$$V_n(\theta_g, \alpha_o) = \frac{P_n^1(\cos\theta_o)\sin\theta_o}{n+1} \int_0^{\pi} P_n^1(\cos\theta)g(\theta)\sin\theta d\theta \qquad (7.23)$$

can be considered as the excitation voltage of the nth eigenmode [*Franceschetti*, 1976].

The series (7.21) and (7.22) assume the knowledge of the gap field distribution $g(\theta)$. This function depends on the details of the feeder goemetry and requires a solution of a generally complicated boundary value problem. Therefore, it is customary to assume *a priori* the field distribution across the gap. However, this can be justified only for very narrow slots since, as demonstrated by *Franceschetti* [1976], the admittance of the spherical antenna is rather sensitive to the field distribution across the gap. Some of the distribution functions used in the literature are listed below.

1. Delta function [*Stratton and Chu*, 1941; *Karr*, 1951; *Van Bladel*, 1964; *Ramo et al.*, 1965]

$$g(\theta) = \mathcal{E}(\theta-\theta_g) \quad , \quad 0 \leq \theta \leq \pi \qquad (7.24)$$

2. Step function [*Infeld*, 1947; *Weeks*, 1964]

$$g(\theta) = \begin{cases} \frac{a}{d} & , \quad \theta_g - d_o \leq \theta \leq \theta_g + d_o \\ 0 & , \quad \text{otherwise} \end{cases} \qquad (7.25)$$

3. Distribution associated with a biconical transmission line feed [*Schelkunoff*, 1952]

$$g(\theta) = \begin{cases} \dfrac{Z_o}{2\pi k_o \sin\theta} & , \quad \theta_g - d_o \leq \theta \leq \theta_g + \alpha_o \\[20pt] 0 & , \quad \text{otherwise} \end{cases} \qquad (7.26)$$

where K_o is the characteristic impedance of the transmission line given by

$$K_o = \frac{Z_o}{2\pi} \ln\left[\cos\left(\frac{\theta_g - \alpha_o}{2}\right) \tan\left(\frac{\theta_g + \alpha_o}{2}\right)\right] .$$

4. Distribution exhibiting the edge singularity [*Baum*, 1969; *Franceschetti*, 1976]

$$g(\theta) = \begin{cases} \dfrac{1}{\pi\alpha_o} \dfrac{1}{\sqrt{1 - \left(\dfrac{\theta_g - \theta}{\alpha_o}\right)^2}} & , \quad \theta_g - \alpha_o \leq \theta \leq \theta_g + \alpha_o \\[40pt] 0 & , \quad \text{otherwise} \end{cases} \qquad (7.27)$$

5. Distribution approaching the delta function as the parameter $m \to \infty$

$$g(\theta) = \frac{(2m+1)!}{2^{2m+1}(m!)^2}(\sin\theta)^{2m+1} \quad , \quad 0 \leq \theta \leq \pi. \qquad (7.28)$$

This distribution was used by *Infeld* [1947] to investigate the convergence properties of (7.22) as a function of the gap model. A peculiar feature of (7.28) is that it reduces the number of terms in the series (7.21) and (7.22) to m.

The series (7.21) and (7.22) converge very slowly (for the delta gap model they diverge). In some cases the nonlinear transformation technique [*Shanks*, 1955] can be used to accelerate the series convergence. This method was successfully applied in a related problem by *Tesche et al.*]1976]. It seems to be more expedient, however, to follow the technique employed by *Schelkunoff* [1952] and, more recently, by *Franceschetti* [1976] (see also *Bucci and Franceschetti*, 1974]).

They observed that the series (7.21-7.22) represents a pure capacitance in the limit as $s \to 0$. If this series is subtracted term-by-term from the admittance series, its convergence properties improve dramatically. For the symmetrical antenna case ($\theta_g = 90°$) they were able to sum the capacitance series explicitly. An application of this technique to (7.21-7.22) results in

$$\tilde{Y}^{int}(s) = s\, C^{int} + \sum_{n=1}^{\infty} -\frac{\pi}{Z_o} \frac{2n+1}{n(n+1)} \frac{s^2 i_{n+1}(s)}{[si_n(s)]'} V_n(\theta_g, \alpha_o) \tag{7.29}$$

and

$$\tilde{Y}^{ext}(s) = s\, C^{ext} + \sum_{n=1}^{\infty} \frac{\pi}{Z_o} \frac{2n+1}{n^2} \frac{s^2 k_{n-1}(s)}{[sk_n(s)]'} V_n(\theta_g, \alpha_o) \tag{7.30}$$

with the unnormalized interior and exterior capacitances given by

$$C^{int} = \sum_{n=1}^{\infty} \frac{\pi a}{Z_o c} \frac{2n+1}{n(n+1)} V_n(\theta_g, \alpha_o) \tag{7.31}$$

and

$$C^{ext} = \sum_{n=1}^{\infty} \frac{\pi a}{Z_o c} \frac{2n+1}{n^2} V_n(\theta_g, \alpha_o) \quad . \tag{7.32}$$

It is shown in Appendix C that for a narrow equatorial slot ($\alpha_o \ll 1$) with a constant field distribution the capacitances C^{int} and C^{ext} are given by

$$C^{int} \cong \frac{2a}{Z_o c} \left[\ln\left(\frac{a}{d}\right) + 1 \right] \tag{7.33}$$

and

$$C^{ext} \cong \frac{2a}{Z_o c} \left[\ln\left(\frac{a}{d}\right) + 2.93 \right] \quad . \tag{7.34}$$

Perhaps the only practical way to drive or load a spherical antenna is through a biconical or a radial transmission line. In such configuration only the external surface of the sphere is excited. Therefore, the following discussion will concentrate on $\tilde{Y}^{ext}(s)$ (the superscript "ext" is dropped in the rest of this chapter).

By defining

$$b_n = \frac{\pi(2n+1)}{Z_o n^2} V_n(\theta_g, \alpha_o) \qquad (7.35)$$

(7.22) and (7.30) can be rewritten, respectively, as

$$\tilde{Y}(s) = \sum_{n=1}^{\infty} b_n \tilde{y}_n(s) \qquad (7.36)$$

with

$$\tilde{y}_n(s) = - \frac{n \, s \, k_n(s)}{[s k_n(s)]'} \qquad (7.37)$$

and

$$\tilde{Y}(s) = s \, C + \sum_{n=1}^{\infty} b_n \tilde{y}'_n(s) \qquad (7.38)$$

with

$$\tilde{y}'_n(s) = \frac{s^2 k_{n-1}(s)}{[s k_n(s)]'} \ . \qquad (7.39)$$

It is of interest to point out that the normalized eigenadmittances $y_n(s)$ and $y'_n(s)$ have their exact circuit equivalents. Namely, using the recurrence relations for the spherical Bessel function [*Abramowitz and Stegun*, 1965] it can be shown that [*Chu*, 1948; *Thal*, 1978]

202

$$\frac{\tilde{y}_n(s)}{n} = \cfrac{1}{\cfrac{1}{s} + \cfrac{1}{\cfrac{2n-1}{s} + \cfrac{1}{\cfrac{2n-3}{s} + \cfrac{}{\ddots + \cfrac{1}{\frac{1}{s}+1}}}}} \qquad . \tag{7.40}$$

This continued-fraction expansion can be realized by the circuit shown in Figure 7.2(a). In like fashion, it can be shown that

$$\frac{\tilde{y}_n'(s)}{n} = \cfrac{-s^2}{s + \cfrac{2n-1}{s} + \cfrac{1}{\cfrac{2n-3}{s} + \cfrac{}{\ddots + \cfrac{1}{\frac{1}{s}+1}}}} \tag{7.41}$$

which corresponds to the circuit shown in Figure 7.2(b). This representation, which employs a gyrator with the gyration impedance j/s, was suggested by *Franceschetti* [1976].

The normalized eigenadmittance $\tilde{y}_n(s)$ can be explicitly expressed as a rational function of s. This can be done by noting that [*Baum*, 1971]

$$k_n(s) = \frac{e^{-s}}{s} \sum_{m=0}^{n} \frac{(n+m)!}{m!(n-m)!} (2s)^{-m} = \frac{e^{-s}}{s} w_n(1/s) \tag{7.42}$$

where $w_n(1/s)$ denotes a Bessel polynomial in $1/s$ [*Balabanian*, 1958]. For notational simplicity it is helpful to define

$$P_n(s) = s^n w_n(1/s) = \sum_{m=0}^{n} \frac{(n+m)! \, s^{n-m}}{2^m m!(n-m)!}$$

$$= \sum_{m=0}^{n} d_{m,n} s^m \tag{7.43}$$

with

$\widetilde{y}_n(s) \rightarrow$

$\dfrac{1}{n(2n-1)}$ $\dfrac{n}{(2n-3)}$ $\dfrac{1}{n(2n-5)}$ $\dfrac{1}{n}$

n elements

(a)

$\widetilde{y}_n'(s) \rightarrow$

j/s

1 $\dfrac{1}{n(2n-1)}$ $\dfrac{n}{(2n-3)}$ $\dfrac{1}{n(2n-5)}$ $\dfrac{1}{n}$

(b) n elements
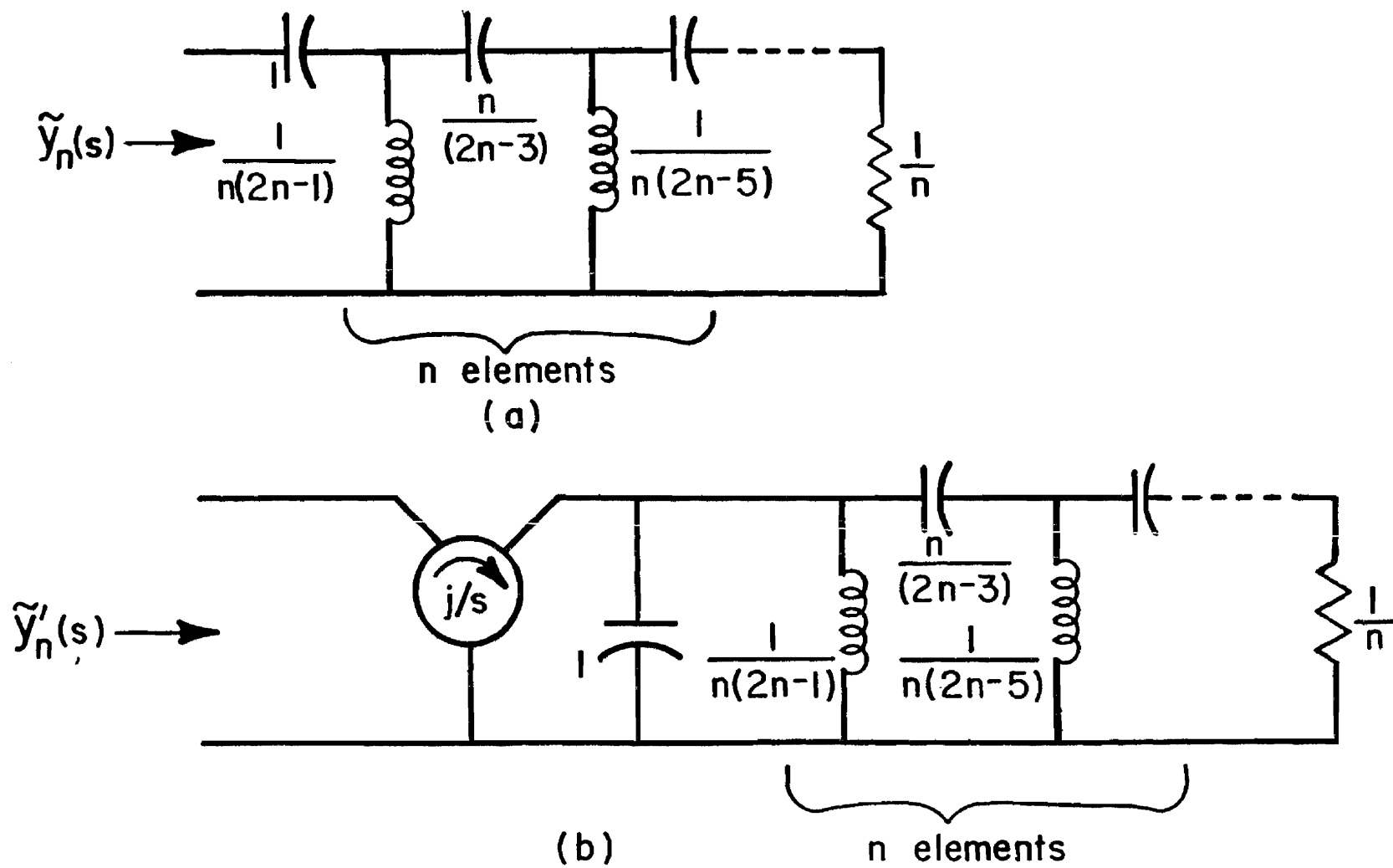
Figure 7.2 Circuit representations of the normalized admittance functions of a spherical antenna.

204

$$d_{m,n} = \frac{(2n-m)!}{2^{n-m}m!(n-m)!} \quad .$$ (7.44)

Then $\tilde{y}_n(s)$ can be written as

$$\tilde{y}_n(s) = \frac{n \, s \, p_n(s)}{n \, p_n(s) + s^2 p_{n-1}(s)}$$

$$= \frac{s \sum\limits_{m=0}^{n} \left(\dfrac{d_{m,n}}{d_{o,n}}\right) s^m}{\left[1 + s + \sum\limits_{m=2}^{n} \left(\dfrac{n \, d_{m,n} + d_{m-2,n-1}}{n \, d_{o,n}}\right) s^m + \left(\dfrac{1}{n \, d_{o,n}}\right) s^{n+1}\right]} \quad .$$ (7.45)

Note that the numerator and the denominator polynomials in (7.45) are of the same order and that $\tilde{y}_n(0) = 0$. It follows from this that the modified pole expansion (2.24) is applicable in the spherical antenna case.

From (7.45) the zeros and poles of $\tilde{y}_n(s)$ can be easily found as the roots of the numerator and the denominator polynomial, respectively. The poles and zeros of the first six eigenadmittances occuring in the upper left quadrant of the complex frequency plane are shown in Figure 7.3. It should be noted that the first layer poles of the sphere are much more damped than the dominant poles of the thin-wire loop and dipole antennas. Incidentally, the zeros of the TM admittances, except for the zero at the origin, are also the poles of the terms associated with the TE eigenmodes in eq. (7.3). Extensive listings of the sphere poles are included in [*Martinez et al.*, 1972; *Granzow*, 1966].

The residue r_{ni} at the ith pole of the nth eigenadmittance s_{ni} can be found as

205
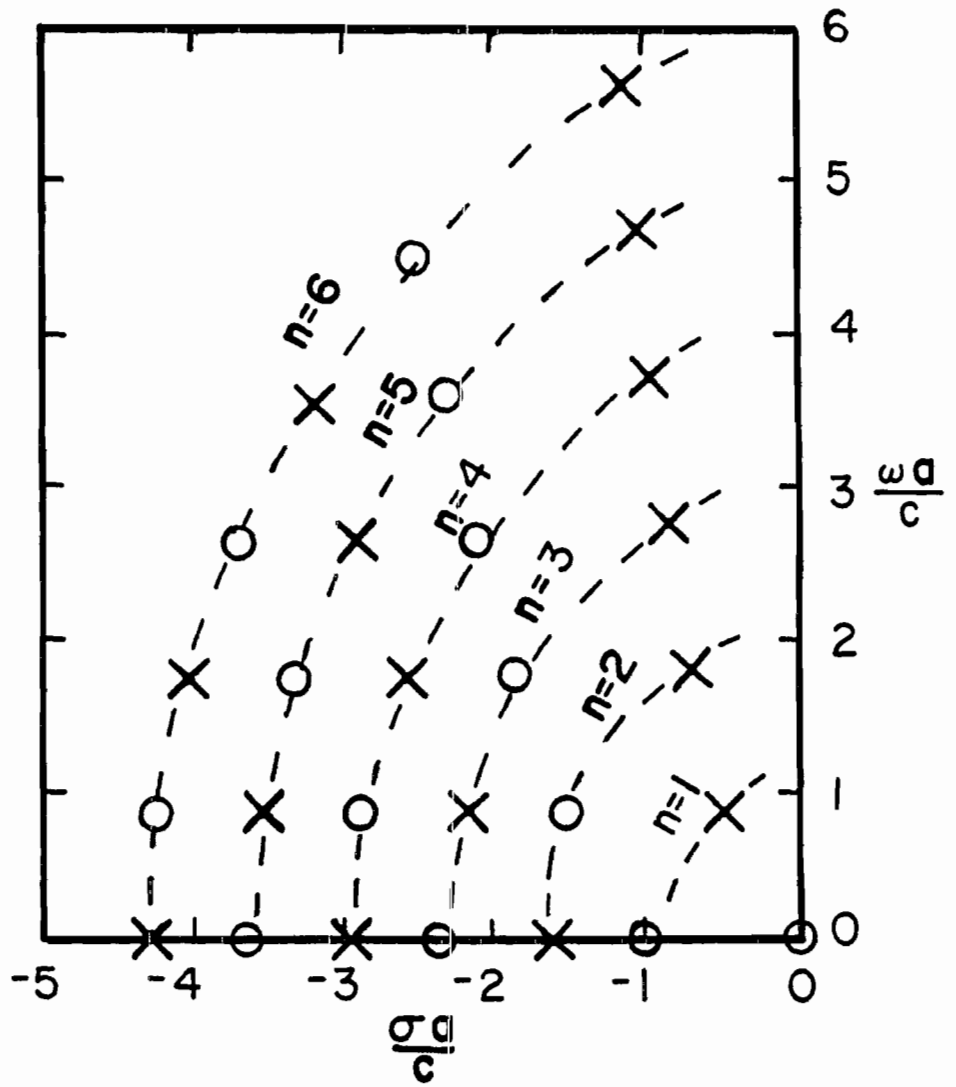
Figure 7.3 Pole (x) and zero (o) distributions of the first six
TM eigenmodes of the sphere (the zero at the origin belongs to all
eigenmodes).

206

$$r_{ni} = - \lim_{s \to s_{ni}} \left\{ (s - s_{ni}) \frac{n \, sk_n(s)}{[sk_n(s)]'} \right\}$$

$$= - \frac{n \, s_{ni} k_n(s_{ni})}{[sk_n(s_{ni})]''} = - \frac{n \, s_{ni}^2}{[s_{ni}^2 + n(n+1)]} \quad . \tag{7.46}$$

This simple expression follows from the Ricatti-Bessel equation [*Baum*, 1971]

$$\frac{s^2}{s^2 + n(n+1)} [s \, k_n(s)]'' - s \, k_n(s) = 0 \quad . \tag{7.47}$$

Denoting the dominant pole of the nth eigenadmittance by s_n and the corresponding residue by r_n, the nth normalized eigenadmittance can be approximated by

$$\tilde{y}_n(s) \cong s \left[\frac{r_n}{s_n(s - s_n)} + \frac{r_n^*}{s_n^*(s - s_n^*)} \right] \quad . \tag{7.48}$$

Using this in (7.36) and taking N dominant pole pairs gives

$$\tilde{Y}(s) \cong \sum_{n=1}^{N} [\tilde{Y}_n(s) + \tilde{Y}_{-n}(s)] = \sum_{n=1}^{N} \hat{\tilde{Y}}_n(s) \tag{7.49}$$

where the modified pole admittance $\tilde{Y}_n(s)$ and the modified pole-pair admittance $\hat{\tilde{Y}}_n(s)$ are defined by (3.11) and (3.16), respectively, with the admittance residue given by

$$a_n = b_n r_n \tag{7.50}$$

or, more explicitly, by

$$a_n = - \frac{\pi a}{Z_o d} \frac{2n+1}{n(n+1)} \frac{s_n^2}{[s_n^2 + n(n+1)]} \, P_n^1(\cos\theta_o)\sin\theta_o \int_{\theta_g - \alpha_o}^{\theta_g + \alpha_o} P_n^1(\cos\theta)\sin\theta d\theta \tag{7.51}$$

In Figure 7.4 is shown the behavior of $\tilde{Y}(j\omega)$ of a spherical antenna ($\theta_g = 90°$, $d/a = 0.05$) computed from the quickly convergent formula (7.38) with the static capacitance given by (7.34) as $C = 104.74$ a [pF]. It is seen from this figure that the driving-point admittance of the spherical antenna evaluated on the $j\omega$-axis does not exhibit resonances and remains capacitive at all frequencies. On the same figure is plotted the admittance obtained from the dominant-pole approximation (7.49). Shown is also the character of the imaginary part when the dominant pole-pair admittance is augmented by a corrective shunt capacitor adjusting the static capacitance of the circuit to the proper value. It is evident from the comparison of these plots that the dominant-pole formula, even with the capacitive correction, gives a poor approximation to the admittance of the spherical antenna.

7.4 Derivation of the Short-Circuit Current of the Spherical Antenna

For the short-circuit current computation the spherical antenna, with its slot closed, is excited by a plane wave incident field with the polarization as indicated in Figure 7.1. No generality is sacrificed by limiting the discussion to this polarization since the field component parallel to the x,y plane does not contribute to the net current across the gap. Also, the discussion can be simplified by making the propagation vector $\hat{p}$ parallel to the x,z plane. Since the antenna geometry is independent of ϕ, this represents no loss in generality, either.

The plane wave incident field is given by eq. (2.7) of Chapter 2 with $\vec{E}_o = \hat{u} E_o$, where $\hat{u}$ is the unit polarization vector, as shown in Figure 7.1. Since the extent of the gap region of the spherical antenna
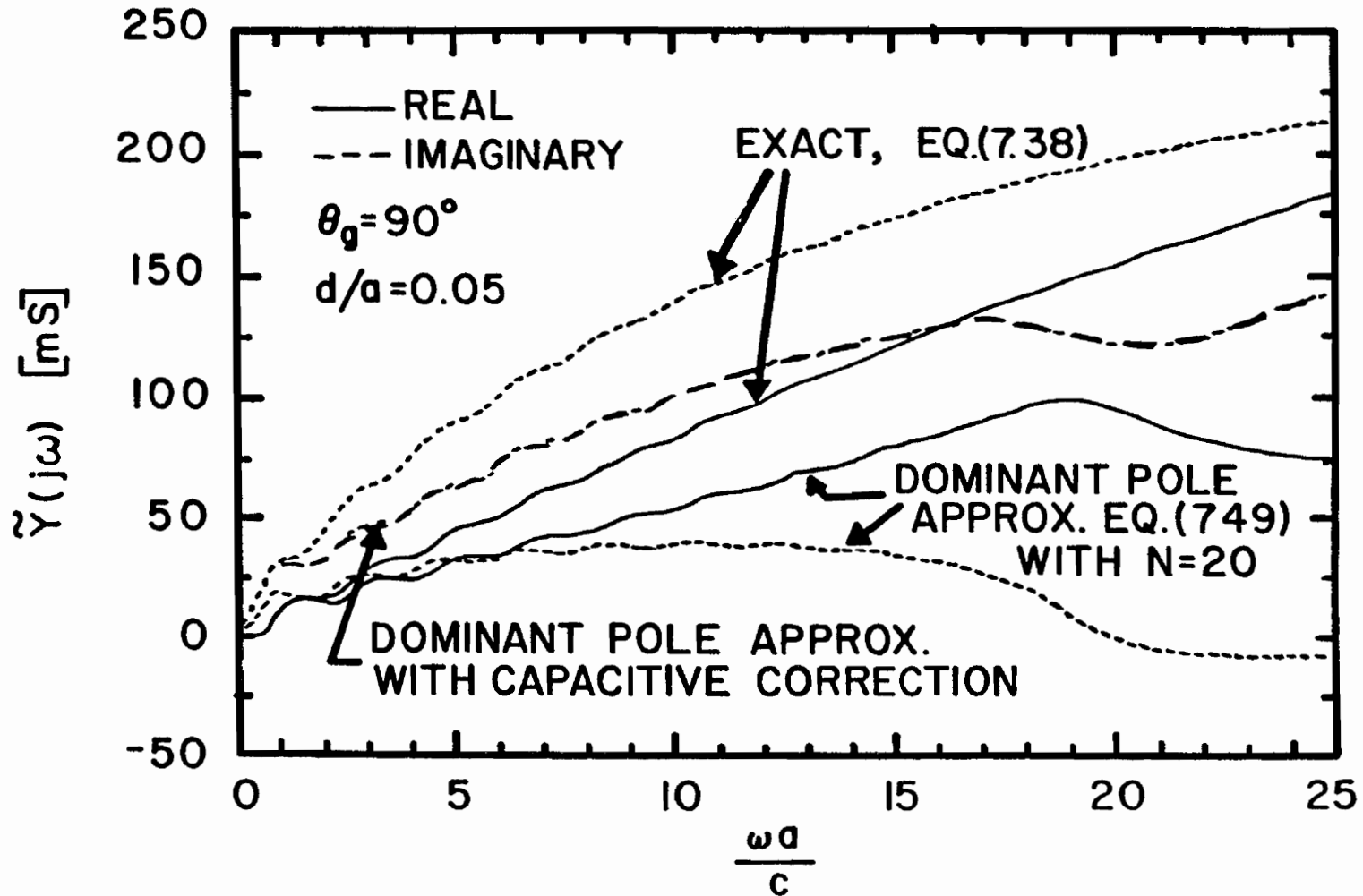
Figure 7.4 The spectrum of the driving-point admittance of a spherical antenna with an equatorial slot. The dominant pole approximation (7.49) is compared with the exact expression (7.38).

cannot be considered electrically small, one cannot choose the time origin location $\vec{r}_o$ independently of the direction of arrival of the incident field. This difficulty is overcome by moving the time origin to the point of the first contact of the incoming wave with the gap region. Thus, with

$$\vec{r}_o = a \ \hat{p} \ \cos(\theta_o + \theta_1) \qquad (7.52)$$

and

$$t_o = - \frac{\hat{p} \cdot \vec{r}_o}{c} = - \frac{a}{c} \cos(\theta_o + \theta_1) \qquad (7.53)$$

the incident field becomes

$$\tilde{\vec{E}}_o^i(\vec{r},s) = \vec{E}_o e^{-\gamma \ \hat{p} \cdot (\vec{r} - \vec{r}_o)} \tilde{f}(s)$$

$$= E_o e^{-s\tau_o} \ \hat{u} \ e^{-\gamma \ \hat{p} \cdot \vec{r}} \qquad (7.54)$$

where $s = \gamma a$ is the normalized complex frequency and $\tau_o = t_o c/a$. The last term in (7.54) can be expanded in terms of the spherical vector wave functions as follows [*Baum*, 1971; *Morse and Feshbach*, 1953]

$$\hat{u} \ e^{-\gamma \ \hat{p} \cdot \vec{r}} = \sum_{n=1}^{\infty} \sum_{m=0}^{n} \left[a_{n,m} \vec{M}_{n,m,o}(\gamma \vec{r}) + b_{n,m} \vec{N}_{n,m,e}(\gamma \vec{r}) \right] \qquad (7.55)$$

where

$$\vec{M}_{n,m,\sigma}(\gamma \vec{r}) = i_n(\gamma r) \vec{R}_{n,m,\sigma}(\theta,\phi) \qquad (7.56)$$

$$\vec{N}_{n,m,\sigma}(\gamma \vec{r}) = n(n+1) \frac{i_n(\gamma r)}{(\gamma r)} \vec{P}_{n,m,\sigma}(\theta,\phi) + \frac{[(\gamma r)i_n(\gamma r)]'}{(\gamma r)} \vec{Q}_{n,m,\sigma}(\theta,\phi) \quad (7.57)$$

with $\vec{Q}_{n,m,\sigma}(\theta,\phi)$ and $\vec{R}_{n,m,\sigma}(\theta,\phi)$ defined in (7.8) and (7.9) and

$$\vec{P}_{n,m,\substack{e\\o}}(\theta,\phi) = \hat{r} \ P_n^m(\cos\theta) \begin{Bmatrix} \cos(m\phi) \\ \sin(m\phi) \end{Bmatrix} . \qquad (7.58)$$

The coefficients in (7.55) are given by [*Baum*, 1969]

$$a_{n,m} = (2 - \delta_{o,m})(-1)^{n+1} \frac{2n+1}{n(n+1)} \frac{(n-m)!}{(n+m)!} m \frac{P_n^m(\cos\theta_1)}{\sin\theta_1} \qquad (7.59)$$

and

$$b_{n,m} = (2 - \delta_{o,m})(-1)^{n} \frac{2n+1}{n(n+1)} \frac{(n-m)!}{(n+m)!} \frac{\partial \, P_n^m(\cos\theta_1)}{\partial\theta_1} \, . \qquad (7.60)$$

With the help of (7.54) and (7.55) the coupling coefficient (normalized to $E_o a$) can be found from (7.14) as

$$\tilde{\eta}_n(s) = b_{n,o} \frac{[s \, i_n(s)]'}{s} e^{-s\tau_o} \int_0^\pi \left[\frac{\partial \, P_n(\cos\theta)}{\partial\theta} \right]^2 \sin\theta d\theta$$

$$= 2(-1)^n \frac{[s \, i_n(s)]'}{s} e^{-s\tau_o} P_n^1(\cos\theta_1) \quad . \qquad (7.61)$$

When (7.61) is substituted for the coupling coefficient in (7.13), the term $[s \, i_n(s)]'$, which is associated with the purely imaginary cavity resonances, is cancelled out. The short-circuit current, normalized to $E_o a$, takes the form

$$\tilde{I}^{sc}(s) = \sum_{n=1}^\infty \frac{2\pi}{Z_o} (-1)^n \frac{2n+1}{n(n+1)} P_n^1(\cos\theta_o)\sin\theta_o P_n^1(\cos\theta_1) \frac{e^{-s\tau_o}}{s[s \, k_n(s)]'} \tilde{f}(s).$$

$$(7.62)$$

To expand (7.62) in terms of its singularities it is necessary to examine the term

$$\frac{e^{-s\tau_o}}{s[s \, k_n(s)]'} = - \frac{e^{-s\tau_o}}{n \, s \, k_n(s) + s^2 k_{n-1}(s)}$$

$$= - \frac{s^n}{n p_n(s) + s^2 p_{n-1}(s)} \qquad (7.63)$$

where the polynomial $p_n(s)$ is defined in (7.43). The comparison of (7.63) with (7.45) shows that $\tilde{I}^{sc}(s)$ has the same poles s_{ni} as $\tilde{Y}(s)$. The residues of (7.63) at these poles can be found as

$$r'_{ni} = \lim_{s \to s_{ni}} \left\{ (s - s_{ni}) \frac{e^{-s\tau_o}}{s[s\, k_n(s)]'} \right\} = \frac{e^{-s_{ni}\tau_o}}{s_{ni}[s\, k_n(s_{ni})]''}$$

$$= \frac{e^{-s_{ni}\tau_o}}{[s_{ni}^2 + n(n+1)]k_n(s_{ni})} = \frac{s_{ni}^{n+1} e^{s_{ni}(1-\tau_o)}}{[s_{ni}^2 + n(n+1)]p_n(s_{ni})} \; . \tag{7.64}$$

In the dominant pole approximation the short-circuit current becomes

$$\tilde{I}^{sc}(s) \cong \sum_{n=1}^{\infty} \frac{2\pi}{Z_o} (-1)^{n-1} \frac{2n+1}{n(n+1)} P_n^1(\cos\theta_o)\sin\theta_o P_n^1(\cos\theta_1)$$

$$\times \frac{s_n^{n+1} e^{s_n(1-\tau_o)}}{[s_n^2 + n(n+1)]p_n(s_n)} \frac{s}{s_n(s - s_n)} \tilde{f}(s) \tag{7.65}$$

which can be rewritten as

$$\tilde{I}^{sc}(s) \cong \sum_{n=1}^{\infty} \tilde{Y}_n(s) T_n \tilde{f}(s) \tag{7.66}$$

with the source coefficients T_n given by

$$T_n = 2(-1)^n \frac{e^{-s_n\tau_o}}{s_n^2 k_n(s_n)} \frac{P_n^1(\cos\theta_1)}{\dfrac{a}{d} \displaystyle\int_{\theta_g - \alpha_o}^{\theta_g + \alpha_o} P_n^1(\cos\theta)\sin\theta d\theta}$$

$$= 2(-1)^n \frac{s_n^{n-1} e^{s_n(1-\tau_o)}}{p_n(s_n)} \frac{P_n^1(\cos\theta_1)}{\dfrac{a}{d} \displaystyle\int_{\theta_g - \alpha_o}^{\theta_g + \alpha_o} P_n^1(\cos\theta)\sin\theta d\theta} \; . \tag{7.67}$$

Combining N conjugate pole-pairs in (7.66) results in

$$\tilde{I}^{sc}(s) \cong \sum_{n=1}^{N} [\tilde{Y}_n(s)T_n + \tilde{Y}_{-n}(s)T_n^*]\tilde{f}(s)$$

$$\cong \sum_{n=1}^{N} \hat{\tilde{Y}}_n(s)\hat{\tilde{T}}_n(s)\tilde{f}(s) \qquad\qquad (7.68)$$

with the pole-pair voltage transfer functions $\hat{\tilde{T}}_n(s)$ defined in (3.24).

In Figure 7.5 the spectrum of the short-circuit current of the spherical antenna ($\theta_g = 90°$, $d/a = 0.05$) computed from (7.62) with the delta function time history ($\tilde{f}(s) = 1$) is compared with the spectrum obtained from the dominant pole approximation (7.68). The agreement between these two spectra, although quite poor, is nevertheless much more satisfactory than the agreement in analogous admittance results (Figure 7.4).

7.5   Equivalent Circuits for the Spherical Antenna With an Equatorial Slot of Width $d/a = 0.05$

In Table 7.1 are listed the admittance residues a_n associated with the first 20 dominant poles of a spherical antenna with an equatorial slot ($\theta_g = 90°$) of width $d/a = 0.05$. Included also for each pole s_n are the quality factor Q_n and the amount of the real part padding G_n required for the realizability of the associated pole-pair admittance. The column denoted "%" gives the ratio (in %) of the padding conductance G_n to the resonance value of the real part of $\tilde{Y}_n(j\omega)$. It is seen from this table that, except for the first few poles, the amount of padding G_n is a significant fraction of the value of the real part at the resonance. Only the first pole pair admittance does not require padding and is realizable in the modified form. This is further
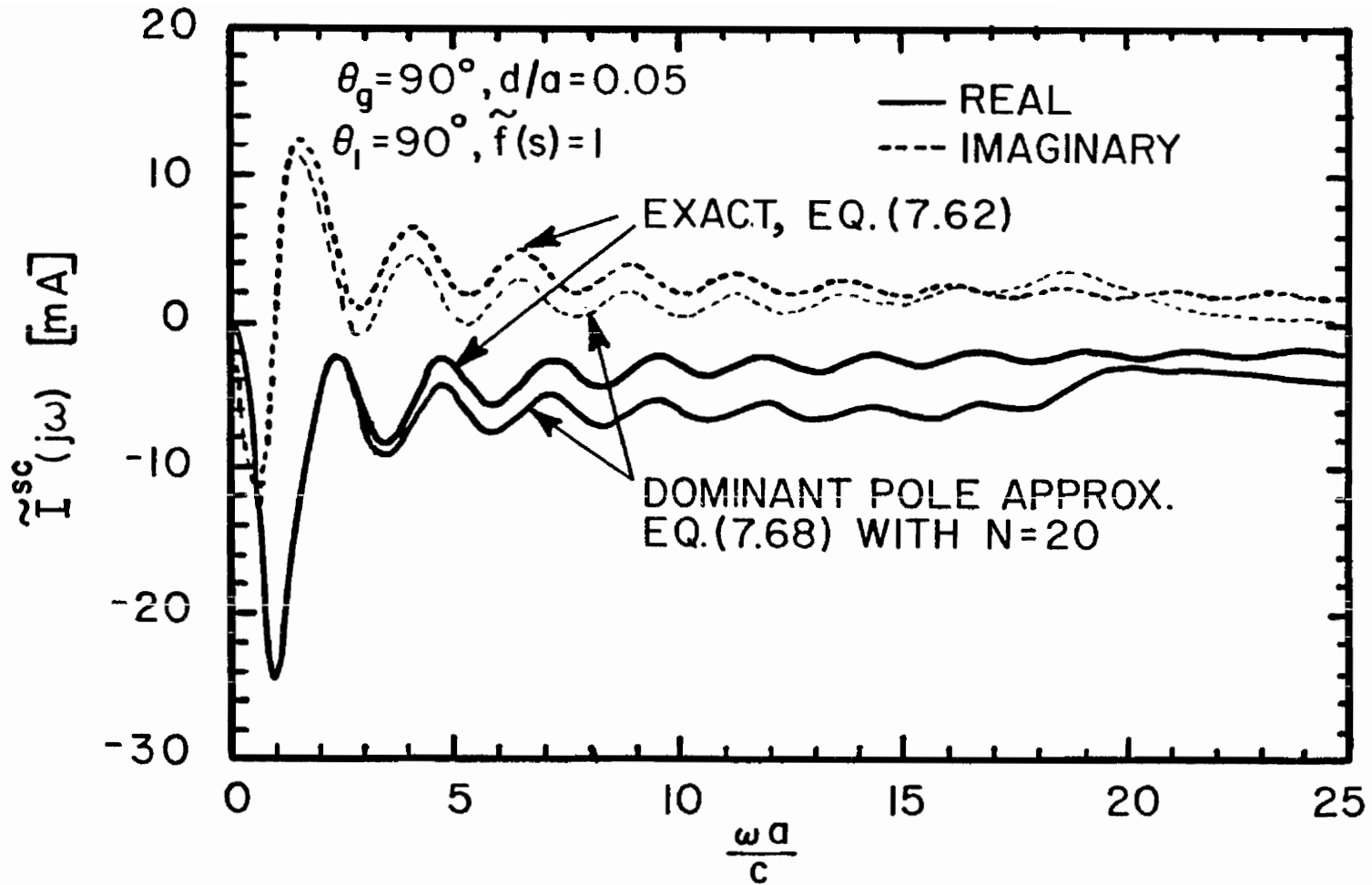
213

Figure 7.5 The spectrum of the short-circuit current excited in a spherical antenna with an equatorial slot by a broad-side-incident delta function plane wave. The dominant pole approximation (7.68) is compared with the exact expression (7.62).

Table 7.1 Admittance residues a_n, quality factors Q_n, and padding conductances G_n associated with the dominant poles s_n^*) of a spherical antenna with an equatorial slot ($\theta_g = 90°$) of width $d/a = 0.05$.

n	$s_n = -\sigma_n + j\omega_n$	Q_n	$a_n = c_n + jd_n$ [mS]	Region -Case	Padding G_n [mS]	%
1	$-0.5000 + j\ 0.8660$	1	$0.0 \quad +j\ 7.2154$	II	–	–
2	$-0.7020 + j\ 1.8073$	1.38	$0.0 \quad +j\ 0.0$	–	–	–
3	$-0.8429 + j\ 2.7579$	1.71	$3.1131 + j12.784$	III–A	0.7846	5.0
4	$-0.9542 + j\ 3.7148$	2.01	$0.0 \quad +j\ 0.0$	–	–	–
5	$-1.0477 + j\ 4.6764$	2.29	$5.6549 + j17.374$	III–A	1.5353	9.3
6	$-1.1289 + j\ 5.6416$	2.55	$0.0 \quad +j\ 0.0$	–	–	–
7	$-1.2012 + j\ 6.6097$	2.80	$7.9140 + j21.396$	III–A	2.1298	12.4
8	$-1.2666 + j\ 7.5801$	3.03	$0.0 \quad +j\ 0.0$	–	–	–
9	$-1.3266 + j\ 8.5525$	3.26	$9.9727 + j25.023$	III–A	2.6173	14.6
10	$-1.3821 + j\ 9.5265$	3.48	$0.0 \quad +j\ 0.0$	–	–	–

Table 7.1 (continued)

n	$s_n = -\sigma_n + j\ _n$	Q_n	$a_n = c_n + jd_n$ [mS]	Region -Case	Padding G_n [mS]	%
11	-1.4339 +j10.502	3.70	11.873 +j28.346	III-A	3.029	16.3
12	-1.4825 +j11.479	3.90	0.0 +j 0.0	-	-	-
13	-1.5284 +j12.456	4.11	13.641 +j31.416	III-A	3.3824	17.6
14	-1.5719 +j13.435	4.30	0.0 +j 0.0	-	-	-
15	-1.6133 +j14.415	4.50	15.293 +j34.268	III-A	3.690	18.7
16	-1.6528 +j15.395	4.68	0.0 +j 0.0	-	-	-
17	-1.6906 +j16.376	4.87	16.839 +j36.924	III-A	3.962	19.6
18	-1.7270 +j17.358	5.05	0.0 +j 0.0	-	-	-
19	-1.7620 +j18.340	5.23	18.287 +j39.398	III-A	4.200	20.4
20	-1.7957 +j19.323	5.40	0.0 +j 0.0	-	-	-

*) The poles s_n and residues a_n are normalized to c/a.

216

illustrated in Figures 7.6-7.11 where the behavior of the real part of some of the dominant pole pair admittances is plotted as a function of the real frequency ω. It is seen that, except for the first pole-pair admittance, there is a significant negative excursion of the real part on the $j\omega$-axis.

The element values and the circuit topology of the dominant pole-pair admittance networks for the spherical antenna with $\theta_g = 90°$ and $d/a = 0.05$ are included in Table 7.2. The transient response of this equivalent network due to a Gaussian voltage pulse is compared in Figure 7.12 with the "exact" response obtained from (7.38) and an FFT inversion. Shown also is the response of the equivalent circuit augmented by a corrective capacitor. In both cases the discrepancy between the circuit response and the exact response is significant.

In Table 7.3 are defined the dominant pole-pair voltage transfer networks of the spherical antenna ($\theta_g = 90°$, $d/a = 0.05$) for the case of a broad-side plane wave incident ($\theta_1 = 90°$).

The short-circuit current response of the complete equivalent network for the spherical antenna due to a plane wave incident field ($\theta_1 = 90°$) carrying a step function time history is compared in Figure 7.13 with the "exact" response obtained from (7.67) by an FFT inversion. Again, the agreement between these curves is not satisfactory.

7.6 Conclusions

The spherical antenna, with its resonances so highly damped, provides an extremely stringent test for the dominant-pole-at-at-time equivalent circuits. The dominant-pole approximation, which works so well for the thin wire loop and dipole antennas (Chapters 5 and

217
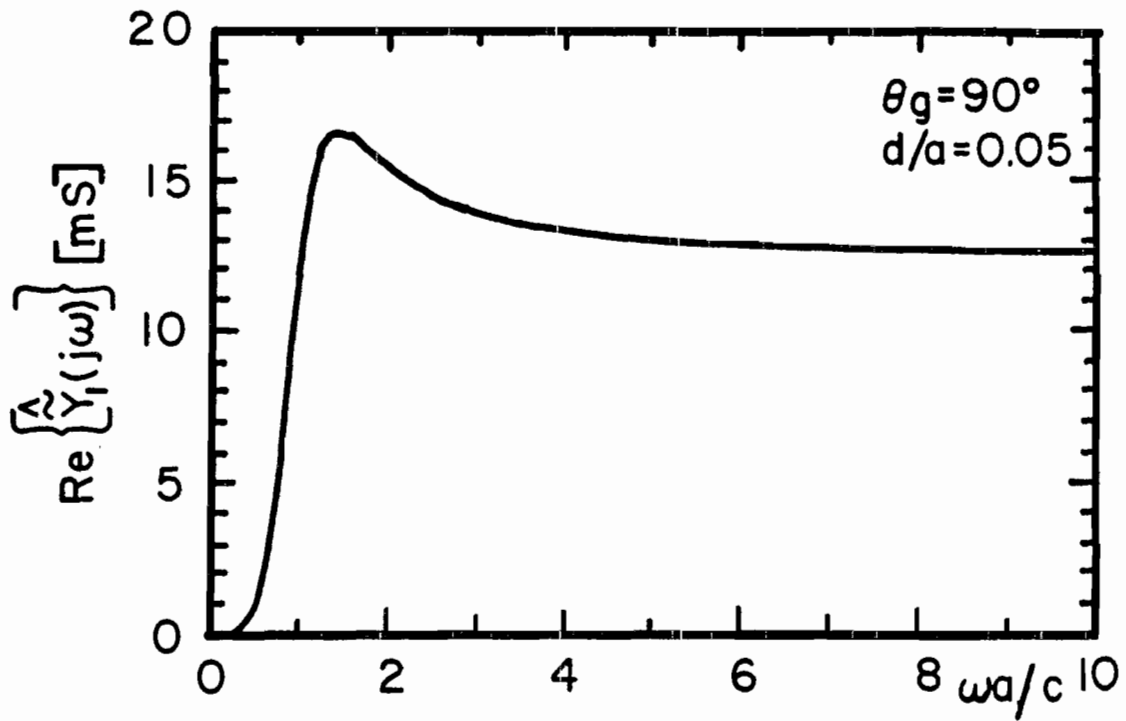
Figure 7.6 Real part behavior of the 1st dominant pole-pair admittance of the spherical antenna with an equatorial slot.
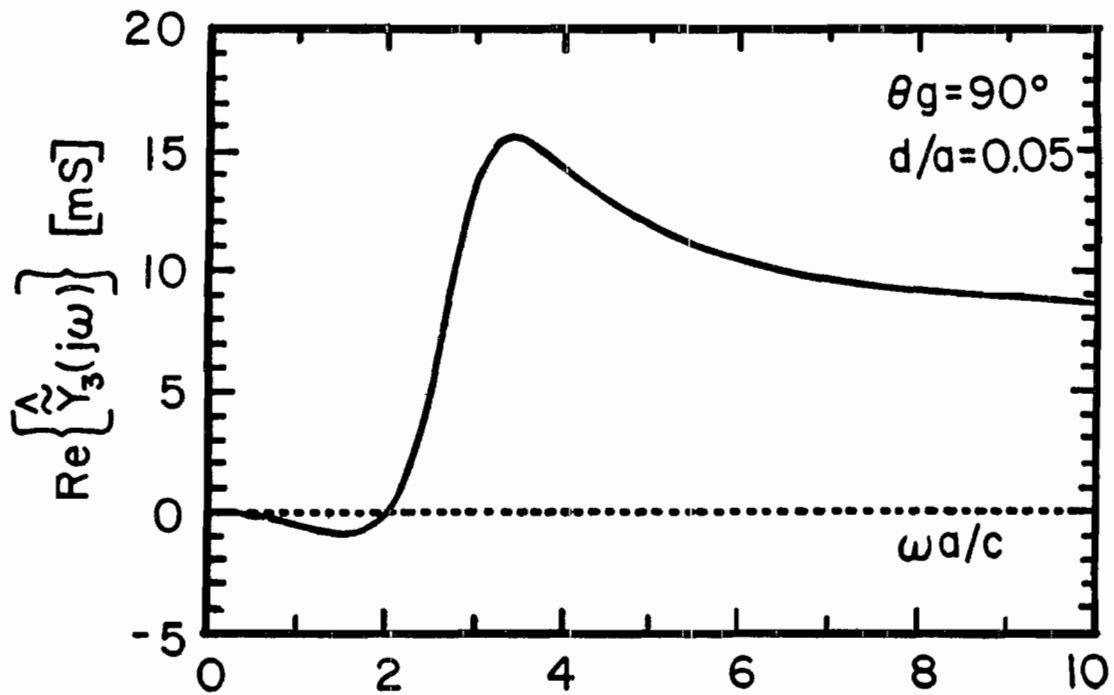
Figure 7.7 Real part behavior of the 3rd dominant pole-pair admittance of the spherical antenna with an equatorial slot.
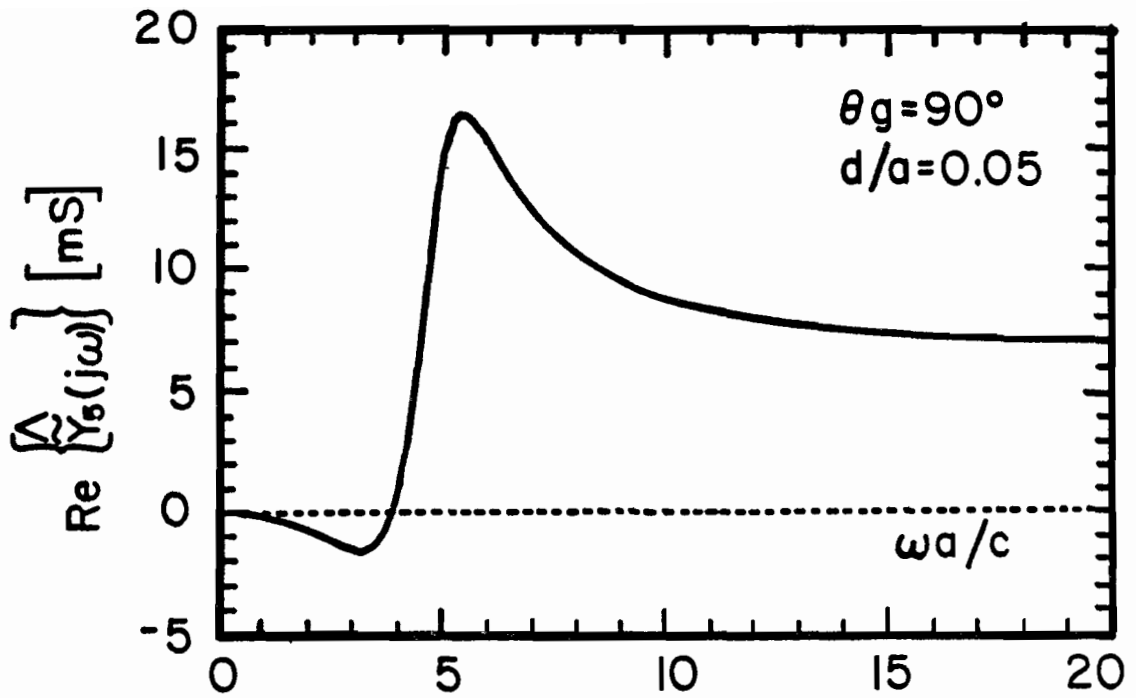
Figure 7.8 Real part behavior of the 5th dominant pole-pair admittance
of the spherical antenna with an equatorial slot.
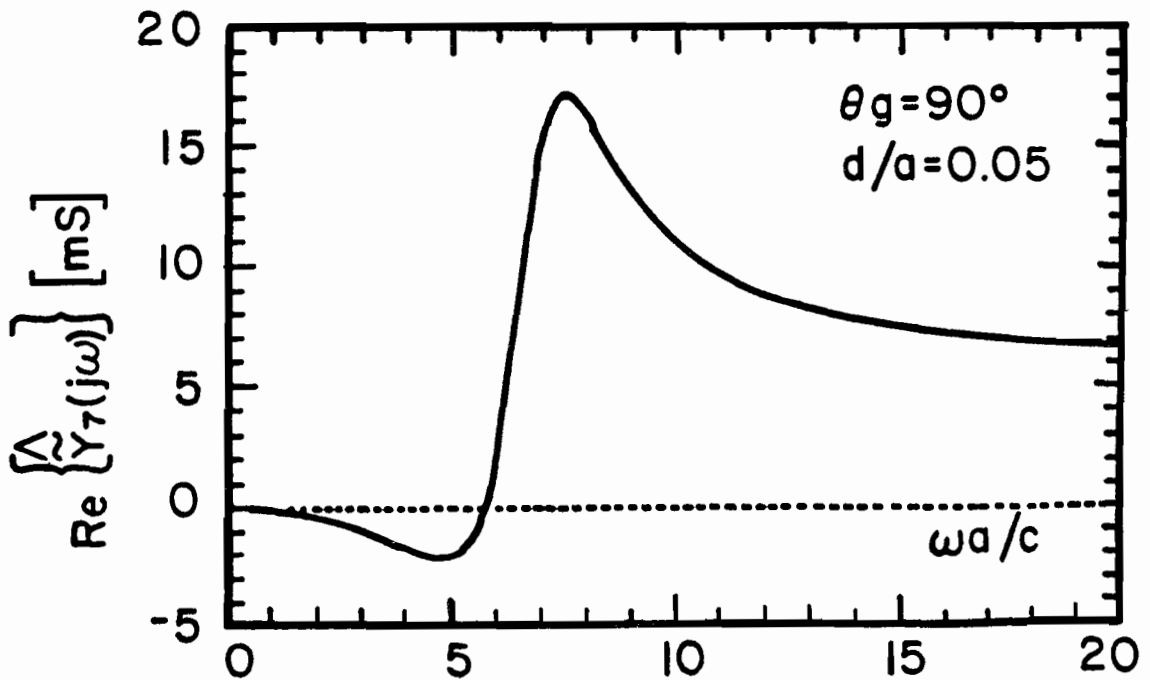
Figure 7.9 Real part behavior of the 7th dominant pole-pair admittance
of the spherical antenna with an equatorial slot.
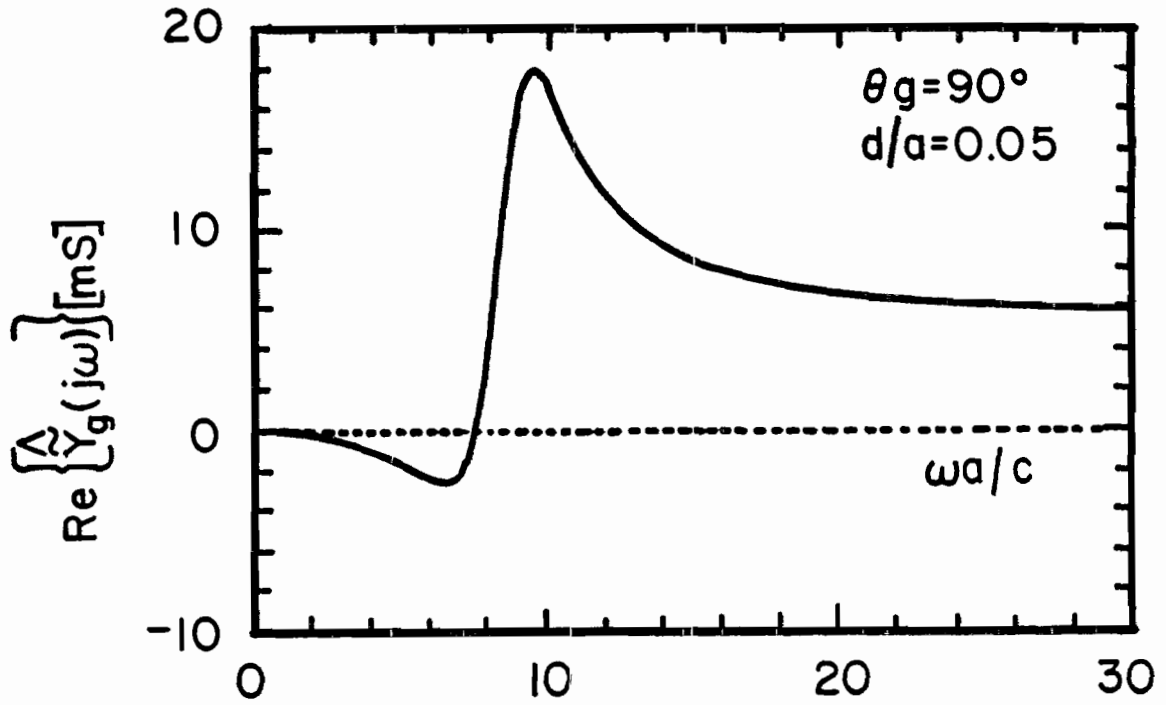
Figure 7.10   Real part behavior of the 9th pole-pair admittance of the spherical antenna with an equatorial slot.
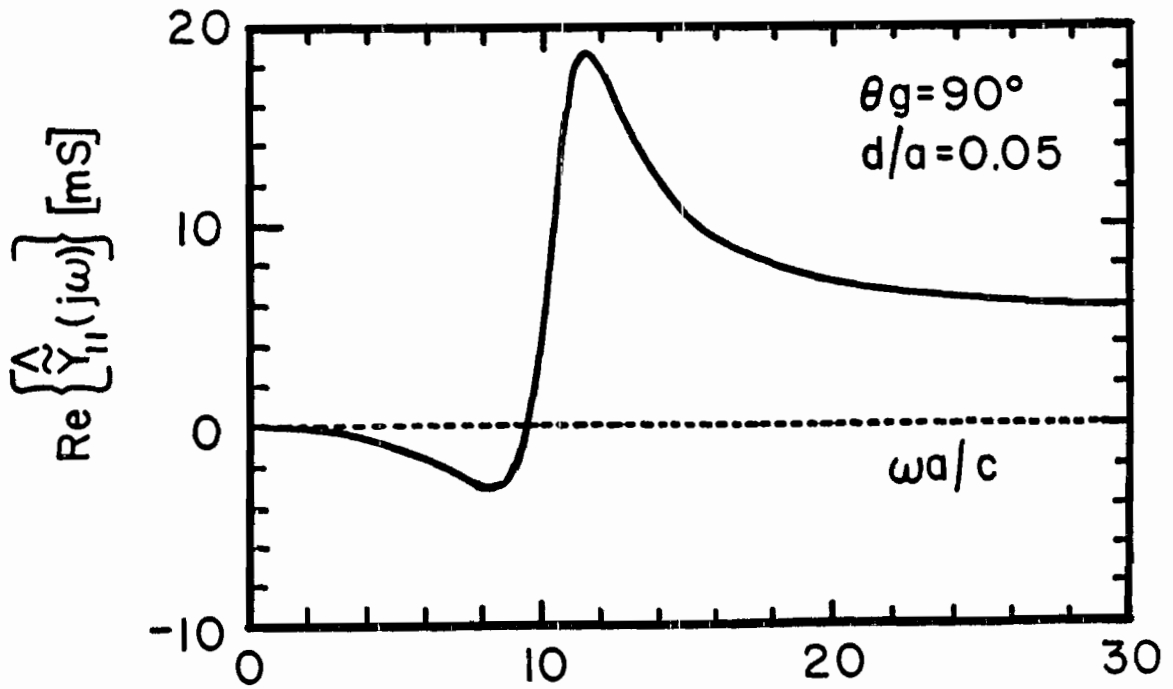
Figure 7.11   Real part behavior of the 11th dominant pole-pair admittance of the spherical antenna with an equatorial slot.

Table 7.2 Element values of the dominant pole-pair admittance
networks for a spherical antenna with an equatorial slot ($\theta_g = 90°$)
of width $d/a = 0.05$.

LADDER CIRCUIT (Figure 4.7(a))			
n	$C_1/a [pF/m]$	$R_1 [\Omega]$	$L_1/a [\mu H/m]$	$R_2 [\Omega]$
1	41.66	0.0	266.71	80.0

BOTT-DUFFIN CIRCUIT-CASE A (Figure 4.12(a))			
n	$C_o/a [pF/m]$	$L_1/a [\mu H/m]$	$C_1/a [pF/m]$	$R_1 [\Omega]$
3	11.923	132.45	33.456	115.84
5	7.269	93.48	11.884	123.54
7	5.348	74.257	6.416	125.38
9	4.282	62.613	4.136	125.34
11	3.597	54.737	2.941	124.61
13	3.115	49.027	2.225	123.66
15	2.755	44.69	1.756	122.67
17	2.474	41.287	1.430	121.75
19	2.246	38.547	1.191	120.96

*) Natural frequencies s_n, $n = 2,4,6,...$ do not contribute to the
driving-point network.
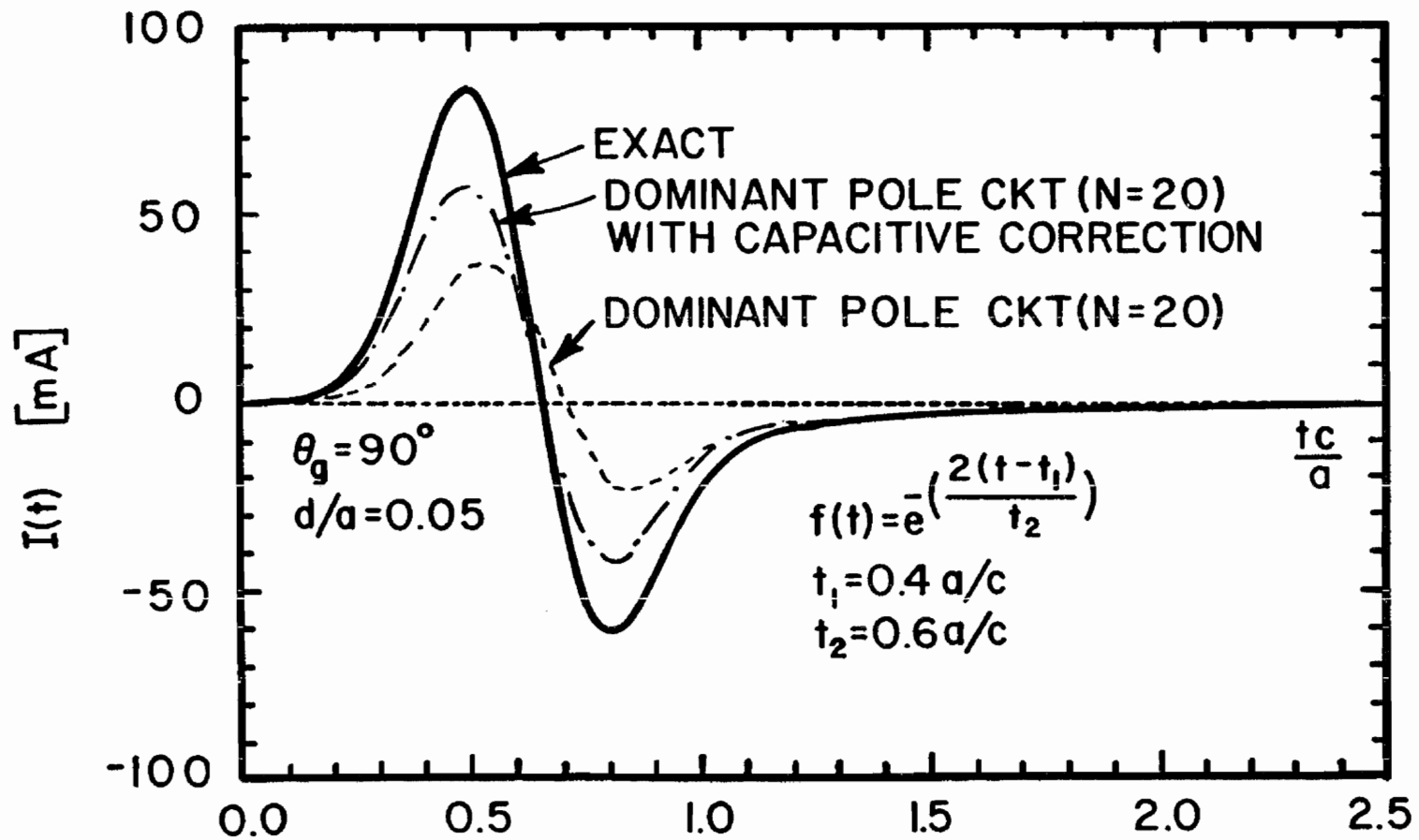
Figure 7.12 Input current of the spherical antenna with an equatorial slot excited by a Gaussian voltage pulse. The responses of the dominant pole equivalent circuit with and without the corrective capacitor are compared with the exact response.

Table 7.3   Element values of the dominant pole-pair voltage trnasfer networks for a spherical antenna with an equatorial slot ($\theta_g = 90°$) of width $d/a = 0.05$, excited by a broadside incident ($\theta_1 = 90°$) plane wave.

n[*]	TOPOLOGY	C_A/a[pF/m]	$R_A[\Omega]$	C_B/a[pF/m]	$R_B[\Omega]$	$\dfrac{\mu}{aE_o}[V^{-1}]$
1	RC LADDER	–	160.16	20.807	–	–2.0
3	RC LADDER	108.37	34.155	–	19.487	–0.9466
5	RC LATTICE	307.41	–	190.03	1.7544	–0.71132
7	RC LADDER	404.90	1.5099	27.119	–	0.45207
9	RC LATTICE	1301.07	5.0309	–	0.43687	0.33530
11	RC LADDER	199.88	0.48753	697.30	–	–0.51363
13	RC LADDER	1165.33	1.2974	–	0.4301	–0.33926
15	RC LATTICE	1933.60	–	963.30	0.11413	–0.38787
17	RC LADDER	1050.50	0.1695	689.50	–	0.33797
19	RC LATTICE	4066.70	0.23794	–	0.09037	0.25900

[*] The transfer networks associated with poles s_n for $n = 2, 4, \ldots$, are not present in the equatorial slot case.

223
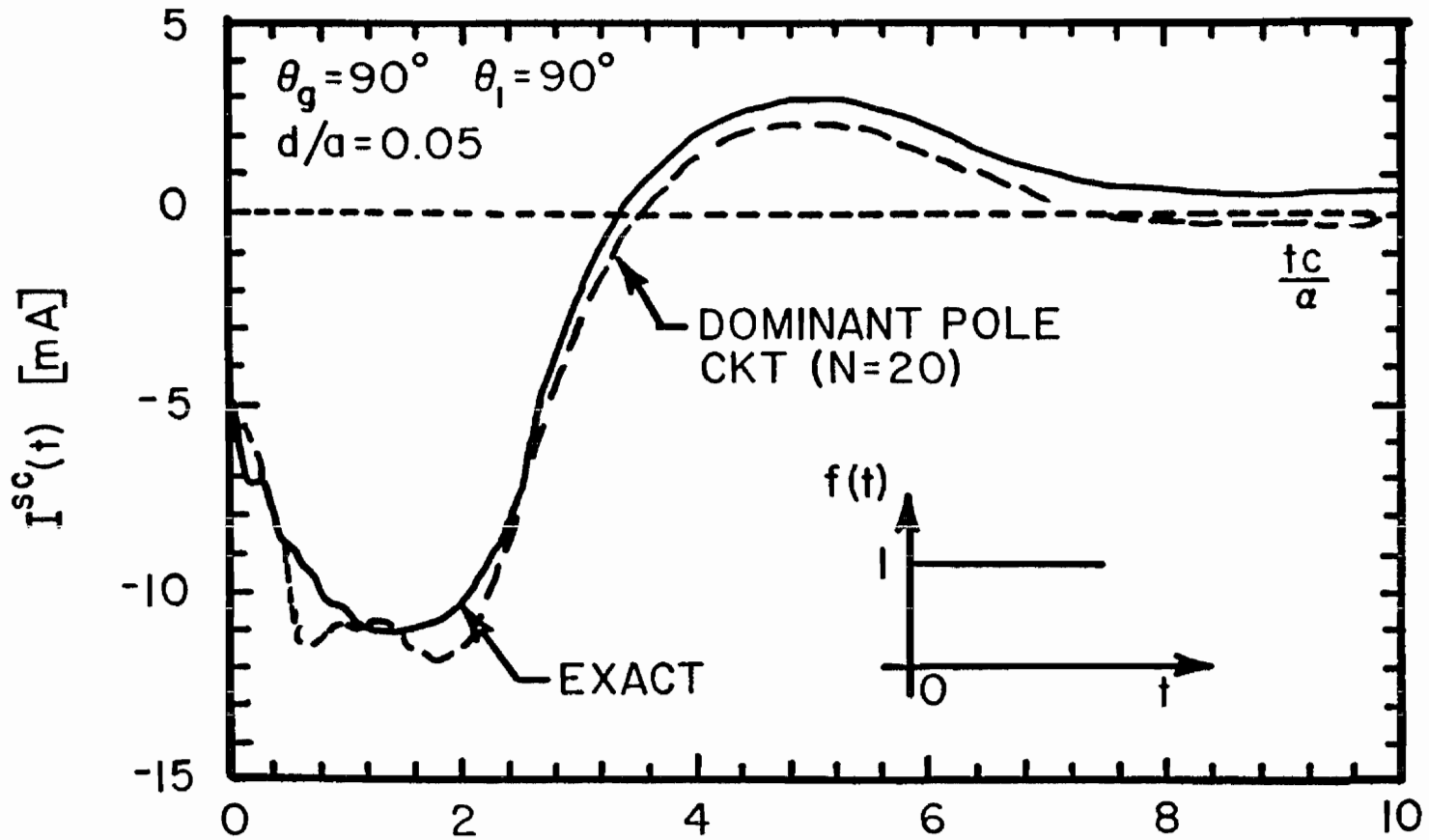
Figure 7.13 Short-circuit current excited in a spherical antenna with an equatorial slot by a broad-side-incident step function plane wave. The response of the dominant pole equivalent circuit is compared with the exact response.

6), is a rather crude one in the spherical antenna case. Also, the
dominant pole-pair admittances of the spherical antenna require a
much larger amount of real-part padding (relative to the value of the
real part of the admittance at the resonance) to render them positive
real than do the loop and dipole antennas. As a consequence of this,
the performance of the dominant pole-pair equivalent circuits for
the spherical antenna is considerably poorer than the performance of
similar circuits for the thin-wire loop and dipole structures, as
demonstrated in Chapters 5 and 6. It seems that most of the inaccuracy
in the circuit response is introduced by the driving-point admittance
part of the equivalent circuit. The performance of the source part
is significantly better than that of the admittance part of the equivalent
network, so that the short-circuit current waveform does not differ
significantly from the true response.

Due to its extreme low-Q character, the spherical antenna provides
a worst case estimate of the performance of the dominant-pole approximation
in the sense that for poles residing so far from the $j\omega$-axis the dominance
of the poles nearest the axis is, at best, weak. Although the dominant
pole results are relatively poor in Figures 7.12 and 7.13, they agree
within 35 percent with more accurately computed results. We therefore
conclude that in the low-Q limit, the approximation fails gracefully
and that for structures whose dominant pole quality factors are inter-
mediate between those of wire structures and the sphere, the dominant
pole-approximation may be sensibly applied.

CHAPTER 8

SUMMARY AND CONCLUSIONS

Practical and systematic procedures have been developed for the
synthesis from the SEM (Singularity Expansion Method) description of
acitve, physically realizable equivalent circuits for electromagnetic
energy collecting structures with identifiable ports. The necessary
SEM information includes the poles $\{s_n\}$ of the structure and the
associated natural modes and normalization coefficients. From the poles
and the associated modal distributions one can compute for a given
incident field the coupling coefficients which weight a given singularity's
contribution to the total response. Two different coupling coefficient
forms have been used in the SEM work to date—the so-called class 1
and class 2 forms [*Baum*, 1976b]. In the SEM equivalent circuit synthesis
only the class 1 form is applicable, which is known to exhibit numerical
instability in early times [*Marin*, 1972; *Pearson*, 1979]. However, it
is demonstrated in Chapter 2 that the simple class 1 coupling coefficient
can be used with success provided the time origin of the problem is
placed in the port zone (gap region); it is also argued that the class
1 expansion is always convergent as $\text{Re}[s_n] \to -\infty$ for this time origin
location.

The SEM expansion for the current density $\tilde{\vec{J}}(\vec{r},s)$ on a scattering
object is derived formally in Chapter 2 from the eigenfunction expansion
of $\tilde{\vec{J}}(\vec{r},s)$ in terms of the eigenvalues and eigenvectors of the electric
field integral equation (EFIE) operator. It is assumed in this
development that a complete set of eigenvectors exists which is not
necessarily true since the EFIE operator is non-selfadjoint. In fact,
it is demonstrated in Appendix A that the eigenvalues of the EFIE

operator may have branch points in the complex frequency plane at which two or more eigenvalues become degenerate so that the inclusion of root vectors in the expansion may be necessary [*Ramm*, 1980]. If an eigenvalue has a branch point, a branch cut must be chosen in the s-plane, resulting in a branch-integral term in its SEM expansion. This can have an important bearing on the SEM equivalent circuit synthesis because in most practical cases these branch-integral constituents are not explicity identifiable. Their omission, however, can result in non-realizable terminal eigenadmittances [*Pearson and Wilton*, 1981].

In the process of expanding the inverse eigenvalue in terms of its singularities one refers to the Mittag-Leffler theorem from the theory of functions of a complex variable. Two basic SEM expansion forms result depending on the large-s asymptotic behavior of the eigenvalue— the so-called modified and unmodified forms [*Baum*, 1976a]. It is observed in Chapter 2 that the modified form imposes less stringent conditions on the asymptotic behavior of the eigenvalues of the integral operator. Therefore this form appears to be preferable in the case of problems solved numerically. This suggestion is supported by the fact that, as shown in Chapter 7, the modified SEM expansion is the proper one in the case of the sphere, which is one of the few structures for which an exact analytical solution is available.

The SEM equivalent network can be derived either from the Norton or from the Thévenin equivalence, leading to two different but equivalent networks. Of course, the SEM parameters which must be supplied are different in those two cases. The short-circuit SEM data are usually found by solving the short-circuit boundary value problem, whereas the

open-circuit parameters result from the solution of the open-circuit

boundary value problem. The open-circuit SEM parameters are much more

difficult to obtain than the short-circuit parameters of the same

object because of the highly localized charge interaction effects

between the two parts of the structure in the vicinity of the gap

which must be modeled precisely in the open-circuit problem. Further-

more, it is enough to solve only one short-circuit boundary value

problem for all possible gap locations on the structure, whereas the

open-circuit problem must be solved for each location. Thus, if for

some reason the Thévenin-based equivalent circuit is preferred over

the Norton-based equivalent, it is perhaps more expedient to derive

it from the short-circuit parameters, as described in Chapter 3.

The SEM equivalent circuit synthesis procedures developed in this

work are based on the first-layer, dominant pole-pairs because they

dominate the response of the structure and they are the ones easiest

to extract by numerical or experimental means. An alternative

approach of grouping the poles according to eignvalues is not

practical, however, because in most cases this collection

of poles is not explicitly identifiable. Also, the number of poles

grows rapidly for higher order modes, making the corresponding circuits

extremely complicated [*Streable and Pearson,* 1981].

The SEM equivalent circuits developed in Chapter 4 have the form

of a connection of simple modules associated with the conjugate pole

pairs of the structure. These pole-pair circuits are synthesized one

at a time, so if the need arises the network can be easily expanded

by adding more pole-pair modules without repeating the whole synthesis

process. By using the network topologies developed in Chapter 4 the

synthesis process is reduced to the realization of a driving-point

function biquadratic in s and a voltage transfer function bilinear in s. The realizability conditions and explicit circuit realizations are given for these functions.

If the driving-point function is realizable, it can be synthesized by simple continued fraction expansion. If a pole-pair driving-point function is initially nonrealizable, a simple padding procedure is described to synthesize an approximating circuit. The padded pole-pair driving-point function is a minimum-real-part function. It appears that the only transformerless realization applicable in this case is the Bott-Duffin network. If the amount of padding is negligible, this network can be simplified by deleting one leg without introducing appreciable error.

It is shown that the pole-pair voltage transfer function can be always realized either in the form of a ladder circuit or in the form of a symmetrical lattice circuit. Unfortunately, the applicability of each of the two topologies is dependent on the direction of arrival of the incident plane wave, so that the circuit topology may change when excitation conditions are changed. In each of the two cases, two equivalent realizations are possible: an RC realization and an RL realization. In the cases tested it was found that the element values of the RC network were more realistic than the element values of the equivalent RL realization.

Each of the transfer networks must be followed by a voltage-controlled voltage source which serves as an impedance buffering stage and as an amplifier to restore the gain lost in the associated transfer network. The controlled sources can be implemented in practice with active devices which, however, usually cannot sustain high voltages.

The synthesis procedures developed are tested on thin-wire loop and dipole antennas (Chapters 5 and 6), as well as on a spherical antenna (Chapter 7). The synthesized equivalent circuits are analyzed by a general circuit analysis program (SCEPTRE) and the responses compared with classical frequency domain and numerical inverse Fourier transform results or with results obtained from the Thin Wire Time Domain (TWTD) code. In the case of the thin-wire structures, the results are very encouraging. The circuit responses agree favorably with the responses obtained by other means. Of course, the quality of the circuit responses is commensurate with the quality of the dominant-pole approximation, which is very accurate in the case of highly resonant (slender) structures. The only additional approximation in the SEM circuit is the possible padding introduced in the synthesis of the pole-pair driving-point function. This padding is negligible in the thin-wire loop and dipole cases; it is rather significant for the spherical antenna. In the case of the spherical antenna the dominant pole approximation breaks down, too. For these reasons the SEM equivalent circuit of the spherical antenna cannot be expected to perform well, unless modules associated with the second and, perhaps, third layer of poles are included in the circuit.

The driving-point responses of the equivalent circuits are considerably poorer than the short-circuit responses excited by a plane wave incident field. This can be attributed mainly to the capacit've deficiency of the SEM equivalent circuit. Namely, the capacitance of the finite equivalent circuit in the limit as $s \to 0$ underestimates the true static capacitance of the structure. Therefore, the early-

time response of an SEM equivalent circuit can often be improved by augmenting it by a shunt capacitor of a proper value. This phenomenon does not influence the short-circuit response because the input terminals of the structure are shorted for that case. Most of the comparisons included in this work involve the short-circuit conditions primarily because only for those cases were benchmark results readily available. In view of the above, these tests may appear to be, perhaps, too forgiving. However, the loaded dipole example included in Chapter 6 indicates that our equivalent circuits also perform well under finite loading conditions. The SEM equivalent circuits with nonlinear loads are analyzed in Appendix B. No data were available for comparison in those cases, but the results lend themselves to a straightforward physical interpretation.

In the thin-wire dipole case the sinusoidal natural-mode approximation can be employed to simplify the SEM equivalent circuits. It is demonstrated in Chapter 6 that this approximation is poor in the case of the driving-point circuits but it can be applied successfully to the voltage transfer networks. For a symmetrical dipole antenna or a cylindrical post over a ground plane, particularly simple and yet reasonably accurate circuits result,

In conclusion, the main objective of this work has been fulfilled. The SEM equivalent circuits developed are physically realizable, simple, and reasonably accurate. These circuits possess most, but not all of the desirable features listed in the Introduction. In particular, the network topology does change with the change of the direction of arrival of the incident field. However, the equivalent circuit does

not depend on the time history of the incident field. Also, the autonomic

voltage source is connected to only one port, and the equivalent circuit

is transformerless, but it does include controlled sources.

ON THE EXISTENCE OF BRANCH-POINTS IN THE EIGENVALUES
OF THE ELECTRIC FIELD INTEGRAL EQUATION (EFIE) OPERATOR
IN THE COMPLEX FREQUENCY PLANE

A.1 Introduction

The Singularity Expansion Method (SEM) [*Baum*, 1971] representation

for the current density on a scattering object can be derived formally

from the eigenfunction expansion involving eigenvalues and eigenfunctions

of the associated integral operator [*Baum*, 1975]. It has generally

been assumed that the inverse eigenvalues are analytic in the complex

frequency plane (s-plane) except for pole singularities [*Pearson and*

Wilton, 1981]. This is suggested by Marin and Latham's result

[*Marin and Latham*, 1972] that in the case of finite extent perfectly

conducting bodies in lossless media, poles are the only singularities

in the SEM expansion. [1] However, as pointed out by *Pearson and Wilton*

[1981], this does not preclude the possibility of the occurrence of

other singularities which cancel in the complete sum representing

the singularity expansion of the current. As it turns out, in fact,

only for bodies such as the sphere or the circular loop antenna, in

which geometrical symmetry completely determines the eigenfunctions

(and hence they are frequency independent), has it been possible to

show (Section 2.3) that such singularities cannot occur.

---

[1] In contrast to finite extent bodies, infinite cylindrical objects
always manifest solutions with a branch point singularity of well-
understood origin at zero frequency. *Schafer and Kouyoumjian* [1975]
discuss this branch point for the case of a conducting circular cylinder.

The presence or absence of branch points has an important bearing on the validity of the Eigenmode Expansion Method (EEM) [*Baum*, 1975] representation of the resolvent kernel, because at a branch-point in the s-plane two or more eigenvalues become degenerate and the inclusion of root vectors [*Ramm*, 1980] in the expansion may be necessary at that point. The expansion of individual reciprocal eigenvalues or any associated "eigen-quantities" to obtain their singularity expansion can also require integrals along the concomitant branch cuts in order for the expansion to be complete. The previously-mentioned meromorphicity result of Marin and Latham for finite extent objects ensures that when the eigenvalue expansions are summed, the branch-integral constituents cancel and the traditionally-used SEM forms result. However, in some applications, singularity expansions are applied on an eigenmode-at-a-time basis and the branch integrals must be retained. For example, the eigenvalues and their reciprocals manifest a "generalized positive-realness" [*Pearson and Wilton*, 1981] which is important in SEM circuit synthesis. To discard the branch-integral constituent of their expansion may compromise this property.

Although the existence of branch-integral constituents in the SEM representation has been speculated upon [*Baum*, 1978; *Pearson and Wilton*, 1981], no specific examples of their occurrence have been cited, to date (except for the well-known infinite cylinder case, mentioned above). The purpose of this paper is to fill this gap.

In Section A.2 we demonstrate simple circuit and transmission line examples in which the eigenvalues of the impedance matrix have branch-points. Although only finite-dimensional impedance operators are involved in these examples, they provide valuable insight into the

234

of the branch-point occurrence. In particular, they clearly demonstrate the role of the object symmetry in the occurrence of branch-points in the eigenfunction expansion of the inverse operator. In Section A.3 we consider the problem of scalar scattering by a prolate spheroid and demonstrate the presence of branch points in the eigenvalues of the associated integral operator which follows from the analysis of the spheroidal wave equation in the complex frequency plane [*Oguchi*, 1970]. In Section A.4, similar analysis of the Mathieu's differential equation [*Blanch and Clemm*, 1969] leads us to the conclusion that branch points besides that associated with the infinite extent of the object exist in the frequency plane behavior of the eigenvalues of the EFIE for an infinite perfectly-conducting elliptic cylinder.

A.2 Branch Points in Circuit and Transmission Line Problems

A.2.1 General Remarks

The terminal quantities of an N-port linear, passive, and bilateral electrical network are related via the equation

$$[Z][I] = [V] \quad , \tag{A.1}$$

where [I] and [V] are column vectors containing N-port Laplace-transformed currents and voltages, respectively, and [Z] is the $N \times N$ symmetric open-circuit impedance matrix. Eq. (A.1) is analogous to the electric field integral equation (2.1). The primary difference is that the electromagnetic problem consists of an uncountably infinite number of ports. Even this distinction vanishes, however, when a numerical solution of (2.1) is undertaken because then a matrix approximation replaces $\overleftrightarrow{\Gamma}$ and column vectors analogous to voltage and current replace $\vec{E}^i$ and $\vec{J}$, respectively [*Harrington*, 1968]. In the following, some conjectures

concerning (2.1) are made based on observations of properties of (A.1).

In general, an eigenvector expansion of the inverse of [Z] can be found as follows:

$$\left[Z^{-1}(s)\right] = \sum_{n=1}^{N} \frac{1}{\lambda_n(s)} \cdot \frac{\left[I_n(s)\right]\left[I_n(s)\right]^T}{\left[I_n(s)\right]^T\left[I_n(s)\right]} \quad , \tag{A.2}$$

where the superscript T denotes transpose and λ_n and $[I_n]$ are eigenvalues and eigenvectors of [Z]. In the regions in the s-plane where (A.2) holds, solution of (A.1) can be found in a form analogous to (2.13). However, it is demonstrated in simple examples below that there may be points in the s-plane where the eigenvalues become degenerate and the simple expansion (A.2) is no longer valid.

Before presenting specific examples it is helpful to investigate what general conclusions can be drawn concerning the eigenvalues of a two-port. The characteristic equation of a lumped reciprocal two-port network described in the form of (A.1) is

$$\det \begin{bmatrix} z_{11}-\lambda & z_{12} \\ \\ z_{12} & z_{22}-\lambda \end{bmatrix} = \lambda^2 - (z_{11}+z_{22})\lambda + z_{11}z_{22} - z_{12}^2 = 0 \quad , \tag{A.3}$$

where z_{11}, z_{12}, and z_{22} are rational functions in s. From (A.2.3) eigenvalues become

$$\lambda_{\frac{1}{2}}(s) = \frac{1}{2}\left[z_{11}+z_{22} \pm \sqrt{\Delta(s)}\right] \quad , \tag{A.4}$$

where the discriminant $\Delta(s)$ is given by

$$\Delta(s) = (z_{11} + z_{22})^2 - 4(z_{11}z_{22} - z_{12}^2)$$

$$= (z_{11} - z_{22})^2 + 4 z_{12}^2 \quad . \tag{A.5}$$

The radical in (A.4) suggests that, in general, the eigenvalues have branch points in the s-plane. Branch points do not occur, however, if one of the following conditions is satisfied:

1. $z_{12} = 0$ (uncoupled ports), which is a trivial case;

2. $\Delta(s) \equiv 0$, which can happen only if $(z_{11} - z_{22}) = \pm j2z_{12}$; however, this situation is not possible since z_{ij} are rational functions with real coefficients;

3. $\Delta(s)$ is frequency independent or of the form $[P(s)/Q(s)]^2$ where $P(s)$ and $Q(s)$ are polynomials in s;

4. $z_{11} = z_{22}$, which holds for a __symmetric__ network.

The role of the network symmetry in eliminating branch points in the impedance matrix can also be illustrated in the example of a three-port with rotational symmetry. The impedance matrix of such a network is given by

$$[Z] = \begin{bmatrix} z_{11} & z_{12} & z_{12} \\ z_{12} & z_{11} & z_{12} \\ z_{12} & z_{12} & z_{11} \end{bmatrix} \tag{A.6}$$

The characteristic equation

$$\det([Z] - \lambda[I]) = (z_{11} + 2z_{12} - \lambda)(\lambda + z_{12} - z_{11})^2 \tag{A.7}$$

yields the eigenvalues

$$\lambda_1 = z_{11} + 2z_{12} \tag{A.8a}$$

and

$$\lambda_2 = z_{11} - z_{12} \tag{A.8b}$$

which have no branch points if z_{11} and z_{12} are rational, but where λ_2 is of algebraic multiplicity 2. The eigenvector corresponding to λ_1 is

$$[I_1] = \begin{bmatrix} 1 \\ 1 \\ 1 \end{bmatrix} \quad , \qquad\qquad (A.9a)$$

and the eigenvectors corresponding to λ_2 are

$$[I_{2,1}] = \begin{bmatrix} 1 \\ e^{j2\pi/3} \\ e^{j4\pi/3} \end{bmatrix} \quad , \quad [I_{2,2}] = \begin{bmatrix} 1 \\ e^{j4\pi/3} \\ e^{j2\pi/3} \end{bmatrix} \quad . \qquad (A.9b)$$

Since two independent eigenvectors corresponding to λ_2 could be found, its geometric and algebraic multiplicities are equal. Also, owing to the symmetry of the network, we see that the eigenvectors are the so-called "symmetrical components" and are frequency independent.

The impedance matrix of the last network example has properties similar to the EFIE operator in the case of the circular loop antenna and the spherical antenna—both rotationally symmetric bodies. As in the case given above, both the circular loop and the spherical antenna have multiple eigenvalues for which independent eigenfunctions can be found. These eigenfunctions are frequency independent, too.

A.2.2 Two-Port Example—Lumped-Element Circuit

The simple two-port of Fig. A.1(a) provides an example explicitly illustrating the occurrence of branch points in the eigenvalues of an impedance matrix and their mutual cancellation in the singularity expansion of the inverse of the matrix. The impedance matrix of the circuit is
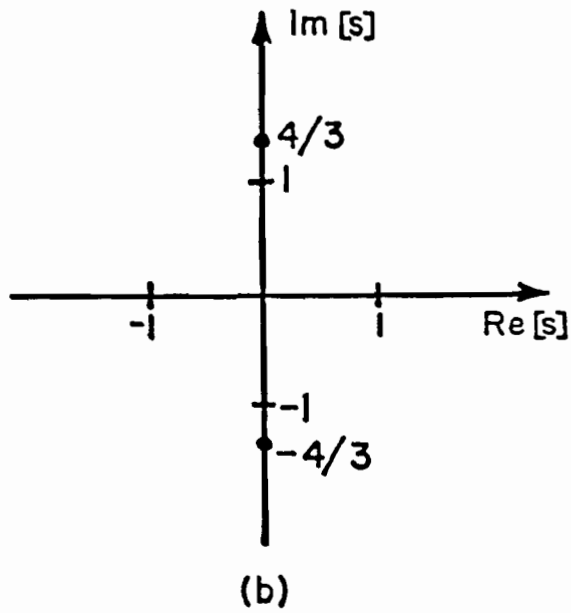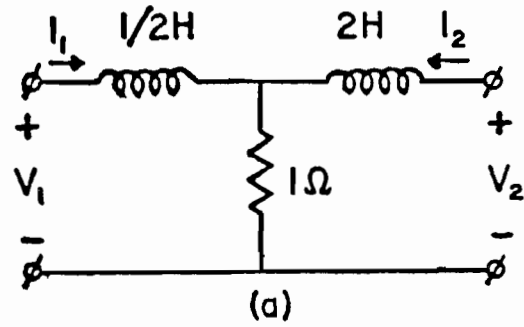
Figure A.1 (a) Two-port circuit and (b) branch points of the eigenvalues of the impedance matrix.

$$[Z] = \begin{bmatrix} 1 + s/2 & 1 \\ & \\ 1 & 1 + 2s \end{bmatrix} \tag{A.10}$$

with the eigenvalues

$$\lambda_{\genfrac{}{}{0pt}{}{1}{2}}(s) = 1 + \frac{5}{4} s \pm \sqrt{\Delta(s)} \quad , \tag{A.11}$$

where

$$.\Delta(s) = 1 + \left[\frac{3}{4} s\right]^2 , \tag{A.12}$$

and with the eigenvectors

$$\left[I_{\genfrac{}{}{0pt}{}{1}{2}}(s)\right] = \begin{bmatrix} 1 \\ \\ \frac{3}{4} s \pm \sqrt{\Delta(s)} \end{bmatrix} . \tag{A.13}$$

From (A.11) one finds that $\lambda_1(-5/2) = 0$ and $\lambda_2(0) = 0$, and hence $[Z^{-1}]$ has poles at $s = 0$ and $s = -5/2$. However, there are also branch points at $s = \pm j4/3$, where the eigenvalues become degenerate (Fig. A.1(b)). Away from these isolated points we can find $[Z^{-1}]$ according to (A.2) as

$$\left[Z^{-1}(s)\right] = \frac{1}{1 + \frac{5}{4} s + \sqrt{\Delta(s)}} \frac{\begin{bmatrix} 1 & \frac{3}{4} s + \sqrt{\Delta(s)} \\ \frac{3}{4} s + \sqrt{\Delta(s)} & \left[\frac{3}{4} s + \sqrt{\Delta(s)}\right]^2 \end{bmatrix}}{2\sqrt{\Delta(s)} \left[\sqrt{\Delta(s)} + \frac{3}{4} s\right]}$$

$$+ \frac{1}{1 + \frac{5}{4} s - \sqrt{\Delta(s)}} \frac{\begin{bmatrix} 1 & \frac{3}{4} s - \sqrt{\Lambda(s)} \\ \frac{3}{4} s - \sqrt{\Delta(s)} & \left[\frac{3}{4} s - \sqrt{\Delta(s)}\right]^2 \end{bmatrix}}{2\sqrt{\Delta(s)} \left[\sqrt{\Delta(s)} - \frac{3}{4} s\right]} . \tag{A.14}$$

At the branch points the denominators of (A.14) vanish and the expansion is not valid. However, if the terms in (A.14) are combined together we obtain

$$\left[Z^{-1}(s) \right] = \begin{bmatrix} \dfrac{2s+1}{s^2 + \frac{5}{2}s} & \dfrac{-1}{s^2 + \frac{5}{2}s} \\[4mm] \dfrac{-1}{s^2 + \frac{5}{2}s} & \dfrac{s/2+1}{s^2 + \frac{5}{2}s} \end{bmatrix} . \qquad (A.15)$$

Obviously, there are no branch points in $\left[Z^{-1}(s) \right]$. Its only singularities are the poles at $s = 0$ and at $s = -5/2$.

At a branch point the root system can be used to expand the inverse matrix. The coefficients of this expansion can be found with the help of the biorthogonal root system [Pease, 1965]. For example, at the branch point $s = +j4/3$, [Z] has a double eigenvalue $\lambda = 1 + j5/3$ and a root system

$$[I_{1,1}] = \begin{bmatrix} 1 \\ j \end{bmatrix} , \quad [I_{1,2}] = \begin{bmatrix} 0 \\ 1 \end{bmatrix} \qquad (A.16)$$

If the scalar product

$$<[I_1], [I_2]> = [I_1]^{\dagger}[I_2] \qquad (A.17)$$

is introduced where $\dagger$ denotes the Hermitian transpose, a biorthonormal root system can be found as

$$\left[W_{1,1} \right] = \begin{bmatrix} 1 \\ 0 \end{bmatrix} , \quad \left[W_{1,2} \right] = \begin{bmatrix} j \\ 1 \end{bmatrix} . \qquad (A.18)$$

Using (A.16) and (A.18) $[Z^{-1}]$ can be expanded at the branch point $s = +j4/3$ as

241

$$\left[Z^{-1}\left(j\frac{4}{3}\right)\right] = \frac{1}{\left(1+j\frac{5}{3}\right)}\begin{bmatrix} 1 & 0 \\ 0 & 1 \end{bmatrix} + \frac{1}{\left(1+j\frac{5}{3}\right)^2}\begin{bmatrix} j & -j \\ -j & j \end{bmatrix}, \qquad (A.19)$$

with a similar conjugate representation at the other branch point, $s = -j4/3$. Note that the eigenfunction expansion (A.14) is valid throughout the complex s-plane except at the two isolated branch points.

One might speculate that the resistive element in this circuit is the feature which leads to the branch points. Since we wish to draw analogies with scattering from lossless surfaces, this would indeed be untimely. However, one can readily construct LC circuit examples as well, where the branch points arise. Furthermore, examples are easily constructed in which the branch points lie in the right half plane.

A.2.3 Two-Port Example—Non-Uniform Transmission Line

To illustrate that the branch point occurrence in the eigenvalues is not limited to lumped systems, we consider a section of lossless non-uniform transmission line of length L (Fig. A.2(a)). The impedance and admittance per unit length are assumed to vary exponentially with the distance x along the line according to, respectively, $z(x) = \exp(2\alpha x)$ and $y(x) = y\exp(-2\alpha x)$, where $z = s\ell$ and $y = sc$ and ℓ and c denote, respectively, the per-unit-length inductance and capacitance of the line. Viewing the line as a two-port network we may find its chain-parameter matrix by the method described in [Bertnolli, 1967]. From the chain-parameter description the impedance matrix can be found as

$$[Z] = \begin{bmatrix} \frac{\Gamma}{y}\,\text{ctnh}(\Gamma L) + \frac{\alpha}{y} & \frac{\Gamma}{y}\,\frac{e^{\alpha L}}{\sinh(\Gamma L)} \\ \frac{\Gamma}{y}\,\frac{e^{\alpha L}}{\sinh(\Gamma L)} & \left[\frac{\Gamma}{y}\,\text{ctnh}(\Gamma L) - \frac{\alpha}{y}\right]e^{2\alpha L} \end{bmatrix}, \qquad (A.20)$$
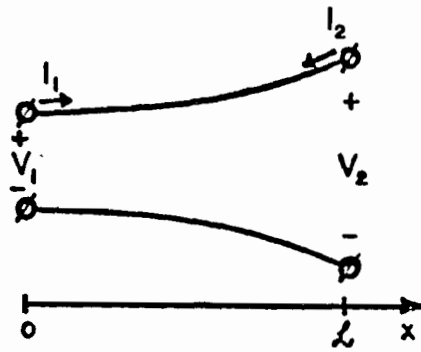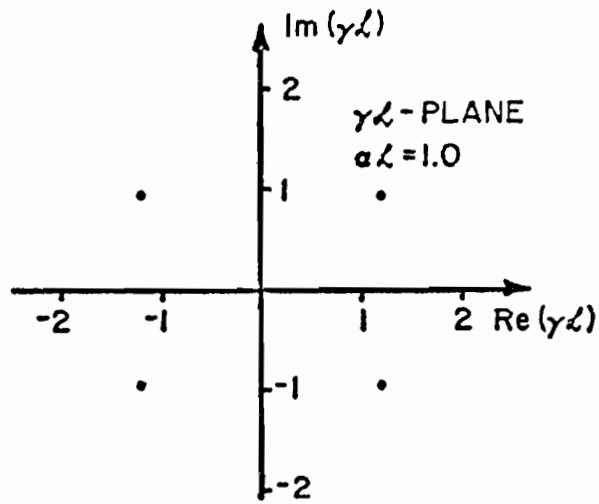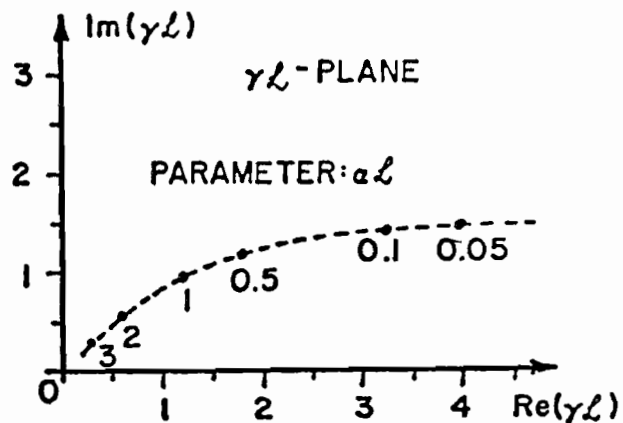
Figure A.2 (a) Exponential transmission line, (b) branch points of the eigenvalues of the impedance matrix and (c) branch-point trajectory as a function of the taper parameter.

where $\Gamma = \overline{\sqrt{\alpha^2 + zy}} = \overline{\sqrt{\alpha^2 + (s/v)^2}}$ with $v = 1/\sqrt{\ell c}$ denoting the speed of light
(a deviation from the generally accepted notation is made here because
the symbol c is used in this section to denote the per-unit-length
capacitance of the line). The inverse of [Z] can be readily found as

$$
\left[Z^{-1}\right] = \begin{bmatrix} \dfrac{\Gamma}{z}\,\text{ctnh}(\Gamma L) - \dfrac{\alpha}{z} & -\dfrac{\Gamma}{z}\,\dfrac{e^{-\alpha L}}{\sinh(\Gamma L)} \\[3ex] -\dfrac{\Gamma}{z}\,\dfrac{e^{-\alpha L}}{\sinh(\Gamma L)} & \left[\dfrac{\Gamma}{z}\,\text{ctnh}(\Gamma L) + \dfrac{\alpha}{z}\right]e^{-2\alpha L} \end{bmatrix} \, . \qquad (A.21)
$$

If the hyperbolic functions in (A.21) are expanded in a power series,
it is seen that only even powers of Γ enter the elements of $\left[Z^{-1}\right]$, hence
the inverse matrix has no branch points. Its only singularities are the
infinite number of poles given by

$$
\frac{sL}{v} = \pm j\overline{\sqrt{(n\pi)^2 + (\alpha L)^2}} \, , \quad n = 0,1,2,\dots \qquad (A.22)
$$

The eigenvalues of [Z] can be found to be

$$
\lambda_{\frac{1}{2}} = e^{\alpha L}\left\{ \frac{\Gamma}{y}\,\text{ctnh}(\Gamma L)\cosh(\alpha L) - \frac{\alpha}{y}\,\sinh(\alpha L) \pm \overline{\sqrt{\Delta(s)}} \right\} \, , \qquad (A.23)
$$

where

$$
\Delta(s) = \left(\frac{\Gamma}{y}\right)^2 \text{ctnh}^2(\Gamma L)\cos^2(\alpha L) - \left(\frac{\alpha}{y}\right)\left(\frac{\Gamma}{y}\right)\text{ctnh}(\Gamma L)\sinh(2\alpha L)
$$

$$
\qquad (A.24)
$$

$$
+ \left(\frac{\alpha}{y}\right)^2 \sinh^2(\alpha L) - \frac{z}{y} \, .
$$

Obviously, there are branch points in the eigenvalues (A.23) which can
be found from the equation $\Delta(s) = 0$. A numerical investigation of
(A.24) yields four branch points located symmetrically in the four
quadrants in the s-plane (Fig. A.2(b)). Note that the branch points
are not restricted to the left half-plane. The trajectory of the

first-quadrant branch point for different values of the parameter α is shown in Fig. A.2(c).

We recover a uniform transmission line—$i.e.$, a symmetric structure— by letting $\alpha \to 0$. In the limit, the branch points recede to infinity, continuing the trend indicated in Fig. A.2(c).

A.3 Scalar Scattering from a Prolate Spheroid

The role of symmetry in eliminating the appearance of branch points in the preceding examples suggests that in the scattering problem we should examine a finite-extent structure which, for simplicity, conforms to a separable coordinate system but which is not symmetric under a general rotation, $i.e.$, something separable, but not spherical. The vector Helmholtz equation is not separable in spheroidal coordinates, but the scalar Helmholtz equation is. We therefore consider the associated scalar scattering problem.

The geometry of the structure under consideration and the coordinate system are shown in Fig. A.3. The surface S of the spheroid is defined by the radial coordinate $u = u_0$, and the semifocal distance is ℓ. We are interested in the eigenvalues of the integral equation in ψ defined by

$$\iint\limits_S G_0(\vec{r},\vec{r}',s)\psi(\vec{r}',s)dS' = F(\vec{r},s), \; \vec{r} \in S \quad , \tag{A.25}$$

where $G_0(\vec{r},\vec{r}',s)$ is the scalar Green function defined in (2.4) and $F(\vec{r},s)$ is the forcing function.

Expanding the Green function in (A.25) on the surface S in terms of the spheroidal wave functions gives [$Flammer$, 1957]
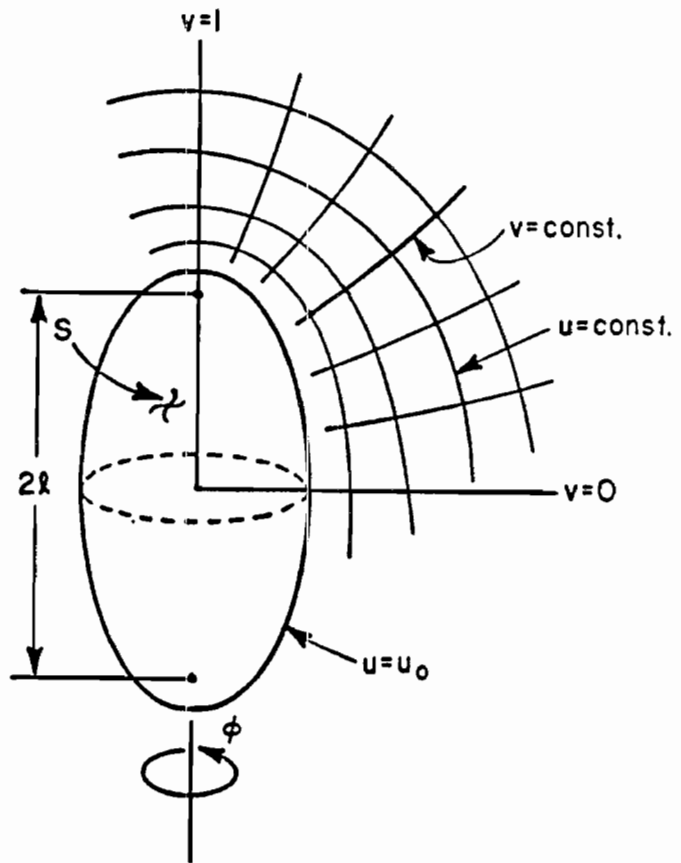
Figure A.3 Geometry of the prolate spheroid.

$$\frac{e^{-\gamma|\vec{r}-\vec{r}'|}}{4\pi|\vec{r}-\vec{r}'|} = -\frac{\gamma}{2\pi} \sum_{m=0}^{\infty} \sum_{n=m}^{\infty} \frac{(2-\delta_{om})}{N_{mn}} S_{mn}(q,v) S_{mn}(q,v')$$

$$\times \cos[m(\phi-\phi')] R_{mn}^{(1)}(q,u_0) R_{mn}^{(4)}(q,u_0), \quad \vec{r}, \vec{r}' \epsilon \, S \quad , \tag{A.26}$$

where δ_{nm} is the Kronecker delta, $q = -j\gamma\ell$ is the frequency parameter, and S_{mn} and $R_{mn}^{(i)} (i = 1,4)$ satisfy the following differential equations which arise in the separation of the Helmholtz equation in prolate spheroidal coordinates [*Flammer*, 1957]:

$$\frac{d}{dv}\left[(1-v^2)\frac{d}{dv} S_{mn}(q,v)\right] + \left[a_{mn}(q) - q^2v^2 - \frac{m^2}{1-v^2}\right] S_{mn}(q,v) = 0 \tag{A.27}$$

and

$$\frac{d}{du}\left[(u^2-1)\frac{d}{du} R_{mn}^{(i)}(q,u)\right] - \left[a_{mn}(q) - q^2u^2 + \frac{m^2}{u^2-1}\right] R_{mn}^{(i)}(q,u) = 0 \quad , \tag{A.28}$$

where m and n are integers and a_{mn} are the separation parameters. The normalization factors appearing in (A.26) are defined through the orthogonality of the angle (periodic) functions

$$\int_{-1}^{1} S_{mn}(q,v) S_{mn'}(q,v) dv = S_{nn'} N_{mn} \tag{A.29}$$

and are found to be[1)]

$$N_{mn} = 2 \sum_{r=0}^{\prime} \frac{(r+2m)! \left[d_r^{mn}(q)\right]^2}{(2r+2m+1)r!} \quad , \tag{A.30}$$

where the functions $d_r^{mn}(q)$ are the coefficients in the expansion of the angle functions S_{mn} in terms of the associated Legendre functions:

[1)] The prime over the summation sign indicates that the summation is over (only) even values when (n-m) is even and over (only) odd values when (n-m) is odd.

$$S_{mn}(q,v) = \sum_{r=0}^{\infty'} d_r^{mn}(q) p_{m+r}^m(v) \quad .$$

(A.31)

The substitution of this expansion into (A.27) yields a three-term recursion formula for the coefficients d_r^{mn}. From this recursion formula, we obtain a transcendental equation, the roots of which are the separation parameters a_{mn} [*Oguchi,* 1970]. This equation has the form

$$U(a_{mn}, q) = 0 \quad .$$

(A.32)

It follows from (4.8) that the separation parameters a_{mn} coupling (A.27) and (A.28) are functions of the frequency parameter q.

The orthogonality given by (A.29) is awkward in identifying (A.26) with an eigenfunction expansion of the (scalar counterpart to) form (2.11), because the weight in the integration of (A.29) is unity, while in (A.25) the surface metric is

$$dS' = \ell^2 \sqrt{(u_o^2 - 1)(u_o^2 - v'^2)} \; dv' d\phi' \quad .$$

(A.33)

However if we interpret

$$\hat{\psi}(v,\phi,s) = \ell^2 \sqrt{(u_o^2 - 1)(u_o^2 - v'^2)} \; \psi(v,\phi,s)$$

(A.34)

as the unknown in (A.25) and define

$$<\Gamma,\psi> = \int_0^{2\pi} \int_{-1}^1 \Gamma\psi \; dv \; d\phi \; ,$$

(A.35)

then our symmetric product yields the orthogonality integral of (A.29). By comparison with (2.11) we find that

$$\lambda_{mn}(q) \propto R_{mn}^{(1)}(q,u_o) R_{mn}^{(4)}(q,u_o) \quad .$$

(A.36)

The radial (non-periodic) functions $R_{mn}^{(i)}$ in the eigenvalues (A.36) can be computed in terms of the spherical Bessel functions [Flammer, 1957]. Here, we are interested only in their analytical properties in the complex q-plane. Since $R_{mn}^{(i)}$ satisfy the differential equation (A.28), their behavior in the q-plane[1] can be inferred from the properties of the associated separation parameters a_{mn}. The branch points of $a_{mn}(q)$ are also branch points of $R_{mn}^{(i)}$, and thus of λ_{mn}. The functions $a_{mn}(q)$ have been investigated in the literature [Oguchi, 1970; Meixner et al., 1980] and, indeed, it has been found that they have branch points in the q-plane. The branch point locations can be computed by the procedure outlines below.

The behavior of the separation parameters a_{mn} in the q-plane is governed by the differential equation [Wilton et al., 1975]

$$\frac{d}{dq} a_{mn}(q) = - \frac{U_q}{U_a} , \qquad (A.37)$$

which results from (A.32) (the subscript denotes a partial differential with respect to the variable indicated). Integration of (A.37) on a closed contour C in the q-plane yields

$$\Delta a_{mn} = - \oint_C \frac{U_q}{U_a} dq . \qquad (A.38)$$

This integral gives a non-zero contribution, i.e., a_{mn} is multi-valued, if the contour C encloses a zero of U_a. The location of the branch point of a_{mn} coincides with the location of the zero of U_a. Thus, the branch points can be found by solving (A.32) together with

_____

[1] Following the convention accepted in the literature we use the q-plane rather than the s-plane here. The normalized frequency plane is related to the q-plane by the trivial mapping $\gamma \ell = jq$.

249

$$U_a(a_{mn}, q) = 0 \quad . \tag{A.39}$$

These simultaneous transcendental equations can be solved by a Newton-like iteration [*Oguchi*, 1970].

A partial listing of branch points in the eigenvalues for a number of indices m,n is given in [*Oguchi*, 1970]. A more complete list is included in [*Meixner et al.*, 1980]. As an example, we display in Table A.1 a number of branch points for m=0-2 and n=0-4. We observe that some of the branch points for different eigenvalues coincide, which means that an eigenvalue for some m,n can be obtained by an analytic continuation into another Riemann sheet in the q-plane of an eigenvalue with different indices. This observation substantiates the degeneracy interpretation of the branch point which is mentioned in Section 2.3.

When the spheroid is deformed into a sphere, which can be accomplished by letting the focal distance ℓ go to zero, the points in the γ-plane corresponding to branch points in the q-plane recede to infinity—a phenomenon analogous to that observed in the case of a non-uniform transmission line (Section A.2.3). Indeed, it is well known that the eigenvalues of the sphere are proportional to the spherical Hankel functions of the second kind, which are meromorphic in the finite complex frequency plane. The absence of branch points can be thus attributed to the geometrical symmetry of this structure, which is lacking in the spheroid case.

Table A.1 Branch points of the eigenvalues in the prolate spheroid problem.

m	n	Branch Points of $a_{m,n}(\gamma \ell)$
0	0,2	$-2.601670 + j\ 1.824770$
0	2,4	$-5.807965 + j\ 2.094267$
0	2,4	$-3.081362 + j\ 5.217093$
0	1,3	$-2.887165 + j\ 3.563644$
1	1,3	$-4.097453 + j\ 1.998555$
1	2,4	$-4.492300 + j\ 3.862833$
2	2,4	$-5.449457 + j\ 2.736987$

A.4 TM Scattering from an Elliptic Cylinder

In this section we consider an electromagnetic scattering problem which demonstrates the introduction of branch points because of its departure from rotational symmetry: that of transverse-magnetic (TM) scattering from a perfectly conducting elliptic cylinder. Since the structure is infinite in extent, a branch point at the origin of the frequency plane appears as in the case of the circular cylinder [*Schafer and Kouyoumjian*, 1975]. It is demonstrated here that the elliptic cross-section introduces additional branch points into the frequency plane.

The geometry of the structure and the coordinate system used are shown in Fig. A.4. The elliptical surface of the cylinder, which is infinite in the z-direction, is defined by the radial coordinate $u = u_o$. The semifocal distance is ℓ. The integral equation for the current density $J_z(\vec{\rho}, \gamma)$ excited by the incident electric field $E_z^i(\vec{\rho}, \gamma)$ is

$$- \frac{j}{4} Z_o \gamma \int_L J_z(\vec{\rho}', \gamma) H_0^{(2)} (-j\gamma |\vec{\rho} - \vec{\rho}'|) dL' = E_z^i(\vec{\rho}, \gamma), \quad \vec{\rho} \in L , \qquad (A.40)$$

where $H_0^{(2)}$ is the Hankel function of the second kind and zeroth order and is the two-dimensional free-space Green function.

The Hankel function can be expanded in terms of Mathieu functions as [*Jones*, 1964]

$$H_0^{(2)} (-j\gamma |\vec{\rho} - \vec{\rho}'|) = 2 \sum_{m=0}^{\infty} ce_m(v, q) ce_m(v', q) Mc_m^{(1)} (u_o, q) Mc_m^{(4)} (u_o, q)$$

$$+ 2 \sum_{m=1}^{\infty} se_m(v, q) se_m(v', q) Ms_m^{(1)} (u_o, q) Ms_m^{(4)} (u_o, q) ,$$

$$\vec{\rho}, \vec{\rho}' \in L . \qquad (A.41)$$
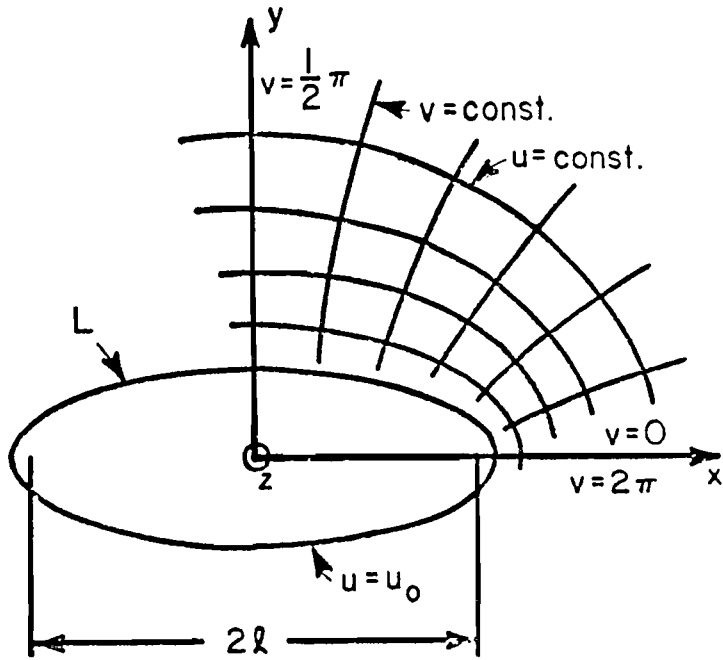
Figure A.4 Cross-sectional geometry of the elliptic cylinder.

The frequency parameter is $q = -(\gamma\ell/2)^2$ and ce_m and se_m are, respectively, the even and odd angular (periodic) Mathieu functions [*McLachlan*, 1947] satisfying

$$\left[\frac{d^2}{dv^2} + \left[\begin{Bmatrix} a_m(q) \\ b_m(q) \end{Bmatrix} - 2q \cos 2v\right]\right]\begin{Bmatrix} ce_m(v,q) \\ se_m(v,q) \end{Bmatrix} = 0 \tag{A.42}$$

and $Mc_m^{(i)}$ and $Ms_m^{(i)}$ ($i = 1,4$) are the radial (non-periodic) Mathieu functions satisfying

$$\left[\frac{d^2}{du^2} + \left[\begin{Bmatrix} a_m(q) \\ b_m(q) \end{Bmatrix} - 2q \cosh u\right]\right]\begin{Bmatrix} Mc_m^{(i)}(u,q) \\ Ms_m^{(i)}(u,q) \end{Bmatrix} = 0 \quad . \tag{A.43}$$

As in the spheroidal equation case in the preceding section, the separation constants $a_m(q)$ and $b_m(q)$ of the Mathieu's equation satisfy transcendental characteristic equations and are dependent on the complex variable q. The angular functions possess the following orthogonality properties:

$$\int_0^{2\pi} ce_m(v,q)ce_n(v,q)dv = \pi\,\delta_{mn} \quad , \tag{A.44a}$$

$$\int_0^{2\pi} se_m(v,q)se_n(v,q)dv = \pi\,\delta_{mn} \quad , \tag{A.44b}$$

and

$$\int_0^{2\pi} se_m(v,q)ce_n(v,q)dv = 0 \quad , \tag{A.44c}$$

while the integration metric is

$$dL = \ell\sqrt{\cosh^2 u_o - \cos^2 v} \; dv \quad . \tag{A.45}$$

By applying reasoning analogous to that used in the spheroid development, we conclude that the frequency variation of the eigenvalues of the operator in (A.40) follows

$$\lambda_{n_0^e}(q) \propto \begin{Bmatrix} Mc_n^{(1)}(u_0,q)Mc_n^{(4)}(u_0,q) \\ Ms_n^{(1)}(u_0,q)Ms_n^{(4)}(u_0,q) \end{Bmatrix} \quad . \tag{A.46}$$

Since the radial functions $Mc_n^{(4)}$ and $Ms_n^{(4)}$ are related to the Hankel functions of the second kind [McLachlan, 1947], they share with them the branch point at the origin—the branch point due to the infinite extent of the scatterer. The radial functions in (A.46) manifest additional branch points, however.

As in the spheroid case, the analytic properties of these functions in the complex q-plane can be inferred from the properties of the separation parameters $a_n(q)$ and $b_n(q)$. These functions have been investigated in the literature [Blanch and Clemm, 1969; Meixner et al., 1980] where it was shown that a_n and b_n have branch points in the q-plane, and the locations of these points were computed for a number of values of n by a scheme similar to that outlined in Section A.3. The listing of branch points in a_n and b_n in $\gamma\ell$-plane for n=0-7 is displayed in Table A.2.

When the elliptic cylinder is deformed into a cylinder with circular cross-section, the eigenvalues of the external scattering problem become the Hankel functions having only a branch point at the origin. Thus we may associate the additional branch points in the elliptic cylinder with the lack of symmetry in this structure.

Table A.2   Branch points of the eigenvalues in the elliptic cylinder problem.

n	Branch Points of $a_n(\gamma\ell)$	n	Branch Points of $b_n(\gamma\ell)$
0,2	-1.713919 + j 1.713919	2,4	-3.722621 + j 3.722621
1,3	-1.917584 + j 3.376788	3,5	-3.968460 + j 5.416204
2,4	-2.046414 + j 4.988464	4,6	-4.159649 + j 7.064678
3,5	-2.140312 + j 6.582698	5,7	-4.316064 + j 8.689667
4,6	-5.739541 + j 5.739541	6,8	-7.758450 + j 7.758450
4,6	-2.213980 + j 8.168790	6,8	-4.448352 + j 10.300680
5,7	-5.895408 + j 7.313526	7,9	-8.027379 + j 9.468520
5,7	-2.274478 + j 9.750397	7,9	-4.562911 + j 11.902630

A.5 Conclusions

It is demonstrated by several specific examples that eigenvalues of impedance-type integral operators can have branch points in the complex frequency plane (s-plane). Through a two-port circuit example, it is demonstrated that as s approaches a branch point two eigenvalues become degenerate, the eigenfunction expansion of the inverse operator becomes invalid, and the root vector expansion must be used to expand the inverse operator at this point. If the terms involving the degenerate eigenvalues are grouped together a representation is obtained which does not exhibit any branch points and simple poles are the only singularities of the inverse operator.

In the eigenanalysis of scattering from a prolate spheroid or elliptic cylinder branch points also occur and two or more eigenvalues become degenerate. In fact, since some of the branch points for different eigenvalues coincide, one of the eigenvalues can be obtained by the analytic continuation into another Riemann sheet in the s-plane of the "neighboring" eigenvalue.

These examples demonstrate that symmetry plays an important role in the presence or absence of branch points in the eigenvalues of the EFIE operator. It is conjectured that branch points may always be present when sufficient object symmetry is lacking. This conjecture is supported by the fact that branch points appear when the sphere is deformed into a spheroid or when a circular cylinder is deformed into an elliptic one. The analogous phenomenon has been observed in the circuit and transmission line problems. For example, when the taper parameter of a non-uniform transmission line goes to zero (the line becomes uniform), the branch points move away to infinity.

The examples substantiate that the previously-speculated-upon branch points do occur in the scattering theory. In addition, they suggest a tie between the branch points and the need for root vectors in a basis spanning the solution space. Whether the need for root vectors in the solution expansion is isolated to branch points in the frequency plane and what ties exist between the branch points and the normal operator condition stated by *Ramm* [1980] remain open questions.

APPENDIX B

AN APPLICATION OF THE SEM EQUIVALENT CIRCUITS TO
THE ANALYSIS OF ANTENNAS WITH NONLINEAR LOADS

In this appendix we give some examples of the application of the
SEM equivalent circuits to the analysis of antennas with nonlinear
loads. Nonlinear effects are important for antenna systems containing
semiconductors, integrated circuits, and voltage limiters when they
may be illuminated by an extremely strong signal, such as that produced
by a lightning strike or an electromagnetic pulse (EMP) [*Liu and
Tesche*, 1976].

One approach to the analysis of nonlinearly loaded energy-collecting
structures has been to solve a space-time domain integral equation for
the current [*Miller et al.*, 1976; *Liu and Tesche*, 1976; *Schuman*, 1974].
At each time step a system of nonlinear algebraic equations must be
solved in this method by a Newton-like iterative procedure. Even
complex-shaped bodies could be treated by this technique if the procedures
developed recently by *Rao et al.* [1981] are applied. This approach
is not very practical, however, since the complex boundary value
problem must be resolved each time the loading is changed.

An original technique for the analysis of antennas with nonlinear
loads has been developed recently by *Tesche and Liu* [1975] (see also
[*Liu and Tesche*, 1976; *Liu et al.*, 1977]. They use frequency domain
data of an unloaded structure and a numerical Fourier transform to
formulate a Volterra-type integral equation for the current in the
time domain. Subsequently, this equation is solved by stepping in
time and iteration procedure.

It is believed that the approach proposed in the present work, *i.e.*, the application of the SEM-derived equivalent circuits and a standard circuit analysis code to the analysis of nonlinearly loaded energy-collecting structures, can be an useful alternative to the method of *Tesche and Liu* [1975]. It has the advantage that no special purpose computer code is required. Furthermore, the input languages of many advanced circuit analysis programs, such as SCEPTRE [*Jensen and McNamee*, 1976], allow one to define almost any real or conceivable loading situation. Also, an EMP with an arbitrary time history can be easily defined.

In the examples given below the nonlinear loading is provided by an 1N414B high-speed switching diode. The diode was represented in the circuit by a voltage dependent current source $I = I_o[\exp(AV)-1]$ with $I_o = 2.9*10^{-7}$ A and $A = 15$ V^{-1} in shunt with a 0.5 pF capacitor modeling the junction capacitance. The diode parameters were taken from [*Liu et al.*, 1977].

In Figure B.1 is plotted the input current response of a circular loop ($\Omega = 15$) driven by a double exponential function voltage source (with a peak voltage of 10V) through a diode connected in the forward direction. Shown is also the input current with the diode removed. The topology and element values of the equivalent circuit used are given in Table 5.2.

In Figures B.2 and B.3 are shown the current and voltage responses at a port of a plane-wave-excited loop antenna ($\Omega=15$) loaded by a diode. The incident wave time history is a step function with a peak field strength $2\pi b$ $E_o^1 = 100V$ (note that the response cannot be magnitude-normalized as in the examples given in Chapters 5 and 6, since the
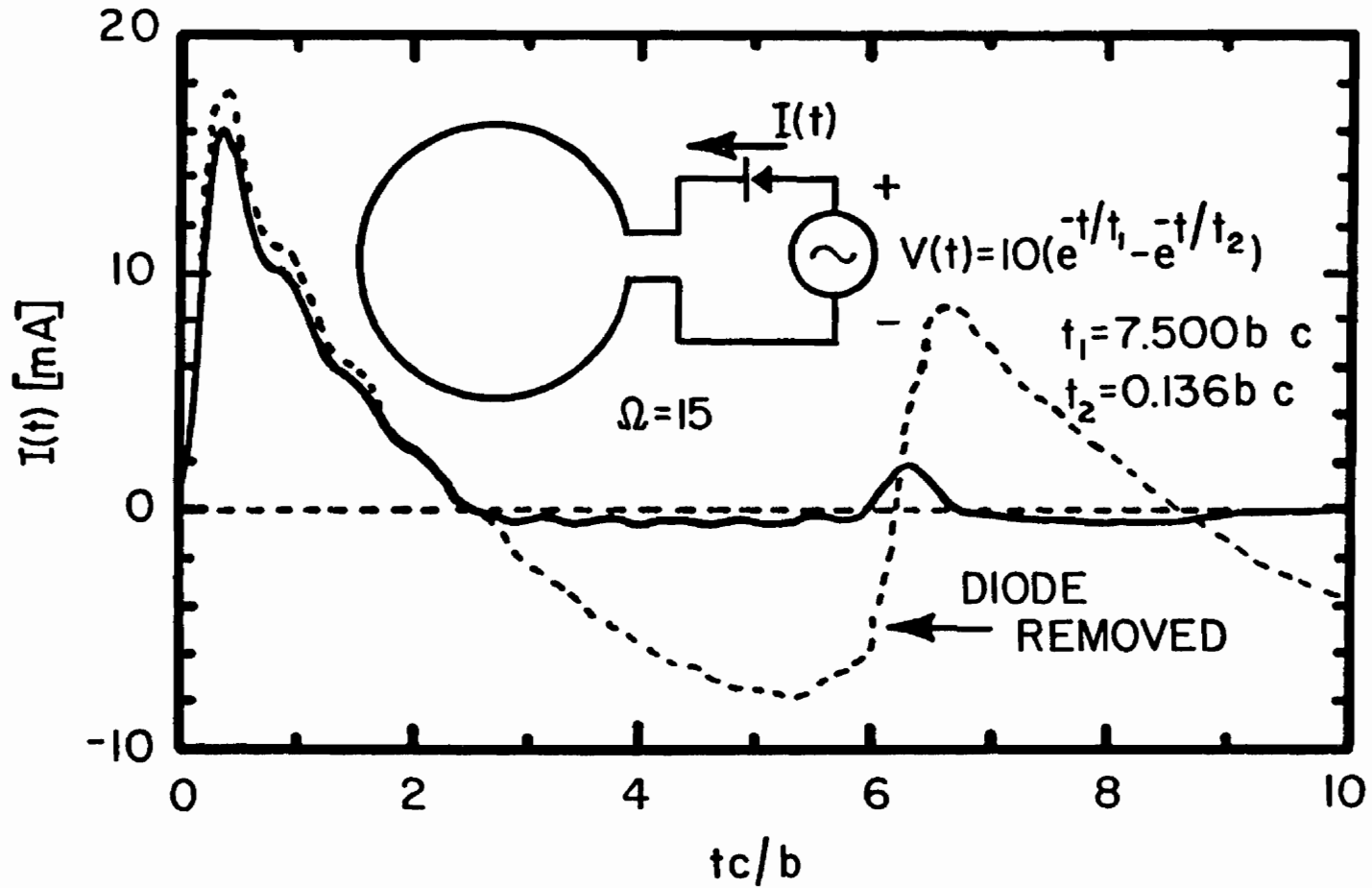
Figure B.1 Input current of a circular loop antenna driven through a diode by a double-exponential voltage source. Shown is also the input current with the diode removed.
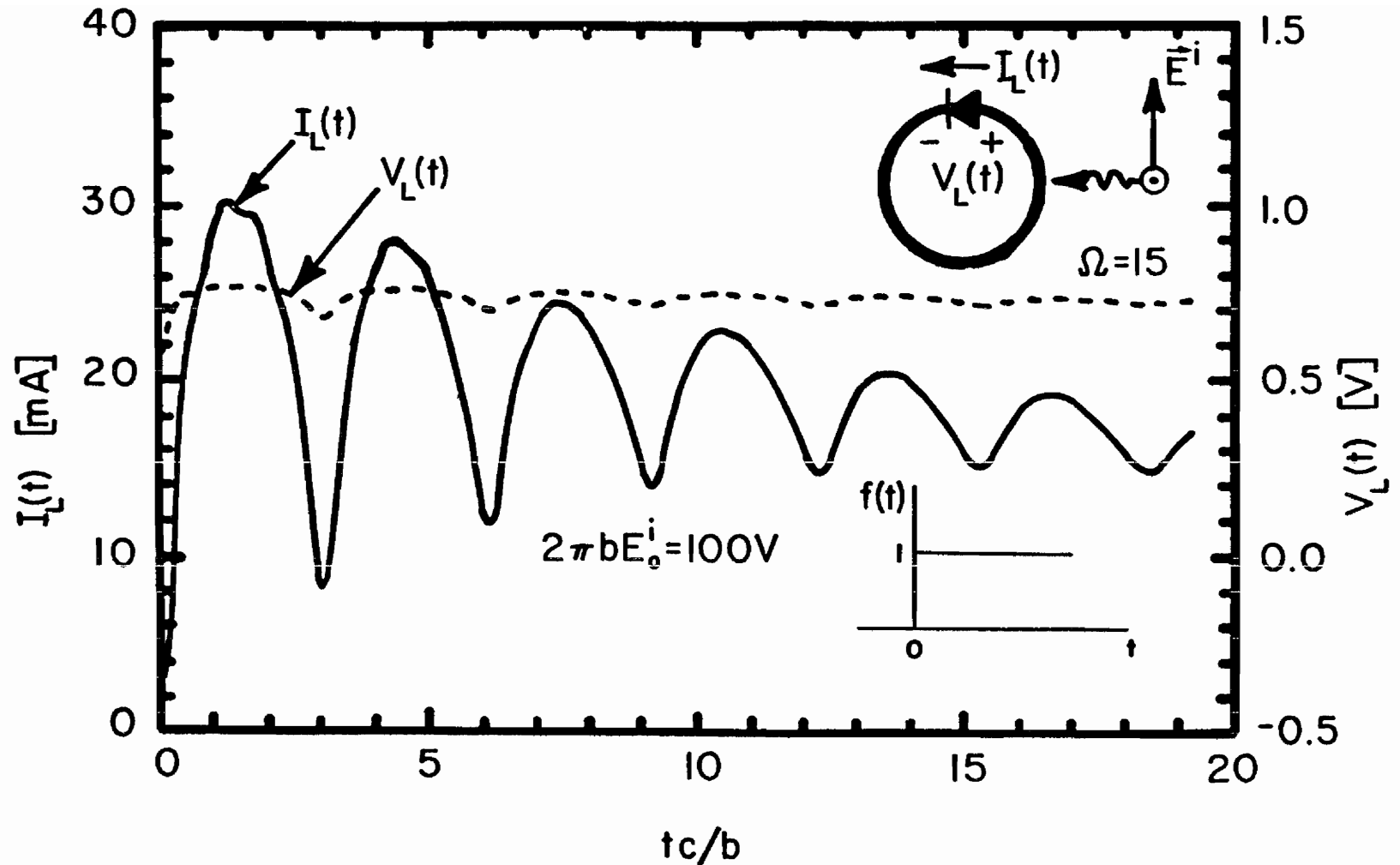
Figure B.2 Port current (solid) and voltage (dashed) responses of a circular loop antenna loaded by a diode and excited by a step function plane wave. The diode is polarized initially in the "forward" direction.
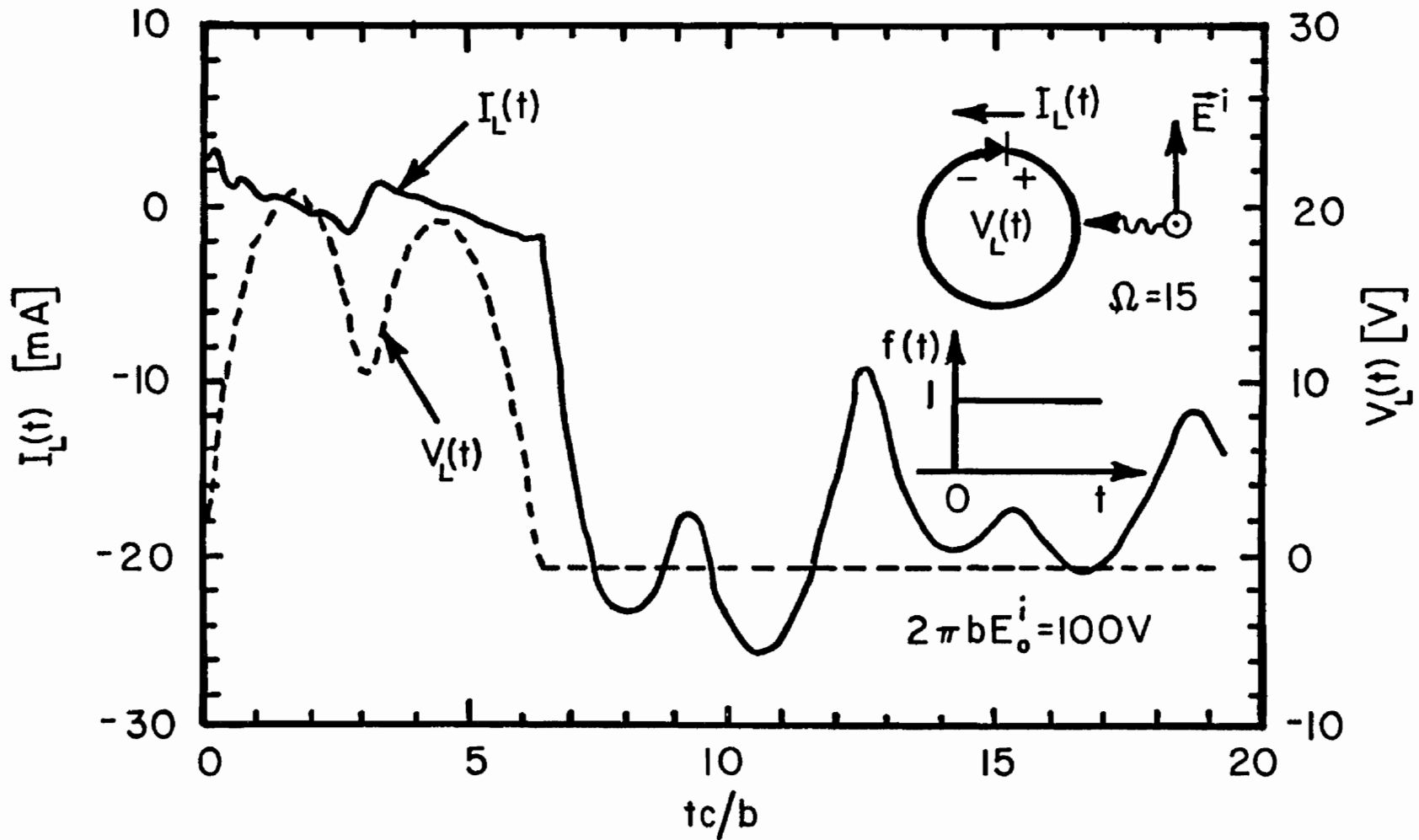
Figure B.3 Port current (solid) and voltage (dashed) responses of a circular loop antenna loaded by a diode and excited by a step function plane wave. The diode is polarized initially in the "reverse" direction.

present problem is nonlinear). In the case of Figure B.2   the diode is connected so that it is polarized in the "on" direction from the beginning and has little influence on the current waveform (*cf*. Figure 5.8). When the terminals of the diode are interchanged the situation changes drastically, as shown in Figure B.3.   The current is initially blocked and then flows in the reverse direction. Also in this case, the reverse voltage on the diode can reach quite high levels in early times. The topology and element values of the equivalent circuit used are defined in Tables 5.2 and 5.4. Only the first eight dominant pole-pair modules were employed. Note that in this case the transfer networks for $n = 1, 3, 5, \ldots$ are not present, as indicated in Table 5.4.

In Figures B.4 and B.5 are plotted the current and voltage wave-forms at a port of a cylindrical dipole antenna ($\Omega = 10.6$) center-loaded with a diode, exicted by a broadside incident plane wave with a double exponential time history and a peak field strength of $\ell E_o^i = 100V$. In Figure B.4   the diode is connected so that it is initially forward conducting. In Figure B.5   the terminals of the diode are interchanged. As expected [*Liu and Tesche*, 1976], the current of the diode for $tc/\ell > 1$ oscillates at about twice the rate of the short-circuit current shown in Figure 6.21. This phenomenon occurs because the diode, when reverse conducting, acts as an open circuit. The antenna thus behaves in effect like two collinear wires, each having its fundamental natural resonance at a frequency roughly twice that of the whole structure. The simplified circuit of Figure 6.19 was used in the SCEPTRE analyses, with the elements defiend in Tables 6.2 and 6.12.

Figure B.4 Port current (solid) and voltage (dashed) responses of a cylindrical dipole antenna loaded at the center by a diode and excited by a double-exponential function plane wave. The diode is polarized initially in the "forward" direction.
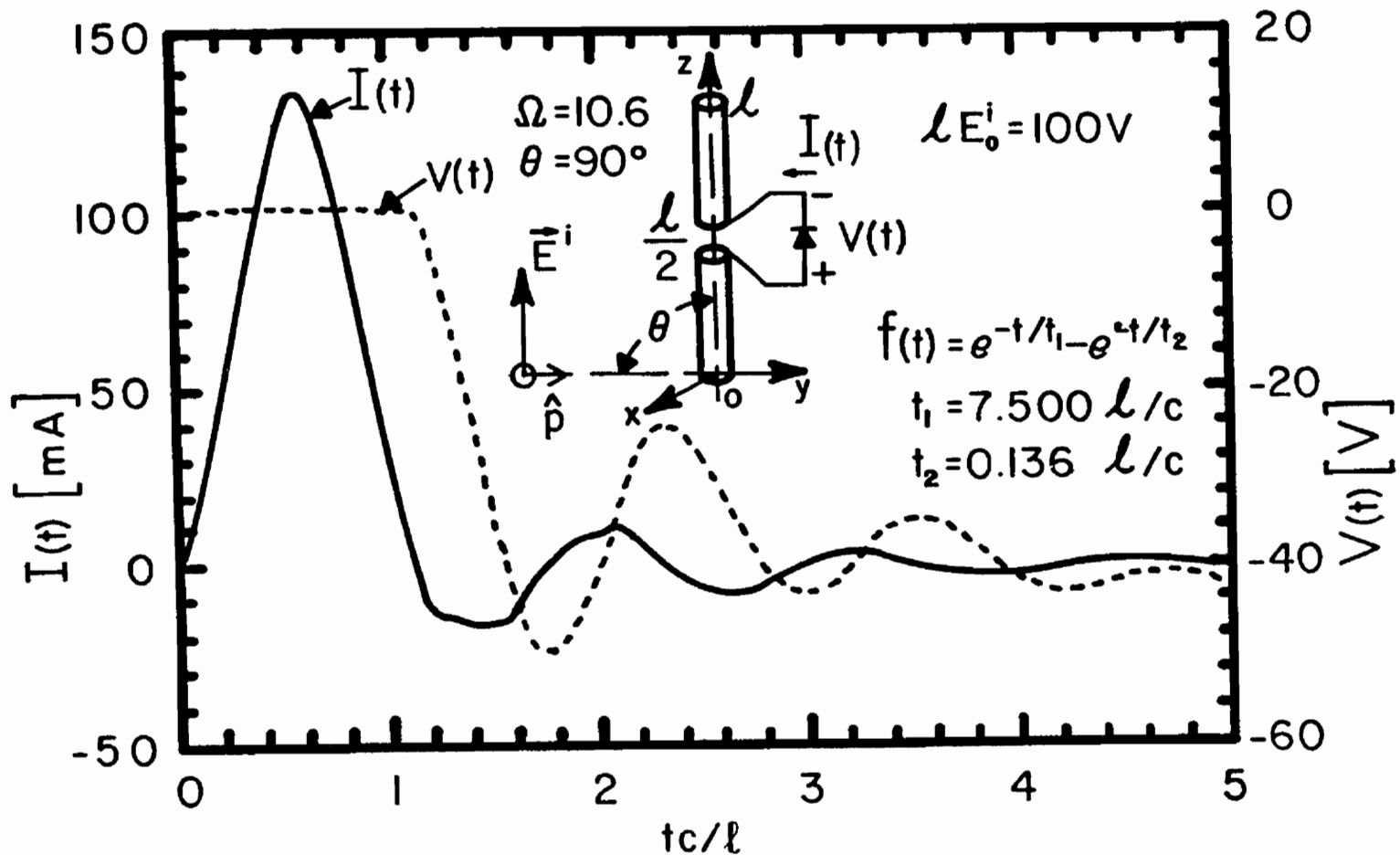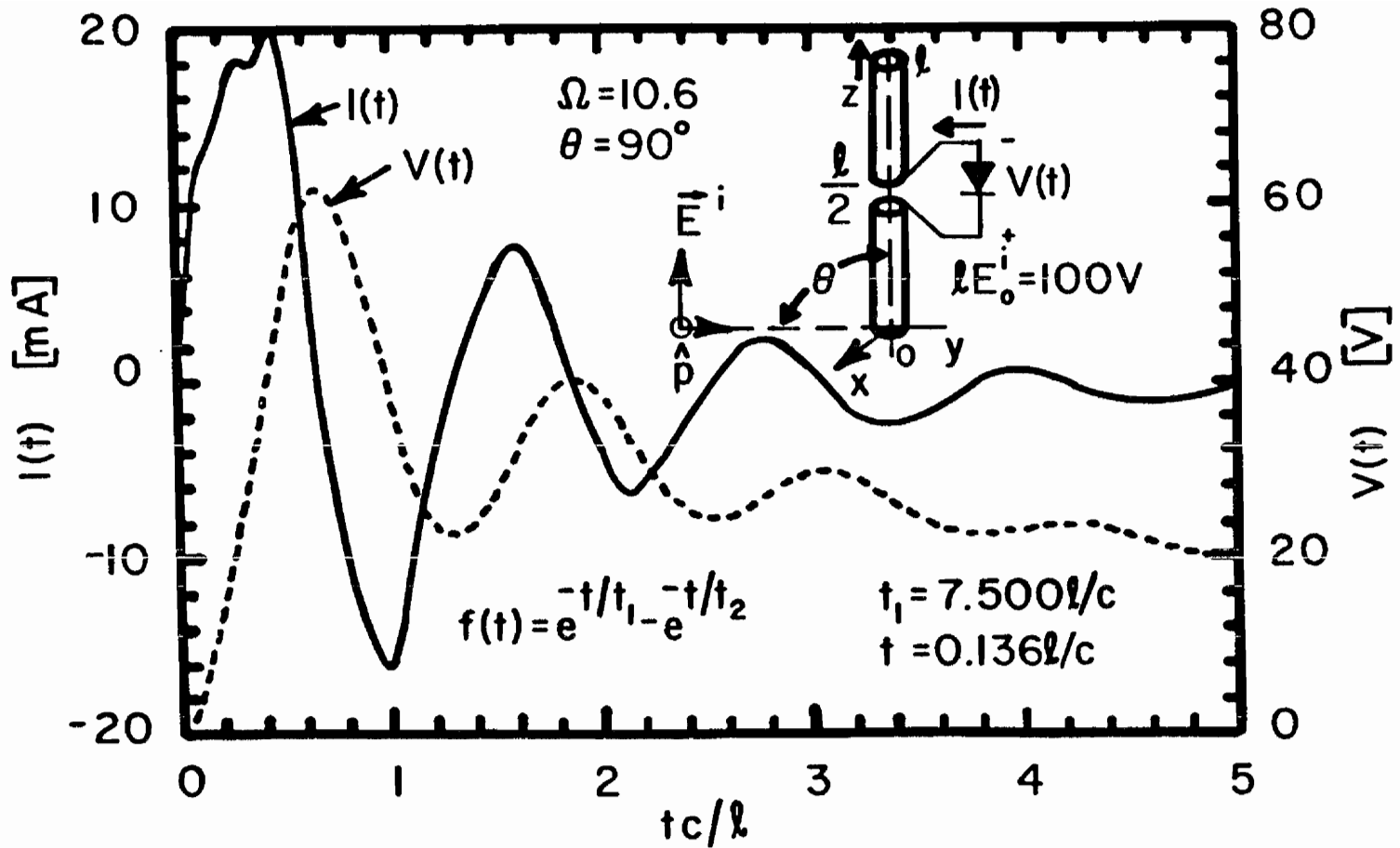
Figure B.5 Port current (solid) and voltage (dashed) responses of a cylindrical dipole antenna loaded at the center by a diode and excited by a double-exponential function plane wave. The diode is polarized initially in the "reverse" direction.

APPENDIX C

STATIC CAPACITANCE OF THE SPHERICAL ANTENNA

C.1 Introduction

The rapidity of the convergence of the eigenfunction or SEM
series for the driving-point admittance of a simply-connected object
can be significantly increased if the static capacitance of the
structure is known, as discussed in Chapter 7. The early time response
of an SEM equivalent circuit can often be improved by adjusting the
static capacitance of the circuit to the proper value as demonstrated
in Chapters 6 and 7. It is in this context that we discuss here the
computation of the static capacitance of the spherical antenna.

In the first part of this appendix approximate closed form formulas
are derived for the internal (C^{int}) and external (C^{ext}) capacitances
of a spherical antenna with an equatorial slot. The derivation
essentially follows that given by *Franceschetti* [1976]. A constant
field distribution in the slot region is assumed. In the second part
a numerical technique is used to compute the total capacitance of
the spherical antenna. Results are presented for $\theta_g = 90°$ (equatorial
slot) and $\theta_g = 60°$ with the slot width $d/a = 0.05$ in both cases.

C.2 Derivation of Closed Form Expressions for the Internal and External Capacitance

In the equatorial slot case the expressions (7.31) and (7.32)
can be rewritten as

$$C^{int} = \frac{\pi a}{Z_o c} \sum_{n=1}^{\infty} \frac{4n-1}{2n(2n-1)} V_n(\pi/2, \alpha_o) \qquad (C-1)$$

and

and

$$C^{ext} = \frac{\pi a}{Z_o c} \sum_{n=1}^{\infty} \frac{4n-1}{(2n-1)^2} V_n(\pi/2, \alpha_o) \tag{C.2}$$

with

$$V_n(\pi/2, \alpha_o) = \frac{P^1_{2n-1}(\eta_o)\sqrt{1-\eta_o^2}}{2n} \frac{1}{2\alpha_o} \int_{-\eta_o}^{\eta_o} P^1_{2n-1}(\eta) d\eta \tag{C.3}$$

where $\eta = \sin\alpha$, $\alpha = \pi/2 - \theta$, and $\alpha_o = d/(2a)$.

Following *Franceschetti* [1976] we define

$$f_n^{\infty}(\alpha_o) = \frac{1}{n} V_n^{\infty}(\alpha_o) \tag{C.4}$$

where $V_n^{\infty}(\alpha_o)$ is the asymptotic expansion of $V_n(\pi/2, \alpha_o)$ for $n \to \infty$.
From [*Franceschetti, 1976*]

$$P^1_{2n-1}(\eta) \sim \sqrt{\frac{4n}{\pi \cos\alpha}} \cos(n\pi) \cos[(2n-\tfrac{1}{2})\alpha] \tag{C.5}$$

it follows that

$$P^1_{2n-1}(\eta_o) P^1_{2n-1}(\eta) \sim \frac{2n}{\pi\sqrt{\cos\alpha_o \cos\alpha}}$$

$$\times \left\{ \cos[(2n-\tfrac{1}{2})(\alpha-\alpha_o)] + \cos[(2n-\tfrac{1}{2})(\alpha+\alpha_o)] \right\} \tag{C.6}$$

and

$$f_n^{\infty}(\alpha_o) = \frac{2\sqrt{\cos\alpha_o}}{n\pi} \frac{1}{2\alpha_o} \int_{-\alpha_o}^{\alpha_o} \sqrt{\cos\alpha} \cos[(2n-\tfrac{1}{2})(\alpha+\alpha_o)] d\alpha \quad . \tag{C.7}$$

Now the series (C.1) and (C.2) can be recast in the following form

$$C^{int} = \frac{\pi a}{Z_o c} \left\{ \sum_{n=1}^{\infty} f_n^{\infty}(\alpha_o) + \sum_{n=1}^{\infty} \left[\frac{4n-1}{2n(2n-1)} V_n(\pi/2, \alpha_o) - f_n(\alpha_o) \right] \right\} \tag{C.8}$$

and

$$C^{ext} = \frac{\pi a}{Z_o c} \left\{ \sum_{n=1}^{\infty} f_n^{\infty}(\alpha_o) + \sum_{n=1}^{\infty} \left[\frac{4n-1}{(2n-1)^2} V_n(\pi/2,\alpha_o) - f_n^{\infty}(\alpha_o) \right] \right\} \quad . \quad (C.9)$$

By using [*Franceschetti*, 1976]

$$\sum_{n=1}^{\infty} \frac{\cos[(2n-\frac{1}{2})x]}{n} = - \cos(x/2)\ell n(2\sin x) + (\pi/2-x)\sin(x/2) \quad (C.10)$$

and assuming a narrow gap ($\alpha_o \ll 1$), the first term in (C.8) and (C.9) can be summed as follows

$$\sum_{n=1}^{\infty} f_n^{\infty}(\alpha_o) = \frac{2\sqrt{\cos\alpha_o}}{\pi} \frac{1}{2\alpha_o} \int_{-\alpha_o}^{\alpha_o} \sqrt{\cos\alpha_o} \sum_{n=1}^{\infty} \frac{\cos[(2n-\frac{1}{2})(\alpha+\alpha_o)]}{n} d\alpha$$

$$\cong - \frac{2}{\pi} \frac{1}{2\alpha_o} \int_{-\alpha_o}^{\alpha_o} \ell n[2(\alpha+\alpha_o)] d\alpha = \frac{2}{\pi} \left[\ell n\left(\frac{a}{2d}\right) + 1 \right] \quad . \quad (C.11)$$

The series in the second terms in (C.8) and (C.9) are uniformly convergent with respect to α_o and their evaluation can be safely performed for $\alpha_o = 0$. Noting that

$$P_{2n-1}^1(0) = 2n \, P_{2n}(0) \quad (C.12)$$

and, for large n,

$$P_{2n}^1(0) \sim \frac{(-1)^n}{\sqrt{n\pi}} \quad (C.13)$$

it is easy to show that

$$V_n(\pi/2,\alpha_o) \sim \frac{2}{\pi} \quad (C.14)$$

and

$$f_n^{\infty}(0) = \frac{2}{n\pi} \quad . \quad (C.15)$$

Using (C.14) and (C.15) it can be shown that

$$\sum_{n=1}^{\infty} \left\{ \frac{4n-1}{2n(2n-1)} V_n(\pi/2,\alpha_o) - f_n^{\infty}(\alpha_o) \right\} = \frac{2}{\pi} \sum_{n=1}^{\infty} \left\{ \frac{4n-1}{2n(2n-1)} - \frac{1}{n} \right\} \cong \frac{2}{\pi} 0.693 \qquad (C.16)$$

and

$$\sum_{n=1}^{\infty} \left\{ \frac{4n-1}{(2n-1)^2} V_n(\pi/2,\alpha_o) - f_n^{\infty}(\alpha_o) \right\} = \frac{2}{\pi} \sum_{n=1}^{\infty} \left\{ \frac{4n-1}{(2n-1)^2} - \frac{1}{n} \right\} \cong \frac{2}{\pi} 2.620 \ . \qquad (C.17)$$

The substitution of (C.11), (C.16) and (C.17) into (C.8) and (C.9)
yields

$$C^{int} \cong \frac{2}{Z_o c} \left[\ell n \left(\frac{a}{d}\right) + 1 \right] a \qquad (C.18)$$

and

$$C^{ext} \cong \frac{2}{Z_o c} \left[\ell n \left(\frac{a}{d}\right) + 2.97 \right] a \qquad . \qquad (C.19)$$

For $d/a = 0.05$ these expressions give $C^{int} \cong 70.66a$ [pF] and
$C^{ext} = 104.74a$ [pF], so that the total capacitance $C^{tot} = C^{int} + C^{ext} \cong$
75.4a[pF].

It is of interest to point out that *Schelkunoff* [1952] derived
the following expression for the capacitance of a symmetrical spherical
antenna driven by a biconical transmission line:

$$C = \frac{2}{Z_o c} \left[\ell n \left(\frac{a}{d}\right) + 0.52 \right] a \qquad (C.20)$$

This expression differs significantly from (C.19), except for very
narrow slots.

C.3 Computation of the Total Capacitance by the MoM Technique

In this part of the appendix the static capacitance of the spherical
antenna is computed by solving numerically the integral equation for

the charge density. The integral equation is formulated in terms of the total charge density on the spherical shell, *i.e.*, it cannot distinguish between the charge residing on the internal and the external side of the shell. As a result the capacitance obtained is the total capacitance, which is a sum of the internal and external capacitances discussed above. The numerical technique applied is the Method of Moments (MOM) [*Harrington*, 1968] with subsectional basis functions.

The charge distribution $\sigma(\vec{r})$ on the spherical antenna (Figure 7.1) can be found from the system of two coupled integral equations

$$\iint\limits_{S_1} \frac{\sigma(\vec{r'})}{4\pi\varepsilon R}\, dS' + \iint\limits_{S_2} \frac{\sigma(\vec{r'})}{4\pi R}\, dS' = \begin{cases} V_1 \;,\; \vec{r} \in S_1 \\[2mm] V_2 \;,\; \vec{r} \in S_2 \end{cases} \tag{C.21}$$

where $R = |\vec{r} - \vec{r'}|$, and S_1 and S_2 denote the upper and lower parts of the sphere, respectively, having the arbitrary constant potentials V_1 and V_2, and ε is the permittivity of the medium. In order to find the capacitance C of the structure, the system (C.21) must be solved with the constraint $Q = Q^1 = -Q^2$ where Q^1 and Q^2 denote the total charges on S_1 and S_2, respectively. Then we have

$$C = \frac{Q}{V_1 - V_2} \;. \tag{C.22}$$

Exploiting the azimuthal symmetry of the problem, eq. (C.21) can be rewritten in the form

$$\int_0^{\theta_g-\alpha_o} \rho(\theta')K(\theta,\theta')d\theta' \; + \; \int_{\theta_g+\alpha_o}^{\pi} \rho(\theta')K(\theta,\theta')d\theta' = \begin{cases} 4\pi^2 \; V_1, & 0 \le \theta \le \theta_g - \alpha_0 \\[2mm] 4\pi^2 \; V_2, & \theta_g + \alpha_o \le \theta \le \pi \end{cases} \qquad (C.23)$$

where

$$\rho(\theta) = \frac{2\pi a}{\varepsilon} \; \sigma(\theta) \qquad (C.24)$$

$$K(\theta,\theta') = \frac{\sin\theta'}{\sin\left[\dfrac{\theta+\theta'}{2}\right]} \; K(\beta) \qquad (C.25)$$

$$\beta = \frac{\sin\theta \; \sin\theta'}{\sin^2\left[\dfrac{\theta+\theta'}{2}\right]} \qquad (C.26)$$

and $K(\beta)$ denotes the complete elliptic integral of the first kind [*Abramowitz and Stegun*, 1965]. In terms of the new function $\rho(\theta)$ the total charge on surface S_1 is given by

$$Q^1 = a \; \varepsilon \int_0^{\theta_g-\alpha_o} \rho(\theta)\sin\theta d\theta \qquad (C.27)$$

with an analogous expression for S_2.

The MoM technique is applied to (C.23) by dividing the surface of the spherical antenna into N subsections and expanding the unknown function $\rho(\theta)$ in terms of the pulse functions as follows

$$\rho(\theta) = \sum_{j=1}^{N} Q_j \; P_j(\theta) \qquad (C.28)$$

where

$$P_j(\theta) = \begin{cases} 1 & , \; \theta_j^m - \dfrac{\Delta\theta_j}{2} \le \theta \le \theta_j^m + \dfrac{\Delta\theta_j}{2} \\[3mm] 0 & , \; \text{otherwise} \end{cases} \qquad (C.29)$$

This is illustrated by Figure C.1.

The substitution of (C.28) into (C.23) and matching the integral equations at θ_j^m results in the matrix equation for the expansion coefficients

$$\sum_{j=1}^{N} a_{ij} Q_j = \begin{cases} 4\pi^2 \, V_1 & , \; 1 \le i \le N_1 \\ 4\pi^2 \, V_2 & , \; N_1 \le i \le N \end{cases} \tag{C.30}$$

with

$$a_{ij} = \int_{\theta_j^m - \frac{\Delta\theta_j}{2}}^{\theta_j^m + \frac{\Delta\theta_j}{2}} K(\theta_i^m, \theta')d\theta' \tag{C.31}$$

where the index i takes on the values $i = 1, 2, \ldots, N$, N_1 and N_2 $(N_1 + N_2 = N)$ denote the number of zones on S_1 and S_2, respectively. The integration is done numerically by a Gaussian quadrature.

The integrand in (C.31) is singular for $i = j$, thus the integration for the self-term cannot be performed directly. This difficulty is taken care of by subtracting the logarithmic singularity of the elliptic integral and integrating the singular term analytically as follows

$$a_{ij} \cong \int_{\theta_i^m - \frac{\Delta\theta_i}{2}}^{\theta_i^m + \frac{\Delta\theta_i}{2}} \left\{ K(\theta_i^m), \theta') + \ln\left|\frac{\theta_i^m - \theta'}{2}\right| \right\} d\theta' - \Delta\theta_i \left[\ln\left(\frac{\Delta\theta_i}{4}\right) - 1 \right] . \tag{C.32}$$

In order to gain some confidence in this method, the capacitance with respect to infinity of a *solid* sphere ($\alpha_o = 0$, $V_1 = V_2 = V$, $Q = Q^1 + Q^2$), $C = Q/V$, was computed first. With $N = 10$ the value 111.267 a [pF] was obtained, which is in an excellent agreement with the exact value $4\pi\varepsilon a$.
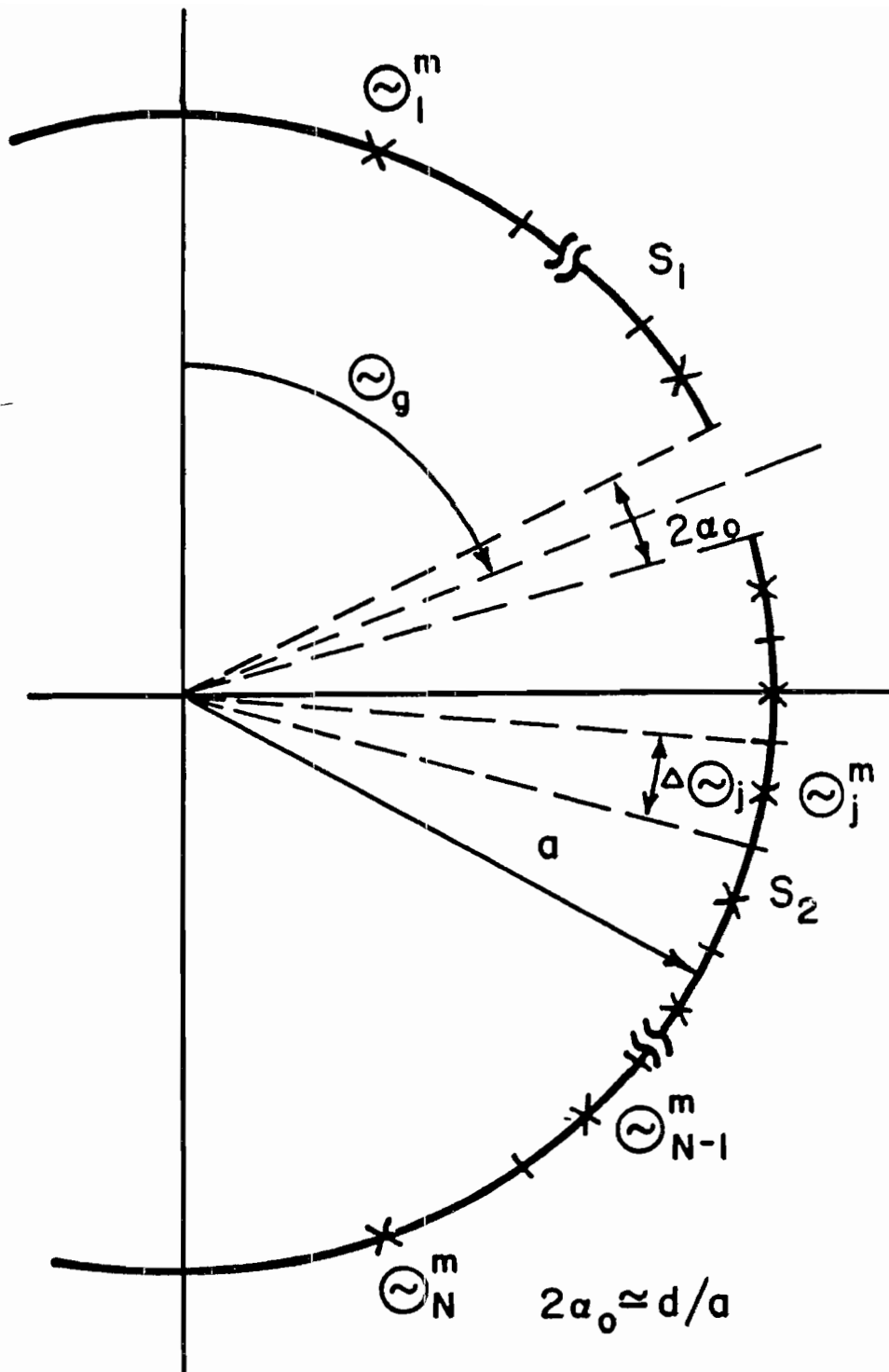
273

Figure C.1 Subdomain placement on the spherical antenna for the capacitance computation by the method of moments.

In order to find the capacitance (or "capacity" [*Adams*, 1972]) of the slotted sphere, the system (B.23) must be solved together with the charge neutrality constraint. However, as pointed out in [*Adams*, 1972; *Lee*, 1978], it is more convenient to solve the unconstrained system (C.23) twice for even and odd voltage excitation modes (Figure C.2) and then suitably superpose the results. It can be shown that the capacity is then given by

$$C = \frac{Q_o^1 Q_e^2 - Q_e^1 Q_o^2}{2V(Q_e^1 + Q_e^2)} \qquad (C.33)$$

where the superscripts "e" and "o" denote, respectively, the even and odd excitation modes.

The capacity of the spherical antenna computed by this scheme is shown in Table C.1 and in Figure C.3 as a function of the number of zones N. The extrapolated values of the normalized capacitances are 165 [pF/m] for $\theta_g = 90°$ and 137 [pF/m] for $\theta_g = 60°$. The width the slot was $d/a = 0.05$ in both cases. The value 165 a [pF] obtained in the equatorial slot case agrees favorably with the value 175.4 a [pF] obtained from the closed form formulas derived in the first part of this appendix, considering that approximations are made in both approaches.
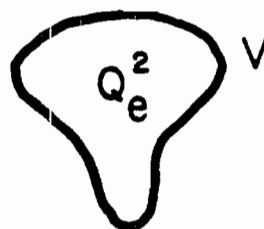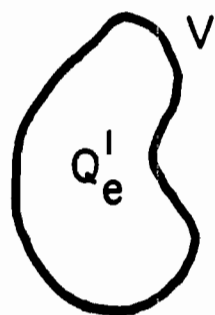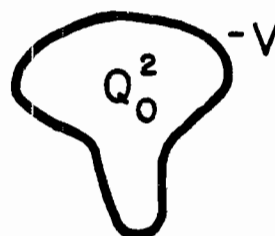
Figure C.2 (a) The even and (b) odd excitation modes of a two-part structure.

Table C.1 The capacitance per unit radius of a spherical antenna with a slot of width $d/a = 0.05$ located at $\theta_g = 90°$ and $\theta_g = 60°$, as a function of the number of zones N in the MoM procedure.

N	C/a[pF/m]	
	$\theta_g = 90°$	$\theta_g = 60°$
10	132.7	107.5
20	145.9	119.4
30	151.5	124.7
40	154.6	127.5
50	156.6	129.3
60	158.0	130.6
70	159.0	131.5

Figure C.3 Capacitance of the spherical antenna with a slot located at
θ = 90° and at θ = 60° as a function of 1/N, where N is the number of zones
in the MoM solution.

REFERENCES

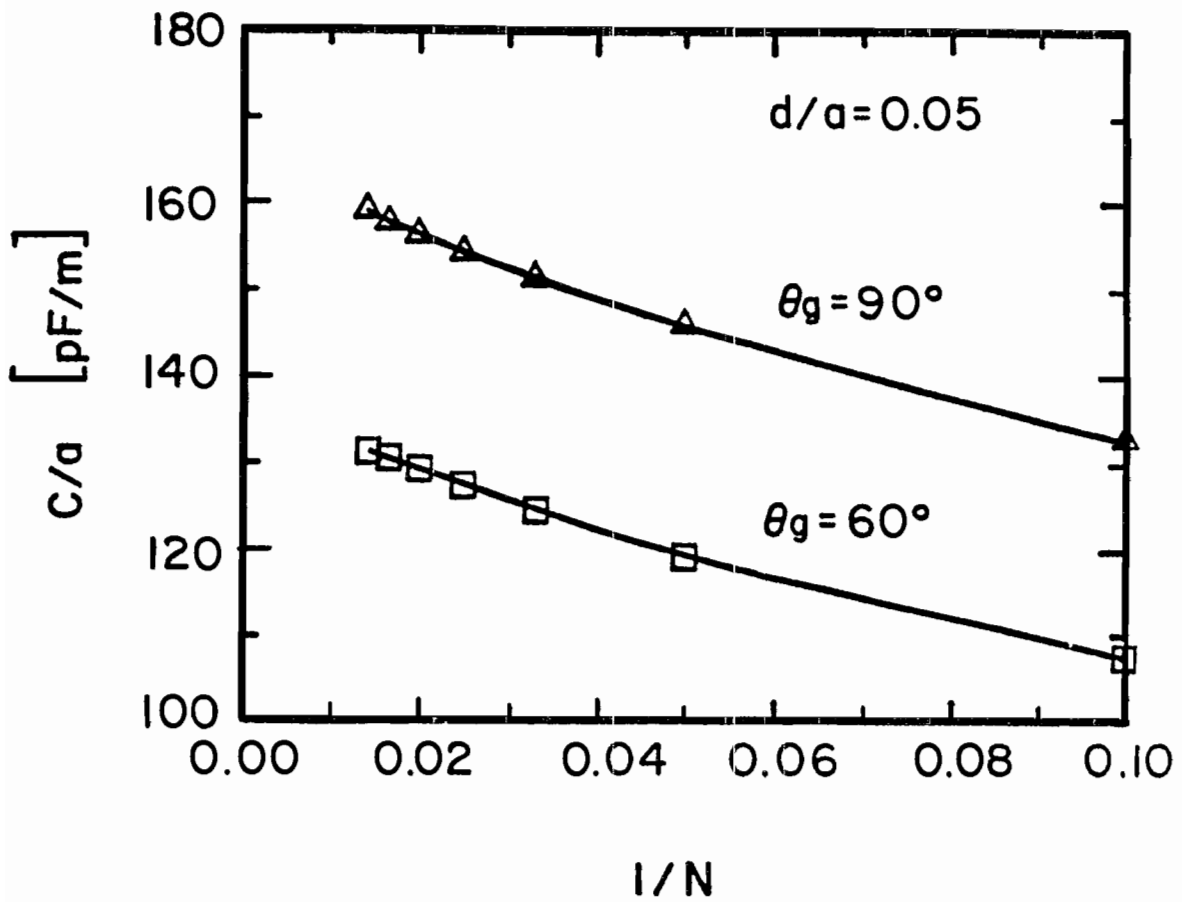Abramowitz, A., and I.A. Stegun (Eds.) (1965), *Handbook of Mathematical Functions*, New York: Dover.

Adams, A.T. (1972), *Electromagnetics for Engineers*, New York: Ronald Press.

Balabanian, N. (1958), *Network Synthesis*, Englewood Cliffs, N.J.: Prentice Hall.

Barnes, P.R. (1973), "On the Singularity Expansion Method as Applied to the EMP Analysis and Simulation of the Cylindrical Dipole Antennas," Oak Ridge National Laboratory, *Interaction Note* 146.

Baum, C.E. (1969), "The Single-Gap Hollow Spherical Dipole in Non-Conducting Media," Air Force Weapons Laboratory, *Sensor and Simulation Note* 91.

-------- (1971), "On the Singularity Expansion Method for the Solution of Electromagnetic Interaction Problems," Air Force Weapons Laboratory, *Interaction Note* 88.

-------- (1972), "On the Singularity Expansion Method for the Case of First Order Poles," Air Force Weapons Laboratory, *Interaction Note* 129.

-------- (1975), "On the Eigenmode Expansion Method for Electromagnetic Scattering and Antenna Problems, Part I: Some Basic Relations for Eigenmode Expansions, and their Relation to the Singularity Expansion," Air Force Weapons Laboratory, *Interaction Note* 229.

-------- (1967a), "Single Port Equivalent Circuits for Antennas and Scatterers," Air Force Weapons Laboratory, *Interaction Note* 295.

-------- (1967b), "The Singularity Expansion Method," in L.B. Felsen (Ed.), *Transient Electromagnetic Fields*, Berlin-Heidelberg-New York: Springer.

-------- (1967c), "Emerging Technology for Transient and Broad-Band Analysis and Synthesis of Antennas and Scatterers," *Proc. IEEE*, 64, 1598-1616.

-------- (1978), "Toward an Engineering Theory of Electromagnetic Scattering: The Singularity and Eigenmode Expansion Methods," in P.L.E. Ushlenghi (Ed.), *Electromagnetic Scattering*, New York: Academic Press.

--------, E.L. Breen, J.C. Giles, J. O'Neill, and G.D. Sower (1978), "Sensors for Electromagnetic Pulse Measurements Both Inside and Away from Nuclear Source Regions," *IEEE Trans. Antennas Propagat.*, AP-26, 22-35.

————, and L.W. Pearson (1981), "On the Convergence and Numerical Sensitivity of the SEM Pole Series in Early-Time Scattering Response," *Electromagnetics*, to be published.

————, and B.K. Singaraju (1980), "The Singularity and Eigenmode Expansion Methods With Application to Equivalent Circuits and Related Topics," in V.K. Varadan, and V.V. Varadan (Eds.), *Acoustic, Electromagnetic, and Elastic Wave Scattering -- Focus on the T-Matrix Approach*, Oxford: Pergamon Press.

Bertnolli, E.C. (1967), "Analysis of the n-Wire Exponential Line," *Proc. IEEE*, 55, 1225.

Blackburn, R.F. (1967), "Analysis and Synthesis of an Impedance-Loaded Loop Antenna Using the Singularity Expansion Method," Ph.D. Thesis, Department of Electrical Engineering, University of Mississippi.

————, K.R. Umashankar, and D.R. Wilton (1978), "Evaluation of the Integral of the Anger-Weber Function With a Complex Argument," University of Mississippi, *Mathematics Note* 57.

————, and D.R. Wilton (1978), "Analysis and Synthesis of an Impedance-Loaded Loop Antenna Using the Singularity Expansion Method," *IEEE Trans. Antennas Propagat.*, AP-26, 136-140.

Blanch, G., and D.S. Clemm (1969), "The Double Points of Mathieu's Differential Equation," *Math. Comp.*, 23, 97-108.

Bott, R., and R.J. Duffin (1949), "Impedance Synthesis Without Use of Transformers," *J. Appl. Phys.*, 20, 816.

Brigham, E.O. (1974), *The Fast Fourier Transform*, Englewood Cliffs, N.J.: Prentice-Hall.

Brune, O. (1931), "Synthesis of a Finite 2-Terminal Network Whose Driving-Point Impedance is a Prescribed Function of Frequency," *J. Math. and Physics*, 10, 191-236.

Bucci, O.M., and G. Franceschetti (1974), "Input Admittance and Transient Response of Spheroidal Antennas in Dispersive Media," *IEEE Trans. Antennas Propagat.*, AP-22, 526-536.

Cho, K.S., and J.T. Cordaro (1979), "Calculation of the Singularity Expansion Method Parameters from the Transient Response of a Thin Wire," University of New Mexico, *Interaction Note* 379.

Chu, L.J. (1948), "Physical Limitations of Omni-Directional Antennas," *J. Appl. Phys.*, 19. 1136-1175.

Cochran, J.A. (1972), *Analysis of Linear Integral Equations*, New York: McGraw-Hill.

Crow, T.T., B.D. Graves, and C.D. Taylor (1972), "Numerical Techniques Useful in the Singularity Expansion Method as Applied to Electromagnetic Interaction Problems," Mississippi State University, *Mathematics Note* 27.

Dolph, C.L., and S.K. Cho (1980), "On the Relationship Between the Singularity Expansion Method and the Mathematical Theory of Scattering," *IEEE Trans. Antennas Propagat.*, AP-28, 888-897.

--------, V. Komkov, and R.A. Scott (1980), "A Critique of the Singularity Expansion and Eigenmode Expansion Methods," in V.K. Varadan, and V.V. Varadan (Eds.), *Acoustic, Electromagnetic, and Elastic Wave Scattering -- Focus on the T-Matrix Approach*, Oxford: Pergamon Press.

Flammer, C. (1957), *Spheroidal Wave Functions*, Stanford, CA: Stanford University Press.

Foster, R.M. (1924), "A Reactance Theorem," *Bell System. Techn. J.*,3, 259-267.

-------- (1955), "Passive Network Synthesis," Polytechnic Institute of Brooklyn, *Proceedings of the Symposium on Modern Network Synthesis*.

Franceschetti, G. (1976), "Topics in Advanced Antenna Theory," Department of Information Engineering, University of Illinois at Chicago Circle, *Communications Laboratory Report 76-2*.

Granzow, K.D. (1966), "Transient Spherical Waves," The Dikewood Corporation, *Theoretical Note* 24.

Guillemin, E.A. (1977), *Synthesis of Passive Networks*, Huntington, N.Y.: Krieger.

Hallén, E. (1930), "Uber die elektrischen Schwingungen in drahtformigen Leitern," *Uppsala Universitete Arsskrift*, No. 1, 1-102.

Harrington, R.F. (1968), *Field Computation by Moment Method*, New York: McMilan.

Hess, R.F. (1975), "EMP Coupling Analusis Using the Frequency (Transfer Function) Method With the SCEPTRE Computer Programm," *IEEE Trans. Electromag. Compat.*, EMC-17, 181-185.

Infeld, L. (1947), "The Influence of the Width of the Gap Upon the Theory of Antennas," *Quart. Appl. Math.*, 5, 113-132.

Jeffreys, H., and B. Jeffreys (1956), *Methods of Mathematical Physics*, Cambridge: University Press.

Jensen, R.W., and L.P. McNamee (Eds.) (1976), *Handbook of Circuit Analysis Languages and Techniques*, Englewood Cliffs, N.J.: Prentice-Hall.

Jones, D.S. (1964), *The Theory of Electromagnetism*, New York: MacMillan.

Karr, P.R. (1951), "Radiation Properties of Spherical Antennas as a Function of the Location of the Driving Force," *J. Res. Nat'l Bur. Stand.*, 46, 411-436.

King, R.W.P. (1956), *The Theory of Linear Antennas*, Cambridge, Mass.: Harvard Univ. Press.

———————— (1967), "The Linear Antenna — Eighty Years of Progress," *Proc. IEEE*, 55, 2-16.

———————— (1969), "The Loop Antenna for Transmission and Reception," in R.E. Collin, and F.J. Zucker (Eds.), *Antenna Theory*, New York: McGraw-Hill.

Landt, J.A., E.K. Miller, and M.L. VanBlaricum (1974), "WT-MBA/LLL1B: A Computer Program for the Time Domain Electromagnetic Response of Thin-Wire Structures," Lawrence Livermore National Laboratory, *Interaction Note* 210.

Langenberg, K.-J. (1978), "Zur transienten Strahlung von Linearantennen und Systemen von Linearantennen," Universitat des Saarlandes, Habilitationsschrift.

Lee, K.S.H. (1978), "Two Parallel Terminated Conductors in External Fields," *IEEE Trans. Electromag. Compat.*, EMC-20, 288-295.

Lee, S.W., and B. Leung (1972), "The Natural Resonance Frequency of a Thin Cylinder and Its Application to EMP Studies," University of Illinois, *Interaction Note* 96.

Liu, T.K., and F.M. Tesche (1976), "Analysis of Antennas and Scatterers with Nonlinear Loads," *IEEE Trans. Antennas Propagat.*, AP-24, 131-139, also as Interaction 223, May 1975.

————————, F.M. Tesche, and F.J. Deadrick (1977), "Transient Excitation of Antennas with a Nonlinear Load: Numerical and Experimental Results," *IEEE Trans. Antennas Propagat.*, AP-25, 539-542.

McLachlan, N.W. (1947), *Theory and Application of Mathieu Functions*, Oxford: Clarendon Press.

Marin, L. (1972), "Natural Mode Representation of Transient Scattering From Rotationally Symmetric, Perfectly Conducting Bodies and Numerical Results for a Prolate Spheroid," Northrop Corporate Laboratories, *Interaction Note* 119.

-------- (1974), "Natural Modes of Certain Thin-Wire Structures," The Dikewood Corporation, *Interaction Note* 186.

--------, and R.W. Latham (1972), "Analytical Properties of the Field Scattered by a Perfectly Conducting, Finite Body," Northrop Corporate Laboratories, *Interaction Note* 92.

--------, and T.K. Liu (1976), "A Simple Way of Solving Transient Thin-Wire Problems," *Radio Sci*, 11, 149-155, also as Interaction 253 Oct 1975.

Martinez, J.P., Z.L. Pine, and F.M. Tesche (1972), "Numerical Results of the Singularity Expansion Method as Applied to a Plane Wave Incident of a Perfectly Conducting Sphere," The Dikewood Corporation, *Interaction Note* 112.

Matthaei, G.L. (1954), "Some Techniques for Network Synthesis," *Proc. IRE*, 42. 1126-1137.

Meixner, J., F.W. Schäfke, and G. Wolf_ (1980), *Mathieu Functions and Spheroidal Functions and Their Mathematical Foundations*, Berlin-Heidelberg-New York: Springer.

Michalski, K.A., and L.W. Pearson (1979), "Synthesis Methods Applicable to SEM Pole-Pair Admittances," University of Kentucky, *Interaction Note* 407.

Miller, E.K., F.J. Deadrick, and J.A. Landt (1976), "Time-Domain Analysis of Nonlinear Loads," Lawrence Livermore National Laboratory, Report UCRL-52172.

Morse, P.M., and H. Feshbach (1953), *Methods of Theoretical Physics*, New York: McGraw-Hill.

Oguchi, T. (1970), "Eigenvalues of Spheroidal Wave Functions and Their Branch Points for Complex Values of Propagation Constants," *Radio Sci.*, 5, 1207-1214.

Pearson, L.W. (1979), "Applications of the Singularity Expansion Method," in Short Course Notes: *Numerical and Asymptotic Techniques for Electromagnetics and Antennas*, Syracuse University and The University of Illinois.

-------- (1981), "The Evidence Which Bears on the Left Half Plane Asymptotic Behavior of the SEM Expansion of Surface Currents," *Electromagnetics*, Vol. 1, No. 4, Oct-Dec 1981.

--------, and Y.M. Lee (1982), "SEM Parameter Extraction Through Transient Surface Current Measurement Using King-Type Probes," *IEEE Trans. Antennas Propagat.*, to appear, also as Sensor & Simulation 265, Dec 79.

--------, and D.R. Roberson (1980), "The Extraction of the Singularity Expansion Description of a Scatterer from Sampled Transient Surface Current Response," *IEEE Trans. Antennas Propagat.* AP-28, 182-190.

————————, and D.R. Wilton (1981), "Theoretical Aspects of the Physical Realizability of Broad-Band Equivalent Circuits for Energy Collecting Structures," *IEEE Trans. Antennas Propagat.*, AP-29, 697-707.

Pease, M.C. (1965), *Methods of Matrix Algebra*, New York: Academic Press.

Ramm, A.G. (1972), "Eigenfunction Expansion of a Discrete Spectrum in Diffraction Problems," *Raido. Eng. Electron. Phys.*, 18, 364-369.

———————— (1980), "Theoretical and Practical Aspects of Singularity and Eigenmode Expansion Methods," *IEEE Trans. Antennas Propagat.*, AP-28, 897-901.

Ramo, S., J.R. Whinnery, and T. VanDuzer (1965), *Fields and Waves in Communication Electornics*, New York: Wiley.

Rao, S.S.M., D.R. Wilton, and A.W. Glisson (1981), "Electromagnetic Scattering by Surfaces of Arbitrary Shape," *IEEE Trans. Antennas Propagat.*, to appear.

Sancer, M.I., and A.D. Varvatsis (1980), "Toward an Increased Understanding of the Singularity Expansion Method," R&D Associates, *Interaction Note* 398.

Schafer, R.H., and R.G. Kouyoumjian (1975), "Transient Currents on a Cylinder Illuminated by an Impulsive Plane Wave," *IEEE Trans. Antennas Propagat.*, AP-23, 627-638.

Schaubert, D.H. (1979), "Application of Prony's Method to Time-Domain Reflectometer Data and Equivalent Circuit Synthesis," *IEEE Trans. Antennas Propagat.*, AP-27, 180-184.

Schelkunoff, S.A. (1944), "Representation of Impedance Functions in Terms of Resonant Frequencies," "*Proc. IEEE*, 32, 83-90.

————————, (1952), *Advanced Antenna Theory*, New York: Wiley.

————————, and H.T. Friis (1952), *Antennas: Theory and Practice*, New York: Wiley.

Schuman, H. (1974), "Time-Domain Scattering From a Nonlinearly Loaded Wire," *IEEE Trans. Antennas Propagat.*, AP-22, 611-613.

Shanks, D. (1955), "Nonlinear Transformations of Diversent and Slowly Converging Sequences," *J. Math. and Phys.*, 34, 1042.

Sharpe, C.B., and C.J. Roussi (1979), "Equivalent Circuit Representation of Radiation Systems," University of Michigan Radiation Laboratory, *Interaction Note* 361.

Singaraju, B.K., and R.L. Gardner (1976), "Transient Response of a Helical Antenna," Air Force Weapons Laboratory, *Interaction Note* 297.

--------, D.V. Giri, and C.E. Baum (1976), "Further Developments in the Application of Contour Integration to the Evaluation of the Zeros of Analytic Functions and Relevant Computer Programs," Air Force Weapons Laboratory, *Mathematics Note* 42.

Stakgold, I. (1967), *Boundary Value Problems of Mathematical Physics*, London: Macmillan.

Stratton, J.A., and L.J. Chu (1941), "Steady-State Solutions of Electromagnetic Field Problems. II: Forced Oscillations of a Conducting Sphere," *J. Appl. Phys.*, 12, 236-240.

Streable, G.W., and L.W. Pearson (1981), "A Numerical Study on Realizable Broadvand Equivalent Admittances for Dipole and Loop Antennas," *IEEE Trans. Antennas Propagat.*, AP-29, 707-717.

Tai, C.-T. (1971), *Dyadic Green's Functions in Electromagnetic Theory*, Scranton, Pens.: Intext.

-------- (1981), "Complex Singularities of the Impedance Functions of Antennas," *Electromagnetics*, Vol. 1, No. 4, Oct-Dec 1981.

Tesche, F.M. (1973), "On the Analysis of Scattering and Antenna Problems Using the Singularity Expansion Technique," *IEEE Trans. Antennas Propagat.*, AP-21, 53-62, also as Interaction 102, April 1972.

--------, and D.V. Giri (1981), "On the Singularity Expansion Method for Analysis of Antennas in Conducting Media," *Electromagnetics*, Vol. 1, No. 4, Oct-Dec 1981

--------, and T.K. Liu (1975), "Transient Response of Antennas With Non-Linear Loads," *Electron. Lett.*, 11, 18-19.

--------, A.R. Neureuther, and R.E. Stovall (1976), "The Analysis of Monopole Antennas Located on a Spherical Vehicle: Part 2, Numerical and Experimental Results," *IEEE Trans. Electromag. Compat.* EMC-18, 8-15.

Thal, H.L. (1978), "Exact Circuit Analysis of Spherical Waves," *IEEE Trans. Antennas Propagat.*, AP-26, 282-287.

Umashankar, K.R., and D.R. Wilton (1974), "Transient Characterization of Circular Loop Using Singularity Expansion Method," University of Mississippi, *Interaction Note* 259.

VanBladel, J. (1964), *Electromagnetic Theory*, New York: McGraw-Hill.